THE BEHAVIOR OF MASONRY STIFFENING WALLS BASED ON THE FULL-SCALE RESEARCH

DOCTORAL DISSERTATION IN THE DISCIPLINE CIVIL ENGINEERING, GEODESY AND TRANSPORT

Krzysztof GRZYB

PROMOTOR

Professor Phd, CEng Radosław JASIŃSKI

GLIWICE 2023

CONTENTS

LIST OF BASIC SYMBOLS

Capital Latin letters

A	–	horizontal section of the masonry wall,
A_c	–	the area of the horizontal layout of the walls,
D	–	ductility index,
E	–	modulus of elasticity,
E_v	–	the shear modulus,
F_t	–	tensile force,
G	–	the shear modulus,
G_f	–	fracture energy,
H	–	storey height,
H_A	–	load (force) acting on stiffening wall A,
H_B	–	load (force) acting on stiffening wall B,
$H_{cr,1}$	–	cracking force in the initial phase,
H_{cr}	–	cracking force,
H_{res}	–	residual force,
H_{tot}	–	total load acting on a building,
H_u	–	maximum horizontal force,
H_x, H_i	–	horizontal shear force,
$^{cal}H_{cr,1}$	–	analytical cracking force in the initial phase,
$^{cal}H_{cr}$	–	analytical cracking force,
$^{cal}H_u$	–	analytical maximum horizontal force,
$^{cal}H_{res}$	–	analytical residual force,
$^{num}H_{cr}$	–	numerical cracking force,
$^{num}H_u$	–	numerical maximum horizontal force,
I	–	the horizontal cross-sectional moment of inertia of the wall element in the direction of bending,
K_{cr}	–	the stiffness of the stiffening wall in the elastic phase,
K_{res}	–	the stiffness of the stiffening wall in the post-peak residual phase,
$K_{tot,cr}$	–	the total stiffness in the elastic phase,
$K_{tot,cr,1}$	–	the total stiffness in the initial phase,
$K_{tot,res}$	–	the total stiffness in the post-peak residual phase,

$K_{tot,u}$ – the total stiffness in the nonlinear phase,
K_u – the stiffness of the stiffening wall in the nonlinear phase,
M – in-plane bending moment,
N_{hd} – the vertical force acting in the plane of the wall, caused by a horizontal design load,
N_{Rd} – design load-bearing capacity of the wall due to vertical loads,
N_{Sd} – design vertical force acing in the plane of the wall,
N_{vd} – the vertical force caused by a vertical load,
O – the geometrical center of the building plan,
O_1 – the geometrical center of the stiffening wall plan,
P – in-plane vertical force,
P_c – total vertical load on the walls,
Q – shear force taken up by the stiffening wall, determined in the elastic stage in the middle of the storey height,
R_{sq} – compressive strength of the masonry determined without the compressive stresses,
V – lateral force (shear force),
V_{Sd} – design shear force caused by horizontal forces in the plane of the wall,
V_{Rd} – design load-bearing capacity of the checked wall section.

Small Latin letters
c – cohesion,
d – the length of the stiffening wall,
f_c – compressive strength,
f_{v0} – initial shear strength,
f_{vd} – design shear strength of the masonry in the direction parallel to the bed joints,
h – clear storey height of the wall,
h_{eff} – effective height of the wall,
h_n – the height of the lintel,
h_{tot} – the overall height of the stiffening wall,
l – length of the masonry wall,
l_c – length of the compressed part of the wall cross-section,
l_s – distance to the adjacent stiffening wall,
t – the thickness of the masonry wall,
u_x – horizontal displacement in the direction x,
u_y – horizontal displacement in the direction y,
w – uniformly distributed wind load,
y – distance from the center of gravity of the wall (together with flanges).

Capital Greek letters

$^{A}\Delta_w$ –   displacement of the lintel,

$^{B}\Delta_w$ –   displacement of the bottom spandrel,

$^{P}\Delta_w$ –   displacement of the vertical pillar,

Δ_{tot} –   the total displacement of the building,

Δ_v –   the shear deformation,

Θ –   strain angle (elastic phase) or shear deformation angle (nonlinear phase),

Θ_A –   shear deformation angle of stiffening wall A,

Θ_{adm} –   the shear deformation angle (polish standard PN-B-03264:2002),

Θ_B –   shear deformation angle of stiffening wall B,

Θ_{cr} –   shear deformation angle corresponding to cracking force,

$\Theta_{cr.1}$ –   shear deformation angle corresponding to cracking force in the initial phase,

Θ_{mv} –   the mean value of the deformation angle of stiffening walls,

Θ_{res} –   shear deformation angle corresponding residual force,

Θ_{Sd} –   the angle of shear deformation calculated for the characteristic values of horizontal shear forces,

Θ_u –   shear deformation angle corresponding to maximum horizontal force.

Small Greek letters

δ_{ave} –   average displacement of the storey at the extreme points of the structure,

δ_{max} –   the maximum displacement of the storey at the extreme points of the structure,

ε –   Strain,

ε_{pl} –   plastic strain,

η_i –   influence coefficient of space performance for each storey of a building,

η_E –   coefficient taking into account the reduction of masonry creep,

φ_∞ –   the final value of the creep coefficient equals,

λ –   shear deformation coefficient,

μ –   friction coefficient,

ν –   Poisson's ratio,

ρ_n –   reduction factor depending on edge restraint or stiffening of the wall,

σ_c –   compressive stress,

σ_n –   the average vertical compression,

σ_t –   tensile stress,

τ_{max} –   the maximum value of shear stress,

ω –   proportions of the shear deformation angles.

1. INTRODUCTION

This monograph is written while the word *crisis* is inflected in all ways. At the end of 2019, the Covid pandemic broke out and paralyzed the normal functioning of the world. The significant problem was the enormous amount of misinformation [139] during the pandemic and the widespread dissemination of fake news. Incomplete three years later - at the beginning of 2022, the war began in Ukraine, resulting in a refugee crisis in Europe. According to statistics [155], more than 5.5 million people, mainly women and children, fled Ukraine on 1 May. However, noticeable geopolitical tensions and turbulences in the economy are not the only challenges facing civilization.

The modern direction of construction development aims to limit negative climate changes, and one of the goals is to reduce CO^2 emissions[1] and use sustainable materials. The eco-strategies in the civil engineering industry are anticipated to result in net-zero emissions by the concrete industry by 2050 [2]. One of the ideas is to replace the conventional clinker (i.e. limestone). In the calcination of the limestone, carbon dioxide is one of the reaction products. Fly ash, foundry sand or filter clay are incorporated as a partial replacement for the clinker. Other strategies include the application of alternative binders or aggregates.

However, it should be mentioned that buildings (implicitly the construction industry) influence the environment during the production of building materials but also throughout the entire life cycle. The Joint Research Centre (JRC) of the European Commission (EC) and Building Performance Institute Europe have documented various initiatives that come from countries to integrate the whole life cycle (WLC) of buildings, Global Warming Potential (GWP) and Life Cycle Assessment (LCA) requirements.

The European Commission defined the concept of Level(s) to tackle environmental challenges posed by construction materials and whole buildings. This approach attempts to constitute a common language in an evaluation set of indicators that can be used to measure and manage the performance of residential and office buildings across Europe [48]. Level(s) scheme consists of sixteen indicators corresponding to six macro-

---

[1] Intergovernmental Panel on Climate Change (IPCC) 'Climate change 2022 mitigation of climate change', 2022

objectives – Fig. 1.1. That life cycle approach is split into three levels that are connected with construction stages:

- Level 1 – to set qualitative objectives at the conceptualization stage,
- Level 2 – to assess quantitative performance at the design and construction stages,
- Level 3 – to evaluate and monitor the performance after completion for as-built and in-use performance.

The careful analysis of macro-objectives indicates the foundations of modern construction based on sustainable materials and optimization of the life cycle cost and value of buildings.
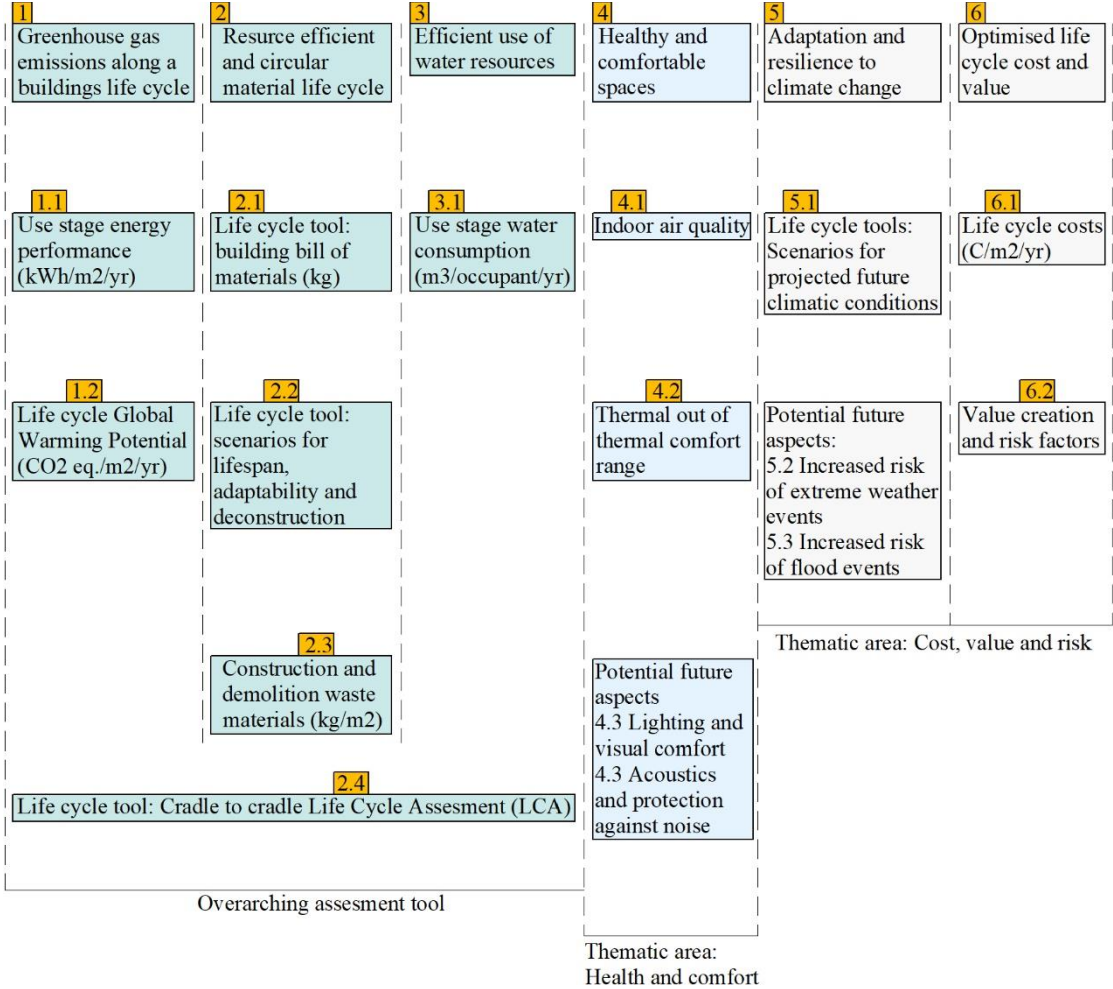

Fig. 1.1 Level(s) scheme with indicators, followed by [48]

Sustainable material will stand out with good thermal insulation performance (reducing the cost of additional wall insulation), fire resistance that meets stringent fire safety requirements, and proper structural performance expected in construction materials.

Autoclaved aerated concrete (AAC) is a material which fits into this philosophy due to its good strength-to-weight ratio and well-desired performance parameters. However, the properties are determined by microstructure (void-paste system) and composition (type of binder, method of pore-formation and curing) [118, 128]. AAC is produced from raw materials – cement, sand water gypsum, lime and aluminum powder [86]. The advantage of this material is also its full recyclability [19, 132, 160]. It has been proven that the use of autoclaved aerated concrete walls leads to a reduction of energy consumption in residential buildings by 7%. Moreover, each square meter of AAC can reduce 350 kg of emission of CO_2 throughout the life cycle of a building [129].

Autoclaved aerated concrete is commonly used to produce masonry units or greater prefabricated elements. Load-bearing walls, partition walls or infill ones are successfully erected with AAC. Though many studies relate to recognising AAC material characteristics, relatively few analyses concern structures made of this material. The masonry unit does not work separately, but the adjacent structure limits its deformations. The interaction between the elements and the mechanics of the structure can be captured on models of larger dimensions.

The development of ecological and sustainable buildings makes AAC applicable in construction. Residential buildings are often erected as load-bearing structures, and multi-storey buildings are built using skeletal frames, in which masonry walls act as filling. Vertical loads are considered the most critical loads on masonry walls in wall-bearing systems. In designing, horizontal loads caused by environmental influences, such as wind, should also be considered. Although the horizontal load on the building can be caused by various factors, such as the uneven settlement of the ground or influences from mining, it is often overlooked. The problem has its historical background - masonry walls were characterized by considerable thickness in former residential buildings, and the horizontal shear problem could be negligible. Contemporary trends aim to optimize the walls' thickness while ignoring the complete computational verification of walls for all impacts - both vertical (induced by dead and live-load) and horizontal (shear).

Stiffening walls are load-bearing elements that transfer horizontal forces to the foundation safely. The primary construction role of the stiffening elements is to ensure the geometrical stability of the building, limiting horizontal deformations and ensuring the comfort of use. Although the significance of these elements is crucial - the awareness of designing masonry stiffening walls is low. Buildings with thinner and thinner walls require the development of computational models and design methods based on experimental background and numerical research.

2. MOTIVATION AND ASSUMPTIONS OF THE DISSERTATION

2.1. Motivation

Masonry stiffening walls have a different specificity than the corresponding reinforced concrete stiffening elements. The masonry is an anisotropic structure in which the mechanical parameters are not a simple sum of individual components. The complex stress state in shear masonry walls results from the simultaneous action of horizontal and vertical loads. The stiffening walls are compressed, sheared and simultaneously bent in the plane, significantly hindering experimental research and correct inference. Using advanced numerical models without validation based on experimental research seems to be the wrong approach.

The lack of a comprehensive scientific approach to stiffening walls creates a significant cognitive gap and demand for miscellaneous research. The justification for writing the doctoral thesis is the need for consistent analysis of stiffening walls from theoretical and experimental points of view. This study was motivated by a few factors:

- omitting the problem of horizontal shearing of walls while reducing the thickness of the wall,
- unclear and imprecise standard recommendations for the design of stiffening walls,
- unknown actual redistribution of internal forces in masonry stiffening walls (even though Eurocode 6 allows for redistribution of internal forces up to 15%),
- lack of a consistent methodology for determining the stiffness of stiffening walls and load distribution,
- no method for determining the location of the torsion center of the building and taking into account the effect of building torsion in the calculations,
- the influence of openings on the stiffness of walls and mechanics of damage,
- no studies (experimental research) of stiffening walls on full-scale models of buildings under monotonical horizontal load.

2.2. Objectives

The primary research problem is the behavior of the stiffening wall made of autoclaved aerated concrete (AAC), both in the elastic and non-linear range. The work is based on a theoretical and experimental approach and can be divided into intermediate goals such as:

- state of knowledge in domestic and foreign literature on stiffening masonry walls,
- systematization of standard provisions concerning the discussed issues,
- method of calculating the stiffness of stiffening walls,
- distribution of loads on the stiffening walls,
- determination of the redistribution of internal forces,
- analysis of the crack propagation and crack morphology of stiffening walls,
- proposal of a method for calculating the location of the torsion center of the building,
- describing the behavior phases of stiffening walls in elastic and post-elastic states,
- numerical analysis of stiffening walls using the finite element method (FEM).

2.3. Statements of the thesis

The in-depth analysis of the state of knowledge allowed the following theses to be put forward:

1. The stiffness of individual parts of the structure determines the distribution of internal forces in masonry buildings.
2. The linear behavior of an unreinforced masonry structure subjected to horizontal shear is small and ends at approximately 30% of the maximum force.
3. The lateral load of the building causes a significant decrease in the structure's stiffness.
4. A building with asymmetric stiffness distribution, subjected to horizontal shear, undergoes rotation and translation.
5. The location of the building torsion center results from the stiffness distribution of the structural elements.
6. The selection method of the masonry homogenization affects the accuracy and reliability of the numerical representation of the stiffening walls.

2.4. Scope

The scope of the monograph encloses theoretical and experimental research undertaken to verify statements (theses) and determine their truth or denial. The monograph encloses the analysis of unreinforced masonry structures (URM) under the monotonic horizontal load. Experimental and theoretical analyzes were undertaken to achieve the set goals of the dissertation. The scope of the work includes the following:

- state of the art regarding stiffening masonry walls,
- own experimental program,
- Finite Element Method analysis,
- proposal of an analytical method for determining the stiffness of shear walls,
- discussion and conclusions.

The doctoral monograph has been divided into chapters devoted to particular issues. Chapter 3 reviews standard regulations concerning stiffening walls, selected tests of unreinforced masonry walls (URM) and buildings, calculation procedures and numerical wall homogenization techniques. Chapter 4 determines the main assumptions of the research campaign and encloses test details as the construction of models, test stand and measuring method. Chapter 5 examines the test results in linear and nonlinear behavior phases of stiffening walls. Chapter 6 uses a digital image correlation (DIC) system to examine crack morphology and crack patterns. Chapter 7 investigates the stiffening walls in numerical calculations. Section 7.1 concerns its own homogenization technique, and section 7.2 encloses advanced nonlinear calculations.

Chapter 8 analyses the results in a critical approach and proposes an engineering method for calculating the stiffening walls. Chapter 9 provides a conclusion and determines the further scope of work. The appendix contains detailed construction drawings of tested walls.

3. EVALUATION OF THE STATE OF KNOWLEDGE

3.1. Standard arrangements for stiffening masonry walls

3.1.1. Regulations in the Eurocode 6

Regulations on the design of stiffening walls in the Eurocode are limited, and the information contained therein is made to general statements. Following the [N7] 1.5.10.10 stiffening wall is a structural element situated perpendicular to other walls, which supports them with the taking of horizontal forces, preventing buckling and contributing to the stability of the building. The stiffening elements are mainly subjected to the horizontal loads acting in the plane of the walls. Therefore, these are primarily shear in the wall plane, which can simultaneously transfer other forces (axial, bending moments) depending on other functions and load distribution in the building. The term stiffening walls is often replaced with shear walls (in this dissertation, these terms are also used interchangeably). In the regulations of Eurocode 6, the definition of a shear wall - point 1.5.10.9 - is distinguished and denotes shear walls whose task is to transfer horizontal forces acting in the wall plane. The separation of the terms stiffening wall and shear wall may cause inaccuracies in naming the walls. Based on the Eurocode, the shear wall can be sheared and at the same time not have a stiffening function. However, it should be considered that if the slab structure allows the horizontal force to be transferred to the walls, it will still function as a stiffening.

In the primary part of Eurocode 6, the chapter on the calculation of masonry structures provides information on calculating the effective height of a wall (section 5.5.1.2):

a) in calculations of the effective height of the wall should be considered the relative stiffness of the structural elements connected to the wall, and the efficiency of the connections,

b) stiffening of the load-bearing wall can be realized by floor, roofs or transversely situated walls or other rigid structural elements,

14

c) the wall stiffening along its vertical edge may be included in the calculations in two cases: when no cracks are expected between the analyzed wall and the stiffening wall (walls are characterized by similar deformability and evenly load) or when the connection has a load-bearing capacity allowing for the transfer of internal forces arising from in combination. Increasing the load capacity of the joint can be obtained by using anchors or construction connectors,

d) the stiffening wall should meet the conditions:

- thickness greater than or equal to 0.3 of the effective thickness of the wall it stiffens,

- a length greater than or equal to 0.2 of the clear height of the wall it stiffens,

e) there may be openings in the stiffening wall; however, the minimum length of the wall between the openings that connect to the stiffened wall should meet the conditions in Fig. 3.1 and should extend beyond each opening for a length of at least 0.2 of the storey height,
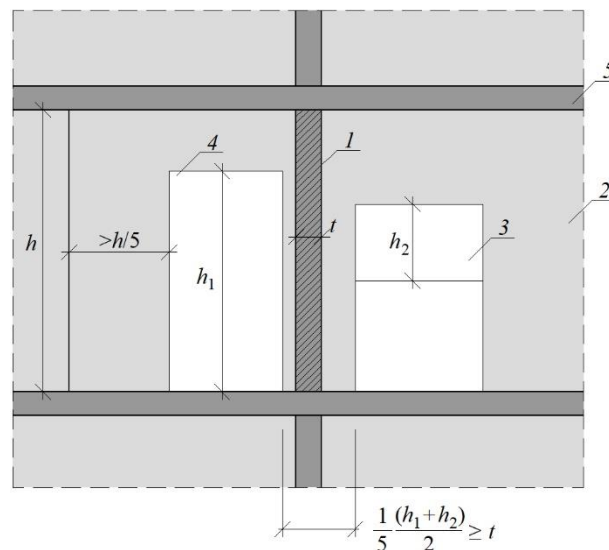
Fig. 3.1 Minimum length of stiffening wall with openings: 1 – stiffened wall, 2 – stiffening wall, 3 – window opening, 4 – door opening, 5 – slab

f) stiffening of the walls can be performed by elements other than masonry ones if their stiffness meets the conditions for masonry walls (point d), and the connections between the walls made of ties, anchors or connectors can absorb compressive or tensile forces occurring in the joint,

g) stiffened walls that meet the following conditions are calculated only as walls restrained at the top and bottom:

- walls stiffened along two vertical edges and $l \geq 30t$,

- walls stiffened along one vertical edge and $l \geq 15t$,

  where:

  l - is the length of the wall between the stiffening walls,

  t - thickness of the stiffened wall,

h) the weakening of stiffened walls above the normative ones - other than in point 6.1.2.1(7), with vertical chases or recesses requires a calculated reduction of the wall thickness t, or the establishment of a free wall edge in the place of chase or recesses. Assuming a free wall edge is required whenever the remaining wall thickness with a chase is made is less than half the wall thickness,

i) it is calculation assumed that the walls have free edges at the opening when at least one of the following conditions is met:

- the opening has a clear height of more than 0.25 of the clear wall height,
- the clear opening width is greater than 0.25 of the wall length,
- the opening has an area greater than 0.1 of the total wall,

j) the effective height of the wall is calculated from the formula (3.1).

$$h_{eff} \; = \; \rho_n \cdot h \qquad\qquad (3.1)$$

where:

h_{eff} – the effective height of the wall,

ρ_n – reduction factor depending on edge restraint or stiffening of the wall, where n takes the values 2,3 or 4,

h – clear storey height of the wall.

Section 5.5.3 of [N7] includes provisions for masonry shear walls subjected to shear loading. Following the standard, elastic stiffness is assumed in the calculations of shear walls, considering fragments of transverse walls connected to the stiffening wall (so-called flanged walls). The effect of shear deformations on the wall stiffness can be neglected if the wall height is twice its length. The cooperating fragments of the transverse walls may be considered in the calculations. However, the connection between the structural elements (stiffened wall and the stiffening wall) must transfer shear forces. Moreover, the part cooperating with the stiffened wall does not lose its stability – it cannot buckle within the assumed length. The length of the perpendicular wall, which can act as a flange as shown in Fig. 3.2, increases the actual thickness of the stiffening wall in both directions by the smallest of the given values:

- $h_{tot} / 5$, where h_{tot} is the overall height of the stiffening wall,
- $l_s / 2$, where l_s - distance to the adjacent stiffening wall,
- distance to the edge of the wall,
- $h / 2$ where h – clear wall height,
- $6t$ where t – intersecting wall thickness (in the draft of the new version of the Eurocode 6, the thickness of $8t$ was proposed [N18]).
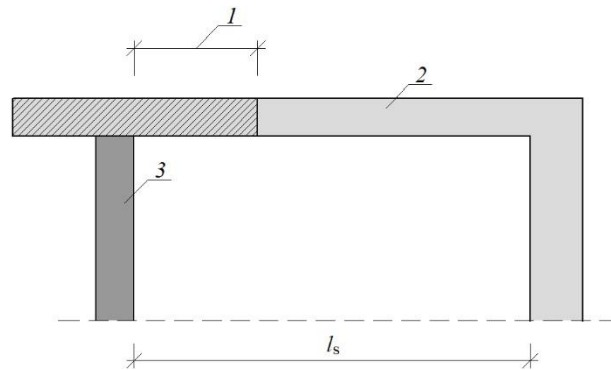

Fig. 3.2 Flange widths that can be assumed for shear walls: 1 – a fragment of the intersecting wall, 2 – intersecting wall, 3 – shear wall, l_s – the distance between shear walls

Openings with dimensions smaller than $h/4$ or $l/4$, made in walls transverse to the stiffening wall, may be neglected by calculations. The edges of openings with dimensions larger than $h/4$ or $l/4$ are taken as wall ends.

The distribution of loads on the stiffening walls depends on the construction of the entire building. Horizontal forces can be transferred to the walls proportionately to their stiffness, provided the floors act as a rigid diaphragm. Suppose the horizontal forces act on an eccentricity relative to the center of gravity of the stiffening walls or the layout of the stiffening walls is asymmetrical. In that case, the torsion effect should be considered in the calculations. It is worth mentioning that this situation occurs in engineering practice in most cases. However, the standard recommendations do not indicate a consistent design methodology for considering the torsion effect or the rules for the possibility of omitting that effect.

When the floors (slabs) cannot act as a rigid diaphragm (the standard specifies the case of precast concrete units that are not interconnected), stiffening walls should take over the horizontal forces from the floor to which they are directly connected. The standard does not specify when it can be unequivocally stated that the floor is not a rigid diaphragm. The exception is the computational semi-rigid analysis, i.e. calculations in a non-linear range. The maximum horizontal load on the calculated stiffening wall can be reduced to 15%, provided that the load on parallel stiffening walls is appropriately

increased. It can therefore be assumed that the standard allows redistribution of internal forces up to a maximum of 15%.

The vertical load applied to bidirectional floor slabs may be distributed evenly across the supporting walls of the floor, provided that the analysis assumes a relevant design load that assists the shear resistance. For the walls of the lower storeys, not loaded directly, the load taken from the area separated at an angle of 45^0 from the slabs or roof panels spanned in one way - can be treated as axial load. The shear stress distribution can be assumed as constant along the compressed part of a wall.

3.1.2. Regulations in the polish standard for masonry structures PN-B-03002:2007

According to the Polish standard [N15], a stiffening wall is a wall transferring forces acting in its plane and a wall located perpendicularly to the stiffened wall, constituting its support when absorbing loads.

Chapter 5.4 of the Polish standard is dedicated to stiffening walls. In the calculations of this type of structural elements, in addition to internal forces resulting from vertical loads, forces acting in the plane of the wall - resulting from the building's spatial construction - are taken into account. The following walls are distinguished:

- stiffening walls due to horizontal load,
- stiffening walls due to vertical displacements of the subsoil.

Case 1: Stiffening walls due to horizontal loads

In the calculations of buildings with reinforced concrete or prestressed slabs, it is assumed that the horizontal load is distributed on the stiffening walls in proportion to their bending stiffness, considering the openings in the walls. The horizontal load is parallel to the direction of the stiffening walls. As a result, the walls must be analyzed separately in the transverse and longitudinal direction of the building. In cases where the floors are not a rigid slab - forces are transferred to the stiffening wall only in the places of direct connection of the wall and the floor. The effect of torsion of the stiffening structure on the distribution of the load on individual stiffening walls and spatial stiffness should be taken into account in the case of:

- the asymmetric layout of the stiffening walls,
- when the resultant horizontal force is located eccentrically to the center of gravity of the layout of the stiffening wall (on an eccentricity greater than 0.05 of the width or length of the building – Fig. 3.3).
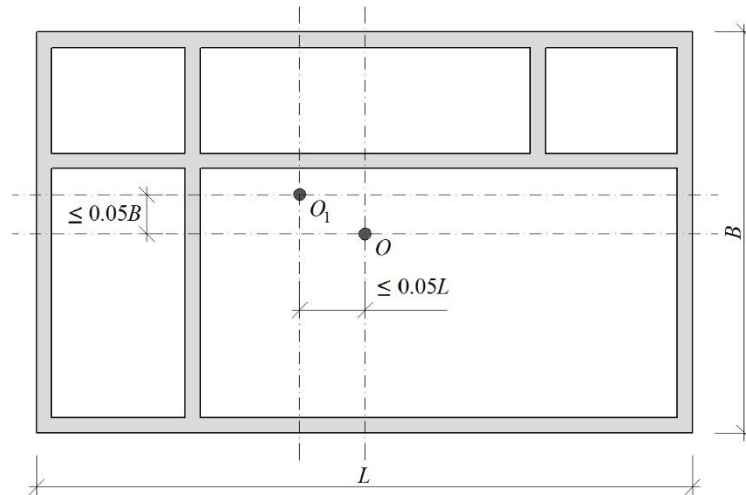
Fig. 3.3 The principle of the layout of stiffening walls: O – the geometrical center of the building plan, O_1 – the geometrical center of the stiffening wall plan

There is a possibility of shaping a stiffening wall with a complex layout – Fig. 3.4. However, the restrictions apply to the part of the wall located perpendicularly to the stiffening wall:

- the length of which does not exceed 1.2 m
- whose length does not exceed 0.2 of the calculated wall length,
- within which no door or window opening was made,
- is connected to the rest of the stiffening walls as required.

If one of the above conditions is not met, the stiffening wall with a complex layout must be analyzed separately as two separate stiffening parts.
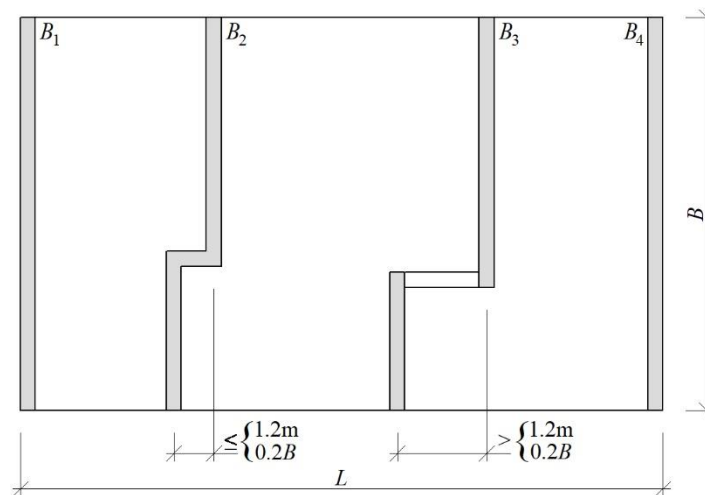

Fig. 3.4 Stiffening wall with a complex layout: B_1, B_2, B_4 – the stiffening wall treated as single stiffening strip, B_3 - the stiffening wall treated as two independent stiffening strip

The guidelines for calculating the length of the sections cooperating with the stiffening wall (flange) are identical to the requirements of Eurocode 6. The design

19

increase in the stiffness and load capacity of the structural stiffness is possible when:

- the height of the wall is not more than twice its length,
- the connection between the section transverse to the wall and the stiffening wall can transfer shear forces,
- the wall flange will not buckle.

When the stiffening wall is not connected with the transverse wall at the level of masonry units - it should be assumed that the entire transverse force is taken over by the reinforced concrete tie beam connecting both walls at the floor level (provided that the load capacity of the tie beam was sufficient and calculated in accordance with the polish standards PN-B-03264:2002). The length of the flange used in the calculations should not be greater than the smallest of the values determined in the same way as in Eurocode 6 (0.2 of the total height of the calculated stiffening wall h_{tot}; 0.5 of the distance to the adjacent stiffening wall l_s; distance to the edge of the wall; 0.5 of the clear storey height h; six times the flange thickness t).

The openings in transverse walls with dimensions smaller than $h/4$ or $l_s/4$ can be neglected in the calculations. If the openings are bigger, their edges should be treated as wall ends. A stiffening wall taking vertical loads other than its the own-weight requires a design check for both vertical and horizontal loads acting in the plane of the wall.

In a stiffening wall that takes vertical loads only resulting from its self-weight within one storey, the deformation angle Θ_{adm} should not exceed the limit value. Shear deformation is caused by the horizontal load acting in the plane of the wall. If the analyzed stiffening wall is also an external wall of the building, its load-bearing capacity should be checked due to horizontal loads acting perpendicularly to its plane. The calculation analysis of stiffening walls includes verification of the wall load capacity for vertical loads in the section above and below the floor and the middle part of the wall, taking the value of the force N_{Sd} as the sum of (3.2):

$$N_{Sd} = N_{vd} + N_{hd} \tag{3.2}$$

where:

N_{vd} – vertical force caused by a vertical load,

N_{hd} – vertical force acting in the wall plane caused by a horizontal design load.

When on the edges of a separated part of width b_0, the difference in stresses resulting from the vertical and horizontal loads is (3.3):

$$\sigma_1 - \sigma_2 \geq 0.33 \cdot \sigma_1 \tag{3.3}$$

Then the force N_{Sd} is (3.4):

$$N_{Sd} = \sigma_0 b_0 t = 0.83 \sigma_1 b_0 t \qquad (3.4)$$

where:

$\sigma_1 \geq \sigma_2$ the force N_{Sd} corresponds to the resultant of the block of evenly distributed stresses σ_0 occurring in the separated part of the wall – Fig. 3.5.

When the stresses on the edges of a separated part of width b_0 meet the following condition (3.5):

$$\sigma_1 - \sigma_2 < 0.33 \cdot \sigma_1 \qquad (3.5)$$

The force N_{Sd} is assumed to be (3.6):

$$N_{Sd} = \sigma_0 b_0 t = 0.5(\sigma_1 + \sigma_2) b_0 t \qquad (3.6)$$

For a fragment of a wall in which tensile stresses occur as a result of the combined horizontal and vertical loads, it is assumed that the force $N_{Sd} = 0$. The width b_0 should be taken as:

- $b_0 = b$ when $b \leq 1.0$ m,
- $b_0 = 1.0$ m when $b > 1.0$ m.
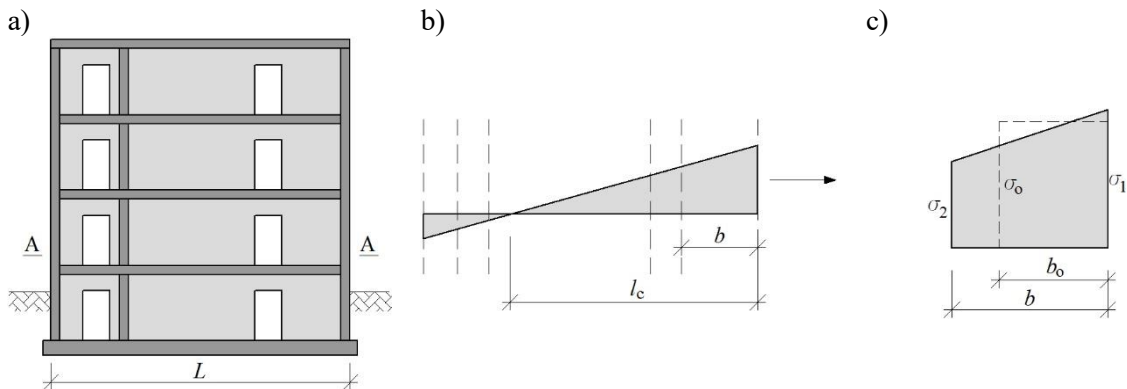
Fig. 3.5 Determining the value of N_{Sd} force: a) cross-section for calculations, b) the resultant diagram of vertical stresses from the simultaneous action of vertical and horizontal loads, c) the hypothetical part with a width of b_0 and solid stress σ_0 for determining the force N_{Sd}

The load capacity of the wall on horizontal loads acting in its plane is verified from the formula (3.7):

$$V_{Sd} \leq V_{Rd} \qquad (3.7)$$

where:

21

V_{Sd} - design shear force caused by horizontal forces in the plane of the wall - equivalent to the resultant of the shear stress block from the design values of actions,

V_{Rd} - design load-bearing capacity of the checked wall section, which is calculated as (3.8):

$$V_{Rd} = f_{vd}\, t l_c \qquad (3.8)$$

where:

f_{vd} – design shear strength of the masonry in the direction parallel to the bed joints,

t – wall thickness,

l_c – length of the compressed part of the wall cross-section.

The stiffening walls should be checked for not exceeding the limit value of the shear deformation angle Θ_{adm} from the general formula (3.9):

$$\Theta_{Sd} \leq \Theta_{adm} \qquad (3.9)$$

in which:

Θ_{Sd} – the angle of shear deformation calculated for the characteristic values of horizontal shear forces V_{Sk} (3.10) – Fig. 3.6:

$$\Theta_{Sd} = \frac{V_{Sk}}{0.2EA} \qquad (3.10)$$

where:

E – modulus of elasticity of the wall,

A – horizontal section of the wall,

Θ_{adm} – the limit value of the shear deformation angle.

The value of the shear deformation angle Θ_{adm} can be assumed for walls:
- with filled vertical joints from Table 3.1,
- with unfilled vertical joints, the values of shear deformation angles from Table 3.1 should be reduced by 50%.

Table 3.1

Maximum values of the shear deformation angle Θ_{adm}, mrad

Group of masonry unit	Cement mortar	Cement-lime mortar
group 1, except autoclaved aerated concrete units	0.4	0.5
group 2,3,4	0.3	0.4
autoclaved aerated concrete units	0.2	0.3

Fig. 3.6 Calculation model to determine the shear deformation angle Θ_{Sd} of a horizontally loaded stiffening wall

Masonry lintels acting as a horizontal spandrel of the vertical piers of the stiffening wall are checked using the formula (3.11) (if the condition is not met, a reinforced concrete lintel should be designed):

$$\frac{V_{Sd}}{0.75 t h_n} \leq f_{vd} \qquad (3.11)$$

where:

V_{Sd} – design shear force in the lintel; the share of the vertical load is usually neglected when the lintel is loaded with the floor,

t – wall thickness,

h_n – the height of the lintel, including the tie beam,

f_{vd} – design shear strength of the wall.

Case 2: Stiffening walls due to the displacement of the ground.

Chapter 5.4.3 regarded checking the load-bearing capacity of the stiffening walls due to the vertical displacements of the subsoil. The first assumption is that the vertical deformations of the ground under the building are transferred entirely to the stiffening wall. The cooperation of the building with the substrate, when calculating the deformation of the building subjected to vertical displacements of the ground, can be estimated using analytical models or programs based on the finite element method (FEM). When determining the flexural stiffness and the deformation state of the stiffening walls, the window and door openings shall be considered in the calculations. Calculations of stiffening walls due to vertical subsoil displacements consist in:

- checking the load-bearing capacity of the stiffening wall for vertical loads,
- checking the shear deformation angle of the wall caused by the characteristic values of vertical shear forces.

Stiffening walls subjected to vertical shear forces or substrate deformations should be checked according to the general formula (3.12) due to vertical compression and

23

horizontal wind loads (section 5.1 of the code, walls loaded mainly vertically). Moreover, the shear deformation angle should not exceed the limit value, following the formula (3.9).

$$N_{Sd} \leq N_{Rd} \qquad (3.12)$$

where:

N_{Sd} – vertical force in the wall caused by the design load,

N_{Rd} – design load-bearing capacity of the wall due to vertical loads.

The reliable value of the shear deformation angle Θ_{Sd} is determined according to Fig. 3.7:

- for a wall of length l_1 (3.13):

$$\Theta_{Sd} = \Theta_{i-1} \frac{|u_i - u_{i-1}|}{l_1} \qquad (3.13)$$

- for a wall of length l_2 (3.14):

$$\Theta_{Sd} = \Theta_{i+1} \frac{|u_i - u_{i+1}|}{l_2} \qquad (3.14)$$

where:

u_{i-1}, u_i, u_{i+1} – values of vertical displacements determined at both ends of the separated parts of the calculated stiffening wall,

l_1, l_2 – lengths of separated parts of the stiffening wall (distances between transverse walls or between openings).
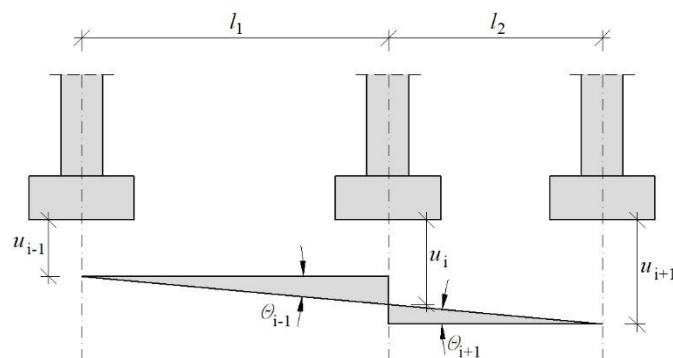

Fig. 3.7 The simplified method of determining the shear deformation angle Θ_{Sd} in the case of known values of transverse walls settlement

If calculations were made using software based on the finite element method – the value of the shear deformation angle is determined from the formula (3.15):

$$\Theta_{\text{Sd}} = \frac{|\Delta u_{\text{i}}|}{l_{\text{i}}} \tag{3.15}$$

where:

Δu_{i} – the value of the difference in vertical displacements determined at both ends of the area (section) with the greatest deformations,

l_1 – length of the area (section) with the greatest deformations for part of the calculated wall.

The values of the shear deformation angle Θ_{adm} for displacements under the building caused by temporary loading can be taken from Table 3.1. Increased values of the permissible shear deformation angle can be taken from formula (3.16) if the vertical displacements of the substrate were caused by long-term load or when rheological processes had already been done in the wall.

$$\Theta_{\text{adm}} (1 + \eta_{\text{E}} \varphi_{\infty}) \tag{3.16}$$

in which:

Θ_{adm} – a permissible value of the shear deformation angle according to Table 3.1,

η_{E} – coefficient taking into account the reduction of masonry creep due to the redistribution of internal forces in the structure and the ratio of the long-term load to the total load of the masonry structure with the value $\eta_{\text{E}} = 0.3$.

φ_{∞} – the final value of the creep coefficient equals $\varphi_{\infty} = 1.5$.

Earlier versions of the standard

It is worth mentioning that earlier editions of the standard [N12, N13] did not contain any guidelines for the design of stiffening walls. The provisions are limited to statements that internal forces should be calculated assuming the elastic behavior of the structure. Static schemes should correspond to the conditions of the structure in the considered limit states. Additionally, in [N12], it is written that for walls subjected to permanent horizontal loads, the limit state of loss of stability by rotation or displacement of the wall should also be checked. In [N14] from 1999, there are rules for the design of stiffening walls, but with some differences to the 2007 version [N15]. The shear resistance of the lintels is checked from formula (3.17); the coefficient in the 2007 version was 0.75 – formula (3.11):

$$\frac{V_{\text{Sd}}}{0.70 t h_{\text{n}}} \leq f_{\text{vd}} \tag{3.17}$$

The value of the shear deformation angle Θ_{Sd} was determined according to the formula (3.18):

$$\Theta_{Sd} = \frac{2(1 + v)}{E}\tau_{max} = \frac{V_{Sk}}{0.4EA} \tag{3.18}$$

where:

E – modulus of elasticity of the wall,

v – coefficient of transverse deformation equals $v = 0.25$,

τ_{max} – the maximum value of shear stress caused by a characteristic shear load equal to V_{Sk}/A_v, in which: A_v – a cross-section of shear area,

A – horizontal section of the wall.

3.1.3. Standard regulations in other European countries

Section 8.7 of the German standard [N6] contains provisions for stiffening masonry walls. Stiffening walls must have an effective length of at least 1/5 of the clear storey height h_s and have a thickness of 1/3 of the thickness of the wall to be stiffened but at least 115 mm. If the stiffening wall has openings, the length of the wall between the perforation must meet the condition shown in Fig. 3.1. The clear opening height is h_1 or h_2.

The swiss standard [N19] rules for calculating the horizontal displacement between storeys v (3.19) and the marginal strain $\varepsilon_{x.max}$ (3.20) for the quasi-permanent load. Displacement marks are shown in Fig. 3.8. Deformation conditions for the serviceability limit state are also given in Table 3.2.

$$v = \frac{6M_{z1}h_w^2 + 4Vh_w^3}{E_{yk}l_w^3 t_w} + \frac{Vh_w}{G_k l_w t_w} \tag{3.19}$$

$$\varepsilon_{x.max} = \frac{6(M_{z1} + Vh_w)}{E_{yk}l_w^2 t_w} - \frac{N_y}{E_{yk}l_w t_w} \tag{3.20}$$
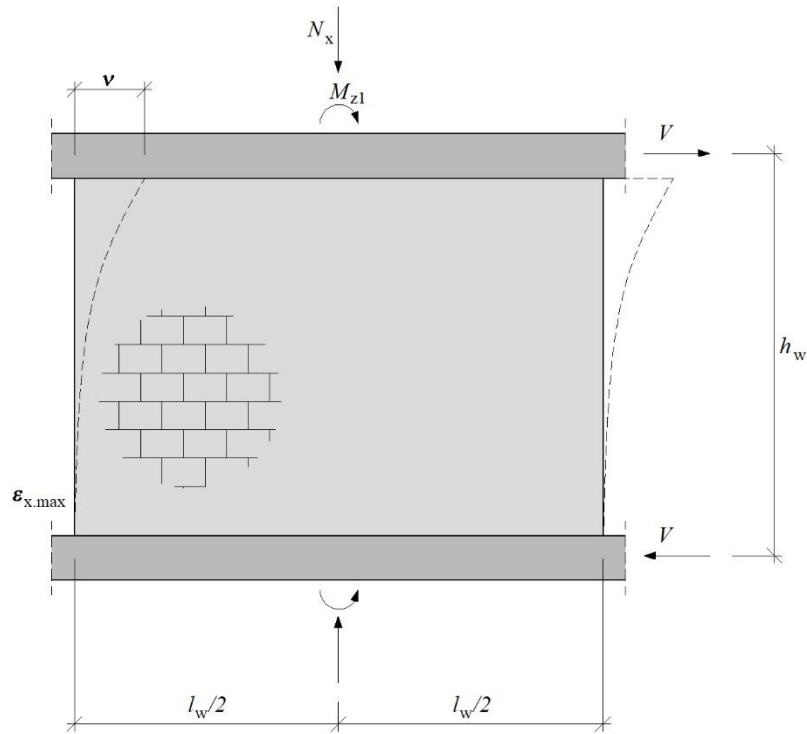
Fig. 3.8 Model for calculating horizontal wall displacements between storeys in the swiss standard

Table 3.2

Deformation conditions based on swiss standard [N19]

Criterion	Normal requirements	High requirements
floor shift	$v \leq 0.001\ h_w$	$v \leq 0.0003\ h_w$
maximum strain	$\varepsilon_{x.max} \leq 1.0\ ‰$	$\varepsilon_{x.max} \leq 0.1\ ‰$

The Russian standard [N20] also does not provide detailed guidelines for the design of stiffening walls. When calculating walls (or their vertical cross-sections) for vertical and horizontal loads, the following should be checked:

a) horizontal cross-sections for compression or eccentric compression load,

b) inclined cross-sections for the principal tensile stresses while bending in the plane of the wall,

c) width of cracks due to the vertical load of walls differently loaded and connected or characterized by different stiffness of adjacent fragments of walls.

Formula 3.21 describes the load capacity of the connection of transverse and longitudinal walls under the horizontal load.

$$T = \frac{QAyH}{I} \leq tHR_{sq} \tag{3.21}$$

where:

R_{sq} – compressive strength of the masonry determined without the compressive stresses,

Q – shear force taken up by the stiffening wall, determined in the elastic stage in the middle of the storey height,

H – storey height,

y – distance from the center of gravity of the wall (together with flanges),

A – area of the cross-section of the flange,

t – wall thickness.

The British regulations [N2] do not systematize stiffening walls' design. The standard includes information presenting shear actions in the connection of walls perpendicular to each other – Fig. 3.9.
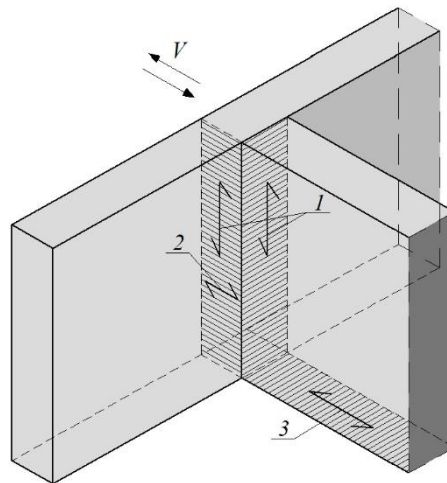

Fig. 3.9 Shear forces acting in vertical and horizontal planes [N2]: 1 – complementary shear acting in the vertical direction in the vertical plane (stress vector), 2 – complementary shear acting in the horizontal direction in the vertical plane (stress vector), 3 – shear acting in the horizontal direction in the horizontal plane (stress vector), V – shear force

3.1.4. Other standards and recommendations

IS:1905-1987 Indian Standard

Indian standard [N10] demands checking the necessity of lateral support when the hall length exceeds 8.0 m. The requirements for the geometry of the transverse walls constituting the horizontal support are shown in Fig. 3.10a. Figure 3.10b presents the connection between the stiffening and the transverse wall.
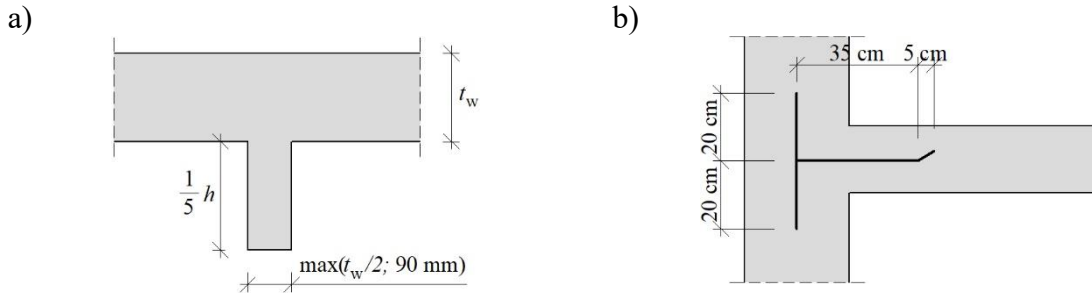
Fig. 3.10 Requirements in Indian standard [N10]: a) minimum dimension for masonry wall or buttress providing effective lateral supports, b) anchoring of stiffening wall with the transverse wall: *h* – the height of the wall

Moreover, the flange geometry is also defined depending on the shape of the cross-section of the wall. In the case of T/I-shaped walls, the maximum size of the flange is 12*t* or *h*/6 – Fig. 3.11a. In L/U-shaped walls, the geometry of the flange is 6*t* or *h*/6 – Fig. 3.11b.
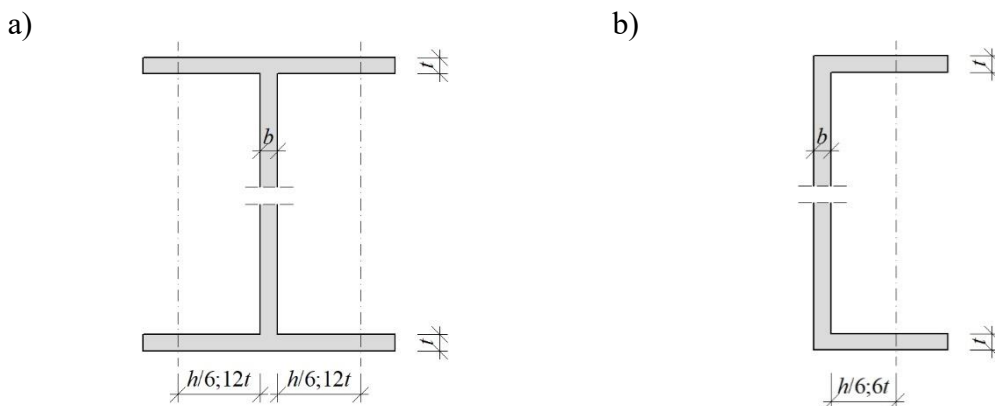

Fig. 3.11 The geometry of flange [N10]: a) T/I-shaped walls, b) L/U-shaped walls: *t* – thickness of bearing wall and *h* – total height of the wall above the level being considered

GB50003-2011. National standard of the people's republic of China

Appendix C: *Statical Calculation of Semi-Rigid Buildings* in Chinese standard [N9] formulates the method for calculating the action of horizontal load (wind load) on buildings. Internal forces can be calculated as a superposition of two steps:

a) in-plane calculation diagram – Fig. 3.12a: a horizontal hinged strut represents the connection between the beam and column on each storey; the internal forces under wind load without lateral displacement and the counterforce R_i of each strut could be calculated,

b) space action of the building – Fig. 3.12b: the counterforce R_i of each strut should be multiplied by the corresponding space performance coefficient η_i – Table 3.3 and applied on the joint reversely.
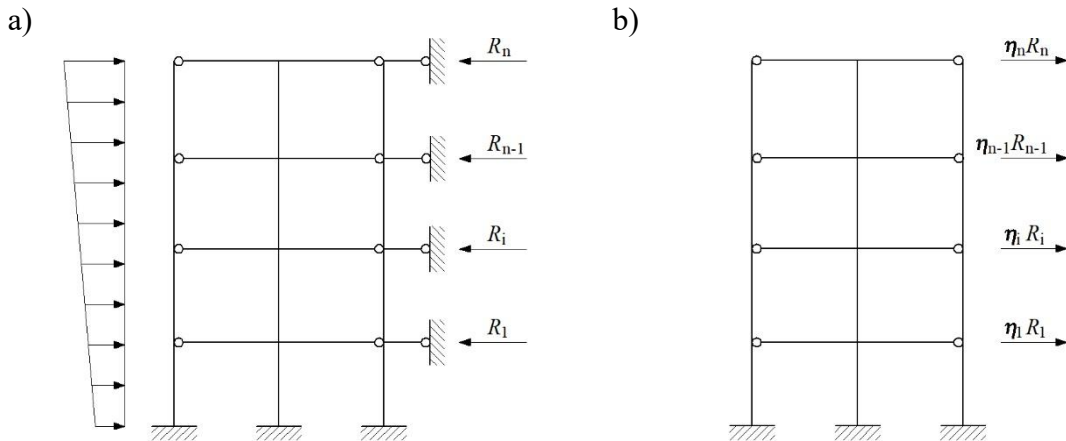
Fig. 3.12 Model of a multi-storey frame used in the calculation of internal forces based on Chinese standard [N9]: a) in-plane model, b) spatial model

<div align="right">Table 3.3</div>

Influence coefficient of space performance for each storey of the building η_i [N9]

*	Transverse wall spacing *s*, m														
	16	20	24	28	32	36	40	44	48	52	56	60	64	68	72
1	-	-	-	-	0.33	0.39	0.45	0.50	0.55	0.60	0.64	0.68	0.71	0.74	0.77
2	-	0.35	0.45	0.54	0.61	0.68	0.73	0.78	0.82	-	-	-	-	-	-
3	0.37	0.49	0.60	0.68	0.75	0.81	-	-	-	-	-	-	-	-	-

This calculation approach assumes that all stiffening walls have the same geometry, and the effect of building torsion is not considered. To sum up, these are calculations carried out on plane models, and equivalent coefficients represent the spatial behavior of the structure.

Canadian Standards Associations CSA S304-14 and NBCC2005

Canadian regulations for analysing walls loaded with a horizontal load focus on structures in seismic areas [N4]. Within the meaning of the standard, structural walls have to resist axial compression (due to the vertical gravity loads), out-of-plane bending (flexure) and shear due to transverse wind, earthquake or blast loads, eccentric vertical loads and in-plane bending and shear due to lateral wind and earthquake loads acting in a direction parallel to the plane of the wall. One of the roles of slabs called diaphragms is to transfer horizontal loads to a lateral load-resisting system. The standard [N4] distinguishes several types of shear walls. A solid wall (Fig. 3.13a) is a term which describes shear walls without openings (door or window openings), while walls with openings are called perforated walls. The parts of the wall between the openings are called piers – Fig. 3.13b. Coupled walls mean shear walls in medium-rise masonry buildings with vertically aligned openings over the height.
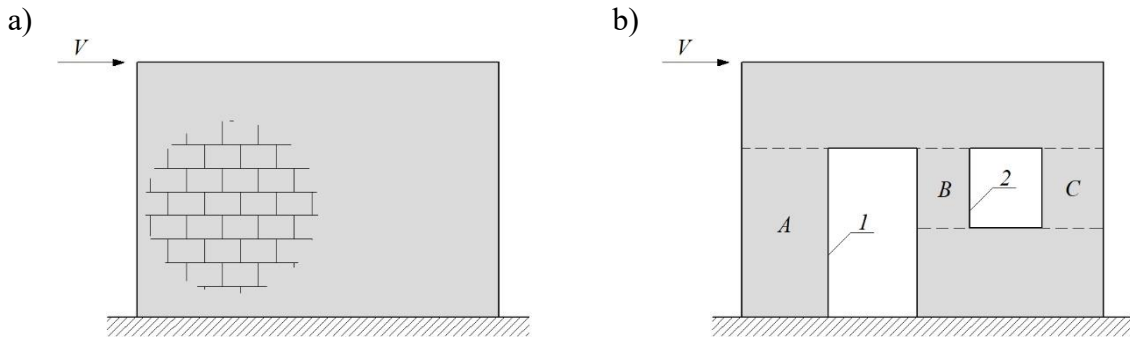
Fig. 3.13 Types of shear walls distinguished in [N4]: a) solid wall, b) perforated wall: 1 – door opening, 2 – windows opening, A, B, C – piers, V – horizontal force

Moreover, the standard [N4] introduces the aspect ratio h_w/l_w (relation between height and length of the shear wall), which enables wall classification based on the geometry – Fig. 3.14. Flexural shear walls mean that the height/length ratio equals 1.0 or higher, and squat walls mean that such a ratio is less than 1.0.
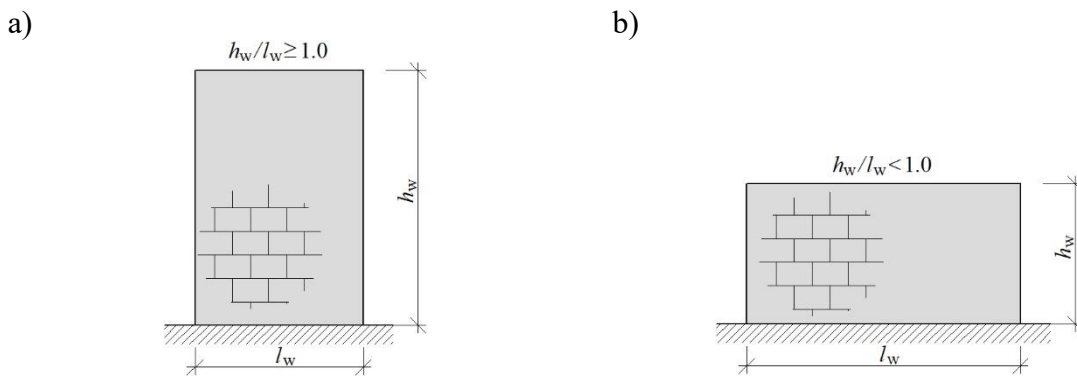

Fig. 3.14 Shear wall classification based on the aspect ratio according to [N4]: a) flexural walls, b) squat walls

Standard assumes the shear forces distribution in a wall is similar to a vertical cantilevered beam fixed at the base – Fig. 3.15. There are reactive forces such as P, which is a sum of vertical forces acting on a wall, V – the sum of horizontal forces and M – the bending moment equals the quotient of the resultant horizontal force V multiplied by the effective height h_e. It is worth mentioning that regulations in [N4] are among the few that draw attention to the static scheme adopted in the calculations.
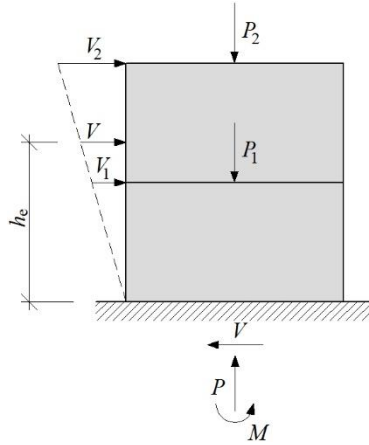
Fig. 3.15 Load distribution in masonry shear wall: P_1 and P_2 – vertical loads, V_1 and V_2 – horizontal loads, h_e – the effective height of acting the resultant horizontal load V, P – vertical reactive force $P = \Sigma P_i$, V – horizontal reactive force $V = \Sigma V_i$, M – in-plane bending moment $M = V \cdot h_e$

The National Building Code of Canada [N11] also include regulations for structures in seismic areas. Point 4.1.8.11(8) included notes on torsional effects. Torsional moments are induced by forces acting on the eccentricity relative to the center of mass. Torsional sensitivity can be determined based on the ratio B_x for each level and each orthogonal direction independently – (3.22):

$$B_x = \frac{\delta_{max}}{\delta_{ave}} \tag{3.22}$$

where:

δ_{max} – maximum displacement of the storey at the extreme points of the structure at level x in the direction of earthquake induced by equivalent static forces acting at distances $\pm\, 0.10\, D_{nx}$ from the center of mass at each floor,

δ_{ave} – average displacement of the storey at the extreme points of the structure at level x in the direction of earthquake induced by equivalent static forces acting at distances $\pm\, 0.10\, D_{nx}$ from the center of mass at each floor,

D_{nx} – plan dimension of the building at level x perpendicular to the direction of seismic loading being considered.

The B value of the building is the maximum one of all values B_x in both orthogonal directions. The torsion of the building is taken into account by calculating the torsional moment of the building (for buildings with $B \leq 1.7$) or by dynamic analysis procedure (for buildings with $B > 1.7$) specified in chapter 4.1.8.12 of [N11].

American regulations ACI 530-05/ASCE 5-05/TMS 402-05 and Army TM 5-809-3
According to the American standard [N3], design assumptions enclose a braced structural system. The distribution of lateral loads depends on the construction of slabs

(if they are diaphragms) and the rigidities of the structural system. Additionally, connections between particular elements, such as walls and slabs, determine if the wall participates in taking horizontal loads. Lateral loads induced by wind or seismic forces are considered in the directions of the principal axes of the building. Torsion of the structure can be caused by load acting at eccentricity to the center of rigidity. The analysis should include the influence of openings on the structure behavior and whether the masonry between openings allows them to act as coupled shear walls – Fig. 3.16.

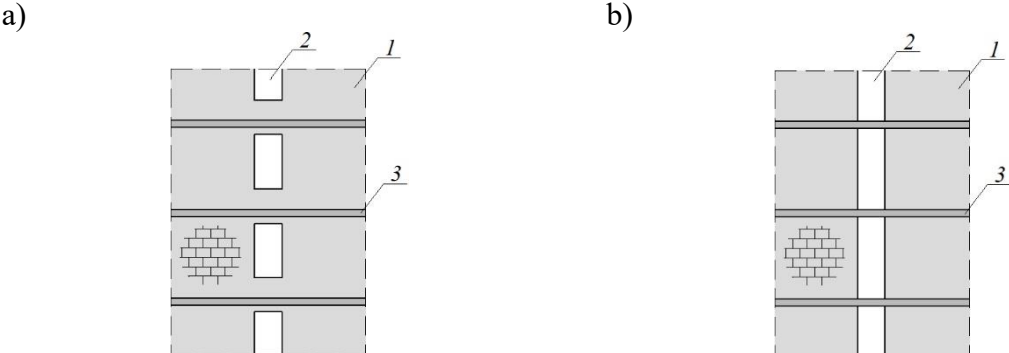a)   b)

Fig. 3.16 The effects of openings in shear walls: a) coupled stiffening wall, b) noncoupled stiffening wall: 1 – stiffening wall, 2 – opening, 3 – slab

In calculation, the stiffness of shear walls should consider shear and flexural deformation. Standard distinguishes three types of solid shear walls based on the relationship between the height h and length d of the wall – Fig. 3.17. There are walls in which shear stiffness predominates – $h/d<0.25$. When the ratio h/d is between 0.25 and 4, both shear and flexural stiffness determine the behavior of the wall. For walls with $h/d>4$, the most crucial is flexural stiffness.

a)   b)   c)
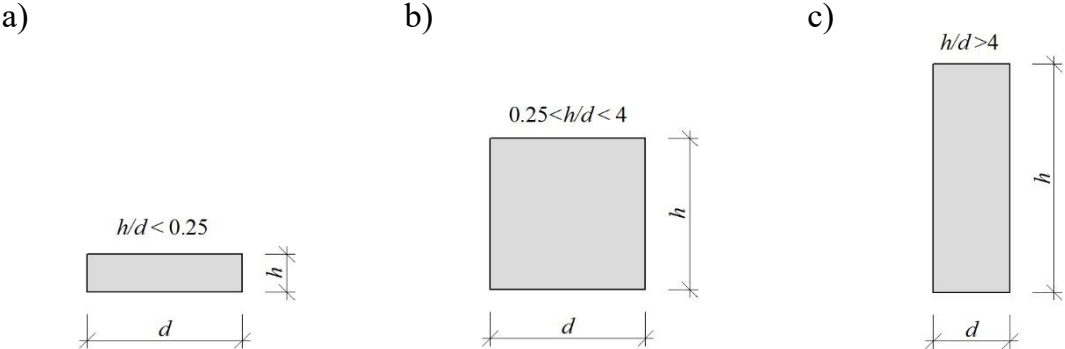
Fig. 3.17 Shear walls stiffness [N3]: a) shear stiffness predominates, b) both shear and bending stiffness are essential, c) bending stiffness predominates

The standard that provides relatively much information on the design of stiffening walls is TM 5-809-3/NAVFAC DM-2.9/AFM 88-3, Chap. 3 [N21] issued by

Departments of the army, the navy and the air force. Chapter 7 deals with reinforced in-plane shear walls, but the guidelines do not apply to structures in seismic areas. The allowable shear stress in the wall depends on the ratio M/Vd, where M is the maximum moment resulting from the shear force V acting in the plane of the wall, and d is the effective length of the wall. The stiffening wall can be considered in two static schemes. A wall between storeys (a multistory shear wall) can be analysed in a double-fixed scheme. Then the bending moment is calculated from the formula (3.23):

$$M = 0.5 \cdot h \cdot V \qquad (3.23)$$

in which,

h – the height of the wall.

The M/Vd value equals $h/2d$. In the second calculation variant, the static scheme of the walls assumes a single restraint only in the base of the wall (a single-story cantilevered shear wall). Then the value of the bending moment can be calculated from (3.24). The value of the M/Vd ratio then becomes h/d. Calculation situations are presented in Fig. 3.18.
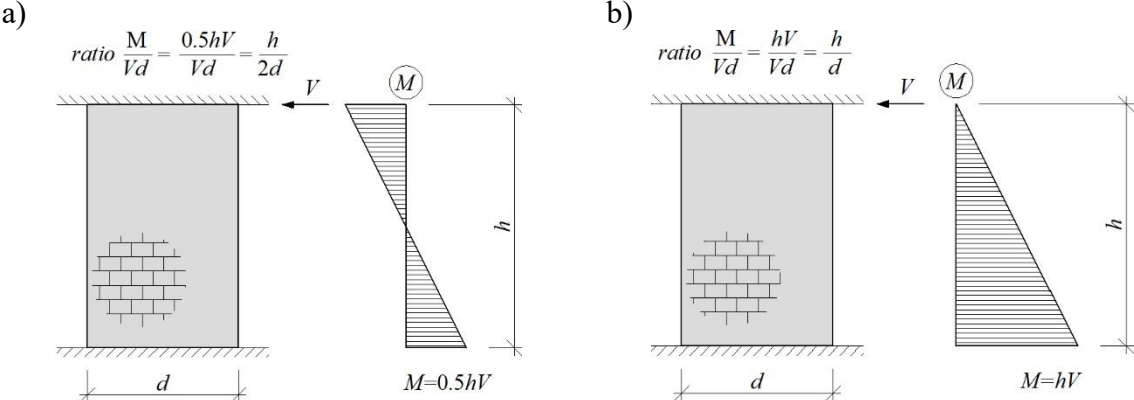
$$M = h \cdot V \qquad (3.24)$$

Fig. 3.18 M/Vd ratios and static schemes for masonry shear walls: a) stiffening wall between floors – fixed top and bottom edge, b) one story cantilever wall – fixed bottom edge: h – the height of the wall, d – the length of the wall, M – in-plane bending moment, V – horizontal force

If the calculated shear stress f_{vm} exceeds the allowable value F_{vm}, shear reinforcement is required. In that case, the reinforcement is designed to transfer the total shear force. The horizontal load capacity of a building depends on the structural system considered an entire construction. The relative shear stiffness of a wall is inversely proportional to its displacement under a unit horizontal force. The total horizontal displacement of the building is the sum of shear and flexural deformations – Fig. 3.19.
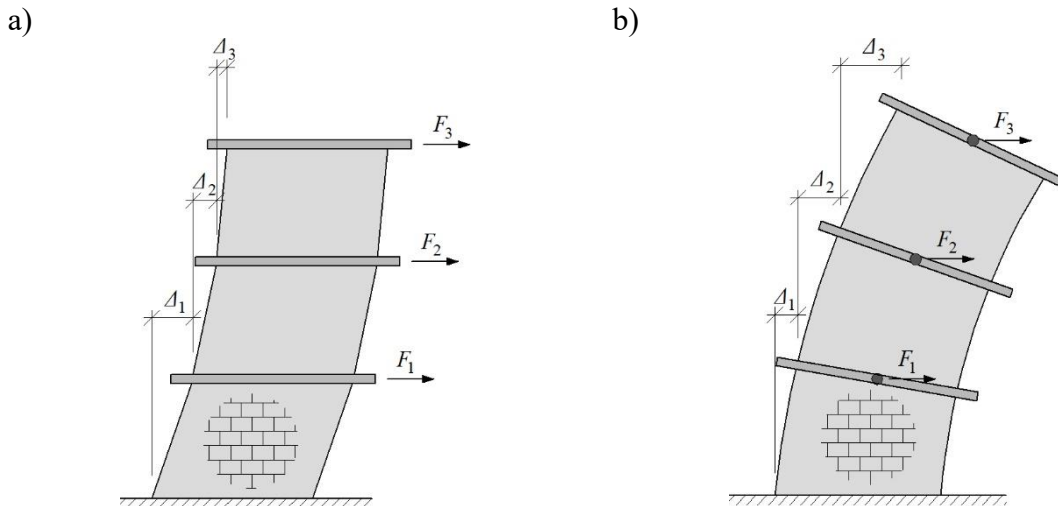
Fig. 3.19 Stiffening wall deformation: a) shear deformation, b) flexural deformation: $\varDelta_1$, $\varDelta_2$, $\varDelta_3$ – horizontal displacements, F_1, F_2, F_3 – horizontal forces

The analysis of the building is based on the division of the structure into stiffening parts considered separately. Structure division points are called control joints. Both the location and the number of control nodes along the stiffening walls can affect the stiffness of the members – especially in the case of bending deformations. In addition, the computational analysis should consider the effect of openings on the stiffness of the elements. Stiffening walls can increase load-bearing capacity by including a fragment of a perpendicular wall to cooperate in transferring loads. The horizontal cross-sections of the stiffening unit (stiffening wall) take the letter 'T' or 'L' shape. Chapter 7-5 (point 3) [N21] stated that the load capacity increase resulting from the cooperation of elements might be difficult to estimate. Moreover, the calculations assume that the soil under the foundation is unyielding or that the soil pressure has a linear distribution. Although this assumption is a significant simplification, it allows the estimation of the structure's stiffness acceptably for design purposes.

The distribution of forces on the stiffening walls depends on their stiffness and the horizontal stiffness of each storey slab. Suppose the floors act as rigid diaphragm at the level of the storey. In that case, the distribution of loads on the walls is proportional to their stiffness. Under symmetrical loading, each element will resist the same proportion of lateral force (all vertical shear wall elements deflect equally). Another situation is when the slabs do not act as a rigid diaphragm. Flexible diaphragms are considered less rigid than shear walls and transfer the load to the walls analogously to a continuous beam scheme without considering the rigidity of the walls. A flexible diaphragm is not able to transfer torsional rotational moments. On the other hand, when the resultant horizontal force does not coincide with the center of rigidity of shear walls, a torsional moment will be generated within the rigid diaphragm (case called rotational shears). The

criterion for floors is not exceeding the permissible deflection u_{adm} (own designation), which is calculated from formula (3.25):

$$u_{adm} = \frac{h^2 F_b}{0.01 \cdot E_m \cdot t} \tag{3.25}$$

in which:

F_b – the allowable flexural compressive stress in masonry, psi (pound per square inch); $F_b = 0.33 f_m$,

E_m – the modulus of elasticity for CMU (concrete masonry unit), psi; $E_m = 1000\, f_m$,

t – the effective thickness of the wall, inches.

This rule ensures that excessive deflection of the roof and floor diaphragms do not cause damage to vertical shear elements. The standard [N21] stipulates that the equation is not technically correct and is only a reference point for the designer, who should consider the maximum allowable deflection of floors that transfer loads to the stiffening walls.

The regulations indicate that calculations should consider the effects of the perforations in the building, and this effect depends on the geometry of openings. The influence of small openings will be minor or negligible compared to larger ones. Additionally, the localization of openings also affects the degree of complexity of the calculations. If perforations occur in regularly spaced vertical rows or piers, the calculation is not as complicated as when the openings do not align vertically or horizontally. Analysis should consider stress concentration areas such as extreme sides of the wall (boundaries) where the lengthening or shortening sides occur due to deep beam action, corner joints or diagonal tension – Fig. 3.20.
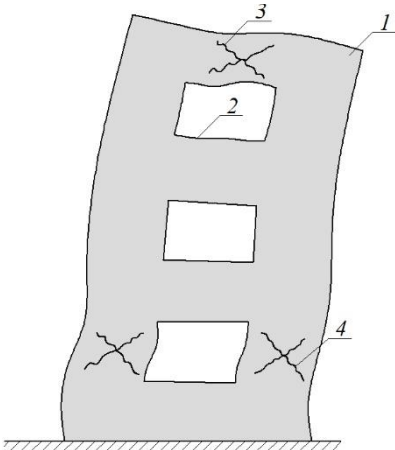

Fig. 3.20 Deformation of structure: 1 – stiffening wall, 2 – window opening, 3 – diagonal tension cracks in spandrels, which can occur at the top or other elevations, depending on the vertical shear distribution, 4 – diagonal tension cracks in piers which can occur at the bottom where horizontal shear is the largest

Moreover, the value of relative stiffnesses of the vertical piers and horizontal wall fragments (spandrels, lintels) between them impacts the type of adopted analysis. Figure 3.21 shows two extreme cases of different stiffness of the external wall of the building. The analysis assumes that the wall is fixed in the foundation.

For rigid vertical cantilever piers (Fig. 3.21a) – spandrels and lintels act as horizontal struts between the vertical piers. In this scheme, the determination of internal forces is relatively simple. It is based on the cantilever flexural behavior of the vertical wall fragments between the openings by ignoring the deformation characteristics of the spandrels. The role of lintels is to transfer forces to vertical elements. It is required that flexural deformation of struts must be compatible with the deformation of vertical cantilever piers. In the second scheme (Fig. 3.21b), the vertical wall fragments are characterized by much lower stiffness than the horizontal elements. In this case, the lintels and horizontal fragments are assumed to be infinitely rigid, and the vertical piers are analyzed as fixed-end columns. The horizontal bands between the windows (spandrels) are designed for the forces induced by the vertical elements.
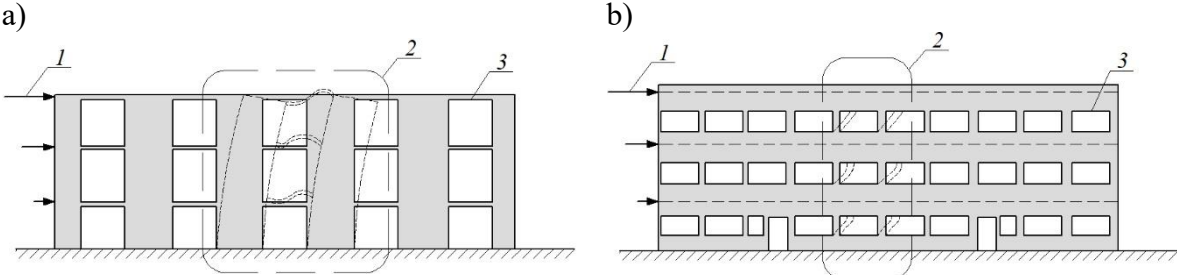

Fig. 3.21 Relative rigidities of piers and spandrels [N21]: a) rigid piers and flexible spandrel, b) flexible piers and rigid spandrel: 1 – horizontal force, 2 – the deflected shape of the building, 3 – opening

Both calculation situations can be considered using wall deflection charts (an example is shown in Fig. 3.22) and standard procedures specified in chapters 7-8 of [N21]. A more complex situation occurs when the rigidity of piers and spandrels is relative – static behavior cannot be clearly defined.

The stiffness of the stiffening wall is inversely proportional to its deflection. The calculations are carried out on a model loaded with a unit horizontal force. The wall dimensions are essential in the analysis - length, height and thickness. Mechanical parameters such as modulus of elasticity, shear modulus and boundary conditions for fixing the element at the bottom and top are also considered.
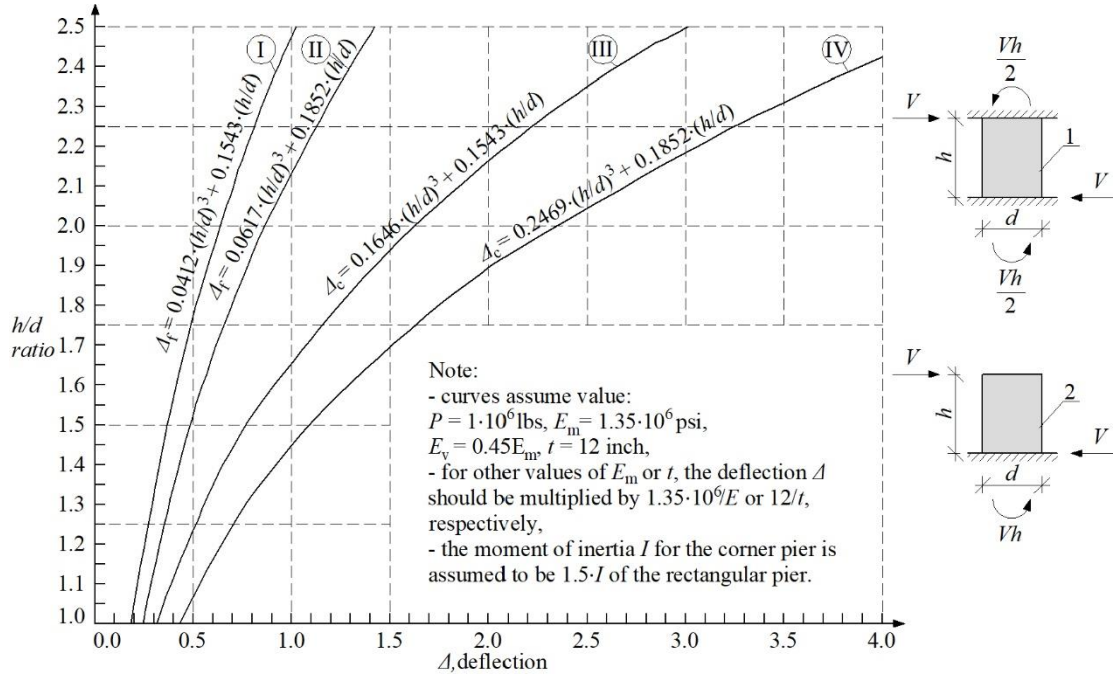
Fig. 3.22 Wall deflection chart according to the [N21]: 1 – fixed pier, 2 – cantilever pier, I – corner pier, fixed: $\Delta_f = 0.0412(h/d)^3 + 0.1543(h/d)$, II – rectangular pier, fixed: $\Delta_f = 0.0617(h/d)^3 + 0.1852(h/d)$, III – corner pier, cantilever: $\Delta_c = 0.1646(h/d)^3 + 0.1543(h/d)$, IV – rectangular pier, cantilever: $\Delta_c = 0.2469(h/d)^3 + 0.1852(h/d)$

The standard considers two static schemes. In the first one, the masonry wall is fixed on top and bottom. Then the horizontal deflection Δ_f (deflection) is the sum of shear and flexural deformations calculated from relation (3.26):

$$\Delta_f = \Delta_b + \Delta_v = \frac{V \cdot h^3}{12 \cdot E_m \cdot I} + \frac{1.2 \cdot V \cdot h}{E_v \cdot A} \tag{3.26}$$

where:

Δ_b – the flexural deflection, inches; and Δ_v – the shear deformation, inches,

A – the horizontal cross-sectional area of the wall element, in^2,

I – the horizontal cross-sectional moment of inertia of the wall element in the direction of bending, in^4,

E_v – the shear modulus of masonry, psi; $E_v = 0.40E_m$

V – horizontal force, and h – the height of the wall.

If the wall or pier is fixed only at the bottom (cantilever scheme), the total horizontal displacement is calculated from the formula (3.27):

$$\Delta_f = \Delta_b + \Delta_v = \frac{V \cdot h^3}{3 \cdot E_m \cdot I} + \frac{1.2 \cdot V \cdot h}{E_v \cdot A} \tag{3.27}$$

It can be concluded that the horizontal displacement of the wall resulting from its flexural deformation is four times greater in the cantilever model compared to the restraint on both sides. However, shear deformations of the wall are the same – regardless of the adopted support conditions. The total stiffness of the shear wall k is the reciprocal of the total horizontal displacement (3.28):

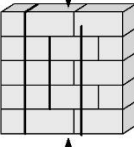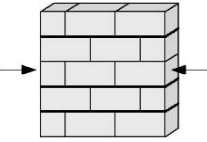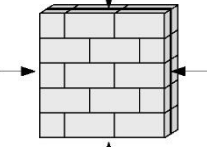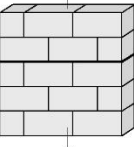$$k \;=\; \frac{1}{\Delta_b} + \frac{1}{\Delta_v} \tag{3.28}$$
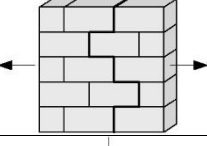
To sum up, openings within the wall significantly impact the methodology of designing stiffening walls. Calculations of solid walls without perforations are relatively simple, and the irregular distribution of openings adversely affects the time and labour consumption of the analysis.

3.2. Selected experimental and numerical studies of stiffening walls

The behavior of a masonry structure is a complex research problem. Both the mechanical parameters of the wall components (e.g. modulus of elasticity, compressive and tensile strength) as well as the type of joints and their thickness are influential. The masonry is most often in a complex stress state resulting from vertical (gravitational loa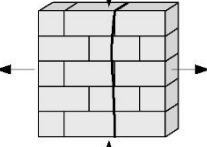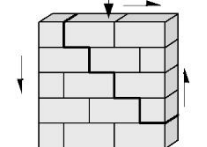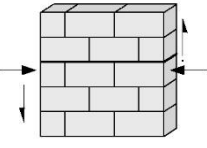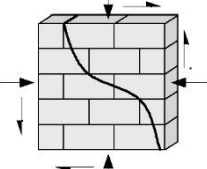ds) and horizontal actions (e.g. wind). These factors in various configurations affect the wall mechanics. The shear of unreinforced masonry is largely resistant due to deformation in mortar bed joints [50]. It is defined conveniently by the Mohr-Coulomb failure envelope that relates the shear strength τ_u to the shear bond strength τ_0, an apparent friction coefficient μ and vertical stress f_v in the joint. However, wall failure may occur in joints, masonry units, or both [33]. The paper [99] distinguishes nine possible mechanisms of wall failure in a plane stress state – Table 3.4. Other failure patterns are possible, but several basic mechanisms have coincided in these cases. Mechanisms 7MF-9MF describe the possible failure of the stiffening masonry walls.

Table 3.4

The primary mechanisms of masonry failure in a plane stress state, based on [99]

Designation	Failure mechanism	A 2-D view of failure	Description
1MF	Separation of columns		vertical cracks through masonry units passing through joints under uniaxial compression
2MF	Separation of layers or several masonry rows		horizontal cracks through bed joint surface under horizontal uniaxial compression
3MF	Parallel splitting		splitting masonry failure under biaxial compression
4MF	Damage along a bed joint		horizontal breakage through bed joint surface under axial tension
5MF	Breakage along a toothing crack		breakage of head joints under horizontal tension
6MF	Vertical breakage through masonry units		vertical breakage through masonry units passing through joints under compression and tension
7MF	Splitting along a stepped crack with shear along the bed joint		stepped crack along the bed and head joints under compression and shear
8MF	Shear along the bed joint		horizontal crack along the bed joint surface under shear
9MF	Splitting along an inclined crack		inclined crack along both masonry units and passing through joints under compression and shear

Moreover, masonry in tension shows other characteristics in tensile strength reduction, and this phenomenon is related to cracks. When masonry is cracked in a stepped pattern, the strength reduction is relatively small, and the wall respond ductile. When an inclined crack occurs in masonry, the behavior indicates a brittle failure with a rapid strength decrease [61] – Fig. 3.23. It should be mentioned that the cracks provide in-depth information about the mechanics of masonry behavior, which justifies conducting experimental research which gives much information about failure patterns.
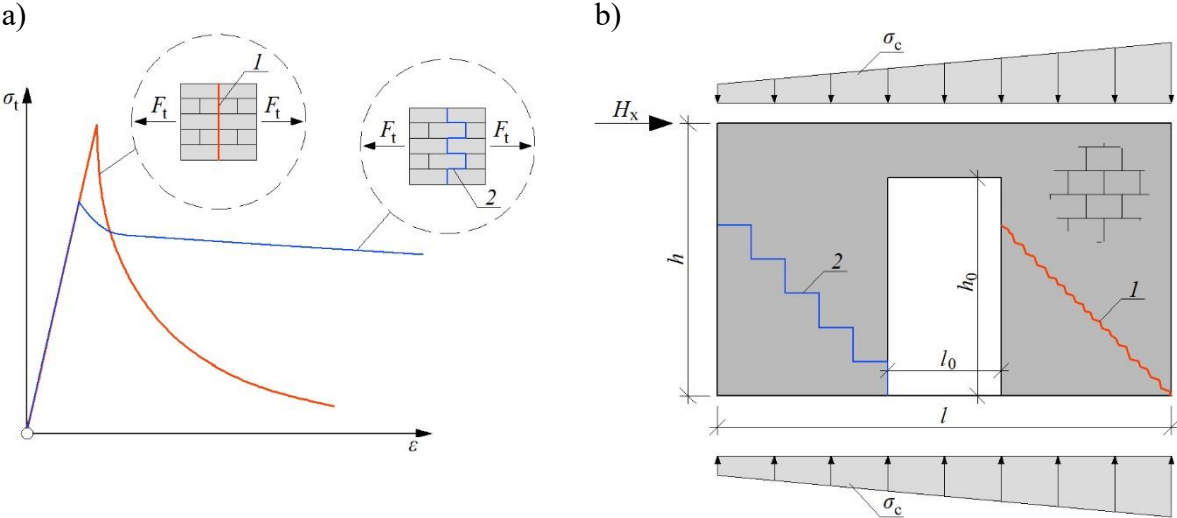
Fig. 3.23 Differences in tensile behavior of masonry: a) straight and stepped crack pattern depends on compressive stress, based on [61], b) behavior of stiffening masonry wall in complex failure mode: 1 – straight crack (high compressive stress), 2 – stepped crack (low compressive stress), σ_c – compressive stress, σ_t – tensile stress, H_x – horizontal shear force, F_t – tensile force.

Shear wall tests are often carried out on small models consisting of several masonry elements connected with mortar [133] (masonry prism), masonry couplet [158] or masonry triplets [15, 101] – Fig. 3.24. Sometimes standard procedures cannot be applied directly; however, they are a reference point for testing walls with complex structures.

Fig. 3.24 Types of shear tests [101]: a) couplet test, b) van der Pluijm test, c) triplet test

The test made by Binda et. al. [20] is an example of a triplet test for twelve three-leaf stone wallets consisting of two outer leaves of ashlar masonry with mortar joints 10 mm thick and an inner core of rubb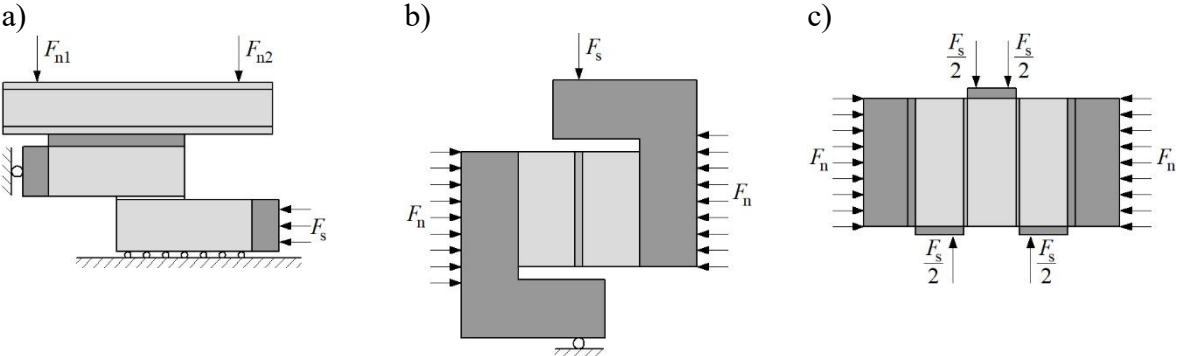le masonry. The shear was similar to the procedure presented in EN 1052-3 [N17] – a monotonic load was applied to the inner leaf while the outer leaves were supported (triplet test). Small models are beneficial for determining basic shear parameters, e.g. initial shear strength f_{v0} [78]. Tests of shear models are commonly performed following the ASTM standard [N1] (models subjected to diagonal testing) [148], or in a variation of this test – the masonry assemblage rests on a plinth, and the force is applied diagonally between the two corners [91]. It should be added that the most important shear parameter, which is the shear modulus, may differ depending on the adopted test method, even for the same masonry wall [44]. Full-scale models [41, 93, 87, 62] or scaled models [17, 11, 90] are used instead to determine the global behavior of the structure.

Most shear masonry studies are cyclic loading analyses [47, 116, 25, 143], and monotonic load tests are rare [84]. The analysis of stiffening walls, both masonry and reinforced concrete, mainly concerns seismic areas [56, 137]. Test type also depends on the type of construction used in a particular world region – e.g. most reinforced masonry constructions in the mid-western and eastern parts of the United States are partially grouted, so it determines the experimental [21, 24] and analytical [6] recognition of such structures. Even in-situ masonry tests are carried out to assess existing structures [16].

Research by Paulo B. Lourenço et al. [103] presented results of experimental research on the structural behavior of dry joint masonry – Fig. 3.25.
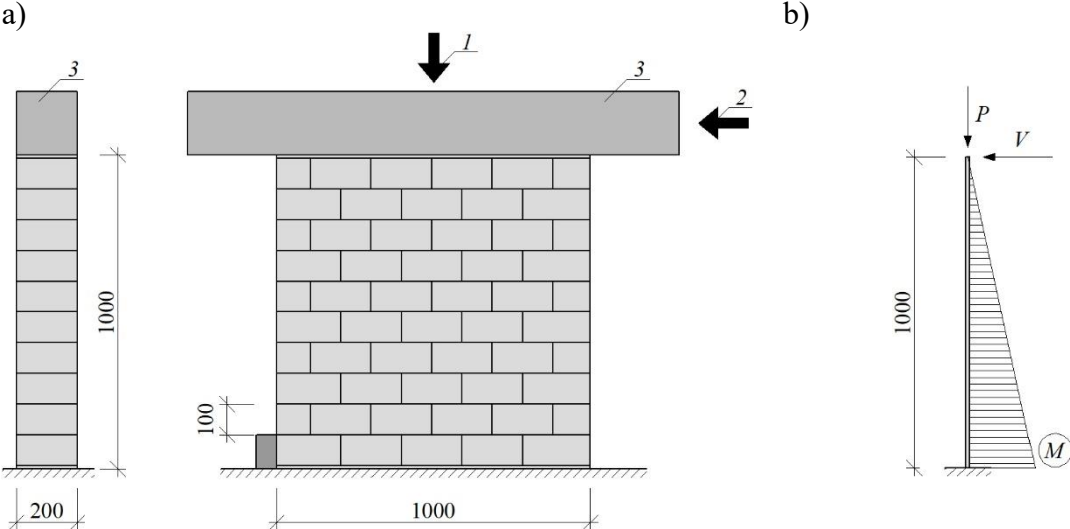

Fig. 3.25 Details of research [103]: a) geometry and test stand, b) static cantilever scheme: 1 – vertical load, 2 – horizontal load, 3 – reinforced concrete beam, P – axial force, V – shear force

Analyses were conducted in collaboration between the Structural Technology Laboratory of the Technical University of Catalonia, Barcelona and the University of Minho. Seven dry masonry walls were tested under combined vertical and horizontal loading. The tested walls were a rectangle with dimensions 1.0x1.0 m, and the thickness of the walls was 0.20 m (Fig. 3.25). Each model was made of locally available stone, known as Montjuic stone (many monuments in Catalonia are made of that). Walls were tested under different compressive normal stresses of 0.15, 0.50, 1.00 and 1.25 N/mm^2, and the vertical load was equal to 30, 200 and 250 kN, respectively – Table 3.5. All the tests were carried out under monotonic loading. Initially, a vertical compressive load was applied using a hydraulic actuator until the set load was applied to the wall. The horizontal load was applied in the next stage by imposing small displacement increments. LVDTs (linear variable differential transformers) measured displacements between units. The models were tested one day after their construction.

Table 3.5

Values of normal stress and corresponding vertical loads in research [103]

Model designation	Normal stress, N/mm^2	Corresponding vertical load, kN
SW.30.1	0.15	30
SW.30.2	0.15	30
SW.100.1	0.50	100
SW.100.2	0.50	100
SW.200.1	1.00	200
SW.200.2	1.00	200
SW.250.1	1.25	250

The results indicated that the stiffness increases with normal stresses, which means that the stiffness of walls depends on the prestress level (Table 3.6) and masonry exhibits a peculiar elastic non-linear behavior with increasing stiffness upon compressive loading.

Table 3.6

The stiffness increase of tested models in research [11]

Model designation	Modulus of elasticity, N/mm^2	
	Test 1	Test 2
SW.100	824	688
SW.200	969	1302
SW.250	1024	1353

Results pointed out that the linear behavior of masonry ended at 30% of the peak load. Then, continuous stiffness degradation takes place under increasing horizontal

displacement. The failure pattern is presented in Fig. 3.26. Observations show that cracks also depend on the level of compressive stress. A typical stepped crack in joints was noticed under lower compression without cracks in masonry units. Damages along stone units were observed in the walls subjected to a higher vertical load. Moreover, the increase in compressive stress applied initially to the model was connected with the increase in obtained maximum horizontal force.
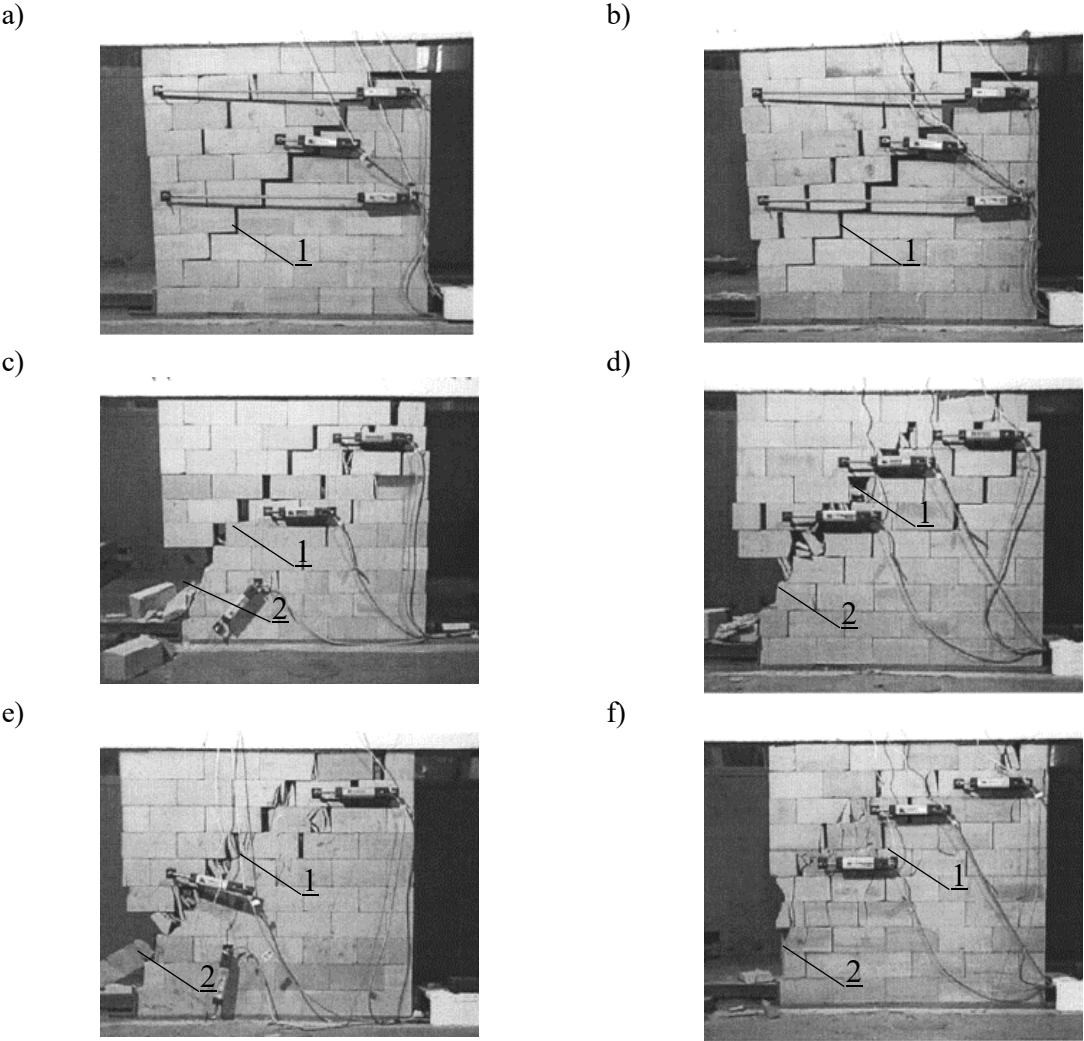
Fig. 3.26 Cracked patterns observed in research [11]: a) model SW.30.1, b) model SW.30.2, c) model SW.100.1, d) model SW.100.2, e) model SW.200.1, f) model SW.200.2: 1 – diagonal crack, 2 – the crushed corner

The paper by M. Shedid et al. [149] describes an experimental study on reinforced concrete masonry shear walls in flexure. The tests concerned the six models under reversed cyclic horizontal load – Fig. 3.27, and research focused on the contribution of flexure and shear deformation to the total horizontal displacements. Tests enclosed six fully-grouted masonry shear walls. Models were 1.8 m long by 3.6 m high and were constructed using hollow 190 mm width concrete blocks. A displacement-controlled

1400 kN hydraulic actuator was used to apply the horizontal load.

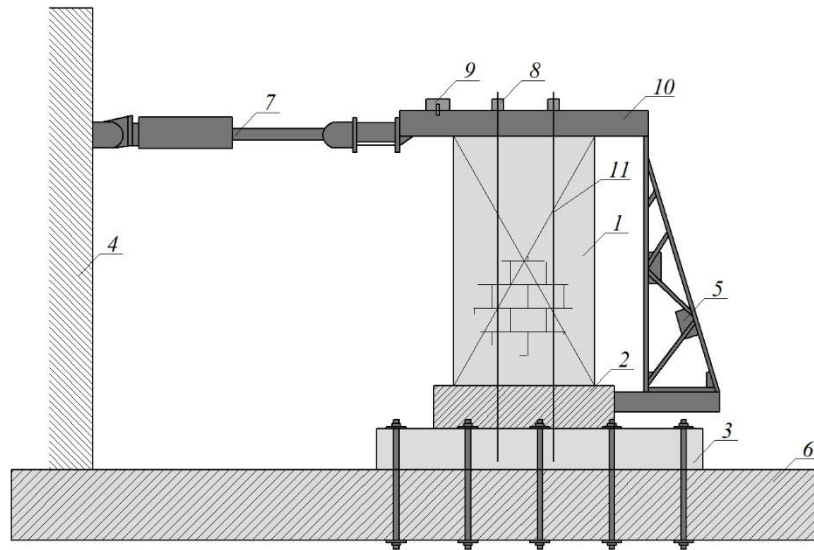Fig. 3.27 Test stand in research [149]: 1 – tested wall, 2 – wall foundation, 3 – concrete slab, 4 – steel reaction frame, 5 – truss, 6 – rigid structural floor, 7 – hydraulic actuator, 8 – hydraulic jack, 9 – out of plane bracing, *10* – U-shape loading beam, *11* – post-tensioned steel tendons

The paper [149] demonstrates that for the aspect ratio of 2.0, shear displacement was 32% of total lateral displacement at the onset of yielding of the outermost vertical bar. The shear displacement equalled 20% of the total lateral displacement for maximum load. Furthermore, walls with a higher amount of vertical reinforcement and walls with higher values of compressive stress resulted in a slight variation in the contribution of shear displacement. The authors suggested that this effect can have a minor or negligible influence on masonry behavior. The results showed that the contribution of shear displacements depends not on the initial compressive stress but, above all, on the wall geometry.

The analysis by R. Senthivel and P.B. Lourenço [146] describes the test performed by Vasconcelos [159] in the Structural Engineering Laboratory at the University of Minho, Guimarães, Portugal. The primary purpose of the experimental research work was to evaluate the in-plane seismic performance of stone masonry shear walls. Three types of walls were tested: dry-stone or dry-stack mortarless stone masonry (type 1), irregular stone masonry with bonding mortar (type 2) and rubble masonry with irregular bonding mortar joint thickness (type 3). The dimensions of the models were 1000x1200x200 mm (length x height x width), and the height/length ratio was equal to 1.2 – Fig. 3.28. Walls were subjected to lateral monotonic and reversed cyclic loads with three values of pre-compression vertical loads – Table 3.7.
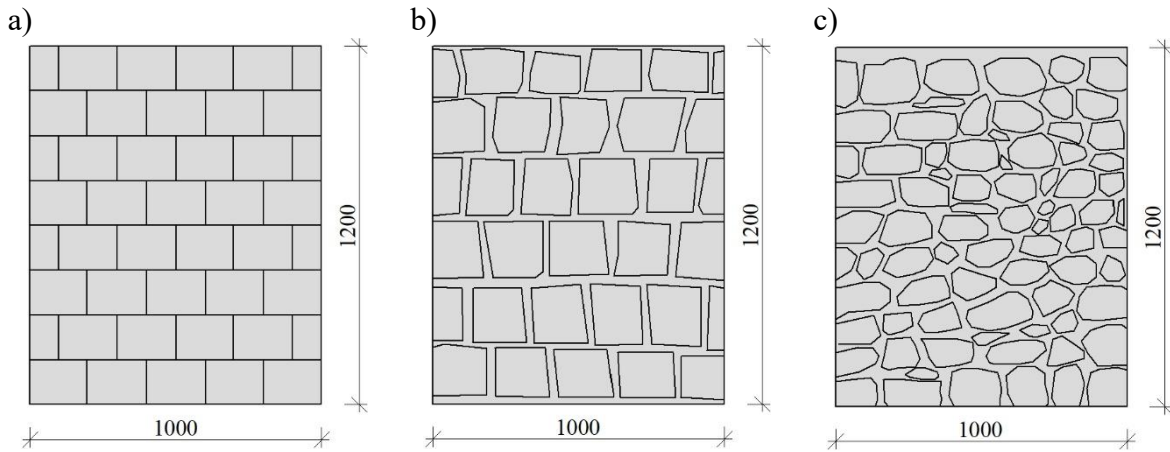
Fig. 3.28 Geometry of tested walls [146, 159]: a) type I - dry stack sawn masonry, b) type II - irregular masonry with bonding mortar joints, c) type III - rubble masonry

<div align="right">Table 3.7</div>

Vertical pre-compression loads for tested wall models [146, 159]

Pre-compression level	Normal stress, N/mm²	Corresponding vertical load, kN
low	0.500	100
moderate	0.875	175
high	1.250	250

Ten walls of the first type and seven walls of type II and III were tested (twenty-four total walls). The load was applied sequentially – first the vertical load, then the horizontal in terms of controlled displacement at 100 μm/s. Deformations were measured by linear variable differential transducers (LVDTs). Numerical simulations were also undertaken [146].

It has been shown that the most important factors influencing the shear walls on load-deformation response and failure pattern are axial pre-compression load and material properties. Although the strength of the masonry was different for each type (I, II and III), the behavior of the wall under high axial load (175 kN and 200 kN) was similar. The lower axial vertical load caused flexural or rocking failures, and the higher vertical load caused rocking, toe crushing and diagonal shear failures along the diagonal direction. Each failure pattern showed cracks through the mortar, and the masonry unit had no damage. Moreover, the flanges affect the effectiveness of transferring the horizontal load through the stiffening wall, and the flange length increases the wall stiffness subjected to horizontal loading and lateral strength [68]. The simplified calculation for effective flange width for shear walls has been proposed in [150].

Simulation of the damage patterns obtained in the tests is possible using numerical calculation. The heterogeneity of materials influences the load-displacement curve and

peak load of unreinforced masonry shear walls. As the heterogeneity index increases, the curve becomes linear, and the peak load is higher than in the low heterogeneity index [163]. The reinforcement also affects the behavior of stiffening walls [81, 82]. The test of confined masonry walls subjected to horizontal load showed that in confined elements compressed to the value of 0.1 and 0.75 N/mm², shear deformation at the cracking moment was lower by 25 and 32% than in unreinforced walls [81]. In confined models, values of shear deformation at the failure moment were higher when compared to unreinforced ones. Moreover, horizontal reinforcement in bed joints constrained the intensity of crack formation.

Paper [88] presents three results of full-scale tests of masonry buildings made of calcium silicate with different opening sizes under a cyclic load. Linear behavior was proven to occur up to 77% of the maximum load. The torsion effect was also demonstrated due to the different stiffness of the walls caused by openings. Masonry walls of tested models cracked in a stair-stepped pattern. In the first model, at the load of 41.82 kN, the first stair-stepped crack occurred on the side corner of the building - after that, a stair-stepped crack started at the corner of the door opening and propagation to the bond beam. At a load of 45.86 kN, the building resistance reached peak value in the push direction, and crack size reached 30 mm wide in the last cycle. In the second model, at a load of 42.84 kN, the first stair-stepped crack started at the corner of the door opening and propagated to the bond beam. These stair-stepped cracks reached 20 mm at the end of the test. At a load of 43.60 kN, in the pull direction, a splitting crack started from the middle point of the window openings and propagated to the floor level. The results show that after the appearance of the first cracks, the building begins to lose its stiffness as further damage occurs quickly. At the load of 44.79 kN, building resistance reached its peak value in the pull direction. In the third case, stair-stepped cracks occurred on the side wall and reached approximately 38 mm wide at the end of the test. At 26.83 kN in the push direction and 36.16 kN in the pull direction, stair-stepped cracks were observed on the side wall pier between the two window openings. The differences in wall stiffness caused the twist of the tested building.

The stiffness of unreinforced shear walls [117] and lateral load capacity [75] can reduce significantly due to wall openings. The numerical simulation showed that the lateral load-carrying unconfined masonry walls might be reduced by up to 28.5% when incorporating only a 1.85% opening - this reduction increases to 76.5% with a 16.5% opening [117]. The full-scale test showed that horizontal displacement suddenly increases near wall openings [141]. In addition, the cracks change the pillars' height between the openings [157].

3.3. Computational models of stiffening walls

Although numerical methods are commonly used in the calculations of stiffening walls, there is a need for simple methods to allow for analytical verification [1] of the structure's behavior. Paper [18] proposed a simplified model for shear walls under compression based on three parameters: the limit strength f_{mk}, the yielding strain ε_y and ductility index $D=\varepsilon_u/\varepsilon_y$. The model considers the wall under shear at the top and the compressed in a vertical direction. Three states (fully elastic, cracked elastic and elastic-plastic) are distinguished depending on the geometry of the cutting line, which separates compressed and inactive zones. The static scheme of the structure is a cantilever wall – Fig. 3.29. The authors compared such an analytical model with experimental data and estimated an average error. The average estimation error of ultimate shear force was equal Δ_v=10.7%, and the corresponding displacement estimation error was Δ_d=26.9% [18].
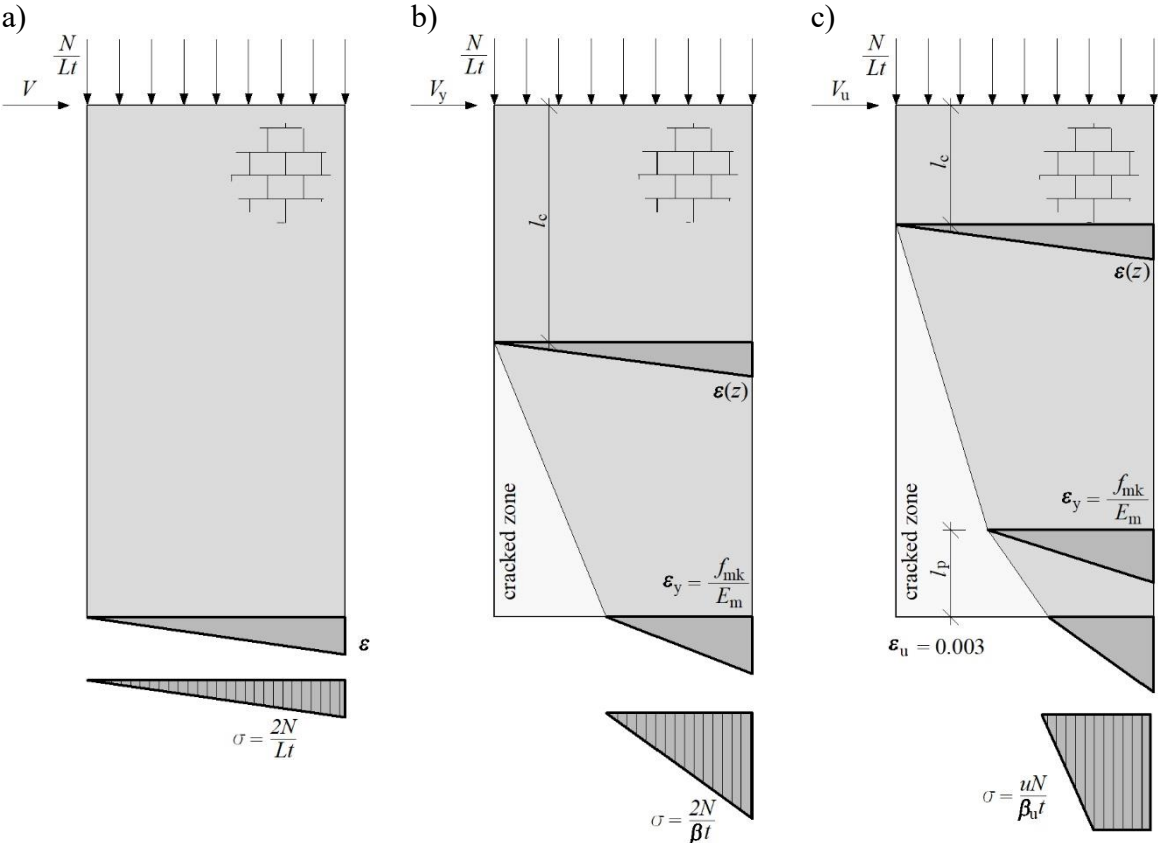

Fig. 3.29 Equilibrium states of a wall under compression and shear based on [18]: a) fully elastic, b) cracked elastic, c) elastic-plastic

Simplified planar models were developed for non-torsional reinforced concrete structures [121]. The tall building is a non-twisting structure when the load is uniformly

distributed over the height, the geometry of the building is symmetric, and the structural system is the same at each floor level. Moreover, the slabs should constrain the horizontal deflections of the walls and frames and be rigid in their planes. In such conditions, the building can be represented by a single-bay moment resisting frame, joined at each slab level by an axially rigid link or a multi-bay system [161].

The equivalent single-bay frame may be considered a planar continuum model in simplified analysis, assuming the structure to be uniform with height. In such a model, accounting for the double-curvature bending of the columns within each story height is necessary when calculating the shear rigidity GA. It is assumed that a continuous medium links columns. Continuum has shear rigidity GA equivalent to the story-average shear rigidity of the frame associated with a double-curvature bending of its columns and beams. Fig. 3.30 shows that the wall is linked with continuously coupled columns by axially rigid connection links with no shear rigidity. The structure can be represented mathematically by equation (3.29). The model may be extended by adding a stiffening panel to analyse the structure with the stiffened intermediate-level story [121].
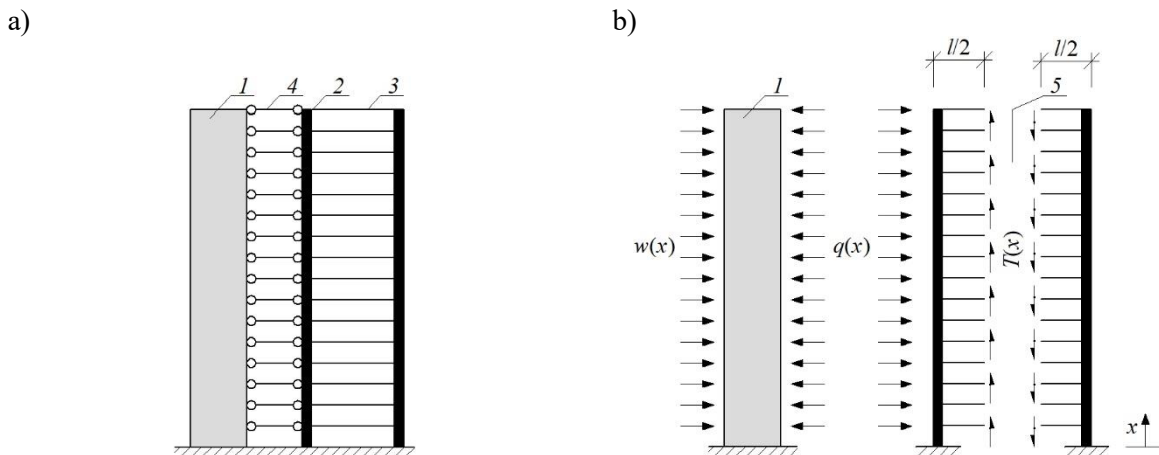

Fig. 3.30 The calculation model of a building: a) continuum representation of wall-frame, b) forces in a structural system, based on [121]: 1 – shear wall, 2 – moment-resisting frame, 3 – shear and bending continuum representing GA property of frame, 4 – horizontal rigid continuum representing axially stiff connecting links, 5 – line of contra flexure

$$\frac{l}{EI}\int_0^x M_E(x)dx - T'(x)\frac{l^2}{GA} + \frac{l^2}{EI}k^2\int_0^x [T(x)]dx = 0 \qquad (3.29)$$

where:

$M_E(x)$ – external moment acting on the building at height x from the base,

$T(x)$ – axial force in the columns at height x due to overturning,

l – the distance between columns of the equivalent one-bay moment resisting frame,

EI – the sum of flexural rigidities of the frame columns and the shear wall,

GA – the racking shear rigidity of the moment-resisting frame.

Continuum models are good predictions of the overall lateral load behavior of uniform coupled wall and wall-frame structures. It is worth mentioning that such an approach is developed for reinforced concrete structures and not involving specific masonry behavior. Therefore, it is insufficient for detailed interactions between the wall and frame, particularly at the bottom and the top of the building.

For the dynamic behavior of stiffened coupled shear walls, also are used discrete-continuous approach [94]. In such calculations, there is a possibility to consider the effect of flexible foundations represented by rotational and translational springs at the base of each shear wall. The analytical model enables a simplified representation of soil-structure interaction. Due to the wind action design needing to be considered the overall building stability and the strength of individual stiffening walls, the book [69] presented an analytical method for wind load analysis based on the simple bending theory – Fig. 3.31. It is assumed that shear walls deform as cantilevers, and the slab is a rigid diaphragm. The deflection at the slab level is the same as the shear wall and is given by formulas (3.30) and (3.31).

$$\Delta_1 = \frac{w_1 \cdot h^3}{3EI_1} + \frac{\lambda w_1 h}{AG} \tag{3.30}$$

$$\Delta_2 = \frac{w_2 \cdot h^3}{3EI_2} + \frac{\lambda w_2 h}{AG} \tag{3.31}$$

where:

w_1, w_2 – lateral forces acting on stiffening walls,

D_1, D_2 – deflections of particular walls,

h – height,

G- modulus of rigidity,

I_1, I_2 – second moments of areas,

λ – shear deformation coefficient (1.2 for rectangular section and 1.0 for flanged section).
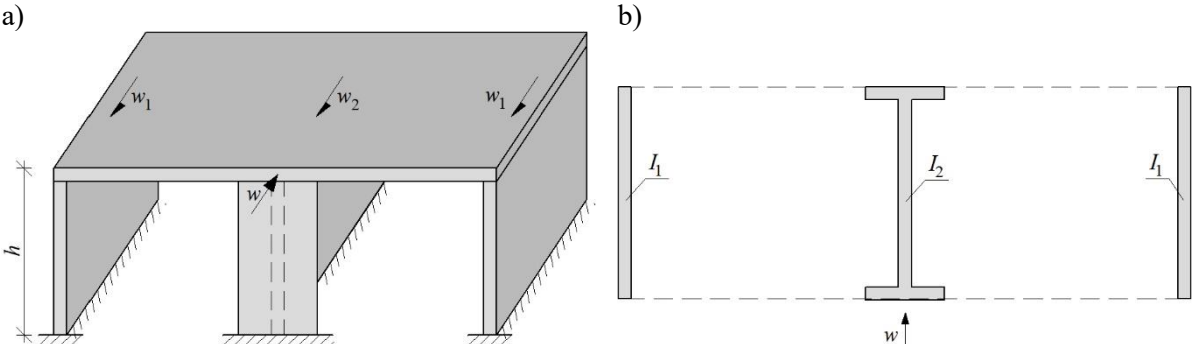

Fig. 3.31 Analytical method [69] for shear walls resisting wind force: a) 3D view, b) plan view

The first part of formulas (3.30) and (3.31) describes bending deflection, and the second part characters the shear displacement. Shear deflection can be neglected if the height/width ratio exceeds 5.0. Equations (3.32) and (3.33) formulate the lateral load that shear walls take.

$$\Delta_1 = \Delta_2 \tag{3.32}$$

$$2w_1 + w_2 = w \tag{3.33}$$

The walls with openings are called coupled walls or pierced shear walls and present a more complex problem in static [4, 43, 152, 92] and dynamic analysis [3]. There are five different calculation models for the analysis of this case: individual cantilever, equivalent frame, wide column frame, continuum model, and model based on the finite element method (FEM) – Fig. 3.32.
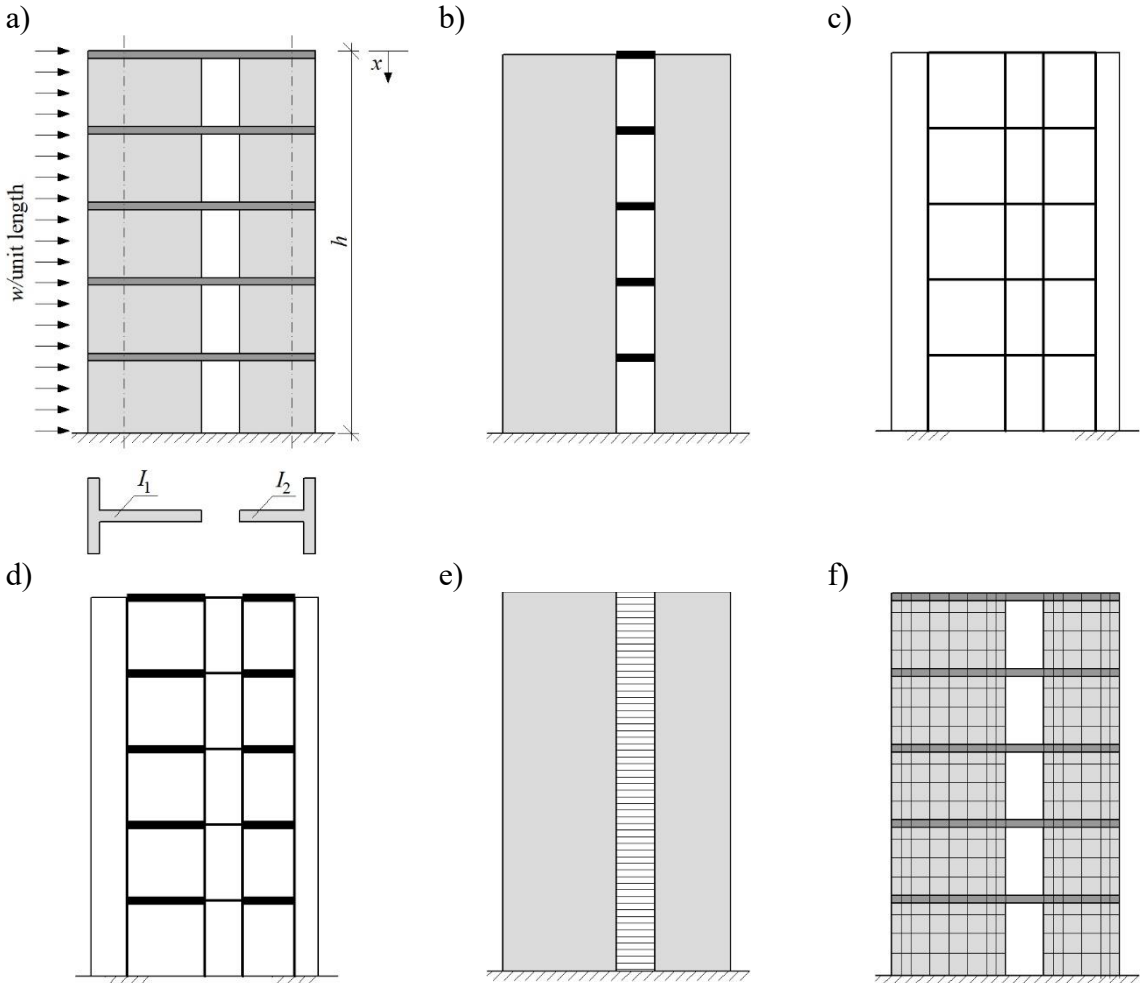

Fig. 3.32 Calculation models for stiffening walls with openings [69]: a) building view, b) individual cantilever, c) equivalent frame, d) wide column frame, e) continuum model, f) model based on finite element method (FEM)

51

When a series of vertical cantilever walls idealize the structure, there is assumed that vertical piers are deflecting together and the slabs transmit only normal forces, neglecting its bending. The load is distributed in proportion to the flexural stiffness of load-bearing elements. The shear wall deflection is calculated by formulas (3.34) – (3.37).

$$\Delta = \frac{w_1}{EI_1}\left(\frac{x^4}{24} - \frac{h^3 x}{6} + \frac{h^4}{8}\right)$$
(3.34)

$$\Delta = \frac{w_2}{EI_2}\left(\frac{x^4}{24} - \frac{h^3 x}{6} + \frac{h^4}{8}\right)$$
(3.35)

$$w_1 = \frac{w}{I_1 + I_2} I_1$$
(3.36)

$$w_2 = \frac{w}{I_1 + I_2} I_2$$
(3.37)

where:

w – uniformly distributed wind load/unit height,

h – the building height,

x – a distance of the section under consideration from the top,

I_1 and I_2 – second moments of areas.

In the equivalent frame approach, walls and slabs are represented by beams with the same flexural stiffness as walls and slabs. A similar model is a wide column frame. In this approach, an equivalent frame idealizes the actual structure, but the interconnecting members are assumed to be of infinite stiffness for part of their length. Another approach is a continuum model in which an equivalent shear medium represents the structure, and the contra-flexure point is taken at the center of the medium. The most complex model is based on Finite Element Method.

In order to compare the results of the analytical methods and the actual behavior of the masonry structure, experimental tests were carried out [69]. A full-scale model of a three-story building was made - the model was loaded horizontally, and the deflections and strains were measured at various level loads. The view of the full-scale model and plan view is shown in Fig 3.33.
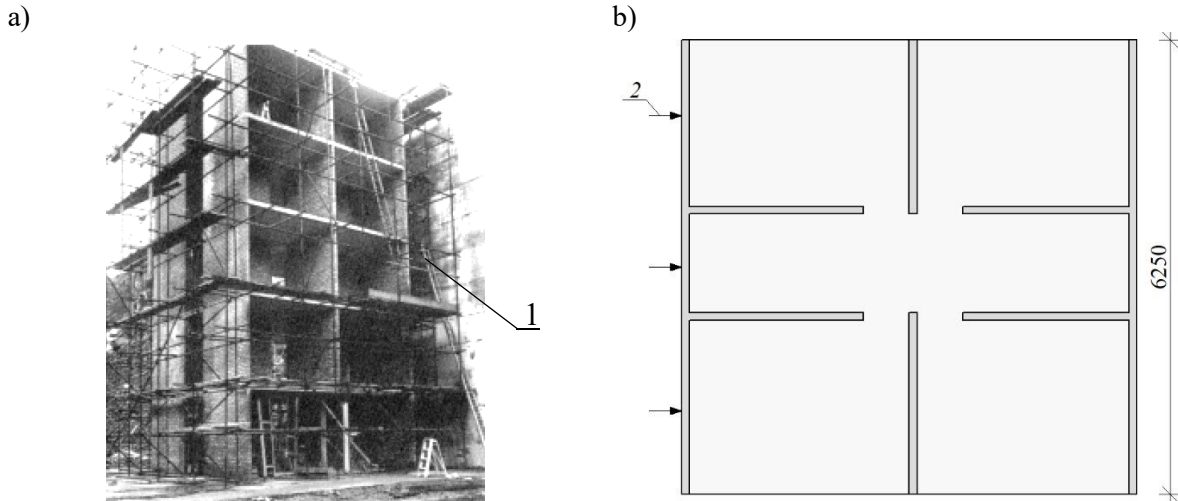
Fig. 3.33 Full-scale building model [69]: a) view of the structure, b) plan view: 1 – tested building, 2 – horizontal load (three jacks per floor)

Results indicate nonlinear stain and stress distribution across the shear wall near ground level. This phenomenon causes analytical calculations not to converge the experimental results because they assumed linear stress variation across the shear wall (except Finite Element Method). The best convergence between the theoretical and experimental results was obtained for the equivalent rigid frame. In such a method, the columns have the same sectional properties as the walls with interconnecting slabs spanning between the columns – Fig. 3.34.
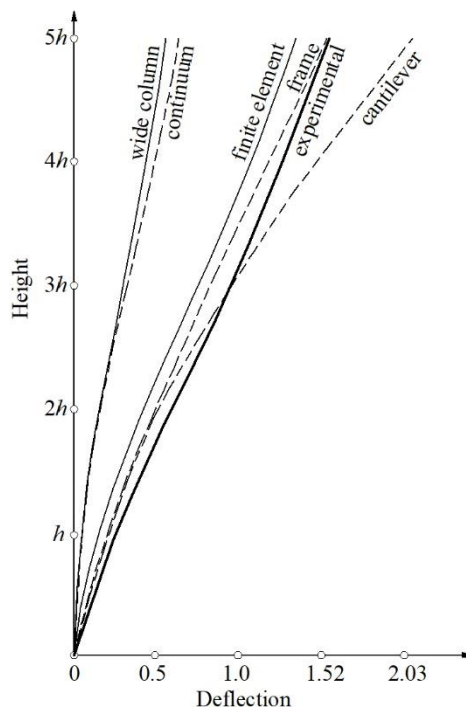

Fig. 3.34 Comparison between the theoretical and experimental results based on the full-scale research presented in [69]

Moreover, A.W. Hendry, B.P. Sinha and S.R. Davies presented in [69] the method of load distribution between the unsymmetrically arranged stiffening walls. The resultant horizontal load caused by the wind, which does not pass through the shear center can be replaced by the load W and twisting moment We – Fig. 3.35. When stiffening walls are arranged symmetrically, the load is distributed proportionally to particular wall stiffness. The deflection of walls must be equal at floor level. Forces in individual walls can be calculated from formulas (3.38) – (3.40).

$$W_A = \frac{WI_A}{I_A + I_B + I_C} = \frac{WI_A}{\sum I} \qquad (3.38)$$

$$W_B = \frac{WI_B}{\sum I} \qquad (3.39)$$
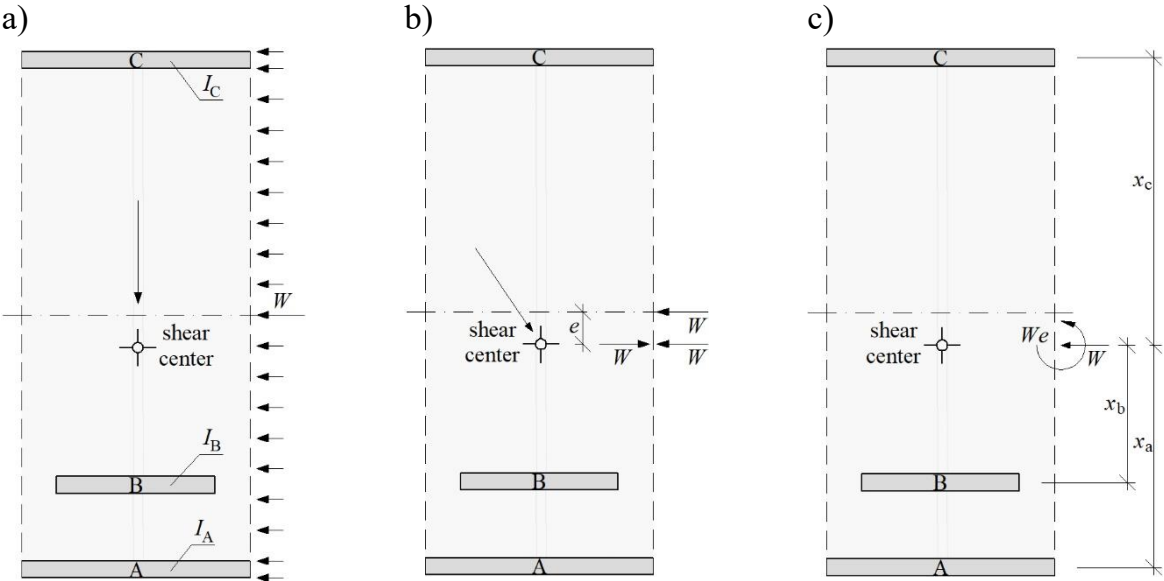
$$W_C = \frac{WI_C}{\sum I} \qquad (3.40)$$

Fig. 3.35 Unsymmetrical arranged stiffening walls subjected to horizontal load, according to [69]

Due to the rotation of the building, in walls arise additional forces W'_A, W'_B W'_C. In walls A and B, forces have the same negative value; in wall C, the force has a positive value. The deflections Δ_a, Δ_b and Δ_c caused by rotation (Fig. 3.36) can be calculated from the following relationships (3.41) – (3.44):

$$\Delta_b = \Delta_a x_b / x_a \qquad (3.41)$$

$$\Delta_c = \Delta_a x_c / x_a \tag{3.42}$$

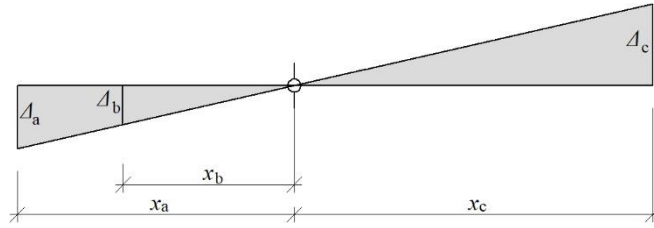$$\Delta_a = W'_A \cdot h^3 / KEI_A \tag{3.43}$$

Fig. 3.36 Horizontal displacements of stiffening walls due to rotation (twisting), according to [69]

where: K is a constant deflection and:

$$\Delta_b = W'_B \cdot h^3 / KEI_B \tag{3.44}$$

Substituting the value of Δ_b from (3.41) and Δ_a from (3.43), there are (3.45):

$$(\Delta_a / x_a) x_b = W_B \cdot h^3 / KEI_B \tag{3.45}$$

or (3.46):

$$(x_b / x_a)(W'_A / I_A) = W_B / I_B \tag{3.46}$$

or (3.47):

$$W'_B = (W'_A I_B / I_A)(x_b / x_a) \tag{3.47}$$

Analogously (3.48):

$$W'_C = (W'_A I_C / I_A)(x_c / x_a) \tag{3.48}$$

The sum of moments must be equal to the rotation moment (3.49) and (3.50):

$$W'_A x_a + W'_B x_b + W'_C x_c = W_e \tag{3.49}$$

$$W'_A \left[x_a + \left(\frac{I_B}{I_A} \right) \left(\frac{x_b^2}{x_a} \right) + \left(\frac{I_C}{I_A} \right) \left(\frac{x_c^2}{x_a} \right) \right] = W_e \tag{3.50}$$

or (3.51):

$$W'_A = \frac{W_e I_A x_a}{I_A x_a^2 + I_B x_b^2 + I_C x_c^2} = \frac{W_e I_A x_a}{\sum I \, x^2} \tag{3.51}$$

Then the other forces are (3.52) and (3.53):

$$W'_B = \frac{W_e I_B x_b}{\sum I \, x^2} \tag{3.52}$$

$$W'_C = \frac{W_e I_C x_c}{\sum I \, x^2} \tag{3.53}$$

The force in each wall can be calculated as the algebraic sum expressed in the relationship (3.54):

$$W'_n = \frac{W_e I_n}{\sum I} + \frac{W_e I_n x_n}{\sum I \, x^2} \tag{3.54}$$

The second term in the equation is positive for walls on the same side of the centroid as the load W. The analytical determination of the location of the flexural center of the building was proposed in the paper [114]. The authors presented the method for dynamic analysis of tall buildings braced by stiffening walls and thin-walled open-section structures – Fig. 3.37. The formulas (3.55) and (3.56) describe the coordinates of center of flexural rigidity for asymmetric structure:

$$\bar{x}_0 = \frac{\sum_q \bar{x}_q EI_{y,q}}{\sum_q EI_{y,q}} \tag{3.55}$$

$$\bar{y}_0 = \frac{\sum_q \bar{y}_q EI_{x,q}}{\sum_q EI_{x,q}} \tag{3.56}$$

$\bar{x}_0, \bar{y}_0$ – the coordinates of the flexural center,
$EI_{x,q}, EI_{y,q}$ – the lateral stiffness of qth shear wall/thin-walled open cross-section.
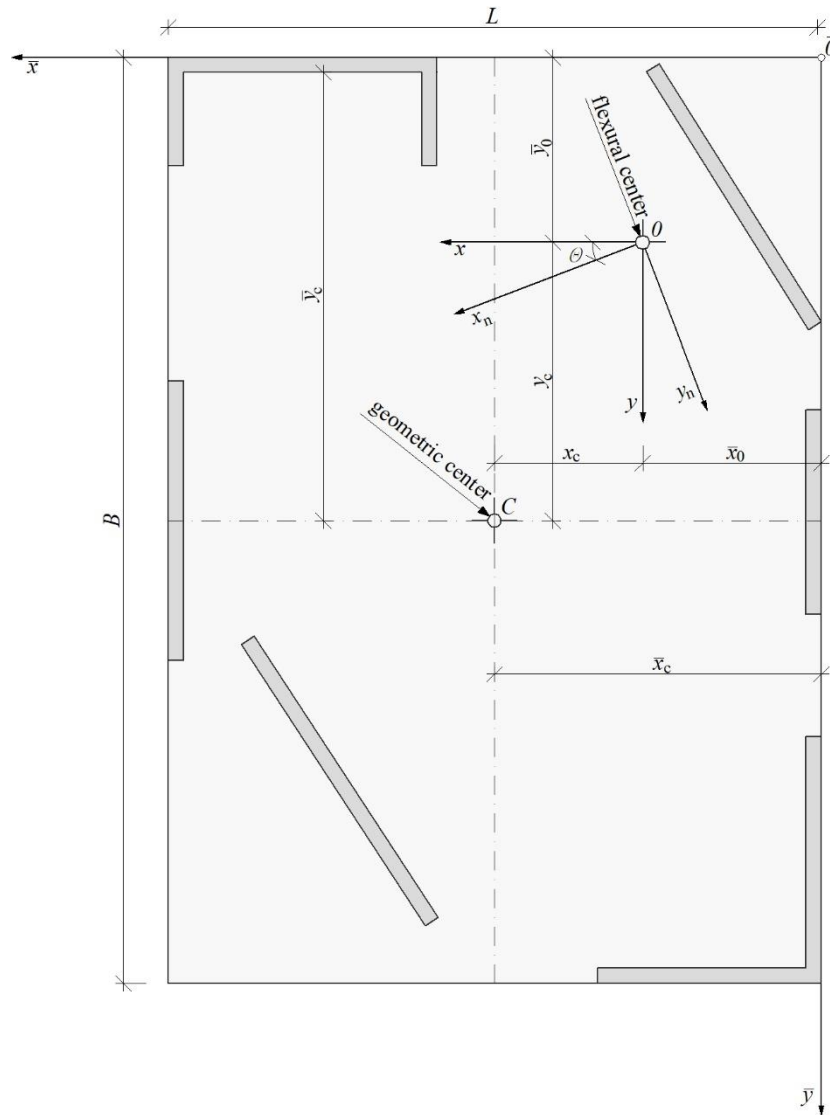
Fig. 3.37 Layout of an asymmetric building with shear walls and thin-walled open cross sections columns, according to [114]

The location of the geometric center (x_c, y_c) can be calculated from equation (3.57) – (3.58):

$$x_c = \bar{x}_C - \bar{x}_0 \tag{3.57}$$

$$y_c = \bar{y}_C - \bar{y}_0 \tag{3.58}$$

$\bar{x}_0, \bar{y}_0$ – the coordinates of the flexural center.

The description of the rotation of the building can be analyzed using Vlasov's theory – the approaches based on that presented in [162, 5]. Although the three-dimensional analysis of shear wall structures with any number of connecting and stiffening beams

can give a faithful representation of tall buildings – it does not consider the specificity of masonry structures. The so-called multi-pier (MP) approach enables the non-linear analysis of the in-plane behavior of masonry walls. The method consists of substituting the 2D continuum with an assemblage of vertical trusses (piers) and braces, exhibiting a monodimensional non-linear behavior with softening [127].

Distribution of loads based on the stiffness of the shear walls is the right approach assuming that the floors act as a rigid diaphragm, but this approach is incorrect in analysing low-rise buildings with slab-rib or wooden ceilings. In this case, floors act as flexible diaphragms, and lateral loads cannot be distributed on shear walls proportionally to their stiffness. Sang-Cheol Kim and Donald W. White proposed an analytical approach for analysing low-rise buildings with flexible diaphragms [89]. The structural separation method is based on the phenomenon that flexible floors within the structure tend to respond independently. The method models each diaphragm and its adjacent walls as separate subassemblies – Fig. 3.38. The in-plane wall horizontal forces are calculated by summing the forces from the adjacent diaphragm subassemblies. Although the method is related to seismic analysis, the methodology can be helpful also in static calculations of low-rise buildings with flexible diaphragms.
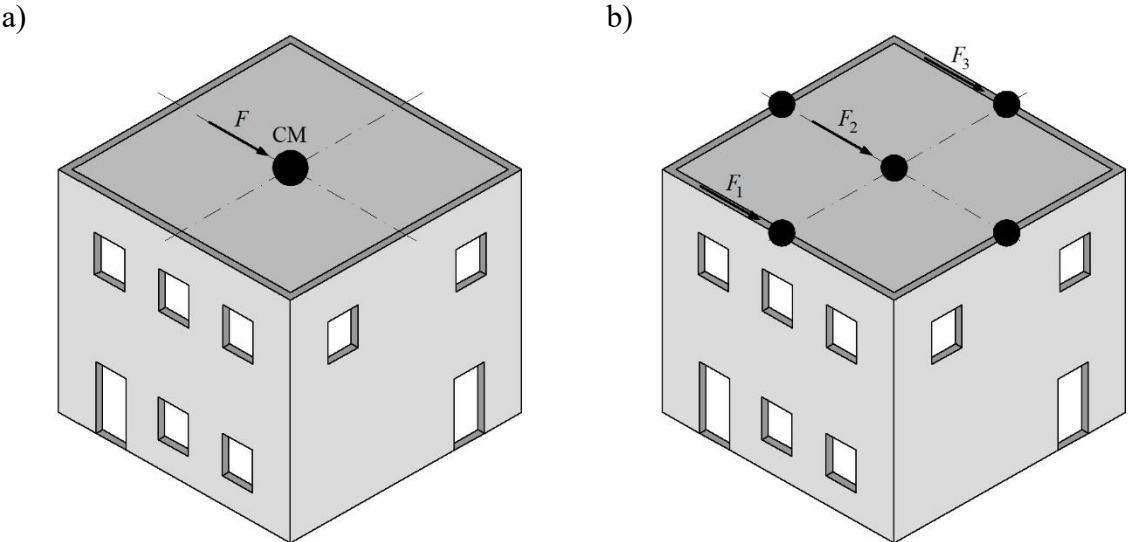

Fig. 3.38 Distribution of the lateral forces in low-rise buildings: a) rigid diaphragm, b) flexible diaphragm, CM – the center of mass, according to [89]

The simple equilibrium model (load-path or strut and tie schemes) is a different calculation approach for stiffening walls. In reinforced concrete structure analysis strut represent the compression zone, and the tie corresponds to reinforcement. Although masonry behaves in another way due to its brittle nature, it is possible to adapt some well-known analytical methods, such as strut and tie models (the S-T), for first-approach

calculations. Pere Roca determined that struts representing the diagonal field of compression stresses and in equilibrium with the external load can be smeared or concentrated [138]. Moreover, the distribution of the compression zone is conditioned by the wall geometry, loads and presence of openings, which disturbance the stresses. The proposed models consist of bars and nodes – Fig. 3.39. Bars can be smeared (sC) or discrete (dC). Nodes can be a punctual connection between ties and struts (CCT) or finite regions (CCS – external load or reaction meet with one converging internal compression force and CCCS - external load or reaction meet with two converging internal compression forces). At least two discrete struts should be assumed to represent the effect of concentrated or partial load on a wall.

Furthermore, such load (or reaction) cause a reverse *bottle-neck* effect. In such cases, two opening struts should be balanced by a tie - Fig. 3.39c. The slope of struts concerning vertical is limited to $\tan\phi$ (ϕ – friction angle of unit-unit interface for dry-joint wall). In the case of a cohesive wall, the slope is restricted to $\tan\alpha$ (3.59). The slope of the ties concerning horizontal is limited by the tensile strength of masonry in a normal direction to the bed joint's surface.

$$\tan a = \tan \phi + \frac{c}{\sigma_n} \qquad (3.59)$$

in which:

$\tan\alpha$ - the angle of friction of the unit-mortar interface,

c – cohesion,

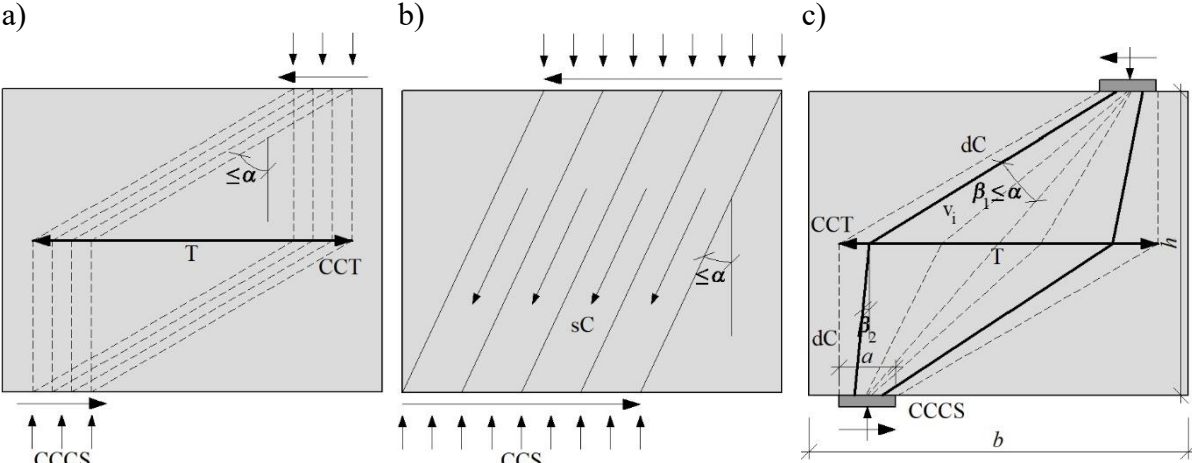σ_n – the average vertical compression.

Fig. 3.39 The strut and tie models for shear walls proposed by Pere Roca [138]: a) deviation of compression stress zone by horizontal tensile forces (T), b) parallel smeared struts (sC) and CCS nodes, c) discrete struts (dC) picturing a reverse *bottle-neck* compression stress field combined with a tie (T), in combination with CCT and CCCS nodes

The presence of openings determines more complex the S-T model. In a wall with a centrally located opening, there is no vertical compression close to the top and bottom edges of the opening. The model presented in Fig. 3.40a can be assumed in very cohesive walls. If the tie cannot emerge, the walls can be estimated using models presented in Fig. 3.40b and 3.40c.
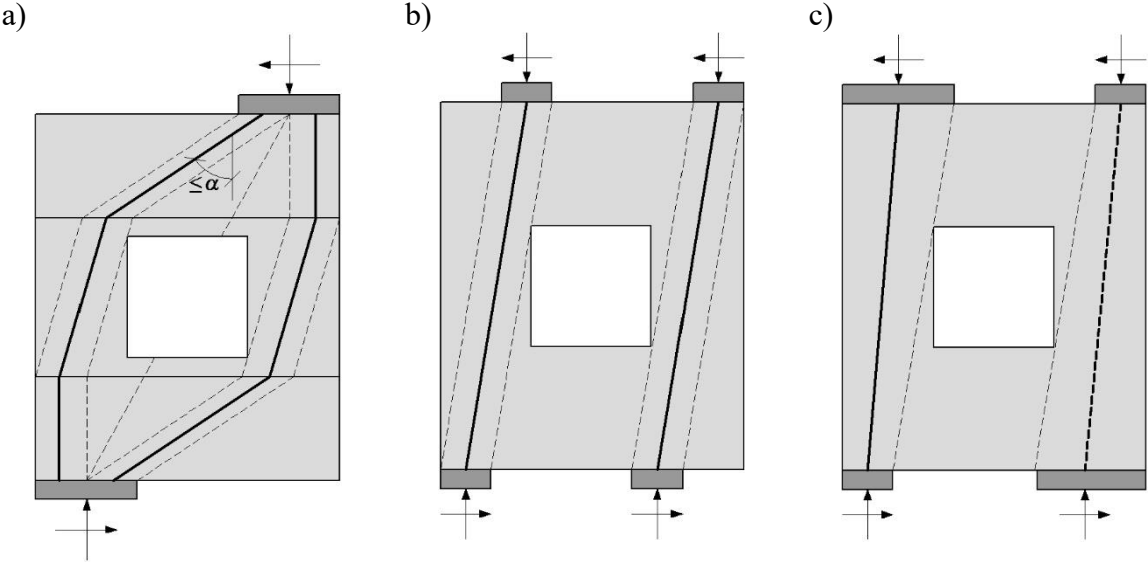

Fig. 3.40 The S-T models for shear walls with openings, according to [138]: a) cohesive walls, b) and c) non-cohesive walls

The S-T models are used for simplified calculation of the shear strength of confined masonry walls subjected to in-plane loads [153]. The analysis encloses confined masonry with and without openings [154]. A single concentric strut constitutive model also can represent the infill response under in-plane horizontal loads [98]. The experimental verification of the models and the mixed model (combined model) is presented in [130, 83].

3.4. Numerical methods of modelling masonry structures

Masonry characterizes the anisotropic behavior because it combines different materials with different mechanical and physical parameters. The modelling strategy for the masonry has to fully represent its behavior discretely or represent the structure using a simplified method with the averaged mechanical parameters of the masonry [105, 107].

The discrete modelling is usually based on the FEM (finite element method) or FDEM (finite-discrete element method). In such an approach, the number of parameters

used to describe the behavior of masonry units, mortar and bonds between them is time-consuming and labour-consuming. This aspect makes discrete modelling unsuitable for large-size structures. Simplified modelling requires fewer parameters than the discrete technique and is much less time-consuming. Thus, this method can be applied to parts of the structure and the whole building. Numerical models should always be validated based on structural test results [147]. Regardless of the choice of homogenization strategy, a sensitivity analysis of the parameters on a numerical model should be performed [32, 55].

Mechanical parameters of masonry components (units, mortar) are not the same as parameters of masonry which there are parts. Homogenized masonry requires a new composite material model with specific mechanical behavior. The homogenization technique should be precise in parameter selection and easily adaptable to another masonry. Various combinations [102] of different masonry units and different types of mortars determine the complexity of the modelling approach for masonry structures [9]. The influence of the uncertainty in material properties on the in-plane lateral behavior can be solved by numerical assessment of an unreinforced masonry (URM) wall using a stochastic analysis in the form of Monte Carlo simulations [63]. Therefore, due to the intricacy of historical buildings with irregular textures, homogenization techniques represent the original structure by the continuum model and make the analysis possible [51].

3.4.1. Classification of homogenization methods

The simple classification of homogenization methods is rather difficult due to the specific nature of the proposed literature solutions. Requirements for small-scale structures are different than in entire masonry buildings. The systematics of modelling masonry structures is considered to appear at the beginning of the 1990s. At that time, two approaches for masonry modelling were introduced in the papers [105, 104] - the first one is based on homogeneous parameters and is defined as the continuum model. The second introduces the concept of the interface model representing the effects observed at the interface between mortar and masonry units.

The paper [107] from 1996 should be considered the first cohesive paper that presents the classification of modelling techniques for masonry structures. The method of discrete (micro) modelling of masonry has been developed. The mechanics of the contact between mortar and masonry units is crucial as this zone is mainly responsible for representing the masonry behavior at the non-linear (post-elastic) phase. The paper

on micro-modelling published in 1997 [124] indicated the need to search for new homogenization methods that simplify the computation. The paper considered whether replacing the actual mortar joints with an interface modelled as interface elements is possible. In 1999, the paper [100] introduced the term meso-model. That was a variety of the macro-model using the original method of calibrating material parameters regarded as a reproducible masonry unit (RVE – representative volume element). The method of validating parameters for homogeneous models was improved in the subsequent years [31, 30], considering the experimental results. The paper [46] describes the additional classification of macro-modelling into the following categories: BBM (block-based models), CM (continuum models), MM (macroelement models), GBM (geometry-based models) – Fig. 3.41. The conventional classification of numerical methods of masonry modelling is different and is illustrated in Fig. 3.42.
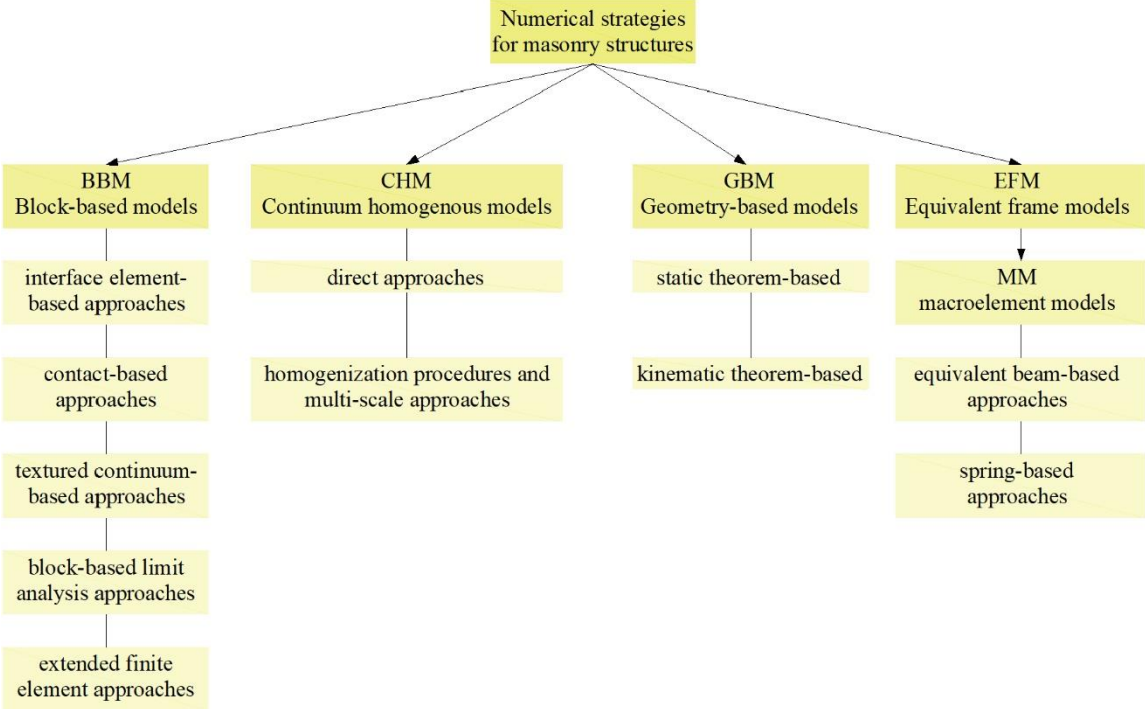

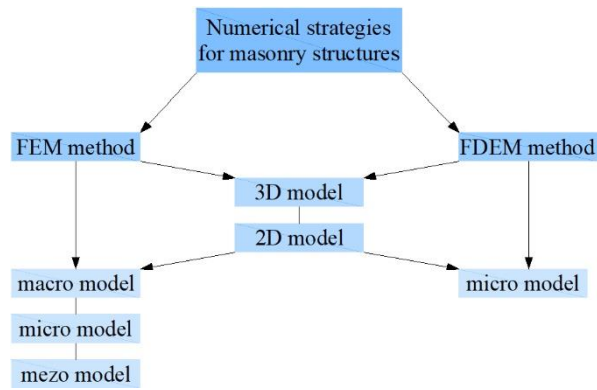Fig. 3.41 Alternative classification of modelling strategies based on [46]

Fig. 3.42 Classification of homogenization techniques in numerical masonry modelling

3.4.2. Macro-modelling

Macro modelling (Fig. 3.43) is the recommended approach to analyse the entire masonry buildings built of other structural components such as wooden or reinforced concrete slabs, reinforced concrete and steel columns, and components of facades and foundations. This method uses the isotropic or anisotropic material model [106] and the equivalent parameters [13] to represent the behavior of a masonry structure. The validation of the implemented parameters conditions the accuracy of the masonry representation. Macro modelling cannot be used to observe in detail the failure pattern of masonry - cohesive cracks between masonry units and mortar. Thus, the calculated results regarding the failure process cannot be regarded as detailed enough. However, the macro modelling approach has many advantages. It significantly accelerates the process of structure modelling, can be used to perform the global analysis of the masonry behavior, is less time-consuming and requires a lower design effort.

Two basic masonry macro-models can be currently identified [12]: continuum finite element macro-models and discontinuum finite element macro-models. The continuum finite element macro-model is similar to the concrete or soil model, considering linear or nonlinear constitutive relations, yield surfaces, and boundary surfaces. On the other hand, the discontinuum models [28, 27] consist of rigid elements connected by flexible ones that represent mortar of linear or non-linear behavior [26]. Due to the minimized number of parameters, the masonry macro-models are used to perform calculations for constructions subjected to static, dynamic and cyclic loading, including safety evaluation for seismic or paraseismic areas [59, 123, 58, 109, 122]. Macro modelling can be adapted to unreinforced masonry (URM) and wide-spaced reinforced masonry (WSRM) [49] or masonry panels confined with reinforced grouted cores [76].
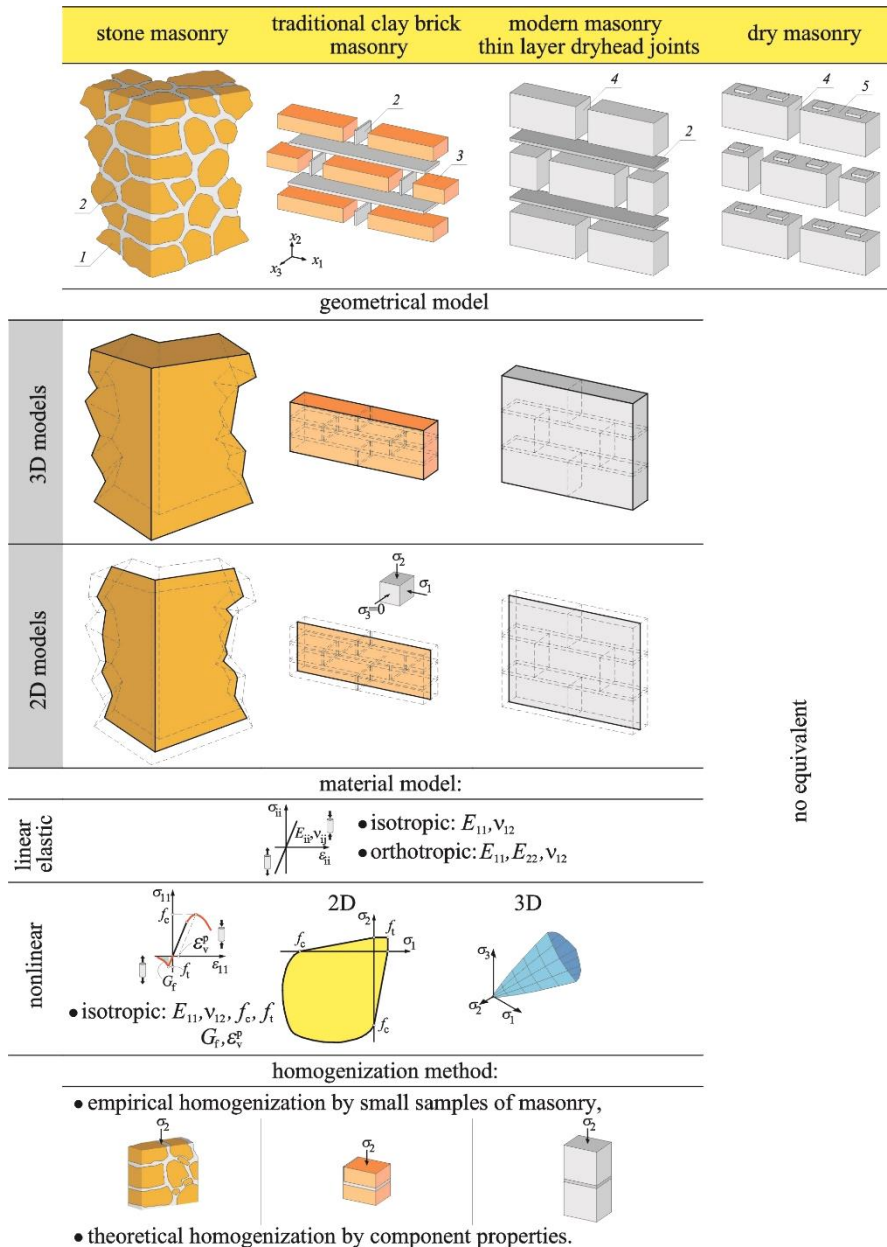
Fig. 3.43 Classification of macro-modelling approach: 1 – unworked stone, 2 – mortar, 3 – solid brick, 4 – unfilled head joint, 5 – unfilled bed joint

3.4.3. Micro-modelling

Micro-modelling (Fig. 3.44) is used to represent in detail masonry and perform a more in-depth analysis of the local effects of cracking morphology and failure process. This type of modelling is more time-consuming and usually extends the computing time. Micro-modelling is based on dividing the masonry structure [13, 7, 14, 64] into specific parts representing actual masonry units and mortar. Joints are represented by additional contact (interface) elements between the masonry units and mortar.
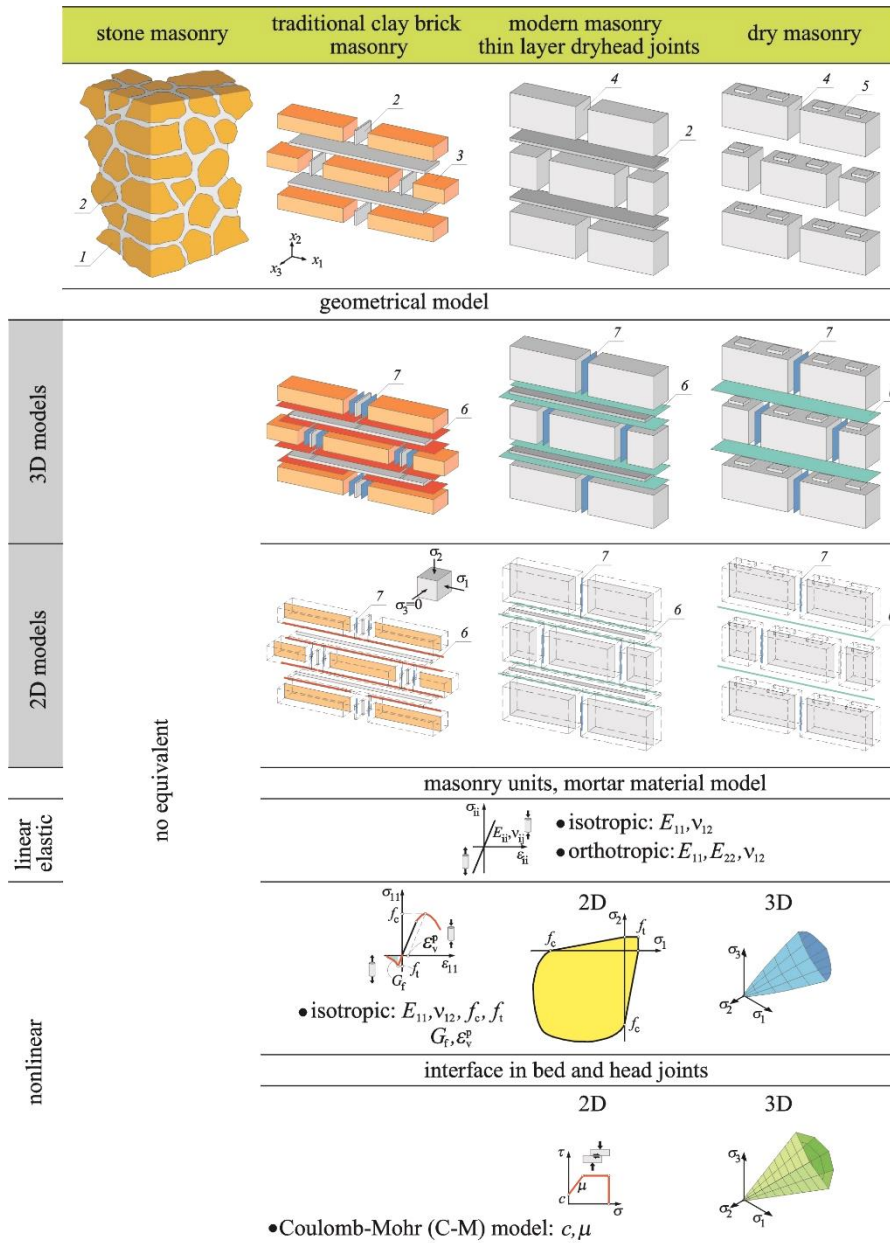
Fig. 3.44 Classification of micro-modelling approach: 1 – unworked stone, 2 – mortar, 3 – solid brick, 4 – unfilled head joint, 5 – unfilled bed joint, 6 – interface element in the bed joint, 7 – contact element in the head joint

Two main types of such modelling can be identified: simplified micro-modelling (masonry as two-phase material) and detailed micro-modelling (masonry as three-phase material) [12]. In the first strategy, the masonry is composed of elements representing the original geometry of the masonry units plus the joint thickness. The mortar is modelled as an interface with zero thickness and suitable mechanical parameters for the bond.

The second strategy – the detailed micro-modelling – is an expanded version of the first strategy. It consists of modelling the masonry as the continuum of elements representing masonry units and mortar. Micro-modelling, due to the high accuracy, can

be applied in computations performed for historical stone masonry with mortar layers [29], walls made of hollow masonry units partially filled with masonry [22], or masonry with multi-perforated units [144]. The strategy for micro-modelling can be applied to evaluate shear walls and shear models [167,126,57,53,35], compressed walls [135, 8, 145], and walls subjected to flexure [65]. Besides the procedures involved in the finite element method (FEM), the finite discrete element method (FDEM) is becoming increasingly common. This method was developed mainly to model unbound materials, such as non-cohesive soil, granular materials, stacks of elements and those showing cohesive fracture [37, 38, 36, 40]. The applied computational algorithm models the behavior of small and big masonry structures. This method is used in computations for dry masonry with the predominant cohesive type damage [151]. It successfully combines FDEM with FEM to consider the failure of masonry units [39].

3.4.4. Meso-modelling

Meso-modelling (Fig. 3.45) combines micro and macro models using the representative volume element RVE [110]. Representative volume element contains each piece of geometrical and physical information of the masonry components (masonry units and mortar) connected by contact elements. This approach is based on a concept similar to the periodic microstructure and can reflect the observed general masonry behavior. Statistical descriptors can define this original structure, and then the statistically equivalent periodic unit cell SEPUC can be found [166]. The papers [111, 125, 52, 54] show masonry analysis using the meso-modelling technique.
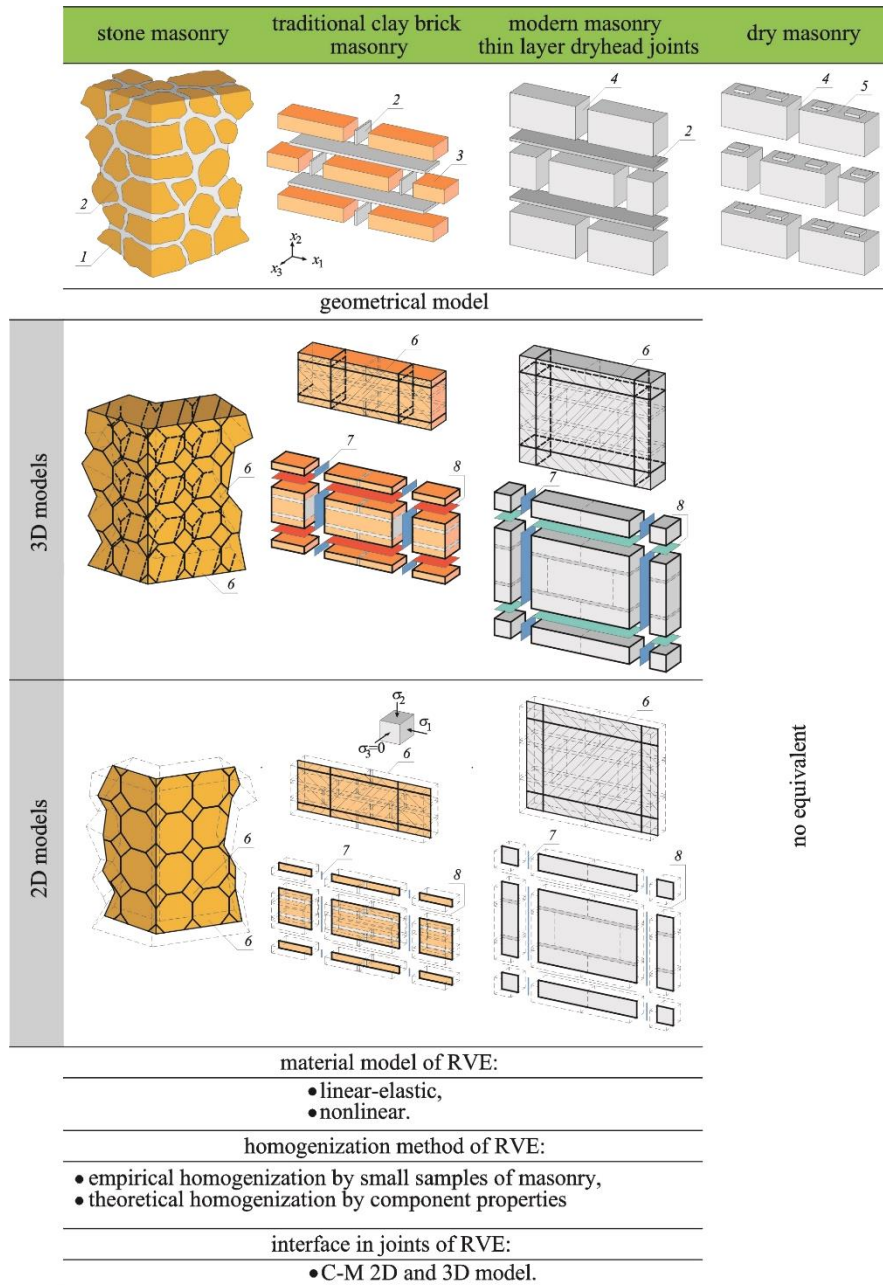
Fig. 3.45 Classification of meso-modelling approach: 1 – unworked stone, 2 – mortar, 3 – solid brick, 4 – unfilled head joint, 5 – unfilled bed joint, 6 – representative volume element (RVE), 7 – contact element in the head joint, 8 – interface element in the bed joint

3.5. Concluding remarks

The standard provisions in the Eurocode 6 are limited to brief, incomplete information regarding the calculation of stiffening walls. Although it was indicated that the horizontal load might be distributed on the stiffening walls in proportion to their stiffness - the methodology for its determination was not provided. Furthermore, no

details are provided on the redistribution of internal forces - except that it is allowed up to 15%.

The American and Canadian procedures include the most extensive provisions concerning shear walls. Despite that, the shear equation of CSAS304-14 [N4] resulted in the most inaccurate predictions of the shear load capacity of unperforated partially grouted masonry wall of both the numerical and experimental datasets, followed by the conclusion of [113]. It can be concluded that the rules for calculating shear walls are incomplete in the entire scope - from load distribution (resulting from the stiffness of the walls) to linear and non-linear analysis.

The most important conclusions resulting from the literature review are formulated in the points below.

1. The tests of monotonically loaded stiffening walls are rare.
2. Most analyses of unreinforced shear walls involve cyclic loads.
3. The horizontal displacement of the walls consists of a component due to shear and due to bending (flexural deformation).
4. The contribution of shear displacements depends not on the initial compressive stress but, above all, on the wall geometry.
5. The initial prestressing of the wall influences shear load capacity – higher compressive stress determines the shear resistance increase.
6. Compressive stress changes the crack morphology of the wall. At low levels of compressive stresses, shear cracking is stepped. When the wall is highly prestressed, the cracks run diagonally through the masonry units.
7. Perpendicular fragments of the stiffening walls (flanged walls) participate in transferring horizontal loads.
8. The stiffness of unreinforced shear walls and lateral load capacity decreases significantly due to wall openings.
9. The openings affect the crack pattern change and the pillars' actual geometry between the openings.
10. The different stiffness of the shear walls caused by the openings determines the building to twist.
11. The method of numerical masonry homogenization should be adapted to the size of the analyzed structure and the purpose of the calculations (representation accuracy).
12. Advanced material models require many input parameters - physical and empirical, and few works provide their values adopted in the calculations.

4. EXPERIMENTAL RESEARCH

4.1. Assumptions

The literature describes the research on single shear walls; however, most tests concern structures subject to cyclic loading, and studies of full-scale building models under monotonic load are scarce. The goal of the work is experimental recognition and description of the behavior of stiffening walls. Own research models were designed to achieve the objectives of the work. Research models were designed according to the following criteria:

a) the models are built of masonry units made of autoclaved aerated concrete,

b) the walls are characterized by thin-layer bed joints and unfilled head joints – tongue and groove joints were used,

c) all models are non-reinforced masonry structures (URM – unreinforced masonry),

d) the models consist of masonry walls and reinforced concrete slab that performs the function of a rigid diaphragm through which the horizontal load is distributed,

e) the initial compressive stresses of the stiffening walls correspond to a single-storey building load (in addition to the self-weight, the applied load is 4.59 kN/m^2, which corresponds to the finishing layers and the live load),

f) the tests can be extended to the analysis of multi-storey buildings by increasing the initial compressive stresses of the walls,

g) the geometry of the walls is designed in a way that the decisive deformations of the walls are shear (not flexural), the h/l ratio is less than 1.0,

h) in building models, window and door openings with geometry corresponding to the actual dimensions of such perforations in housing construction were made,

i) a test stand was designed for testing full-scale building models in the scheme of restraint of walls on the bottom edge and with the initial compressive stresses of the building.
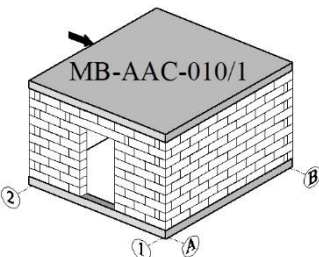
4.2. Research campaign – models and research program

Detailed studies of the mechanical characterization of the masonry components – mortar and autoclaved aerated concrete masonry units are included in the work [131]. For this reason, material parameters were not tested in this monograph. The research program (campaign) was carried out regarding the work's set goals and is focused on global structure behavior.
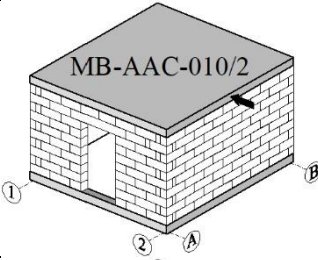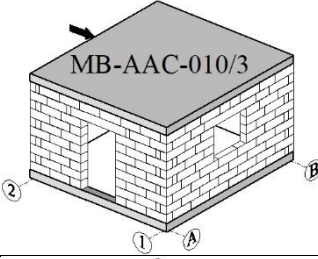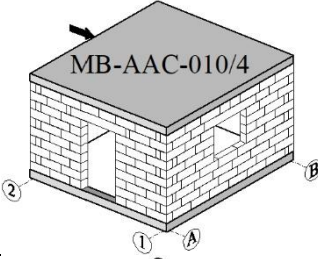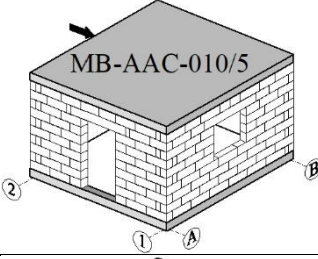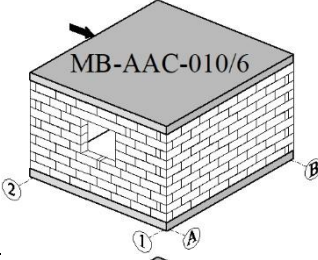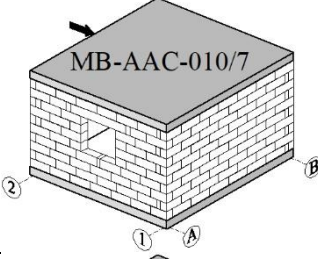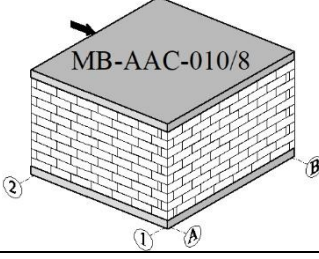
The research models are eight full-scale masonry buildings made of autoclaved aerated concrete. The models were erected on a square plan of 4.0x4.0 m. The height of the buildings is 2.85 m, and the wall thickness is equal to 0.18 m. Each model consists of two stiffening walls marked as A and B (parallel to the horizontal load) and two perpendicular walls marked as 1 and 2. The shape and arrangement of openings in the walls were chosen to reflect the actual structures best. Models are marked with an alphanumeric symbol MB-AAC-010/N, where N is the following number of the tested building, MB – masonry building, AAC – autoclaved aerated concrete, and 010 is a conventional designation of the initial level of compressive stresses. The models were grouped into two or three buildings and an additional reference model. There are four types of buildings (type I, II, III and IV). Models MW-AAC-010/1 and MW-AAC-010/2 have one door opening in stiffening wall A. Models MW-AAC-010/3, MW-AAC-010/4, MW-AAC-010/5 have a door opening in stiffening wall A and windows opening in perpendicular wall 1. Models MW-AAC-010/6 and MW-AAC-010/7 have a window opening in stiffening wall A and a door opening in stiffening wall B. The reference model MW-AAC-010/8 had no opening, and all building walls were solid. At least two models make it possible to verify the correctness of the research and compare the results. The list of the tested full-scale buildings constituting the primary research is shown in Table 4.1.

Table 4.1

The research programme of full-scale masonry buildings

Model designation / 3D view	Wall designation	Opening	Wall description
MB-AAC-010/1	Wall A	door opening	stiffening
	Wall B	solid	
	Wall 1	solid	perpendicular
	Wall 2	solid	

MB-AAC-010/2	MB-AAC-010/2	Wall A	door opening	stiffening
		Wall B	solid	
		Wall 1	solid	perpendicular
		Wall 2	solid	
MB-AAC-010/3	MB-AAC-010/3	Wall A	door opening	stiffening
		Wall B	solid	
		Wall 1	window opening	perpendicular
		Wall 2	solid	
MB-AAC-010/4	MB-AAC-010/4	Wall A	door opening	stiffening
		Wall B	solid	
		Wall 1	window opening	perpendicular
		Wall 2	solid	
MB-AAC-010/5	MB-AAC-010/5	Wall A	door opening	stiffening
		Wall B	solid	
		Wall 1	window opening	perpendicular
		Wall 2	solid	
MB-AAC-010/6	MB-AAC-010/6	Wall A	window opening	stiffening
		Wall B	door opening	
		Wall 1	solid	perpendicular
		Wall 2	solid	
MB-AAC-010/7	MB-AAC-010/7	Wall A	window opening	stiffening
		Wall B	door opening	
		Wall 1	solid	perpendicular
		Wall 2	solid	
MB-AAC-010/8	MB-AAC-010/8	Wall A	solid	stiffening
		Wall B	solid	
		Wall 1	solid	perpendicular
		Wall 2	solid	

In order to ensure the possibility of fully representing and repeating the research by other scientists, detailed information on constructing research models is included. All models were built on the same bottom beam, using such an element repeatedly. Similarly, the slab was designed to be lifted and used in each model without needing to concrete a new one.

4.2.1. Construction of the bottom ring beam

The bottom beam was made on a rectangular plan with dimensions 4.0x4.0 m. Precast L-shaped elements were used to speed up and facilitate the formwork of the element. These elements were made of lightweight concrete. Reinforcement consisting of four 12 mm diameter bars and 6 mm diameter stirrups, spaced every 15 cm, was placed on the L-shaped elements – Fig 4.1a. Each corner has been additionally reinforced with six reinforcing bars with a diameter of 12 mm (3 bars per one level of reinforcement) – Fig. 4.1b. The steel grade of the bar reinforcement is B500SP, and the stirrup is B500B. The view of the formwork structure before concreting is shown in Fig. 4.2
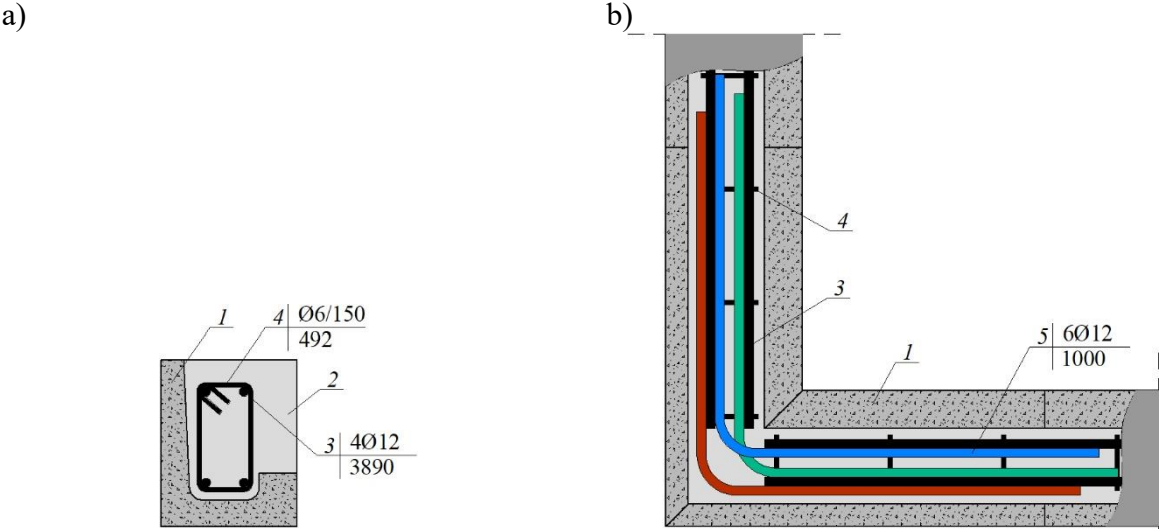

Fig. 4.1 Design of construction details: a) reinforcement of bottom beam, b) corner reinforcement: 1 – L-shaped precast element, 2 – concrete, 3 – bar reinforcement, 4 – stirrups, 5 – corner reinforcement

a)

b)

c)

Fig. 4.2 Execution of construction details of the bottom beam: a) corner reinforcement, b) main bars with stirrups, c) bottom beam formwork

After the preparation of both reinforcement and formwork, the bottom beam was concreted. The concrete class of the lower beam is C25/30. Concreting was carried out using a concrete bucket – Fig. 4.3a and 4.3b. After placing the concrete mix, it was compacted with a vibrator – Fig. 4.3c and 4.3d. This procedure allowed for proper compaction of the concrete mixture, even distribution of aggregate and preventing the segregation process.
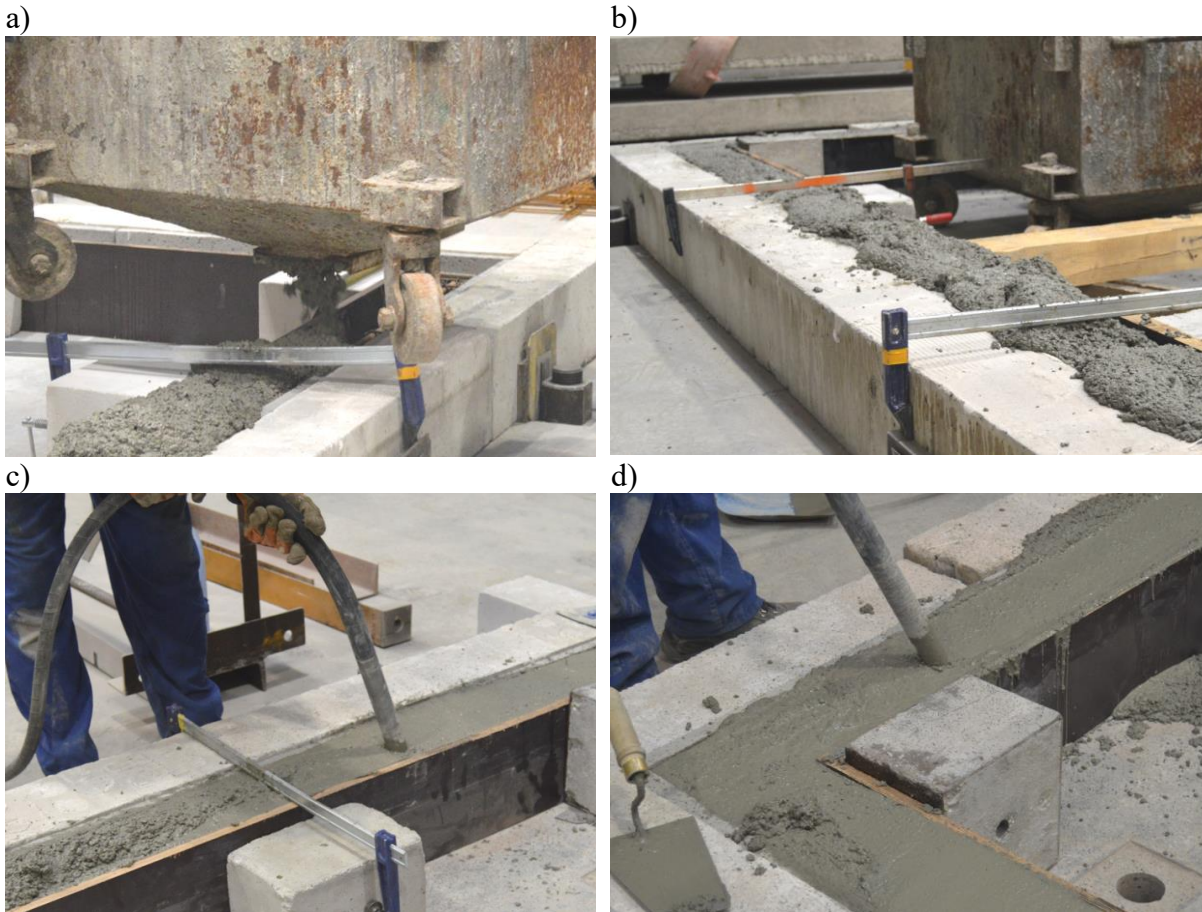
Fig. 4.3 Concreting the bottom beam: a) concrete bucket, b) laying the concrete mixture, c) and d) compaction of concrete with a vibrator

The concreted bottom beam was left to mature for 28 days. Concrete care was carried out during this time by pouring water on the beam at appropriate intervals – Fig. 4.4.
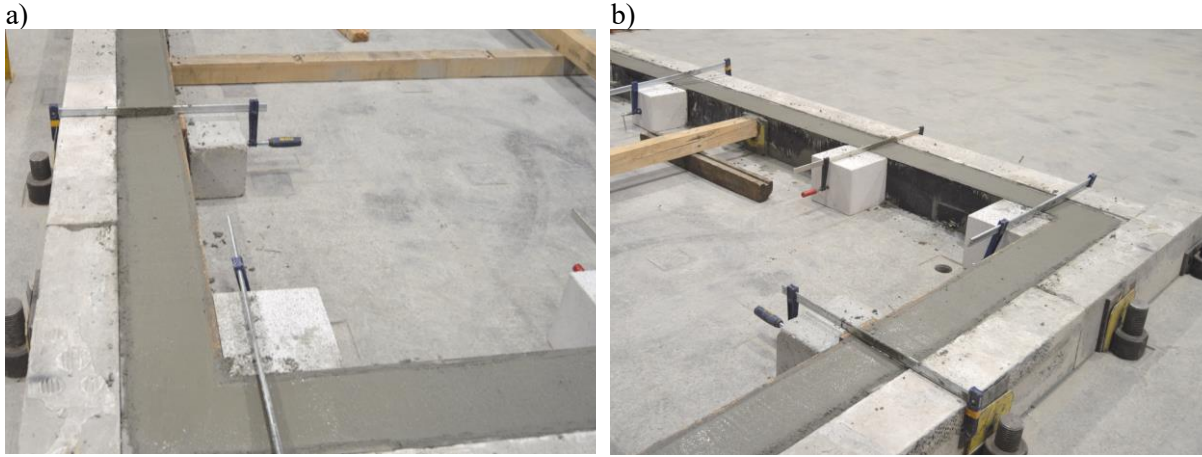

Fig. 4.4 The bottom beam after concreting

4.2.2. Construction of the masonry walls

The walls of the research models were made of autoclaved aerated concrete masonry units. The dimensions of a single block are 180x590x240 mm (width x length x height). The tests used masonry units from the *Solbet Optimal* series with a density of 600 kg/m^3. The walls were built with mortar for thin joints, and bed joints were filled with mortar class M5. Head joints were not filled – the masonry units were connected with a tongue and groove – Fig. 4.5.
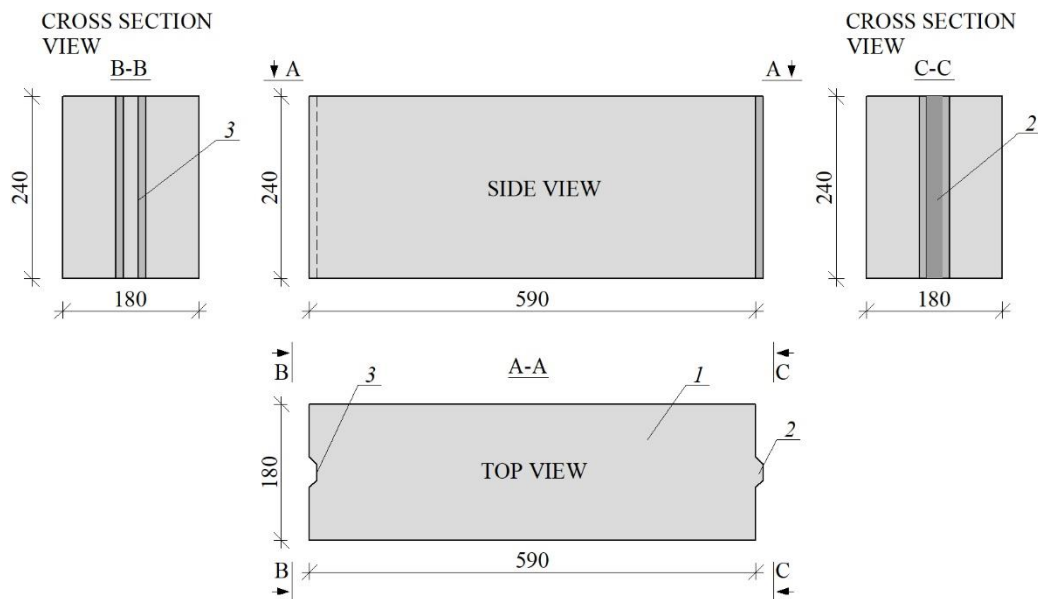

Fig. 4.5 Geometry of a single masonry unit used in the tests: 1 – masonry unit, 2 – tongue, 3 – groove

The dimensions of the masonry walls of the building are 4.0 x 2.4 m. The wall's thickness was equal to a single masonry unit and amounted to 0.18 m. The total height of the building, including the slab and bottom beam, is 2.85 m. Depending on the research model of the building, door or window openings were made in the walls. The dimensions of the door openings are 1.0x1.92 m, and the window openings are 1.0x1.0 m. Even though the models were made in series - two or three buildings the same (except for the reference model), the arrangement of individual masonry units was different. A detailed arrangement of wall elements and lintels for all tested building models to enable the possibility of repeating the tests by other researchers is provided in the Appendix.

The masonry walls were made in stages, starting with the first levelling layer. Works were carried out with platforms enabling the laying of higher parts of the walls – Fig. 4.6. After the works were completed, the walls were cured for 28 days (time for the mortar to reach full strength).
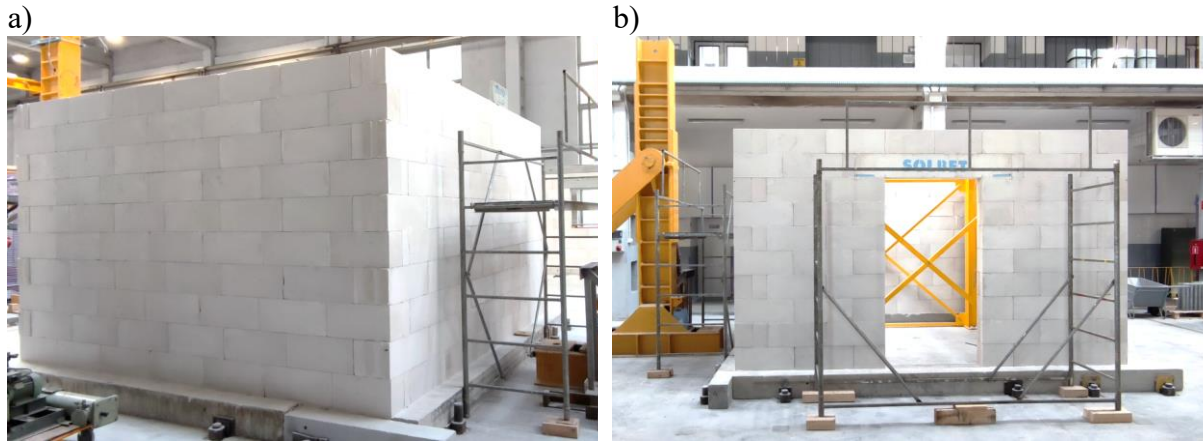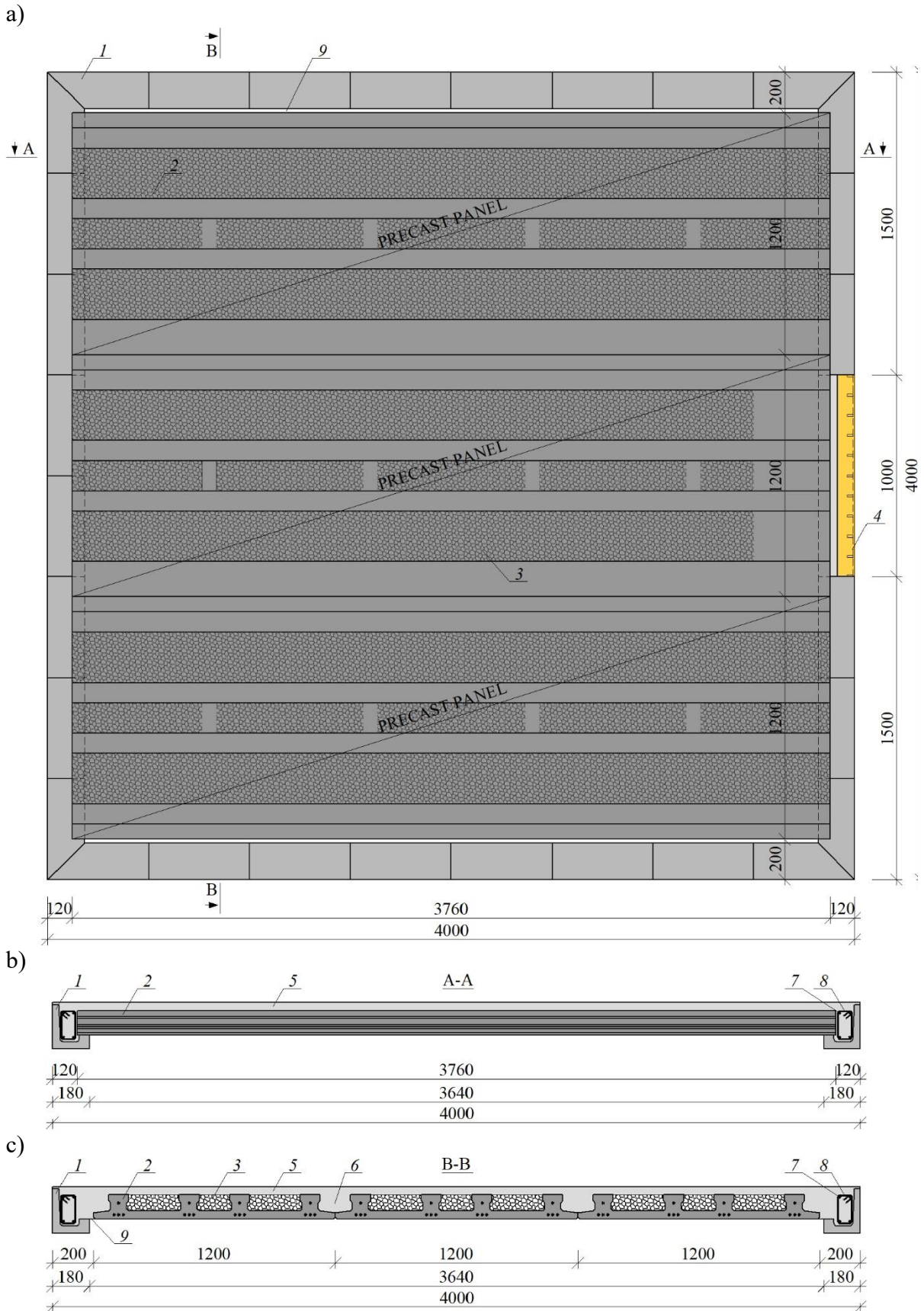
Fig. 4.6 The walls of the MW-AAC-010/1 model after bricklaying: a) view of wall B, b) view of wall A with door opening

4.2.3. Construction of the reinforced concrete slab

The slab was designed as a panel structure, constituting a rigid diaphragm in its plane – Fig. 4.7. Construction of the slab began with laying precast L-shaped elements made of lightweight concrete on masonry walls. In the place of horizontal load, the L-shaped elements were replaced with a ribbed C-section UPE220 with a length of 1.00 m. Then three prestressed concrete precast panels were placed on L-shaped elements. The concrete class of the panels is C40/50, and the prestressing reinforcement is three strands placed at the bottom and one strand at the top. Each strand consists of seven wires and is made of Y2060S7 steel. The diameter of each one is Ø6.85 mm (1xØ2.24 mm + 6 x Ø2.40 mm).

The ends of the strands were anchored in the ring beam. The panels consist of a 4 cm thick slab at the bottom and 12 cm high prestressed ribs. The width of the precast panel is 1.20 m, and the ordered element length is 3.76 m. Polystyrene of 8 cm thickness panels was inserted between the ribs, flush with the upper edge of the ribs. This solution allowed for a significant reduction of the dead weight of the slab. The upper ring beam was made around the panels. The main reinforcement was steel bars B500SP with a diameter of 12 mm and B500B steel stirrups with a diameter of 6 mm spaced every 15 cm. The corners were reinforced in the same way as the bottom beam.

a)

b)

c)

Fig. 4.7 Rigid slab: a) top view, b) cross-section A-A, c) cross-section B-B: 1 – precast L-shaped element, 2 – precast panel, 3 – polystyrene panel, 4 – C-section element, 5 – concrete overlay, 6 – the concrete connection between the panels, 7 – main reinforcement, 8 – stirrups, 9 – assembly tolerance

For the partial negative moment of the restraint, the appropriate upper reinforcement was designed - B500SP steel hooks with a diameter of 10 mm. A 15x15 cm mesh with a diameter of 4 mm was also used against concrete shrinkage. The slab was monolithized with concrete class C30/37. The thickness of the concrete overlay over the precast ribs was 4 cm, so the total thickness of the floor was 16 cm. The construction details are shown in Fig. 4.8.
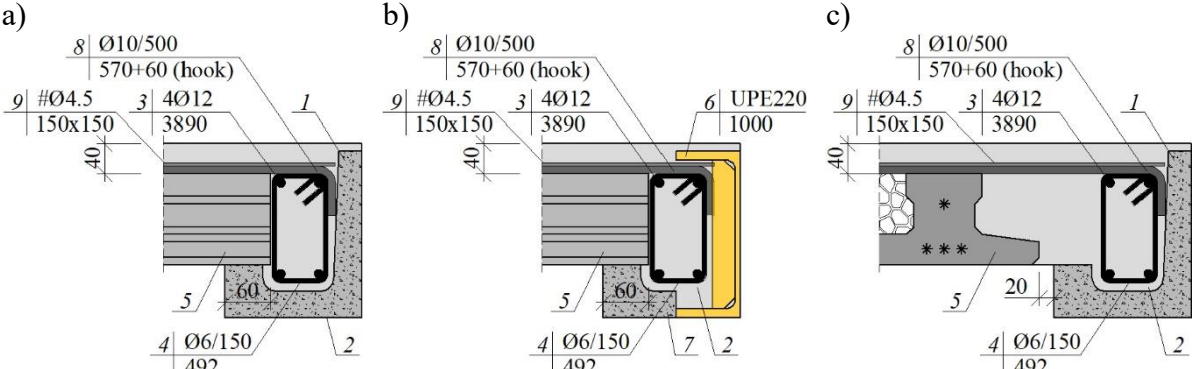

Fig. 4.8 Structural details of the slab support on the top ring beam: a) supporting the panels on the L – shaped element, b) cross-section through UPE220 steel element, c) cross-section through a precast slab panel with visible assembly tolerance: 1 – precast L-shaped element, 2 – concrete, 3 – main reinforcement, 4 – stirrups, 5 – precast panel, 6 – C-section steel element, 7 – cut L-shaped element, 8 – steel hook (upper reinforcement), 9 – steel mesh 15x15 cm with a diameter of 4 mm

A view of structural elements before built-in is in Fig. 4.9. Figure 4.9a shows protruding prestressing strands for anchoring in the upper ring beam. The L-shaped elements are shown in Fig. 4.9b, and the upper reinforcements are in Fig. 4.9c – hooks and Fig. 4.9d – steel mesh.

Figure 4.10 shows the reinforcement of the slab. Polystyrene was removed in place of the planned horizontal load on the model – Fig. 4.10b. These areas were filled with a concrete overlay. As the span of the slab was about 4 m, one line of assembly supports in the middle of the span was sufficient – Fig. 4.11a. Before concreting, the formwork of the slab and the upper beam was prepared – Fig. 4.11 b.
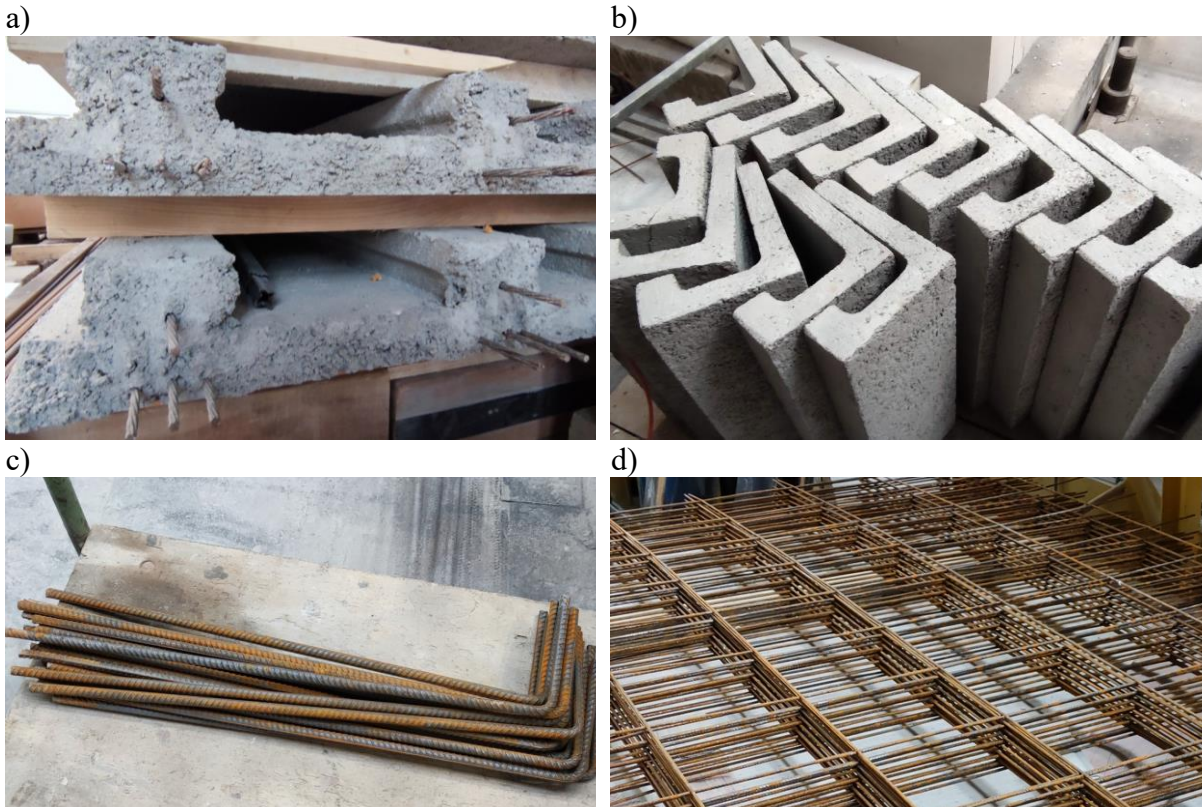
Fig. 4.9 Slab components: a) precast panels, b) L-shaped precast elements, c) Ø10 mm hooks (upper reinforcement), d) Ø4 mm diameter nets with a mesh size of 15 cm (upper reinforcement)
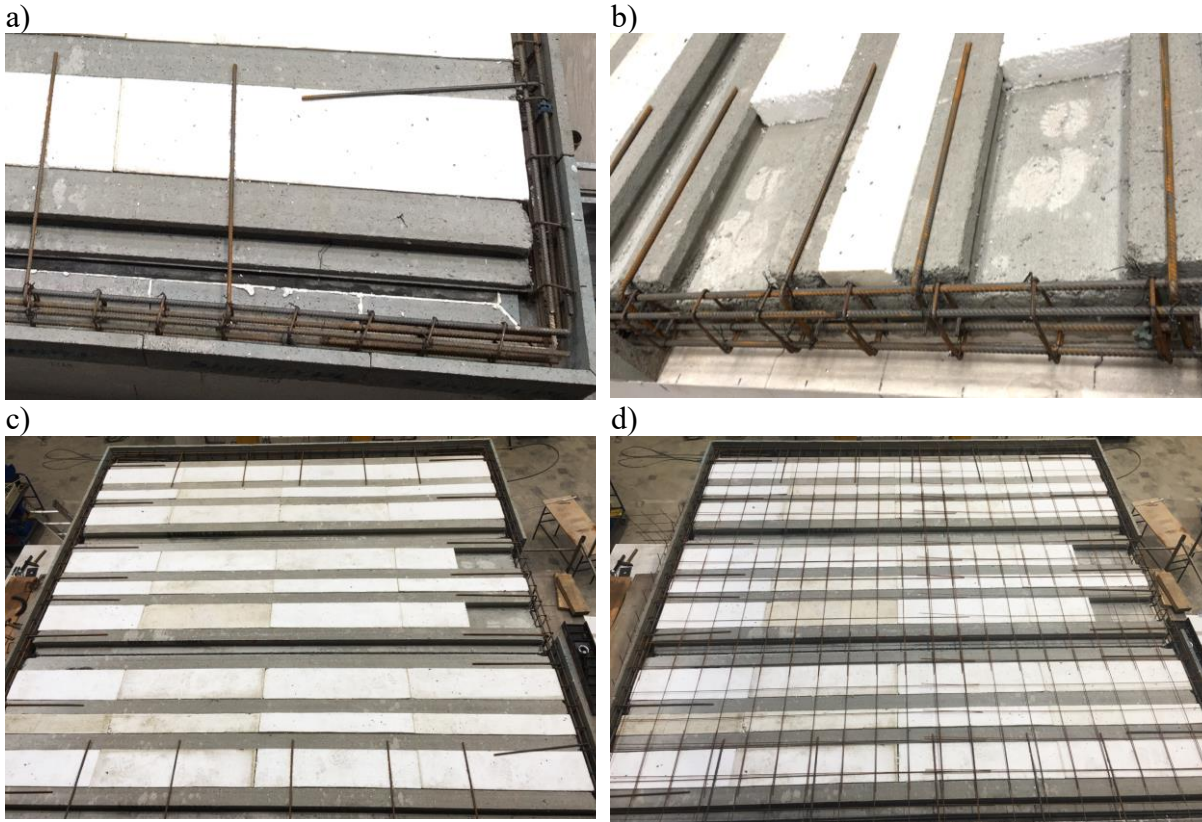

Fig. 4.10 Construction details at the stage of making the slab: a) reinforcing the corner, b) removing polystyrene in the place of the planned horizontal load, c) upper reinforcement with steel hooks, d) upper reinforcement with steel mesh

a)

b)
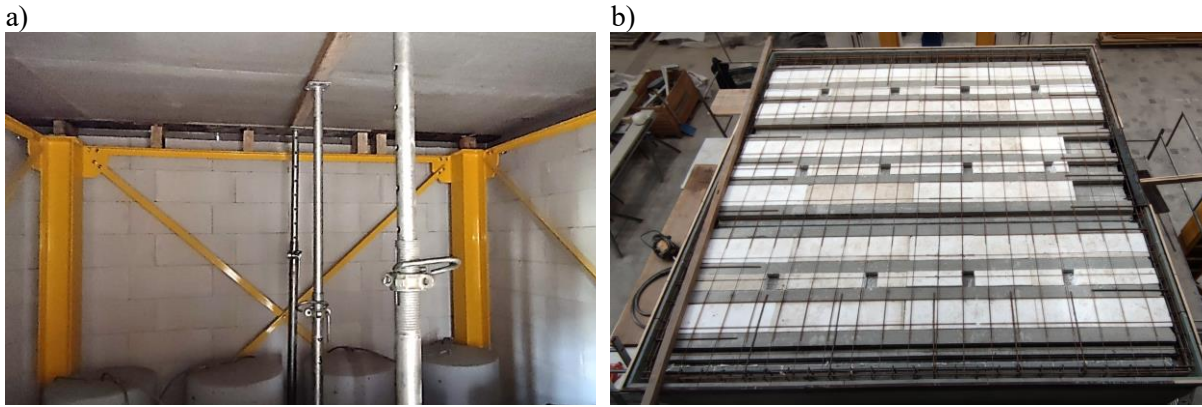
Fig. 4.11 Preparation of the floor for concreting: a) formwork supports, b) top view on the ring formwork

The concrete mix was placed using a concrete bucket – Fig 4.12a. The works were carried out in stages - the laid concrete mix was compacted each time using a vibrator (Fig. 4.12b). Concreted and compacted slab fragments were finished to a levelled surface (Fig. 4.12c). The slab was made and left for 28 days of maturation – Fig. 4.12d. Concrete care was carried out at that time by pouring water on the slab, and this curing work prevented the shrinkage of the concrete.

a)

b)

c)

d)

Fig. 4.12 Concreting the slab and the upper beam: a) concrete bucket, b) compaction of concrete using a vibrator, c) laying the concrete mix, d) finishing of concrete

4.2.4. Construction of steel supporting structure

During the test, there was a risk of the slab falling onto the laboratory floor. A steel supporting structure was designed to be inside the research models and protect the research site. Furthermore, this structure aimed for safe transfer forces in case masonry walls collapse. The structure consists of four columns HEA 200 connected diagonal and horizontal angle bars L50x50x7 – Fig. 4.13a. Structural nodes were made of 10 mm thick steel sheets – Fig. 4.13b. The steel grade of the supporting structure was S355JR. The elements were joined using M16 class 8.8 bolt connectors. Holes in the bottom plates with a diameter of 65 mm were made to fasten the structure to the laboratory floor. The overall dimensions of the interior steel structure in the column axes were 3.00x3.21 m, and the total height is 2.54 m, so there is no collision with the research buildings. Eventually, the structure was painted yellow as part of the test stand.

a) b)
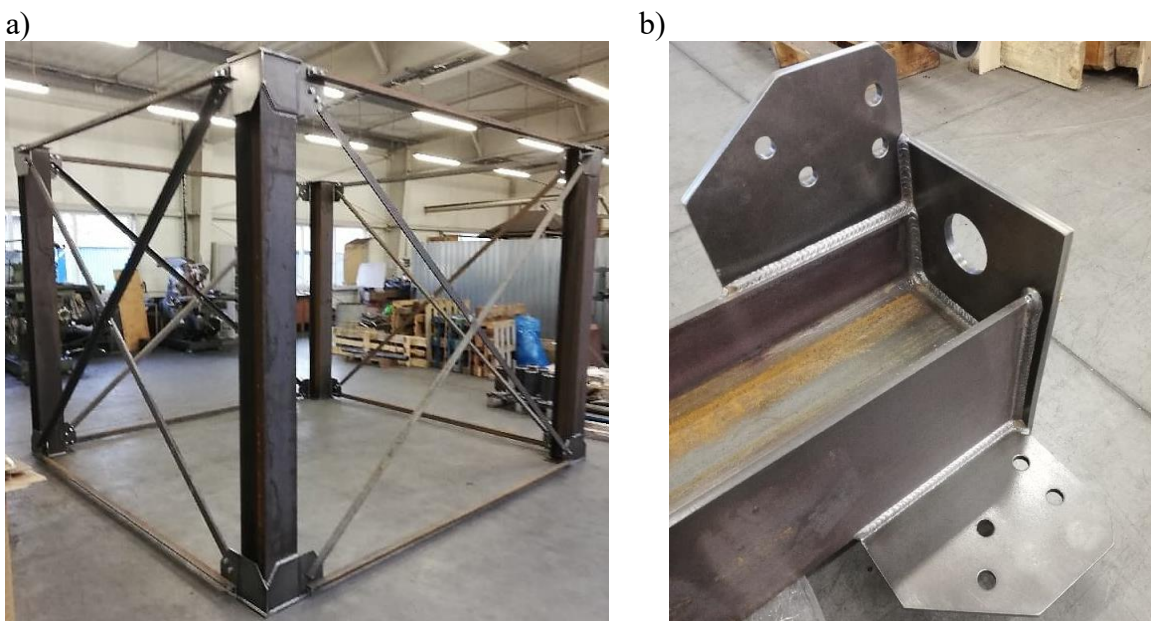
Fig. 4.13 Steel supporting structure after completion: a) illustrative photo, b) construction node detail

4.2.5. Construction phases of subsequent models

In the tests, the slab performs only a rigid diaphragm transferring the horizontal load to the masonry walls of the building, and it was designed to be reused many times. This solution shortened the model building time and depended mainly on building new walls. The surface of the upper ring beam (precast L-shaped elements) required cleaning and surface preparation each time to ensure adhesion.

The construction of research models can be divided into the following stages:
- I – building the first model,
- II – test of the research building,
- III – cutting off the walls from the slab and lifting it with an overhead crane,
- IV – laying the slab on assembly supports based on a steel structure,
- V – demolition of the walls of the tested building,
- VI – building a new model and laying the slab.

Figure 4.14 shows the model of the building after the test with partial and complete demolition of load-bearing walls. During these works, the slab was based on temporary supports located on the steel structure.
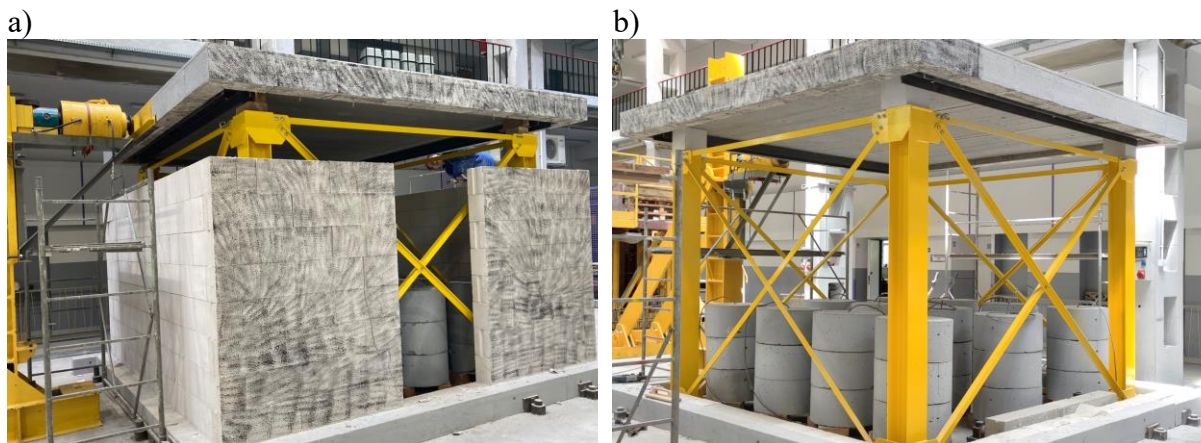
a)

b)

Fig. 4.14 Procedure of reusing the slab: a) demolition of masonry walls after the test, b) slab left on supporting steel structure

4.3. Test stand

The test stand was designed based on the purpose of the work - the determination of the behavior of masonry stiffening walls. The tests were carried out in the Faculty of Civil Engineering laboratory at the Silesian University of Technology. The test stand enables applying vertical and horizontal load on the tested building.

The research model was fixed in a strong floor. The restraint was carried out by additional horizontal beams that surrounded the model's bottom beam and were anchored with a diameter of 65 mm bolts to the laboratory floor. A steel column with a brace was located next to the model. The horizontal force was induced by a hydraulic actuator of 1000 kN range supported by steel construction mounted on the steel column.

The horizontal load was monotonically applied to the building at the geometric center of the slab halfway along the masonry wall. The force gauge of range 250 kN enabled the measurement of horizontal force. The building model in the test stand is shown in Fig. 4.15.
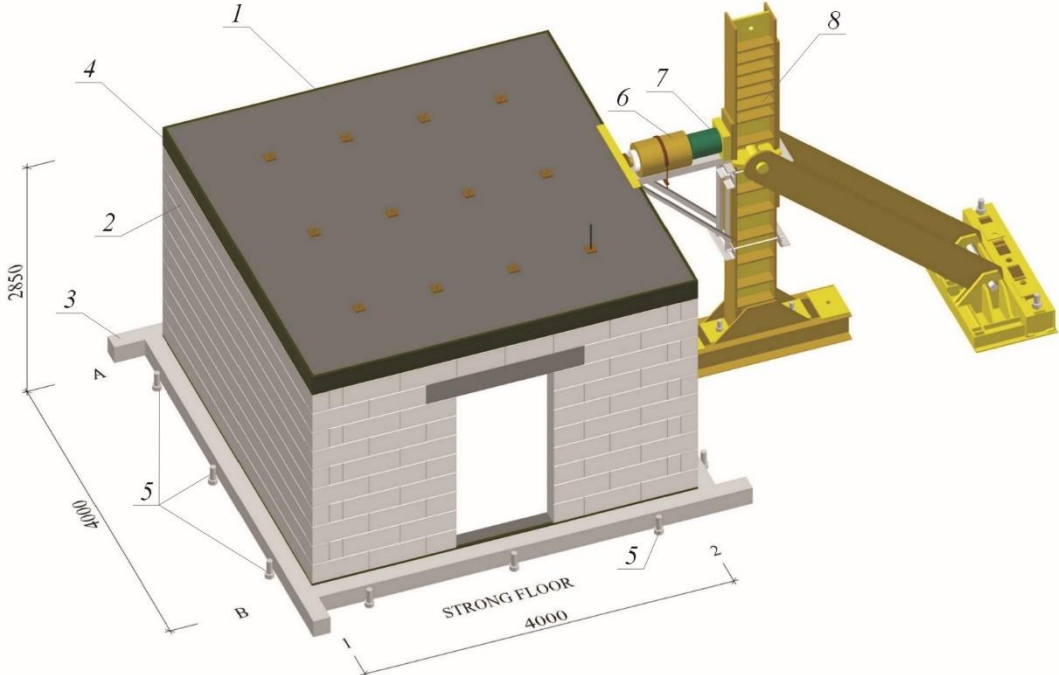

Fig. 4.15 Research model in the test stand: 1 – slab, 2 – masonry wall made of autoclaved aerated concrete units, 3 – bottom beam, 4 – top beam, 5 – fixing the building model in the slab of great forces, 6 – hydraulic actuator, 7 – force gauge, 8 – steel column

A vertical load was also designed corresponding to the actual load on the building's slab with the weight of the finishing layers and the live load. The weights with a diameter of 60 cm and a height of 30 cm were used to induce initial compressive stress in masonry walls. The vertical load was suspended on the twelve steel rods with a diameter Ø16 mm, and on each rod hung three weights – Table 4.2. The values of initial compressive stresses are in Table 4.3.

Table 4.2

Vertical loads applied to building model

Types of load	Value, kN	Description
Dead-load	57.00	Self-weight of slab
Live-load	2.04	One weight
	6.12	Load per one steel rod (three weights)
	73.44	Total load of 12 steel rods
	4.59 kN/m^2	Live-load for floor

Table 4.3

Values of initial compressive stress in masonry walls of a research model

Value	Description
$P_c = 130.44$ kN	total vertical load on the walls
$A_c = 2.82$ m^2	the surface of the horizontal layout of the walls
$\sigma_c = 46.26$ kN/m^2 = 0.05 N/mm^2	compressive prestress of the walls

Holes with a diameter of 25 mm were made in the slab to pass steel rods with weights. The vertical loads have been planned so that the steel rods pass between the prestressed ribs of the panel slabs - so as not to damage the prestressing strands. The layout of vertical loads is shown in Fig. 4.16. The view of vertical and horizontal loads on the test stand is in Fig. 4.17 and Fig. 4.18.
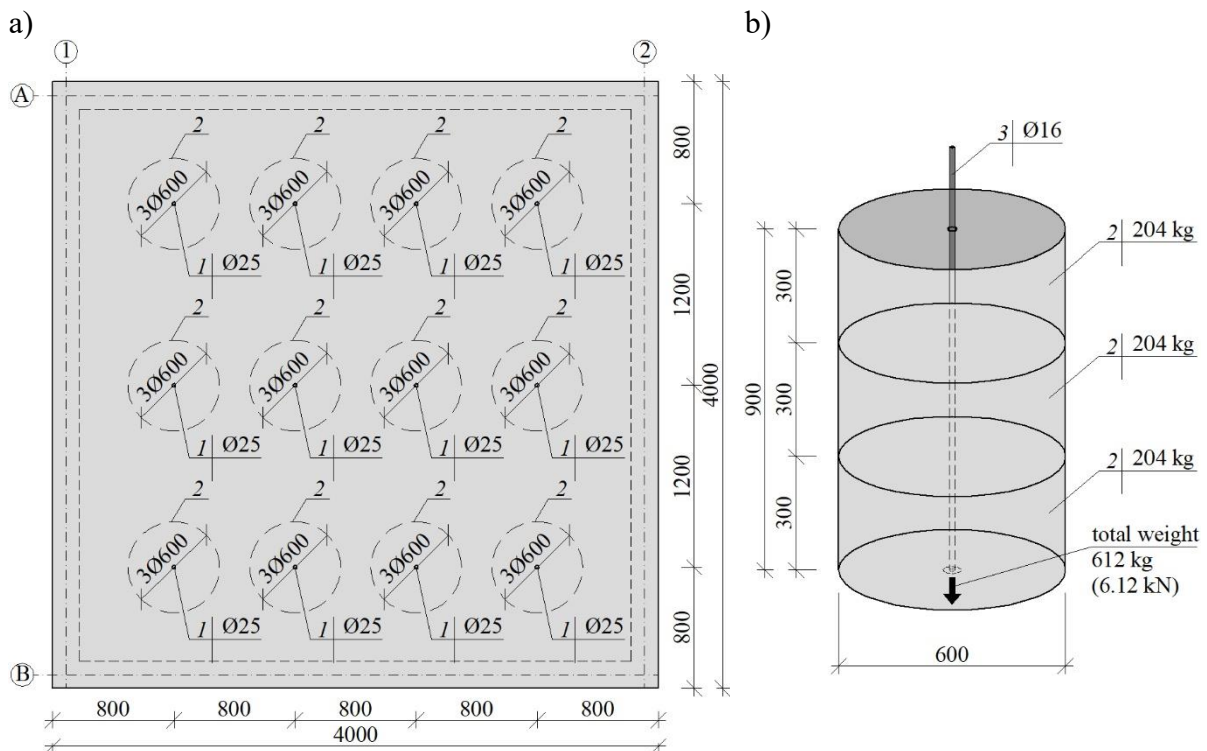

Fig. 4.16 Vertical loads: a) layout of weights, b) geometry of one set of weights: 1 – hole with diameter Ø25 mm in the slab, 2 – weight, 3 – steel rod Ø16 mm
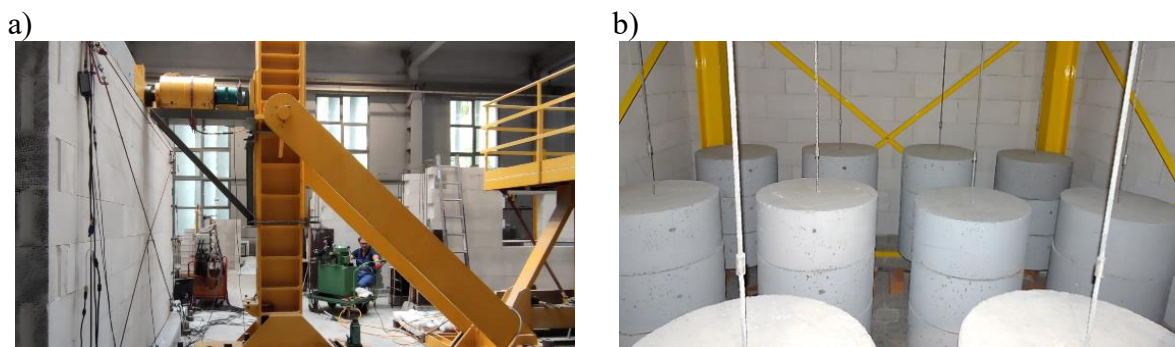

Fig. 4.17 Loads of research model at test stand: a) horizontal load, b) vertical load
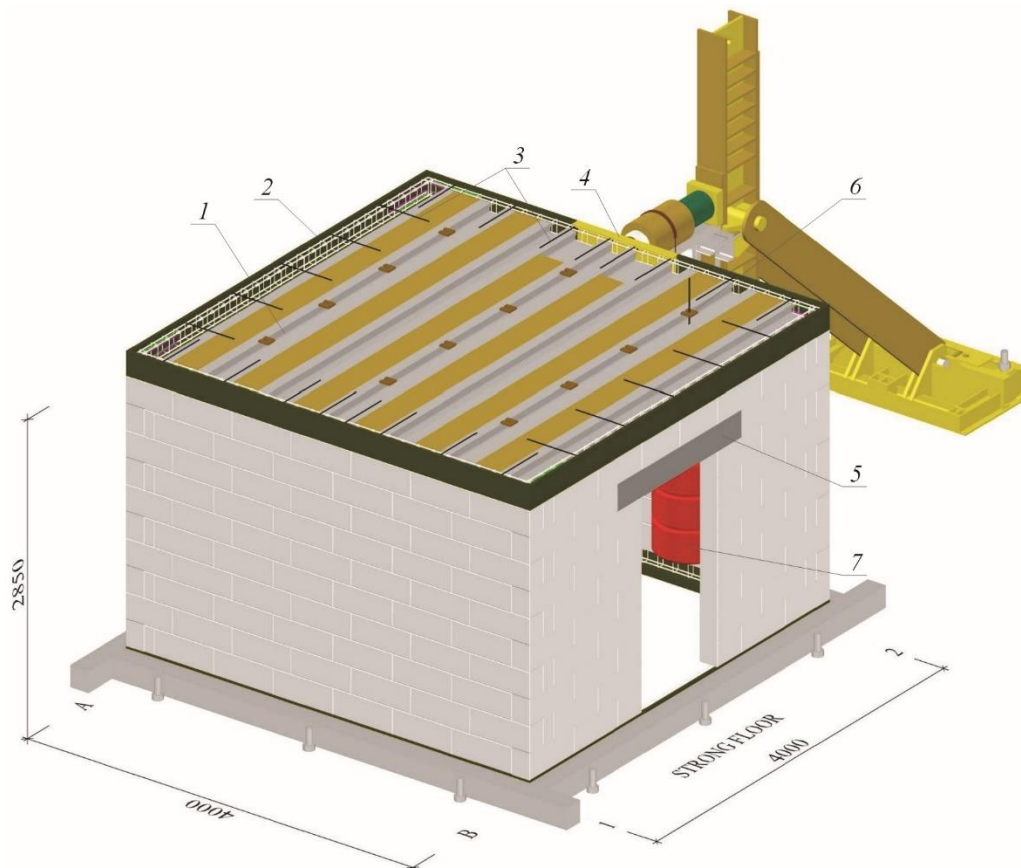
Fig. 4.18 Research model in the test stand: 1 – prestressed precast slab panel, 2 – reinforcement of the top ring beam, 3 – top reinforcement of the slab, 4 – steel C-profile, 5 – precast lintel, 6 – load suspension points, 7 – visible weights.

4.4. Measuring methods

4.4.1. Measurement of displacements with LVDT sensors

Measuring bases (frame) were mounted on the wall of the research model. The size of the frame system was designed to cover the largest possible area of the wall and avoid edge disturbances. The frames were rectangular, 3260 mm long, and 2150 mm high – Fig. 4.19. Linear variable differential transformer (LVDT) sensors [142] measured the change in vertical and horizontal segments and the length of diagonals of the measuring base. LVDT sensors with a measuring range of 20 mm (PJX-20) were mounted on the diagonals and LVDT sensors with a range of 10 mm (PJX-10) on the vertical and horizontal frames. The resolution of the indications was 0.002 mm. The measuring base was attached to the masonry wall point-by-point in the corners with screws. This solution allows the measurement of the shear strain in the elastic range and the deformation angle in the non-linear range.
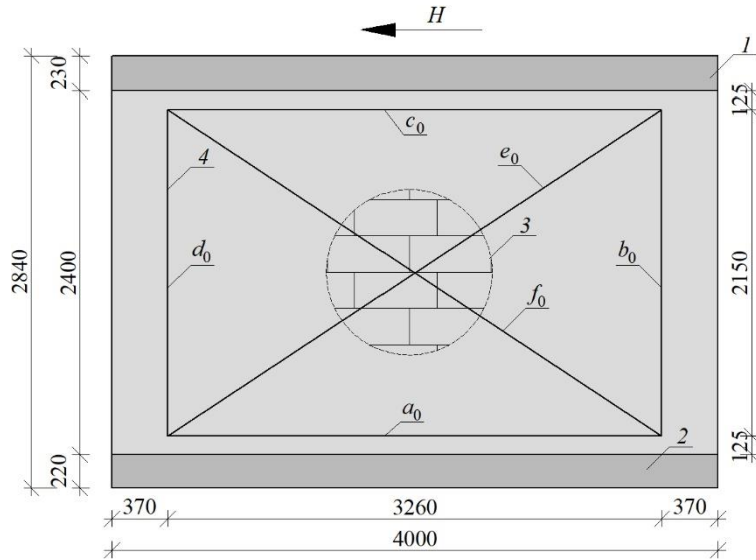
Fig. 4.19 Frame system mounted on each research model to measure shear strain and deformation angle: H – horizontal shear force, 1 – rigid diaphragm; 2 – bottom beam; 3 – masonry wall made of AAC, 4 – measuring base, a_0, c_0 – horizontal part of the frame system, b_0, d_0 – vertical part of the frame system, e_0, f_0 – diagonal part of the frame system

The basic lengths of the measuring frame fragments changed by a value of Δ_a, Δ_b, Δ_c, Δ_d, Δ_e, Δ_f. After deformation, the total length of vertical fragments was calculated from equations (4.1) and (4.2), horizontal fragments from equations (4.3) and (4.4) and diagonals from (4.5) and (4.6).

$$b_d = b_0 + \Delta_b \tag{4.1}$$

$$d_d = d_0 + \Delta_d \tag{4.2}$$

$$a_d = a_0 + \Delta_a \tag{4.3}$$

$$c_d = c_0 + \Delta_c \tag{4.4}$$

$$e_d = e_0 + \Delta_e \tag{4.5}$$

$$f_d = f_0 + \Delta_f \tag{4.6}$$

The value of the change in the length of the measuring frame fragments was used to determine the partial deformation angles Θ_i (where $i = 1, 2, 3, 4$) isolated from the deformed measuring system – Fig. 4.20. The partial values of the global deformation angle were calculated based on the law of cosines relations (4.7) – (4.10).

$$f_d^2 = a_d^2 + d_d^2 - 2a_d d_d \cdot \cos\left(\frac{\pi}{2} + \Theta_1\right) \rightarrow$$

$$\Theta_1 = -\frac{\pi}{2} + acos\left(\frac{a_d^2 + d_d^2 - f_d^2}{2a_d d_d}\right)$$

(4.7)

$$e_d^2 = c_d^2 + d_d^2 - 2c_d d_d \cdot \cos\left(\frac{\pi}{2} - \Theta_2\right) \rightarrow$$

$$\Theta_2 = \frac{\pi}{2} - acos\left(\frac{c_d^2 + d_d^2 - e_d^2}{2c_d d_d}\right)$$

(4.8)

$$e_d^2 = a_d^2 + b_d^2 - 2a_d b_d \cdot \cos\left(\frac{\pi}{2} - \Theta_3\right) \rightarrow$$

$$\Theta_3 = \frac{\pi}{2} - acos\left(\frac{a_d^2 + b_d^2 - e_d^2}{2a_d b_d}\right)$$

(4.9)

$$f_d^2 = b_d^2 + c_d^2 - 2b_d c_d \cdot \cos\left(\frac{\pi}{2} + \Theta_4\right) \rightarrow$$

$$\Theta_4 = -\frac{\pi}{2} + acos\left(\frac{b_d^2 + c_d^2 - f_d^2}{2b_d c_d}\right)$$

(4.10)
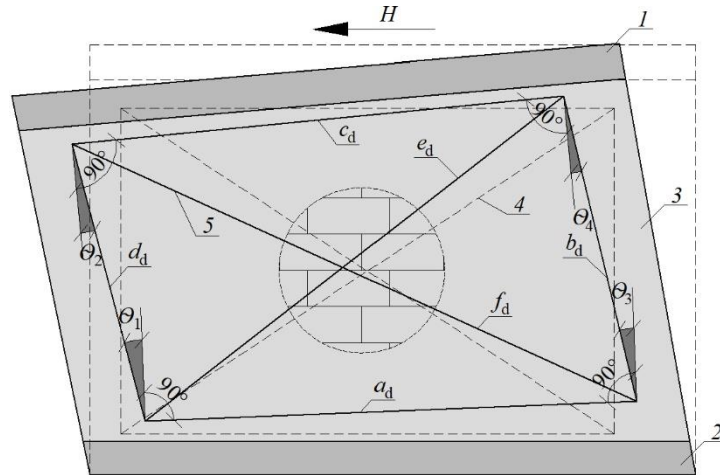
Fig. 4.20 Deformation of measuring base (frame system) due to the action of shear force: H – horizontal shear force, 1 – rigid diaphragm, 2 – bottom beam, 3 – masonry wall made of AAC, 4 – measuring base before the deformation, 5 – measuring base after deformation, a_d, c_d – deformed horizontal part of the frame system, b_d, d_d – deformed vertical part of the frame system, e_d, f_d – deformed diagonal part of the frame system

The global value of the deformation angle Θ at the following load levels was calculated as the arithmetic mean of the partial values of deformation angles Θ_i (where $i = 1, 2, 3, 4$) – relation (4.11).

$$\Theta = \frac{1}{n} \sum_{i=1}^{n=4} |\Theta_i| \qquad (4.11)$$

The total angle of strain deformation determined from relation (4.11) includes both deformations resulting from in-plane bending (Fig. 4.21) and shear (Fig. 4.22). As a result of bending, the lengths of the vertical bases change and horizontal lengths remain unchanged. Thanks to that, trigonometric relationships (4.12) and (4.13) enable calculating the lengths of diagonals caused by bending moments.

$$c_1 = \sqrt{c_0^2 - \left(\frac{d_d - b_d}{2}\right)^2} \qquad (4.12)$$

The diagonal lengths resulting from the flexural deformations can be calculated according to the formula (4.13).

$$e_1 = f_1 = \sqrt{c_1^2 + \left(d_d - \left(\frac{d_d - b_d}{2}\right)\right)^2} \rightarrow$$

$$e_1 = f_1 = \sqrt{c_0^2 + d_d^2 - 2 \cdot d_d \left(\frac{d_d - b_d}{2}\right)} \qquad (4.13)$$

The differences in the length of the diagonals are calculated by subtracting from the total lengths of the deformed diagonals (f_d and e_d) the lengths of diagonals resulting from only in-plane bending (f_1 and e_1) – relationships (4.14) and (4.15).

$$\Delta f_1 = f_d - f_1 \qquad (4.14)$$

$$\Delta e_1 = e_d - e_1 \qquad (4.15)$$

The diagonal lengths resulting from the shear deformations can be calculated according to formulas (4.16) and (4.17).

$$f_s = f_0 + \Delta f_1 \qquad (4.16)$$

$$e_s = e_0 + \Delta e_1 \qquad (4.17)$$
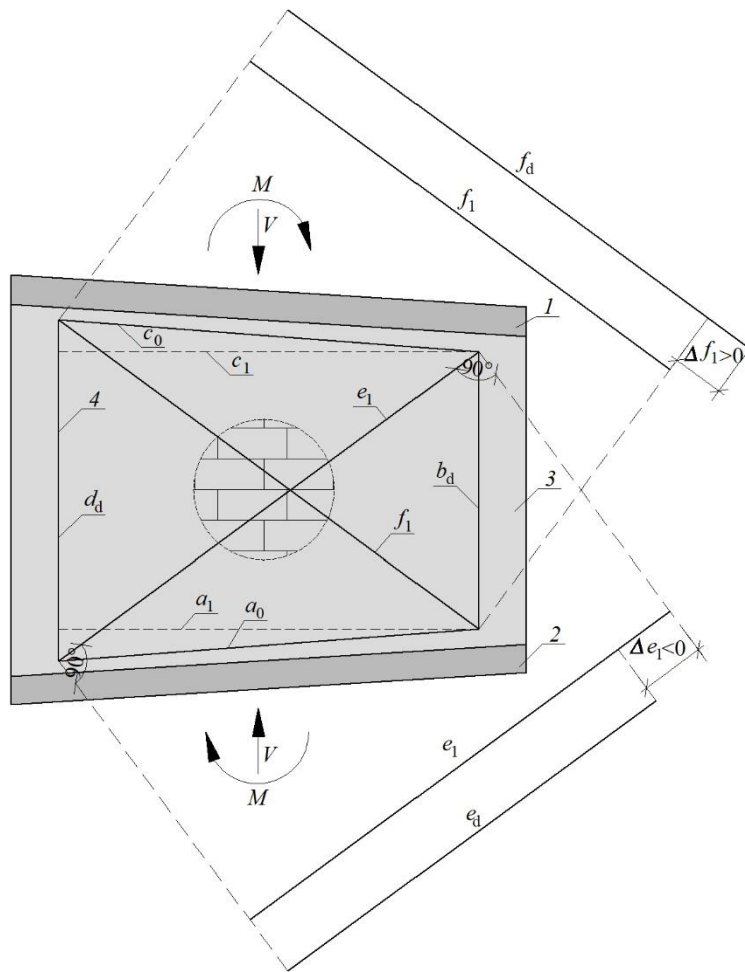
Fig. 4.21 Deformation of measuring base resulting from flexural deformation: V – vertical force, M – in-plane bending moment, 1 – rigid diaphragm, 2 – bottom beam, 3 – masonry wall made of AAC, 4 – measuring base before the deformation, a_0, c_0 – undeformed horizontal part of the frame system, e_1, f_1 – deformed diagonal part of the frame system results from flexural deformation

Fig. 4.22 Deformation of measuring base resulting from shear deformation: H – horizontal shear force, 1 – rigid diaphragm, 2 – bottom beam, 3 – masonry wall made of AAC, 4 – measuring base before deformation, 5 – measuring base after deformation, a_d, c_d – deformed horizontal part of the frame system, b_0, d_0 – undeformed vertical part of the frame system, e_s, f_s – deformed diagonal part of the frame system

result from shear deformation, Θ_{1s}, Θ_{2s}, Θ_{3s}, Θ_{4s} – values of partial strain deformation angles

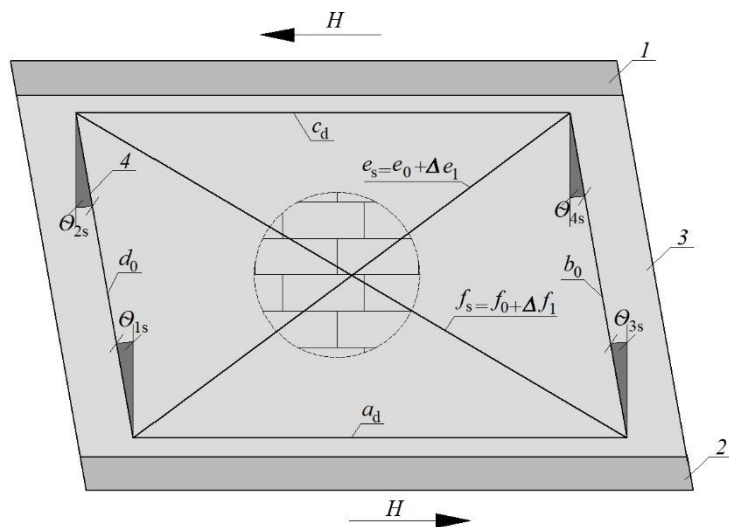Values of the partial angle of strain deformation can find it from the law of cosines – formulas (4.18) – (4.21):

- the triangle formed by lines d_0, f_s and a_d:

$$f_s^2 = d_0^2 + a_d^2 - 2d_0 a_d \cdot \cos\left(\frac{\pi}{2} + \Theta_{1s}\right) \rightarrow$$

$$\Theta_{1s} = -\frac{\pi}{2} + acos\left(\frac{d_0^2 + a_d^2 - f_s^2}{2d_0 a_d}\right) \tag{4.18}$$

- the triangle formed by lines c_d, e_s and d_0:

$$e_s^2 = c_d^2 + d_0^2 - 2c_d d_0 \cdot \cos\left(\frac{\pi}{2} - \Theta_{2s}\right) \rightarrow$$

$$\Theta_{2s} = \frac{\pi}{2} - acos\left(\frac{c_d^2 + d_0^2 - e_s^2}{2c_d d_0}\right) \tag{4.19}$$

- the triangle formed by lines a_d, e_s and b_0:

$$e_s^2 = a_d^2 + b_0^2 - 2a_d b_0 \cdot \cos\left(\frac{\pi}{2} - \Theta_{3s}\right) \rightarrow$$

$$\Theta_{3s} = \frac{\pi}{2} - acos\left(\frac{a_d^2 + b_0^2 - e_s^2}{2a_d b_0}\right) \tag{4.20}$$

- the triangle formed by lines b_0, f_s and c_d:

$$f_s^2 = b_0^2 + c_d^2 - 2b_0 c_d \cdot \cos\left(\frac{\pi}{2} + \Theta_{4s}\right) \rightarrow$$

$$\Theta_{4s} = -\frac{\pi}{2} + acos\left(\frac{b_0^2 + c_d^2 - f_s^2}{2b_0 c_d}\right) \tag{4.21}$$

The mean value of the partial strain deformation angle caused by shear is determined by the formula (4.22).

$$\Theta_s = \frac{1}{n}\sum_{i=1}^{n=4}|\Theta_{is}| \tag{4.22}$$

The geometry of the walls of the tested buildings makes shear deformations

negligible, and the total shear deformation angle coincides with the partial shear deformation angle. The total shear angle is considered in further analysis of the behavior of the building. This approach is also helpful in determining the stiffness of walls calculated from the total angle of shear deformation.

Measuring bases were fixed on the outside of the wall. The frame was mounted inside the building if the wall was painted a specific pattern used in the digital image correlation system. Measurement frames mounted on solid walls and walls with openings are shown in Fig. 4.23.

a)

b)
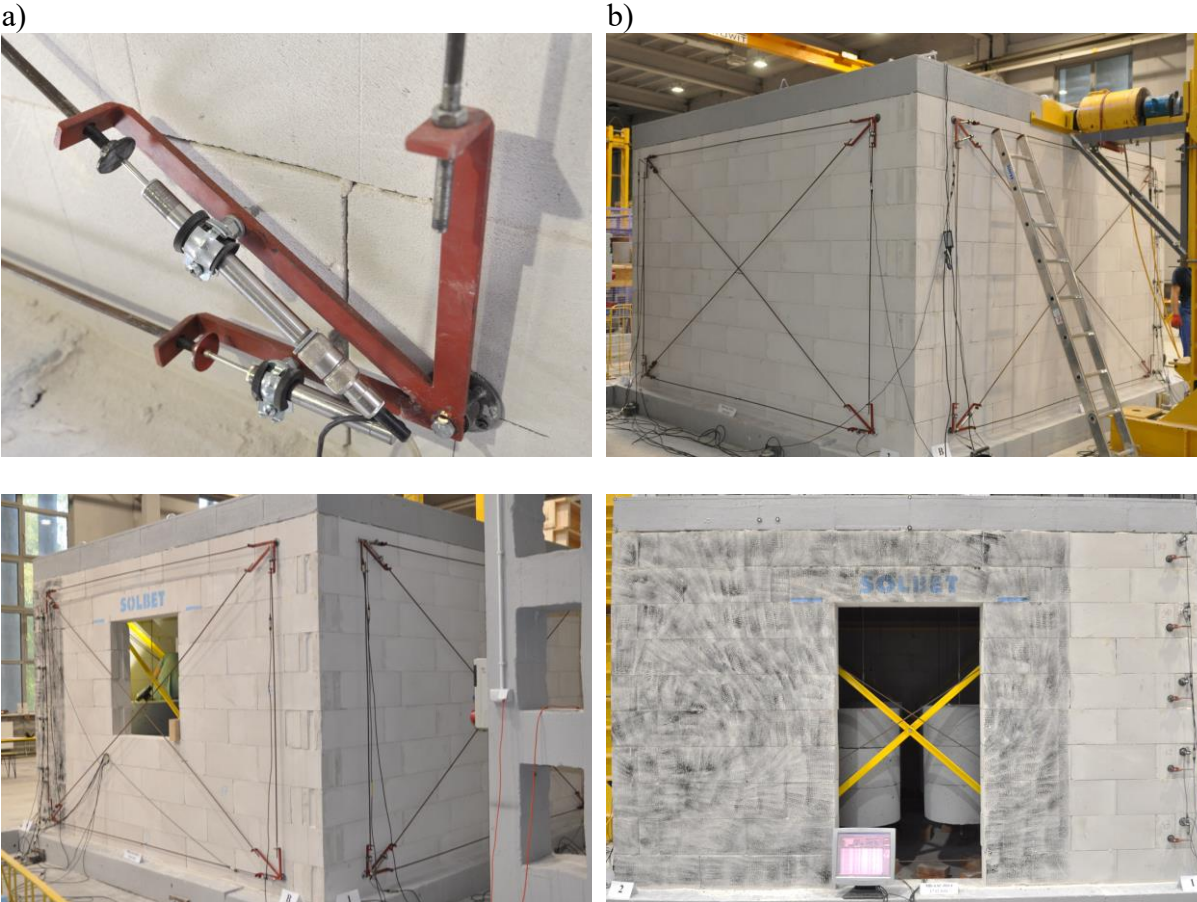
Fig. 4.23 Measuring bases: a) corner detail with LVDT – PJX-20, b) measuring frame bases, c) measuring frame on the wall with the window opening, d) measuring frame inside the building (wall analyzed by the GOM system)

4.4.2. Measurement of displacements, strains, deformations and crack propagation using a digital image correlation system (DIC)

Digital image correlation (DIC) belongs to non-contact measurement techniques. The analysis is based on solid mechanics and includes changes in geometry and localization of points before and after material deformation [80]. The system assigns the

coordinates to small areas and records changes in the shape and location of that zone.

The DIC system [108] consists of the proper illumination of an object. The light intensity reflected from the (undeformed) object surface $f(x, y)$ before the object is loaded and from any surface $f_1(x_1, y_1)$ in the next stage after applying the load that results in deformation is analysed - Fig. 4.24. This procedure is used for measuring deformation within small areas and then presenting the deformation distribution on a greater, actual surface of the object.
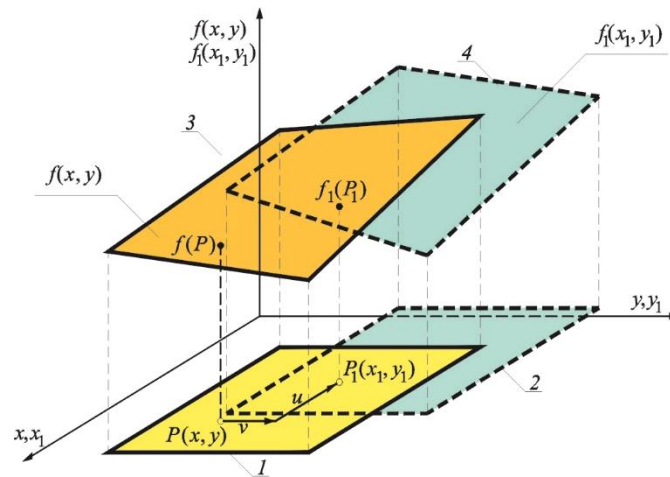

Fig. 4.24 Pattern of analysed images of surfaces against the scanning area [42]: 1 – scanning area, 2 – the area of scanning after deformation, 3 – the image of the undeformed surface, 4 – the image of the deformed surface

The principle of the DIC technique was developed from the fundamentals of the mechanics of continuous media [74]. The analysis includes changes in dimensions and location of short segments determined by positioning two points before (P, Q) and after (P_1, Q_1) deformations – Fig. 4.25, expressed by the following equations in a 3D rectangular Cartesian system of coordinates (4.23) – (4.24):

$$P_1 = (x_1, y_1, z_1) = [x + u(P), x + v(P), z + w(P)] \qquad (4.23)$$

$$Q_1 = (x_1 + dx_1, y_1 + dy_1, z_1 + dz_1) =$$
$$\begin{bmatrix} x + u(P) + u(Q) - u(P) + dx, y + v(P) + v(Q) - v(P) + dy \\ z + w(P) + w(Q) - w(P) + dz \end{bmatrix} \qquad (4.24)$$

where: u, v, w are displacement components towards x, y or z axis, respectively.

The length of segments PQ and P_1Q_1 are expressed by the relationships (4.25) and (4.26):

$$|PQ|^2 = (ds)^2 = dx^2 + dy^2 + dz^2 \qquad (4.25)$$

$$|P_1Q_1|^2 = (ds_1)^2 = dx_1^2 + dy_1^2 + dz_1^2 \qquad (4.26)$$

The equations (4.23) – (4.26) and simple transformations result in the following relationships defining components of deformation in the two-dimensional system of coordinates (which define components of the strain tensor in a plane stress state) – relationships (4.27) – (4.29):

$$\varepsilon_{xx} \cong \frac{\partial u}{\partial x} + \frac{1}{2}\left[\left(\frac{\partial u}{\partial x}\right)^2 + \left(\frac{\partial v}{\partial x}\right)^2\right] \qquad (4.27)$$

$$\varepsilon_{yy} \cong \frac{\partial v}{\partial y} + \frac{1}{2}\left[\left(\frac{\partial u}{\partial y}\right)^2 + \left(\frac{\partial v}{\partial y}\right)^2\right] \qquad (4.28)$$

$$\varepsilon_{xy} \cong \frac{1}{2}\left(\frac{\partial u}{\partial y} + \frac{\partial v}{\partial x}\right) + \frac{1}{2}\left[\frac{\partial u}{\partial x}\frac{\partial u}{\partial y} + \frac{\partial v}{\partial x}\frac{\partial v}{\partial y}\right] \qquad (4.29)$$

Components in a spatial state can be determined similarly. The undeformed surface is analysed by assigning coordinates to small areas (pixels) – Fig. 4.26. Separating the undeformed reference zone is the next step. Changes in the shape and location of that zone are analysed during the test and recorded in the system of 0_{xy} and 0_{x1y1} coordinates.

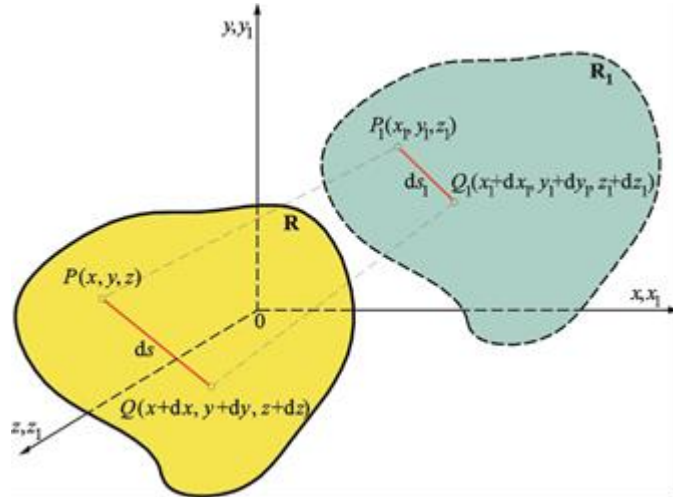Fig. 4.25 Characteristic area before (R) and after (R$_1$) deformation [42]

DIC has been successfully used in construction areas such as concrete structures [95,112,164,60], corrosion process [97], structural health monitoring [10,45,119] and also the masonry analyses of 1/6th scale masonry wall [70], soil-masonry structure interaction [120], infill masonry [134,23], and unreinforced masonry (URM) [73].
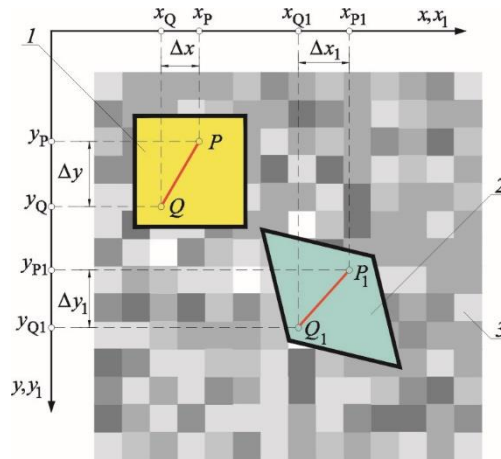
Fig. 4.26 Graphical interpretation of deformations for selected scanning area in a 2D system of coordinates [80, 42]: 1 – scanning area, 2 – scanning area after deformation, 3 – pixel sub-images of the structure

The measuring process is based on the correlation principle and the technique of searching points of the same coordinates. The area (contour) should be defined to perform the analysis and record its shape – Fig. 4.27a. In order to do that, square or rectangular areas (relatively small, e.g. 15 x 15 pixels), known as *facets* - are assigned to characteristic points of the analysed surface – Fig. 4.27a and 4.27b.
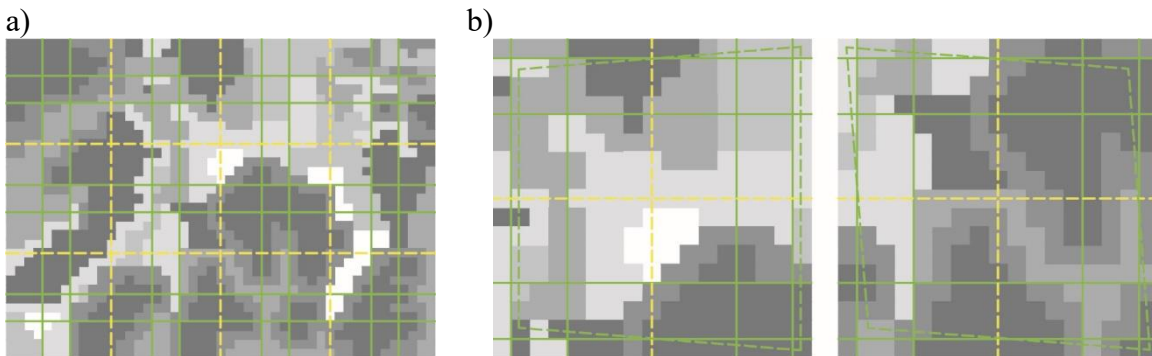
Fig. 4.27 Principle of image correlation [85]: a) segment of measuring area with arranged facets marked with green lines, b) enlarged segment of un analysed area with facet contour

A segment of gradient measuring area is characterized by digital measuring areas of rectangular shape and dimensions of 15 x 15 pixels subjected to changes in the DIC software and by typical areas of 2 x 2 pixels - Fig. 4.27a. Common areas were used to reduce an error in measuring strains as each analysed area (facet) contained elements from the adjacent area and the same boundary conditions. Each rectangular area has its unique pattern. The identification of common areas is necessary for the DIC technique. The size of facets also impacts the accuracy and rate of calculations. An increase in their size deteriorates the accuracy of measurements. However, the test result is obtained faster. Rectangular areas are directly used in analysing displacement/strain components.

The next stage includes loading, where displacement components are determined in 2D or 3D areas. Then, values of displacement components are used to calculate components of strain/stress as the field image. The DIC system determines the coordinates of the 2D system based on the reorientation of the rectangle/rhombus/facet midpoint – Fig. 4.27b. Coordinates determined with both cameras and an angle between their axes can be used to describe the coordinates of the 3D system. In subsequent stages of the analysis, the specific layer with the pattern is identified to use its position for determining the displacement. Number "0" is assigned to the initial stage (Stage 0), and other stages have numbers: "1", "2", "3", etc. Difficulties with the DIC systems are mainly caused by the preparation of the surface and the technique of camera positioning using the calibration plate. The DIC system for testing big deformations can be successfully applied to determining Young's modulus and Poisson's ratio, identifying the process of material softening or hardening within a wide range of plastic strain. It can also be employed for high ductility (exceeding 100%) materials and determining parameters of crack mechanics.

This system is based on recording and analysing changes in the positions of points on the specimen surface. According to papers [85,108,96] two models are analysed. The first type uses the Normalized Cross-Correlation ρ (NCC), and the second one the Least Squares Method (LSM). The first method calculates normalized cross-correlation (4.30) between each point's initial and current location. The closest location is chosen at the level of pixel pattern on the surface by choosing the minimum value of the common normalized cross-correlation. Estimating the function of normalized cross-correlations is conducted within the searched area, and its maximum indicates the best match. The correlation ρ is calculated as a discrete function of changes in displacements (Δx, Δy) and average values from grey areas and compared windows of the equation (4.30):

$$\rho = \frac{\sum_x \sum_y \left(f(x, y - \bar{f})(g(x + \Delta x, y + \Delta y) - \bar{g})\right)}{\sqrt{\sum_x \sum_y \left(f(x, y - \bar{f})\right)^2 \sum_x \sum_y \left((g(x + \Delta x, y + \Delta y) - \bar{g})^2\right)}} \qquad (4.30)$$

The normalized correlation coefficient takes values from the range of [-1, 1]. When the reference image texture coincides with the deformed area image's brightness, this coefficient equals 1. When they do not coincide, the coefficient is 0. The value -1 means reverse correlation.

The NCC algorithm is fast but only includes displacements of points on the vertical and horizontal axis, not point rotation. Such an approach is not appropriate for testing

mineral-asphalt mixtures or other road materials with such occurrences [140,165]. The LSM method employs more complex models considering the points' displacements and rotation. The best match is defined by minimising a difference in grey intensity between two consecutive analysis windows using the least squares method [140]. The correction of parameters taking into account displacements and rotations is determined from the equation (4.31), where (a_1, a_2, b_1, b_2) are variable parameters of the model shape, and (a_3, b_3) are displacement parameters [140]:

$$f(x_1, y_1) + e(x_1, y_1) = r_0 + r_1 g\big(x_2(u,v), y_2(u,v)\big)$$
$$= \bar{g}(r_0, r_1, a_1, a_2, a_3, b_1, b_2, b_3) \tag{4.31}$$

The function $\bar{g}(r_0, r_1, a_1, a_2, a_3, b_1, b_2, b_3)$ is linearized and solved following the least squares estimator by the Gauss–Markov theorem.

These tests used the Aramis 6M system – Fig. 4.28a consisting of two digital cameras (each with a resolution 6MPx), a high-performance computer as the control unit, a GOM Testing Controller, certified calibration elements and GOM Correlate software. The measuring area for Aramis 6M system ranges from 150x170 mm to 2150x2485 mm. Objectives were used in the studies with a focal length of 12.5 mm for area mapping with a strain measurement resolution of ±0.01%. The stiffening walls (A and B) located in the direction of the horizontal load were analysed. The walls were covered with irregular contrasting patterns obtained by applying black paint with a brush with stiff hair – Fig. 4.28b. Benchmarks were also stuck on the wall surface. The slab was painted grey, the invisible interior edges of the walls were marked with a blue dashed line, and the axes of the building were marked with red lines – Fig. 4.29.

a)   b)
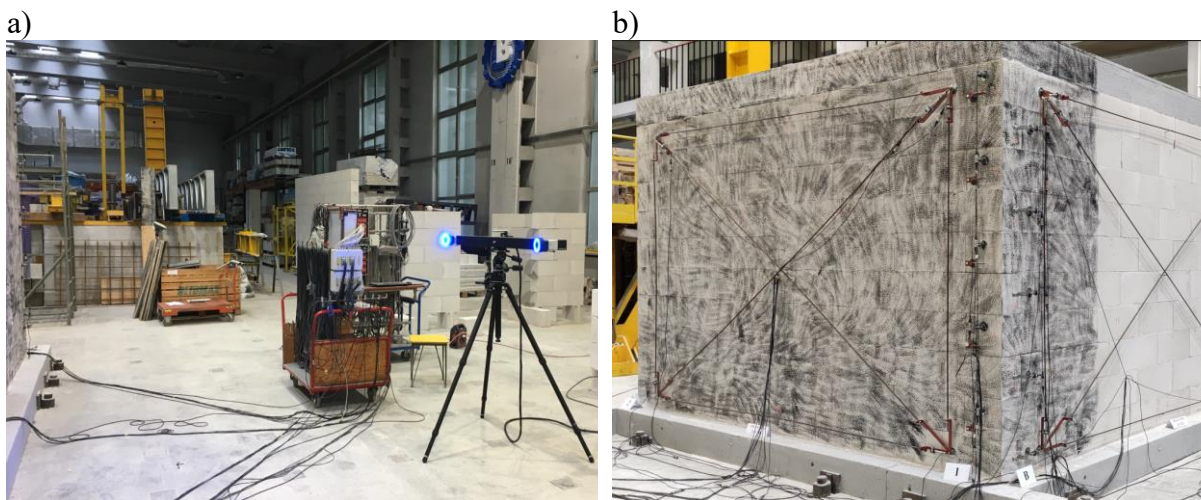
Fig. 4.28 Digital image correlation system: a) location of measurement cameras – Aramis 6M, b) wall painted with a pattern

On the slab were placed benchmarks for digital image correlation. The designations of the points are shown in Fig. 4.30. A Canon EOS 500D camera with a Canon EF-S 10-18 mm, f/4.5-5.6 lens was used to analyze the displacements of the slab. The equipment was suspended on a metal arm above the tested building model – Fig. 4.31.

a)

b)

Fig. 4.29 Painting the slab: a) measurement points, b) measurement points in the corner
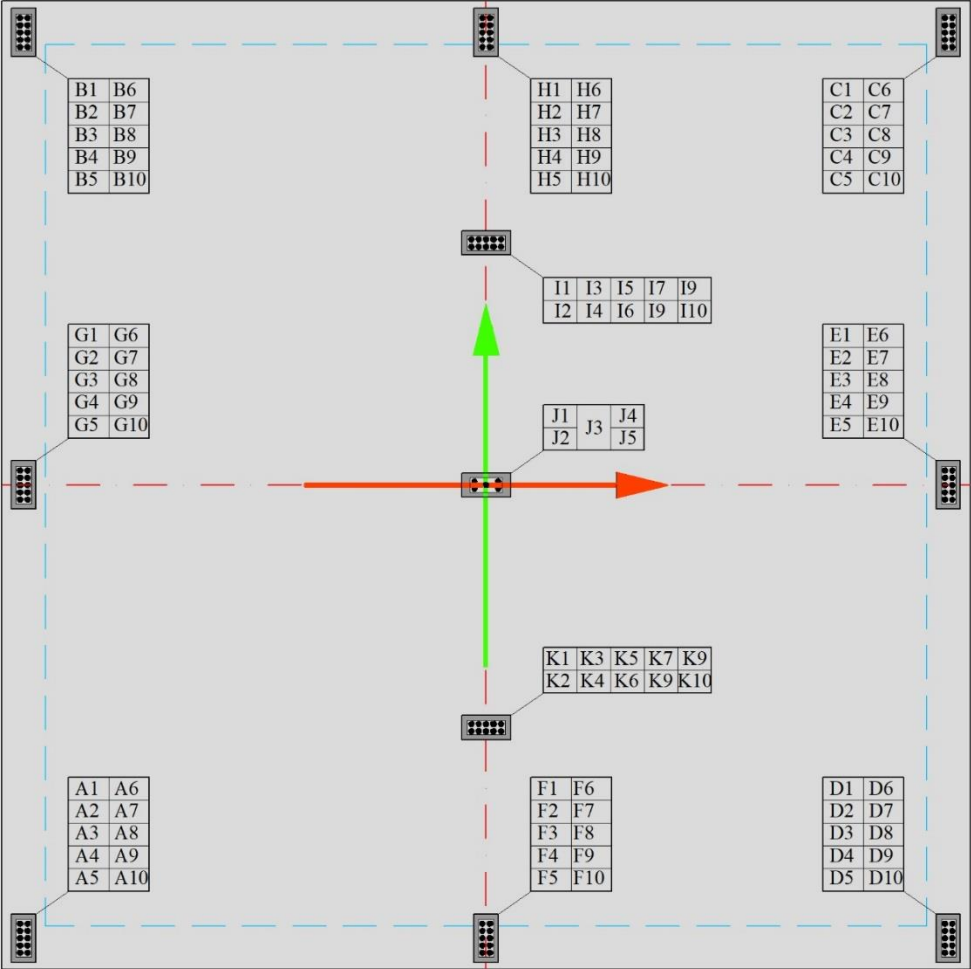
Fig. 4.30 Measurement point markings for the DIC system

Fig. 4.31 Research model on the test stand

4.4.3. Measurement of horizontal force

A hydraulic cylinder induced the horizontal load. Force value was measured using a force gauge of range 250 kN ± 0.1 kN and a pressure sensor P10 of the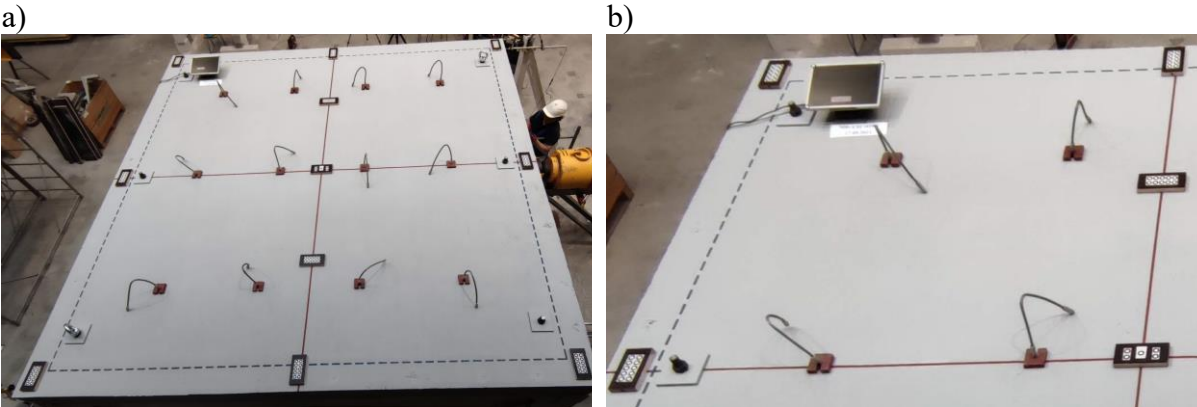 range 1000 bar ± 0.1 bar. A constant increment in displacements of 1 cm/mm was set. The measuring apparatus is shown in Fig. 4.32.
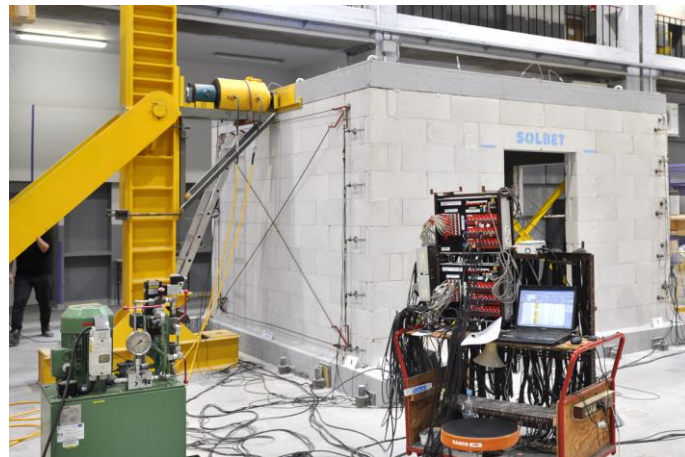
Fig. 4.32 Measuring apparatus

4.4.4. Additional methods

In addition to using LVDT and Aramis system, macroscopic damage assessment was performed. Observed damage and cracks are marked on the walls of buildings in blue (Fig. 4.33a). A GoPro Hero 8 camera was used to observe the building during the test (Fig. 4.33b). A Canon EOS 40D camera was also used for the DIC system. Each measurement method allowed for wall and slab displacement registration during the test.

a)

b)
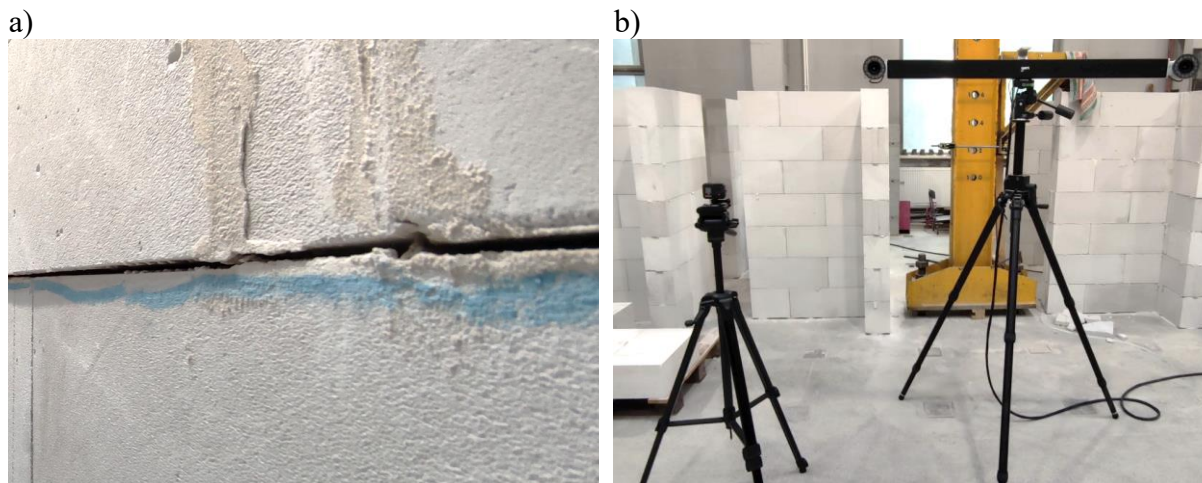
Fig. 4.33 Additional methods: a) blue markings of cracks, b) GoPro camera next to the Aramis system

5. BEHAVIOR OF MASONRY STIFFENING WALLS

5.1. Behavior phases

The behavior of the stiffening walls is presented in diagrams of the normalized horizontal force (H_i/H_u) to the shear deformation angle Θ_i. Moreover, the normalized lateral load – horizontal displacement charts were done. The horizontal displacements based on shear deformation angles were calculated following formula (5.1). The test results were grouped with a series of models with the same geometry – types I, II, III, and IV.

$$u_i = \Theta_i \cdot h \qquad\qquad (5.1)$$

in which:

u_i – horizontal displacement in the direction x along to load (u_x) or direction y perpendicular to load (u_y),

Θ_i – shear strain angle in linear phase and shear formation angle in non-linear phase,

h – the height of the model and equal $h = 2.63$ m.

5.1.1. Results for models with door opening in stiffening wall A – type I models

Figures 5.1 and 5.2 show the relationship between the normalized horizontal force and shear deformation angle for MB-AAC-010/1 and MB-AAC-010/2 models. Figures 5.3 and 5.4 present the normalized lateral load-horizontal displacement chart for particular building models. The results for model MB-AAC-010/1 are incomplete due to problems with diagonal LVDT sensors during the test. The charts were prepared for both stiffening and perpendicular walls.
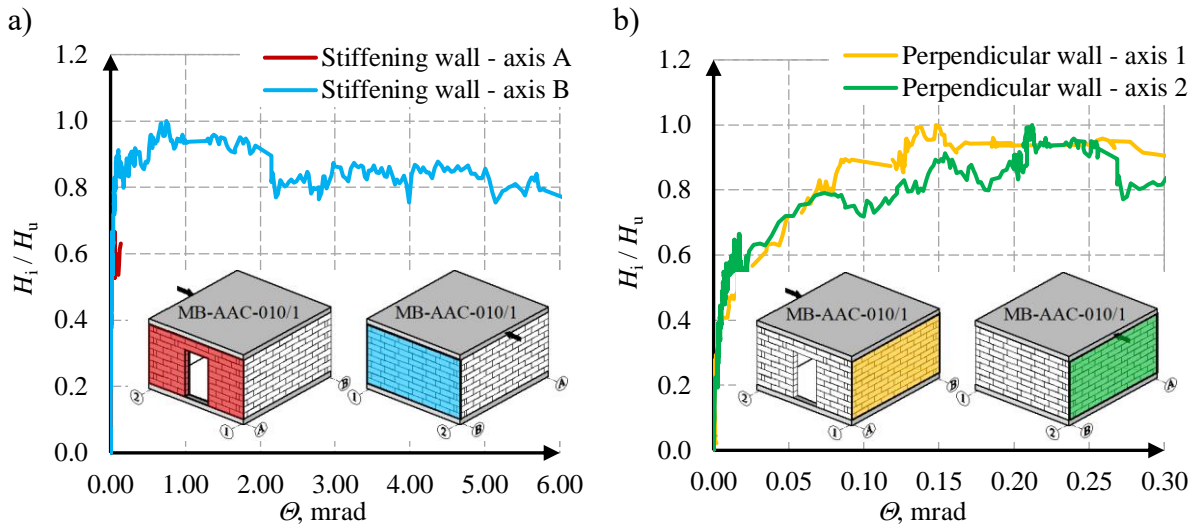
Fig. 5.1 Relationship between the horizontal force and shear deformation angle for the MB-AAC-010/1 model: a) results for A and B walls, b) for 1 and 2 walls
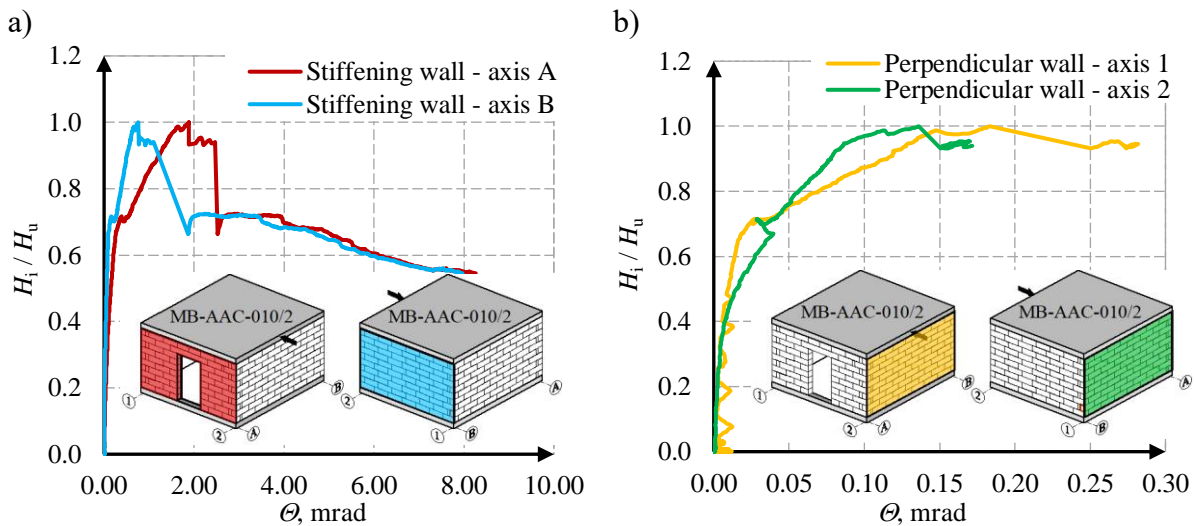
Fig. 5.2 Relationship between the horizontal load and shear deformation angle for the MB-AAC-010/2 model: a) results for A and B walls, b) for 1 and 2 walls

Based on the diagram – Fig. 5.2a, it can be concluded that the behavior of the stiffening walls was similar. However, walls are characterised by different stiffness due to the door opening in wall A. Shear deformation angles in stiffening walls are greater than in perpendicular walls (by order of magnitude). The maximum horizontal displacement in the direction of the load was over 21 mm, and in the transverse direction, it was about 0.7 mm (MB-AAC-010/2 model). In the MB-AAC-010/1 model, these displacements were successively over 16 mm (wall B) and about 1.1 mm (wall 2). Displacements in the transverse direction indicate the rotation of the building caused by the different stiffness of wall A about the other walls.
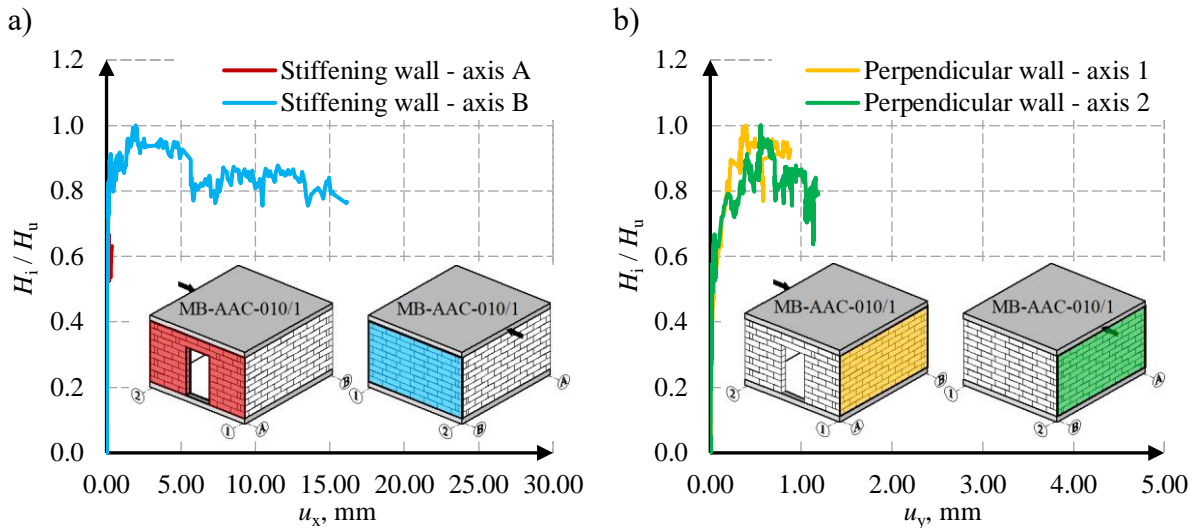
Fig. 5.3 The normalized lateral load – horizontal displacement chart for the MB-AAC-010/1 model: a) results for A and B walls, b) for 1 and 2 walls
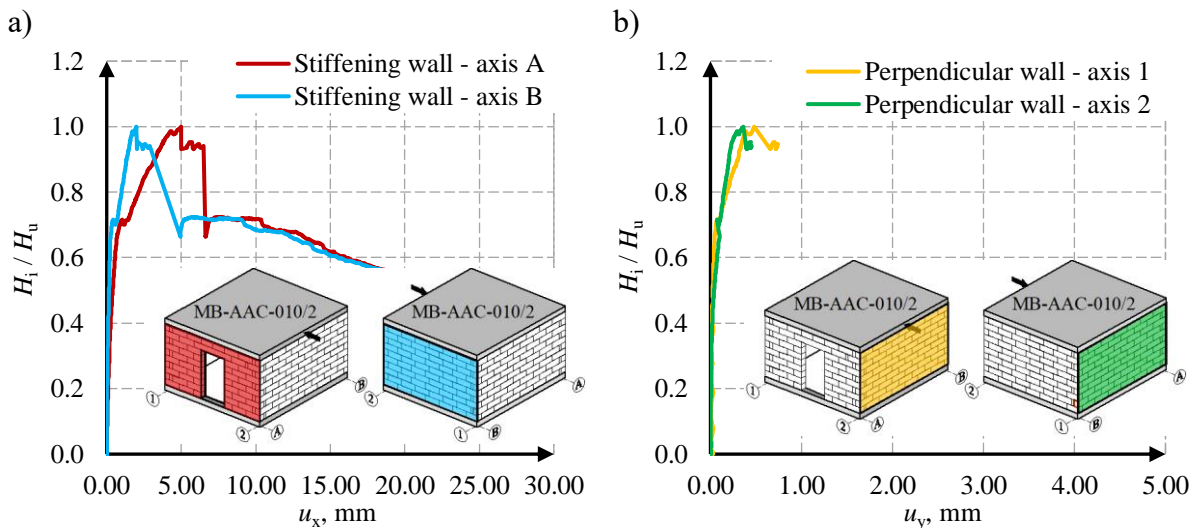
Fig. 5.4 The normalized lateral load – horizontal displacement chart for the MB-AAC-010/2 model: a) results for A and B walls, b) for 1 and 2 walls

Based on the test results, a table containing the characteristic values of the cracking forces and the corresponding shear deformation angles was prepared to capture the phases of the walls' behavior. The moment of the first crack occurring within the corner of wall A was distinguished. The assumed force representing the limit of the elastic behavior of the wall was 49.9 kN (model MB-AAC-010/1) and 49.6 kN (model MB-AAC-010/2). The maximum forces in the tests are consecutively 57.8 kN and 69.3 kN, and residual forces are 45.3 kN and 45.9 kN. Detailed values of forces and corresponding deformations are shown in Table 5.1. The graphical representation of behavior phases of a wall with a door opening in Fig. 5.5 and a solid wall in Fig. 5.6.

Table 5.1

The values of horizontal forces and deformation angles based on test results

Model	Model wall	Initial phase		Elastic phase		Nonlinear phase		Post-peak residual phase	
		$H_{cr,1}$, kN	$\Theta_{cr,1}$, mrad	H_{cr}, kN	Θ_{cr}, mrad	H_u, kN	Θ_u, mrad	H_{res}, kN	Θ_{res}, mrad
MB-AAC-010/1	A	29.108	0.002	-	-	58.784	-	-	-
	B	-	-	49.935	0.071		0.743	45.291	2.210
MB-AAC-010/2	A	9.759	0.020	49.615	0.389	69.247	1.890	45.894	2.522
	B	-	-	49.615	0.162		0.756	45.894	1.874
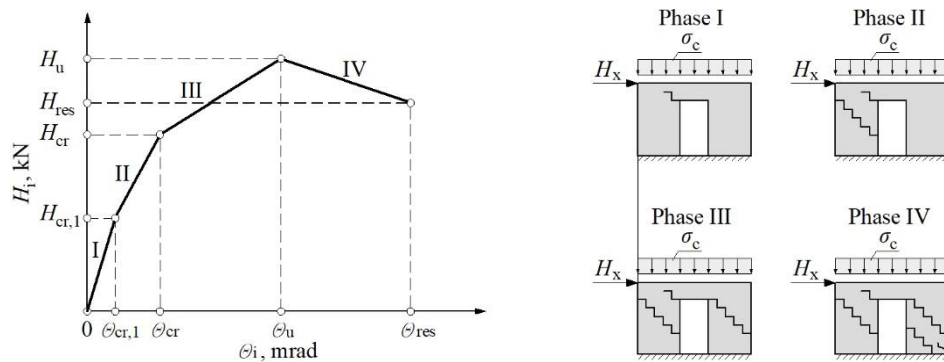
Fig. 5.5 Behavior phases of stiffening walls with door opening: I – initial phase, II – elastic phase, III – nonlinear phase, IV – post-peak residual phase
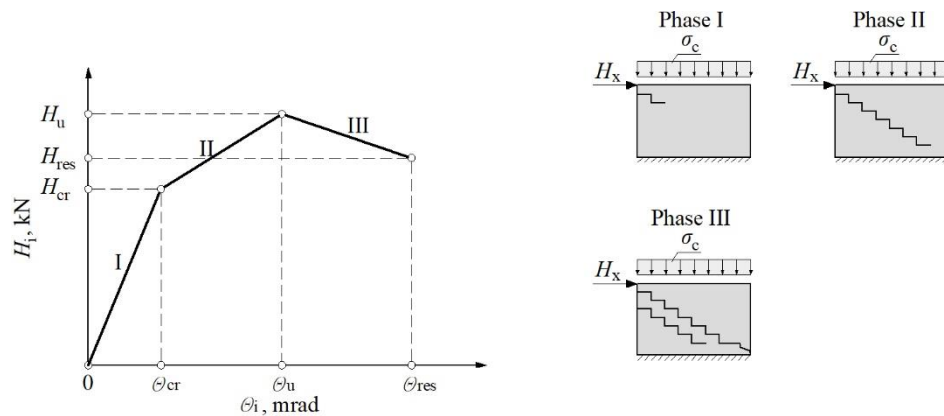
Fig. 5.6 Behavior phases of solid stiffening walls: I – elastic phase, II – nonlinear phase, III – post-peak residual phase

There is no initial phase in walls without openings, which consists of cracking the tensile opening corners. The behavior of walls with openings is more complex than the corresponding solid wall. The range of actual elastic behavior (linear behavior up to the first crack) is smaller than in walls without openings.

5.1.2. Results for models with door opening in stiffening wall A and windows opening in perpendicular wall 1 – type II models

Models MB-AAC-010/3, MB-AAC-010/4 and MB-AAC-010/5 were assigned to the second type of models in which the stiffening wall A had a door opening, and the transverse wall 1 had a window opening. Analogously to the previous diagrams of the normalized horizontal force to the angles of shear deformation – Fig. 5.7 – Fig 5.9 and about the horizontal displacements – Fig. 5.10 – Fig 5.12 of the walls were prepared.
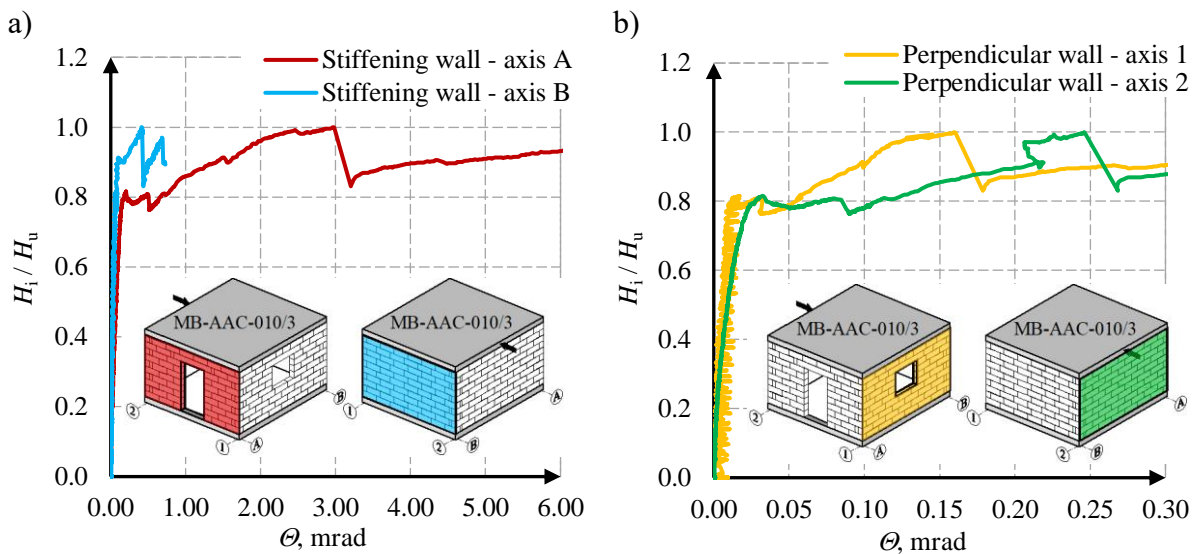
Fig. 5.7 Relationship between the horizontal force and shear deformation angle for the MB-AAC-010/3 model: a) results for A and B walls, b) for 1 and 2 walls
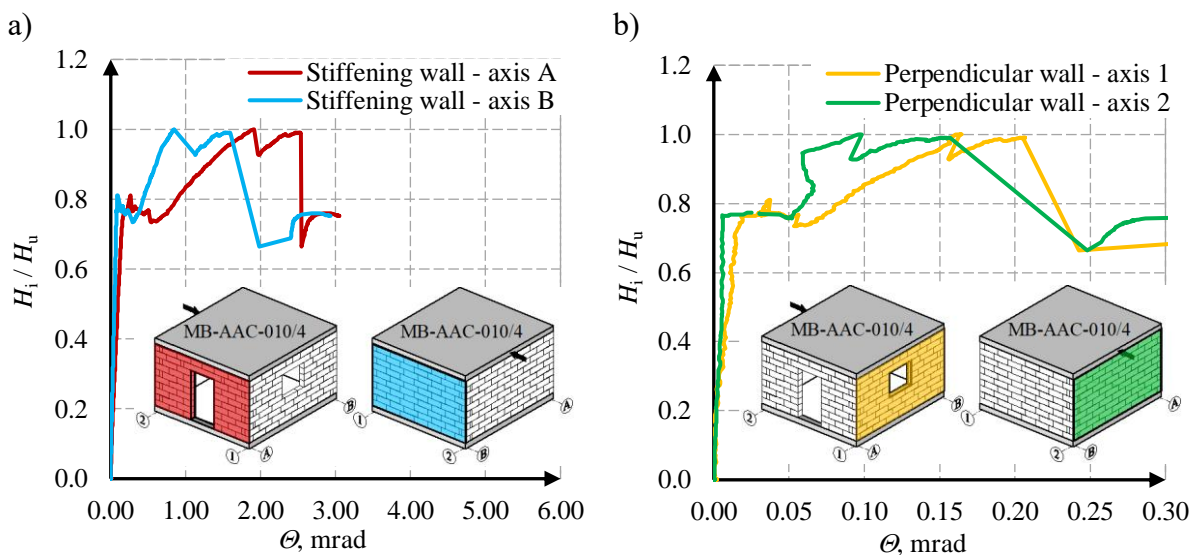
Fig. 5.8 Relationship between the horizontal force and shear deformation angle for the MB-AAC-010/4 model: a) results for A and B walls, b) for 1 and 2 walls
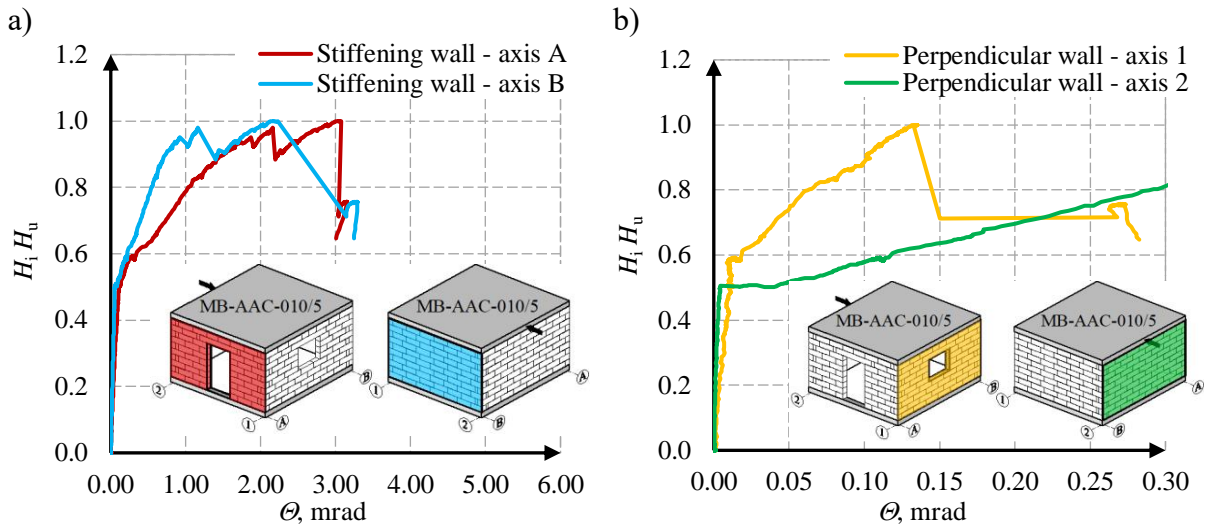
Fig. 5.9 Relationship between the horizontal force and shear deformation angle for the MB-AAC-010/5 model: a) results for A and B walls, b) for 1 and 2 walls
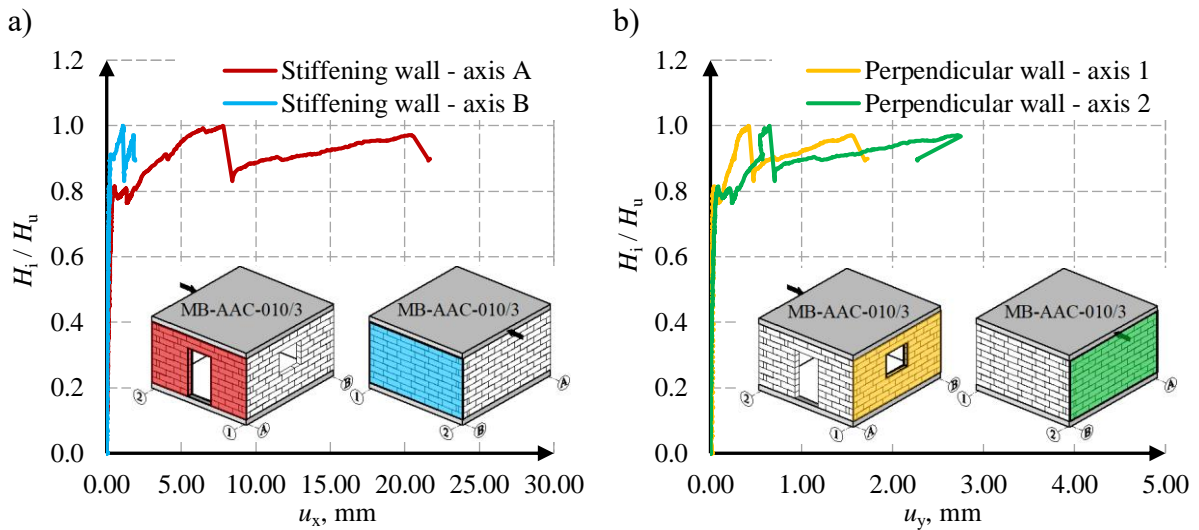
Fig. 5.10 The normalized lateral load – horizontal displacement chart for the MB-AAC-010/3 model: a) results for A and B walls, b) for 1 and 2 walls

Fig. 5.11 The normalized lateral load – horizontal displacement chart for the MB-AAC-010/4 model: a) results for A and B walls, b) for 1 and 2 walls

Fig. 5.12 The normalized lateral load – horizontal displacement chart for MB-AAC-010/5 model; a) results for A and B walls, b) for 1 and 2 walls

The largest horizontal displacements were observed in model MB-AAC-010/3. The horizontal displacement for the stiffening wall A is 21.7 mm, and for the transverse wall 2 is about 2.3 mm. The behavior phases of the stiffening walls were the same as in type I models. The course of the dependencies is similar - after reaching the maximum force, there is a rapid decrease and successive increases. The values of the cracking forces within the door opening are 20.8, 17.7 and 20.2 kN. The maximum forces are in order 74.1, 84.9 and 87.5 kN. The detailed results of the forces and the corresponding deformation angles are shown in Table 5.2.

Table 5.2

The values of horizontal forces and deformation angles based on test results

Model	Model wall	Initial phase		Elastic phase		Nonlinear phase		Post-peak residual phase	
		$H_{cr,1}$, kN	$\Theta_{cr,1}$, mrad	H_{cr}, kN	Θ_{cr}, mrad	H_u, kN	Θ_u, mrad	H_{res}, kN	Θ_{res}, mrad
MB-AAC-010/3	A	20.768	0.034	60.385	0.202	74.048	2.967	61.455	3.202
	B	-	-	67.631	0.098		0.410	61.455	0.436
MB-AAC-010/4	A	17.677	0.034	68.738	0.267	84.860	1.900	78.633	1.973
	B	-	-	68.738	0.097		0.840	78.633	1.128
MB-AAC-010/5	A	20.192	0.040	51.461	0.258	87.532	3.042	62.282	3.038
	B	-	-	51.461	0.198		2.180	62.282	3.145

5.1.3. Results for models with a window opening in stiffening wall A and door opening in stiffening wall B– type III models

Models MB-AAC-010/6 and MB-AAC-010/7 were assigned to type III models due to the geometry of the building. A window opening was formed in the stiffening wall A, and a door opening in the stiffening wall B. The results are presented in the same way as before as graphs of the dependence of the normalized horizontal force in relation to the shear deformation angles – Fig. 5.13 and Fig. 5.14 and about the horizontal displacements of the walls – Fig. 5.15 and Fig. 5.16.

Fig. 5.13 Relationship between the horizontal force and shear deformation angle for the MB-AAC-010/6 model: a) results for A and B walls, b) for 1 and 2 walls


Fig. 5.14 Relationship between the horizontal force and shear deformation angle for the MB-AAC-010/7 model: a) results for A and B walls, b) for 1 and 2 walls
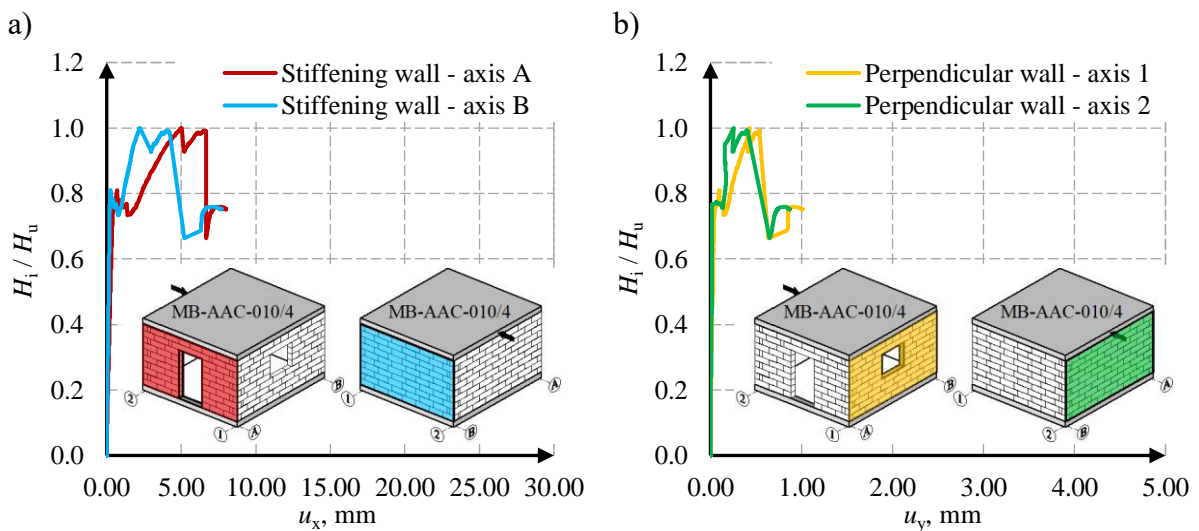
Fig. 5.15 The normalized lateral load - horizontal displacement chart for the MB-AAC-010/6 model: a) results for A and B walls, b) for 1 and 2 walls
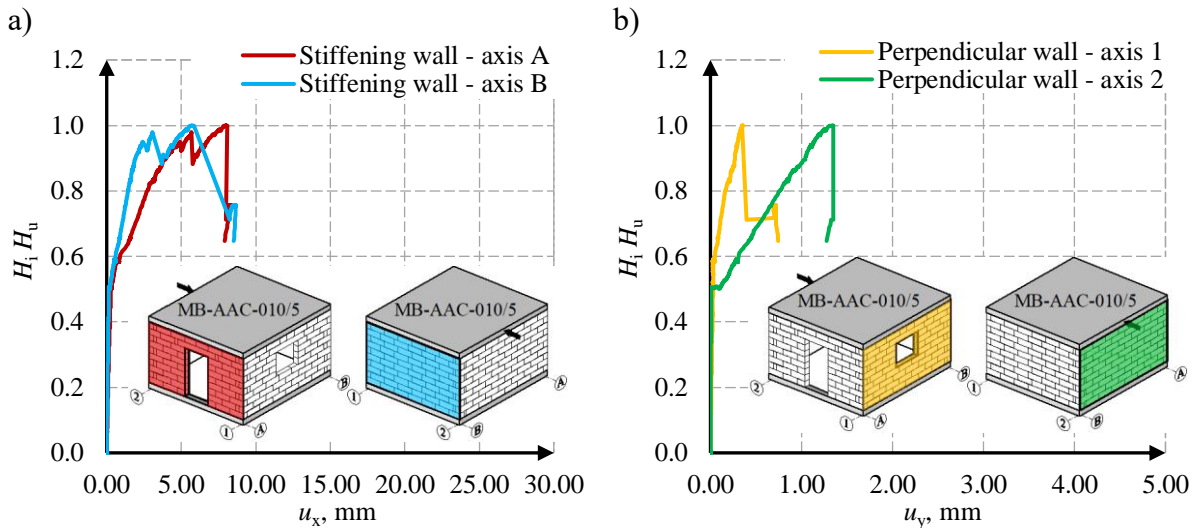

Fig. 5.16 The normalized lateral load - horizontal displacement chart for the MB-AAC-010/7 model: a) results for A and B walls, b) for 1 and 2 walls

The diagrams show that after reaching the maximum force, load capacity still increases with increasing displacements. The actual range of the elastic phase is small due to the slight cracks in the wall within the openings (the initial phase limit is about 0.35% of the maximum force). The assumed elastic range is about 0.75% of the maximum force. MB-AAC-010/6, stiffening wall A with greater stiffness, after cracking in the elastic phase, was finally characterized by higher deformation values than wall B with lower stiffness. This means that the cracking of wall A significantly reduced its stiffness so that the displacements increased faster than in wall B, and there was no rapid redistribution of internal forces between the walls. The exact values of the behavior phases of the stiffening walls are shown in Table 5.3. The behavior phases for the wall with a window opening were developed – Fig. 5.17.

108

Table 5.3

The values of horizontal forces and deformation angles based on test results

Model	Model wall	Initial phase		Elastic phase		Nonlinear phase		Post-peak residual phase	
		$H_{cr,1}$, kN	$\Theta_{cr,1}$, mrad	H_{cr}, kN	Θ_{cr}, mrad	H_u, kN	Θ_u, mrad	H_{res}, kN	Θ_{res}, mrad
MB-AAC-010/6	A	26.047	0.043	56.508	0.148	74.529	2.392	64.136	2.911
	B	17.877	0.041	56.508	0.211		2.766	64.136	2.885
MB-AAC-010/7	A	27.304	0.043	52.039	0.120	66.693	2.255	55.237	2.613
	B	23.625	0.043	52.039	0.154		1.266	55.237	1.338
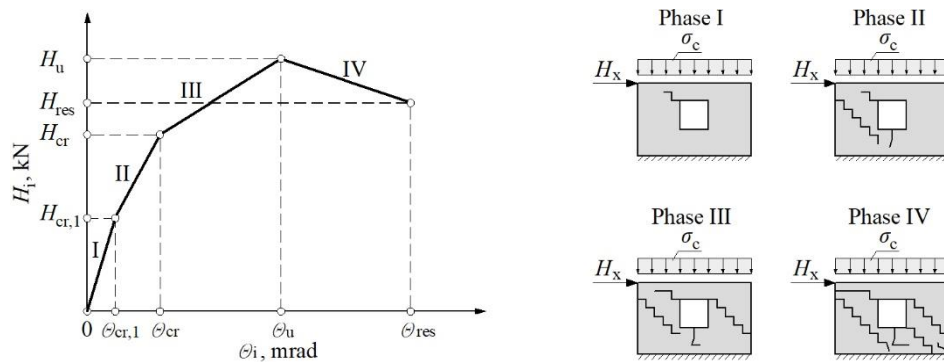
Fig. 5.17 Behavior phases of stiffening walls with window opening: I – initial phase, II – elastic phase, III – nonlinear phase, IV – post-peak residual phase

5.1.4. Results for reference model –– type IV models

Model MB-AAC-010/8 is a reference model in which the walls are devoid of openings. Figures 5.18 and 5.19 present the charts of masonry building behavior.
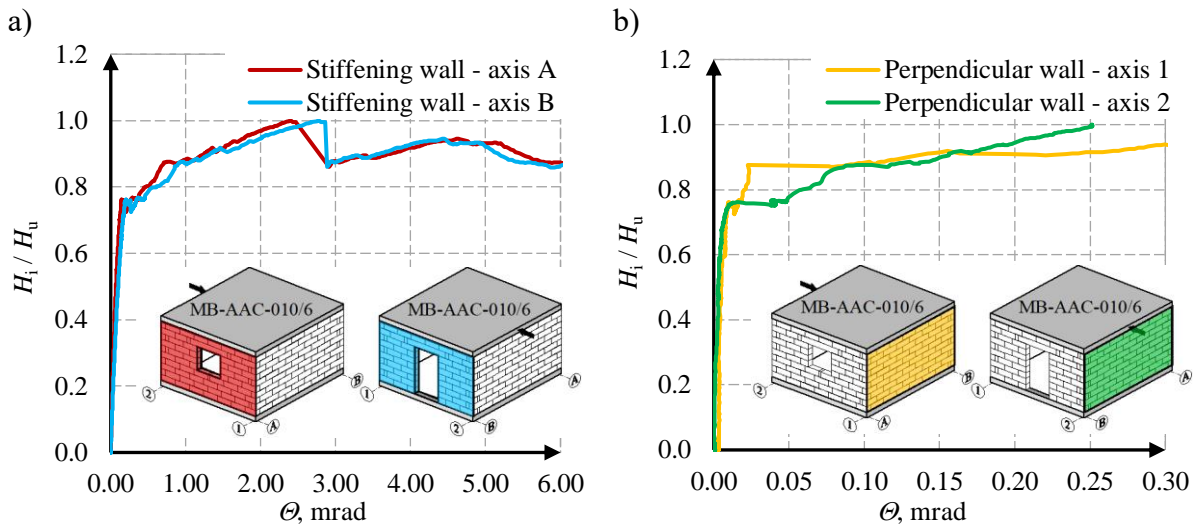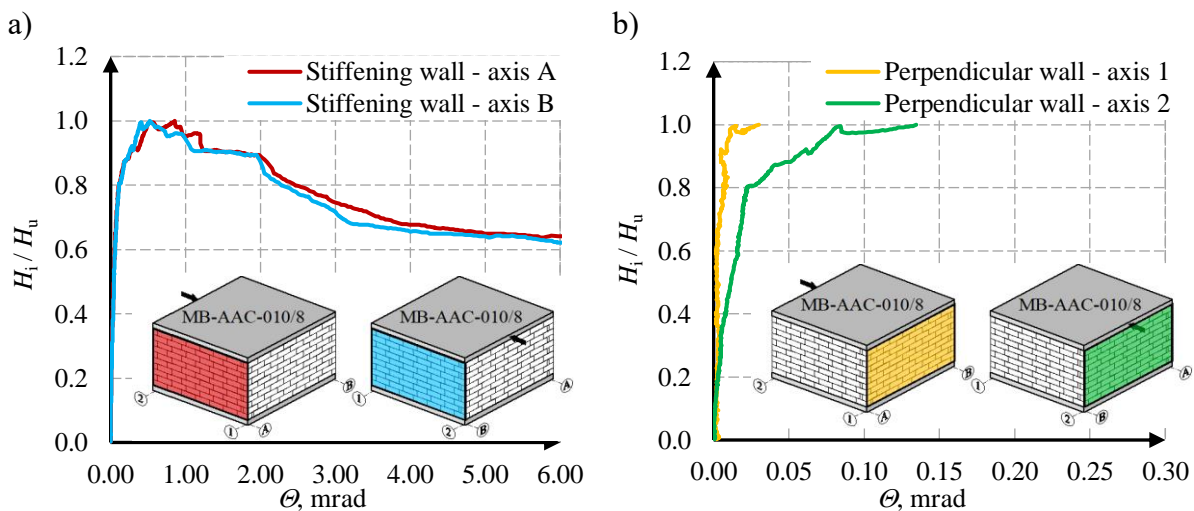

Fig. 5.18 Relationship between the horizontal force and shear deformation angle for the MB-AAC-010/8 model: a) results for A and B walls, b) for 1 and 2 walls
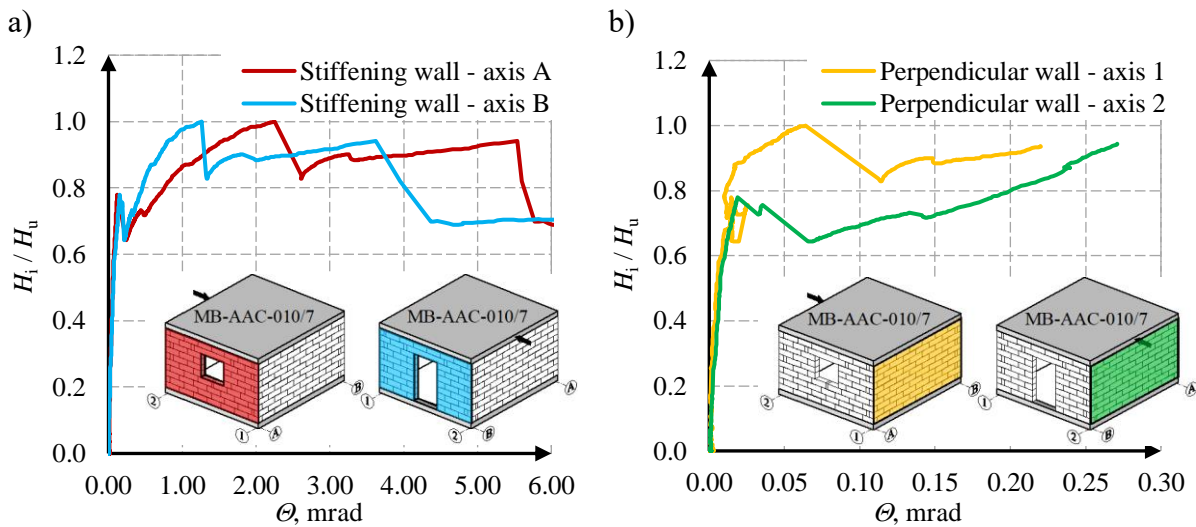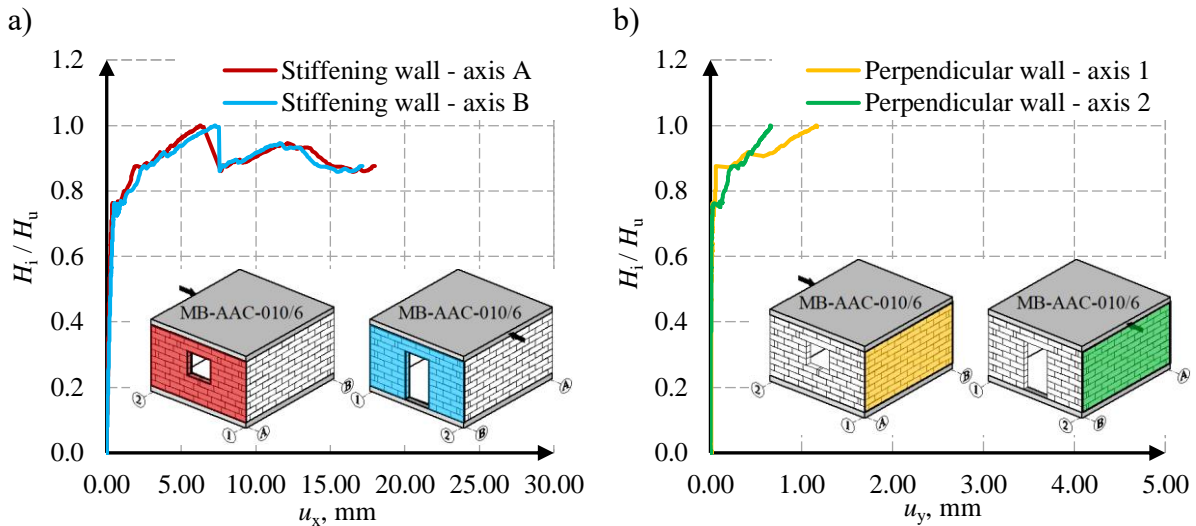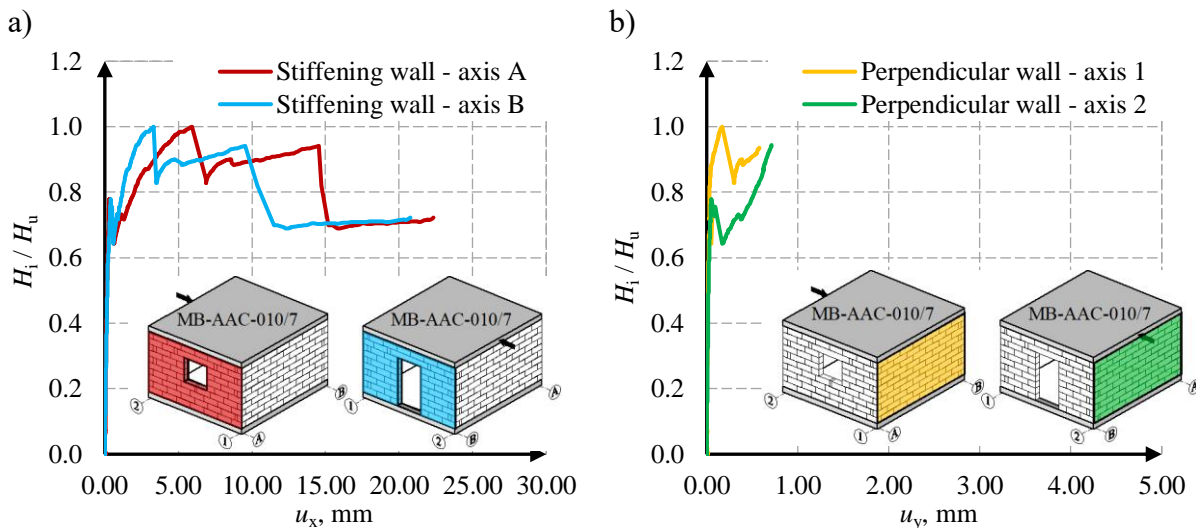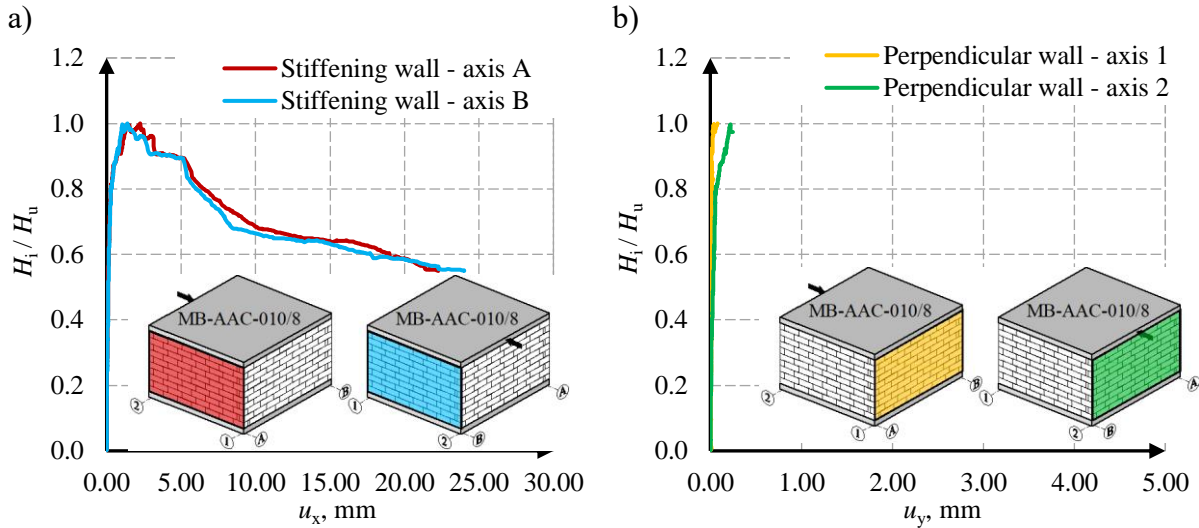
Fig. 5.19 The normalized lateral load – horizontal displacement chart for the MB-AAC-010/8 model: a) results for A and B walls, b) for 1 and 2 walls

The stiffnesses of all walls are the same in the reference model. Theoretically, such a building should not rotate but only translate. Tests have shown that the load capacity does not increase after reaching the maximum force, and this phenomenon is observed in buildings with openings. After reaching the maximum force, a gradual decrease in the stiffness of the building and increasing horizontal displacements are observed. The range of elastic behavior (elastic phase) reached 80% of the maximum force. The results suggest that opening the walls not only reduces the stiffness of the building but also determines the range of the elastic phase. The maximum horizontal displacements in the MB-AAC-010/8 model are 22.3 mm (wall A) and 24.0 mm (wall B). The values of forces and shear deformation angles in elastic, nonlinear and post-peak residual phases are presented in Table 5.4.

Table 5.4

The values of horizontal forces and deformation angles based on test results

Model	Model wall	Initial phase		Elastic phase		Nonlinear phase		Post-peak residual phase	
		$H_{cr,1}$, kN	$\Theta_{cr,1}$, mrad	H_{cr}, kN	Θ_{cr}, mrad	H_u, kN	Θ_u, mrad	H_{res}, kN	Θ_{res}, mrad
MB-AAC-010/8	A	-	-	52.870	0.114	65.521	0.856	59.309	1.283
	B	-	-	52.870	0.118		0.526	59.309	1.148

110

5.2. Analysis of test results

One of the goals of the dissertation is to determine the actual stiffness of the walls. The test results were analyzed, and a proposal for the empirical calculation of the wall stiffness was presented in section 5.2.1. The redistribution of internal forces was estimated based on comparing the actual forces representing the behavior phases of the stiffening walls (test results) with theoretical values - section 5.2.2.

5.2.1. The proposition of an Empirical Method of Load Distribution on Stiffening Walls

Forces acting on individual stiffening walls depend on the stiffness defined as the quotient of the total load corresponding to the displacement (5.2):

$$K = \frac{H}{\Delta} = \frac{H}{\Theta \cdot h} \qquad (5.2)$$

in which:

H – total load acting on the wall,

Δ – horizontal displacement,

Θ – shear deformation angle,

h – wall height.

The total stiffness of the building can be calculated as follows (5.3):

$$K_{tot} = \frac{H_{tot}}{\Delta_{tot}} = \frac{H_{tot}}{\Theta_{mv} \cdot h} \qquad (5.3)$$

where:

H_{tot} – total load acting on a building,

Δ_{tot} – total displacement of the building,

Θ_{mv} – mean value of deformation angle of stiffening walls, calculated following (5.4):

$$\Theta_{mv} = \frac{\Theta_A + \Theta_B}{2} \qquad (5.4)$$

in which:

Θ_A – shear deformation angle of stiffening wall A,

Θ_B – shear deformation angle of stiffening wall B.

Based on the formulas total stiffness of tested buildings was calculated. The results in Table 5.5 include the wall behavior phases and the corresponding values of the average shear deformation angles of the tested buildings.

The total stiffness of tested buildings

Model	Model wall	Initial phase		Elastic phase		Nonlinear phase		Post-peak residual phase	
		$\Theta_{cr,1,mv}$ mrad	$K_{tot,cr,1}$, kN/mm	$\Theta_{cr,mv}$ mrad	$K_{tot,cr,1}$, kN/mm	$\Theta_{u,mv}$ mrad	$K_{tot,u}$, kN/mm	$\Theta_{res,mv}$ mrad	$K_{tot,res}$, kN/mm
MB-AAC-010/2	A, B	-	-	0.28	75.00	1.32	21.81	2.20	8.70
MB-AAC-010/3	A, B	-	-	0.15	177.62	1.69	18.27	1.82	14.07
MB-AAC-010/4	A, B	-	-	0.18	157.09	1.37	25.79	1.55	21.13
MB-AAC-010/5	A, B	-	-	0.23	94.16	2.61	13.97	3.09	8.39
MB-AAC-010/6	A, B	0.04	216.82	0.18	130.83	2.58	12.04	2.90	9.22
MB-AAC-010/7	A, B	0.04	246.52	0.14	158.68	1.76	15.78	1.98	11.65
MB-AAC-010/8	A, B	-	-	0.12	190.10	0.69	39.53	1.22	20.33

The results indicate a significant degradation of the stiffness under the building load. The highest stiffness values are in the initial phase (first cracks in the corner of openings) - a significant decrease in stiffness occurs in the non-linear range. The distribution of the total horizontal load depends on the actual stiffness of the stiffening walls. For this purpose, based on tests, the stiffness of each of the stiffening walls was determined separately – Table 5.6.

Table 5.6

Stiffness of stiffening walls based on the test

Model	Model wall	Initial phase	Elastic phase	Nonlinear phase	Post-peak residual phase
		$K_{cr,1}$, kN/mm	K_{cr}, kN/mm	K_u, kN/mm	K_{res}, kN/mm
MB-AAC-010/2	A	205.58	53.12	15.26	7.58
	B	-	127.51	38.16	10.20
MB-AAC-010/3	A	254.61	124.40	10.40	8.00
	B	-	287.39	75.26	58.68
MB-AAC-010/4	A	216.71	107.10	18.61	16.61
	B	-	294.59	42.00	29.04
MB-AAC-010/5	A	212.68	83.21	11.99	8.54
	B	-	108.42	16.73	8.25
MB-AAC-010/6	A	251.34	158.57	12.98	9.18
	B	180.66	111.36	11.23	9.26
MB-AAC-010/7	A	263.47	181.43	12.32	8.81
	B	229.45	141.00	21.96	17.21
MB-AAC-010/8	A	-	193.82	31.91	19.26
	B	-	186.51	51.95	21.52

The larger the opening, the lower the initial stiffness of the wall. The values of the initial stiffness of the walls were over 200 kN/mm. In the non-linear residual phase, the stiffness of the walls decreased significantly. In order to determine the load acting on individual stiffening walls, relationships that determine the proportions of the shear deformation angles ω was introduced (5.5):

$$\omega = \Theta_A / \Theta_B \tag{5.5}$$

in which:

Θ_A – shear deformation angle of stiffening wall A,

Θ_B – shear deformation angle of stiffening wall B,

Selected diagrams of the deformation of stiffening walls ω for models MB-AAC-010/4 and MB-AAC-010/8 are shown in Fig. 5.20.

a)

b)
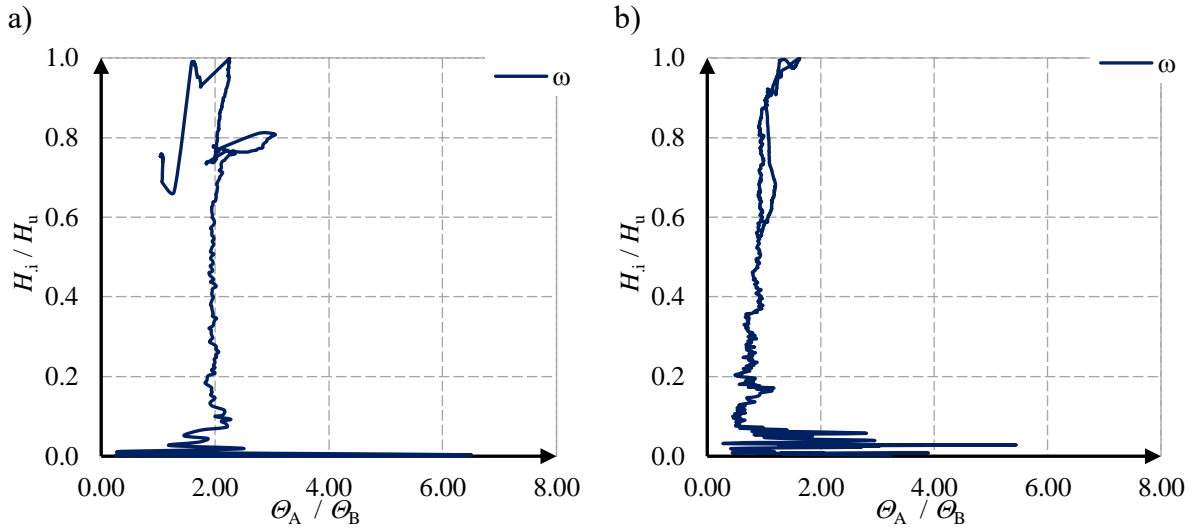
Fig. 5.20 The charts between the normalized horizontal force and proportion of shear deformation angles: a) the MB-AAC-010/4 model, b) the MB-AAC-010/8 model

The forces in the stiffening walls balance the total force acting on the building H_{tot}, and the equilibrium condition is as follows (5.6):

$$H_{tot} = H_A + H_B \tag{5.6}$$

where:

H_A – load (force) acting on stiffening wall A,

H_B – load (force) acting on stiffening wall B.

The above formula (5.6) can be expanded as shown below in (5.7):

$$K_{tot} \cdot \Delta_{tot} = K_A \cdot \Delta_A + K_B \cdot \Delta_B = K_{tot} \cdot \Theta_{mv} = K_A \cdot \Theta_A + K_B \cdot \Theta_B$$
$$= K_A \cdot \Theta_B \cdot \omega + K_B \cdot \Theta_B = (K_A \cdot \omega + K_B)\Theta_B \rightarrow$$

$$\frac{K_{tot}}{(K_A \cdot \omega + K_B)} = \tag{5.7}$$

$$\frac{\Theta_B}{\Theta_{mv}}$$

Having regard to that (5.8):

$$K_B = \frac{H_B}{\Theta_B \cdot h} \rightarrow \Theta_B = \frac{H_B}{K_B \cdot h} \tag{5.8}$$

In addition, the following equation can be formulated (5.9):

$$\frac{K_{tot} \cdot \Theta_{mv}}{(K_A \cdot \omega + K_B)} = \Theta_B = \frac{H_B}{K_B \cdot h} \tag{5.9}$$

The value of the force acting on the stiffening wall B can be calculated from the formula (5.10). The results are summarized in Table 5.7.

$$K_B = \frac{H_B}{\Theta_B \cdot h} \rightarrow \Theta_B = \frac{H_B}{K_B \cdot h}$$
$$H_B = K_B \cdot h \frac{K_{tot} \cdot \Theta_{mv}}{(K_A \cdot \omega + K_B)}$$

(5.10)

Table 5.7

Forces acting on particular stiffening walls

Model	Model wall	Initial phase	Elastic phase	Nonlinear phase	Post-peak residual phase
		$H_{cr,1}$, kN	H_{cr}, kN	H_u, kN	H_{res}, kN
MB-AAC-010/2	A	-	24.81	34.62	22.95
	B	-	24.81	34.62	22.95
	ω	2.04	2.40	2.50	1.35
MB-AAC-010/3	A	-	32.64	37.02	30.73
	B	-	31.37	37.02	30.73
	ω	2.65	2.40	7.24	7.34
MB-AAC-010/4	A	-	34.37	42.43	39.32
	B	-	34.37	42.43	39.32
	ω	2.00	2.75	2.26	1.75
MB-AAC-010/5	A	-	25.73	43.77	31.14
	B	-	25.73	43.77	31.14
	ω	1.49	1.30	1.40	0.97
MB-AAC-010/6	A	10.77	28.25	37.26	32.07
	B	11.19	28.25	37.26	32.07
	ω	0.69	0.70	0.86	1.01
MB-AAC-010/7	A	12.82	26.02	33.35	27.62
	B	12.64	26.02	33.35	27.62
	ω	0.88	0.78	1.78	1.95
MB-AAC-010/8	A	-	26.44	32.76	29.65
	B	-	26.44	32.76	29.65
	ω	-	0.96	1.63	1.12

5.2.2. Determination of internal forces by the analytical method

In addition to the empirical method of determining internal forces in stiffening walls, the own method [79] was used to calculate the stiffness and load distribution. The shear forces in the walls due to acting horizontal forces H_x and H_y can be calculated by formulas (5.11) and (5.12).

$$H_{x,i} = H_x \frac{K_{y,i}}{\Sigma_i K_{y,i}} \tag{5.11}$$

$$H_{y,i} = H_y \frac{K_{x,i}}{\Sigma_i K_{x,i}} \tag{5.12}$$

Moreover, the shear forces caused by the torsional moments M_{sx} and M_{sy} are (5.13-5.16):

$$H_{xs,i} = \pm M_{sx} \frac{\bar{a}_{xi} K_{y,i}}{\Sigma_i \bar{a}_{xi}^2 K_{x,i} + \Sigma_i \bar{a}_{yi}^2 K_{y,i}} \tag{5.13}$$

$$H_{ys,i} = \pm M_{sx} \frac{\bar{a}_{xi} K_{y,i}}{\Sigma_i \bar{a}_{xi}^2 K_{x,i} + \Sigma_i \bar{a}_{yi}^2 K_{y,i}} \tag{5.14}$$

$$H_{xs,i} = \pm M_{sy} \frac{\bar{a}_{xi} K_{y,i}}{\Sigma_i \bar{a}_{xi}^2 K_{x,i} + \Sigma_i \bar{a}_{yi}^2 K_{y,i}} \tag{5.15}$$

$$H_{ys,i} = \pm M_{sy} \frac{\bar{a}_{xi} K_{y,i}}{\Sigma_i \bar{a}_{xi}^2 K_{x,i} + \Sigma_i \bar{a}_{yi}^2 K_{y,i}} \tag{5.16}$$

in which:

$\bar{a}_{xi}, \bar{a}_{yi}$ – distances between the gravity center of the wall fragments and the rotation centre (RC),

h_m – wall height.

The bending moments due to load H_x and H_y can be calculated following formulas (5.17) – (5.18). Formulas (5.19) – (5.20) express the bending moments due to torsional moments M_{sx} and M_{sy}.

$$M_{ox,i} = M_{ox} \frac{K_{x,i}}{\Sigma_i K_{x,i}} \tag{5.17}$$

$$M_{oy,i} = M_{ox} \frac{K_{y,i}}{\Sigma_i K_{y,i}} \tag{5.18}$$

$$M_{sx,i} = \pm H_{xs,i} h_m \tag{5.19}$$

$$M_{sy,i} = \pm H_{ys,i} h_m \tag{5.20}$$

The coordinates of the rotation centre (RC) are calculated according to formulas (5.21) and (5.22):

$$x_R = \frac{\sum_i (a_{xi} K_{xi})}{\sum_i K_{xi}} \tag{5.21}$$

$$y_R = \frac{\sum_i (a_{yi} K_{yi})}{\sum_i K_{yi}} \tag{5.22}$$

in which:

a_{xi}, a_{yi} – the distance between the load centre (LC) and the rotation center of the wall or stiffening group,

K_{xi}, K_{yi} – stiffness of the wall or stiffening group.

The total stiffness method [79] was used to calculate the stiffness of the walls. The wall with a window or door opening was divided into vertical pillars, a lintel band, and a bottom spandrel. The total displacement of the upper edge of the wall Δ_w from the unit load is the sum of the displacements of the bottom spandrels, inter-opening pillars and lintels (5.23).

$$\Delta_w = {}^A\Delta_w + {}^P\Delta_w + {}^B\Delta_w \tag{5.23}$$

in which:

${}^A\Delta_w$ – displacement of the lintel,

${}^B\Delta_w$ – displacement of the bottom spandrel,

${}^P\Delta_w$ – displacement of the vertical pillar.

The displacements of the wall components (parts) depend on the geometry and boundary conditions. The geometrical parameters of walls with openings adopted for calculations are shown in Fig. 5.21. Moreover, if the height ratio to the length of the wall is $h/l > 2$, the effects of tangential stresses in determining the wall stiffness can be neglected. Otherwise, the stiffness should be calculated, considering shear deformations. Wall stiffness depending on the boundary conditions is shown in Table 5.8.
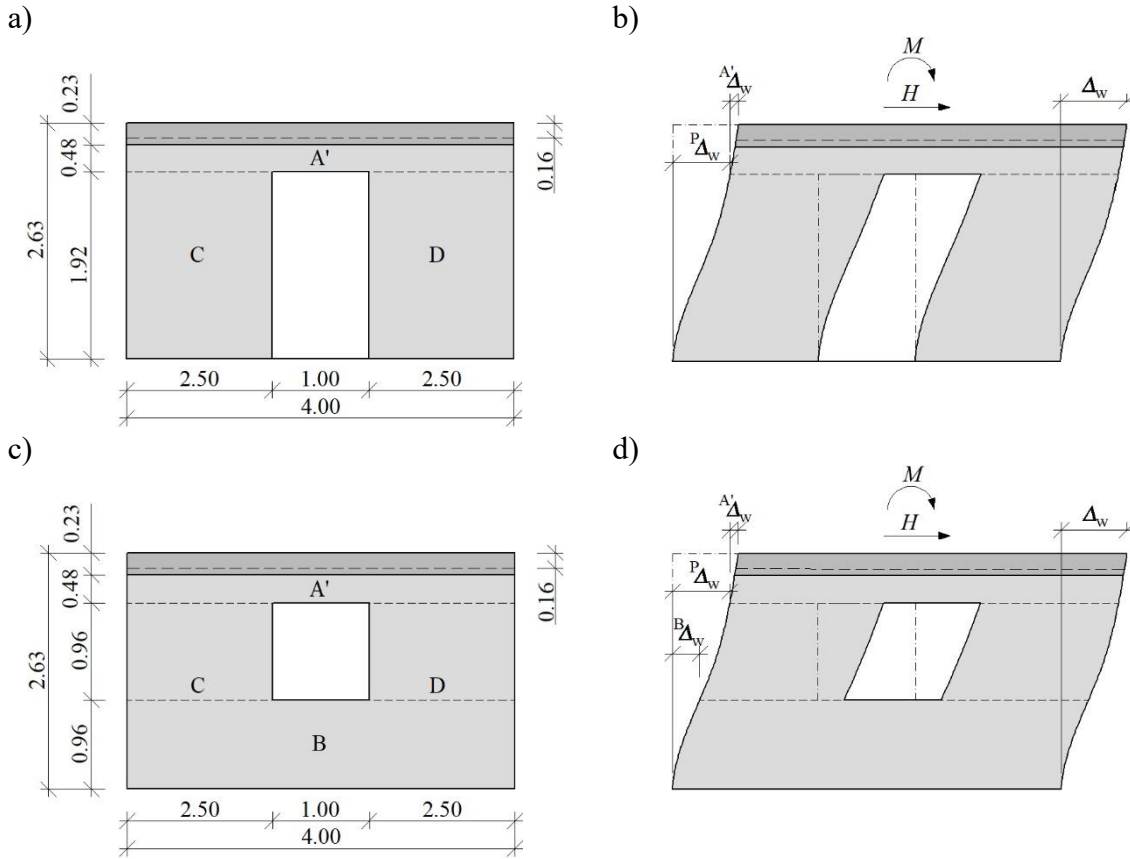
Fig. 5.21 The geometrical parameters adopted for calculation in the total stiffness method: a) division of a wall with a door opening into component elements, b) deformations of a wall with a door opening, c) division of a wall with a window opening into component elements, d) deformations of a wall with a window opening

Table 5.8

Stiffness of solid walls in the total stiffness method

Static scheme	$h/l \leq 2$		$h/l > 2$	
	Force P	Moment M	Force P	Moment M
Cantilever type C	$K_p = \dfrac{1}{\dfrac{h_m^3}{3EI} + \dfrac{1.2h_m}{GA}}$	$K_M = \dfrac{2EI}{h_m^2}$	$K_M = \dfrac{3EI}{h_m^3}$	$K_M = \dfrac{2EI}{h_m^2}$
Double-fixed type F	$K_p = \dfrac{1}{\dfrac{h_m^3}{12EI} + \dfrac{1,2h_m}{GA}}$	-	$K_M = \dfrac{12EI}{h_m^3}$	-
		-		-

After calculating the total displacement of the wall, its stiffness can be estimated following the formula (5.24).

$$K_w = \frac{1}{\Delta_w} \qquad (5.24)$$

where:

Δ_w - the total displacement of the top edge of the wall due to unit load $H = 1$.

The analytical calculations of the stiffening walls were carried out according to the following procedure:

1. The length of the transverse wall fragment (flange) b_{eff1} was assumed following the recommendations of Eurocode 6.
2. The wall with the opening was divided into fragments, as shown in Fig. 5.21. Moments of inertia of the wall components were calculated, considering the transverse b_{eff1} parts.
3. Static schemes of each component were established: "C" - cantilever wall, "F" - restrained wall.
4. The stiffness K of the wall components were determined according to the formulas in Table 5.8.
5. The stiffness of the walls was determined according to Fig. 5.21 and formula (5.24), and results are collected in Tables 5.9 – 5.12.
6. The distances a_{xi}, a_{yi} to the load center (LC) were assumed.
7. The localization of the rotation center was calculated according to formulas (5.21) and (5.22) – Table 5.13.
8. The internal forces in walls were calculated according to (5.11) –(5.20).

Table 5.9

Geometric and stiffness characteristics of walls for type I models

Model type I - MB-AAC-010/1 and MB-AAC-010/2						
Wall or component		Moment of inertia I, m^4	Static scheme	*Distance GC-LC a, m	Stiffness K, kN/mm	
A	A'	1.59	F		592.75	
	C	0.09	F	1.91	47.22	81.46
	D	0.09	F		47.22	
B		1.59	F	-1.91	113.96	
1		1.59	F	-1.91	113.96	
2		1.59	F	1.91	113.96	

* distance from the center of gravity of the wall to a point LC (load center)

Table 5.10

Geometric and stiffness characteristics of walls for type II models

Model type II - MB-AAC-010/3, MB-AAC-010/4 and MB-AAC-010/5						
Wall or component		Moment of inertia I, m^4	Static scheme	*Distance GC-LC a, m	Stiffness K, kN/mm	
A	A'	1.59	F	1.91	592.75	81.46
	C	0.09	F		47.22	
	D	0.09	F		47.22	
B		1.59	F	-1.91	113.96	
1	A'	1.59	F	-1.91	592.75	102.35
	B	1.59	F		294.89	
	C	0.09	F		106.56	
	D	0.09	F		106.56	
2		1.59	F	1.91	113.96	

* distance from the center of gravity of the wall to a point LC (load center)

Table 5.11

Geometric and stiffness characteristics of walls for type III models

Model type III - MB-AAC-010/6 and MB-AAC-010/7						
Wall or component		Moment of inertia I, m^4	Static scheme	*Distance GC-LC a, m	Stiffness K, kN/mm	
A	A'	1.59	F	1.91	592.75	102.35
	B	1.59	F		294.89	
	C	0.09	F		106.56	
	D	0.09	F		106.56	
B	A'	1.59	F	-1.91	592.75	81.46
	C	0.09	F		47.22	
	D	0.09	F		47.22	
1		1.59	F	-1.91	113.96	
2		1.59	F	1.91	113.96	

* distance from the center of gravity of the wall to a point LC (load center)

Table 5.12

Geometric and stiffness characteristics of walls for type IV models

Model type IV - MB-AAC-010/8				
Wall or component	Moment of inertia I, m^4	Static scheme	*Distance GC-LC a, m	Stiffness K, kN/mm
A	1.59	F	-1.91	113.96
B	1.59	F	-1.91	113.96
1	1.59	F	-1.91	113.96
2	1.59	F	1.91	113.96

* distance from the center of gravity of the wall to a point LC (load center)

Table 5.13

The coordinates of the torsion center for each model type

Model type	Coordinates of torsion center	
	x_r, m	y_r, m
I	0.00	-0.32
II	0.10	-0.32
III	0.00	-0.10
IV	0.00	0.00

The values of internal forces in stiffening walls were calculated based on formulas of the total stiffness method. The analysis encloses the elastic and non-linear phases in Table 5.14. The theoretical results were compared with the forces calculated by the empirical method (test results) – Table 5.15.

Table 5.14

The values of internal forces in the total stiffness method

Model	Model wall	Elastic phase			Nonlinear phase		
		$^{cal}H_{cr,I}$, kN	$^{cal}H_{cr,si}$, kN	$^{cal}H_{cr}$, kN	$^{cal}H_{u,I}$, kN	$^{cal}H_{u,si}$, kN	$^{cal}H_u$, kN
MB-AAC-010/2	A	-20.68	-1.88	-22.56	-28.87	-2.62	-31.48
	B	-28.94	1.88	-27.06	-40.38	2.62	-37.77
MB-AAC-010/3	A	-26.68	-2.42	-29.10	-30.87	-2.80	-33.67
	B	-37.33	2.42	-34.91	-43.18	2.80	-40.38
MB-AAC-010/4	A	-28.65	-2.60	-31.25	-35.37	-3.21	-38.58
	B	-40.09	2.60	-37.49	-49.49	3.21	-46.28
MB-AAC-010/5	A	-21.45	-1.95	-23.40	-36.49	-3.31	-39.80
	B	-30.01	1.95	-28.06	-51.04	3.31	-47.73
MB-AAC-010/6	A	-23.56	-2.14	-25.69	-31.07	-2.82	-33.89
	B	-32.95	2.14	-30.82	-43.46	2.82	-40.64
MB-AAC-010/7	A	-21.69	-1.97	-23.66	-27.80	-2.52	-30.32
	B	-30.35	1.97	-28.38	-38.89	2.52	-36.37
MB-AAC-010/8	A	-22.04	-2.00	-24.04	-27.31	-2.48	-29.79
	B	-30.83	2.00	-28.83	-38.21	2.48	-35.73

* signs of internal forces concerning the global coordinate system (Fig. 4.30)
$^{cal}H_{cr,I}$ – elastic force due to shear, $^{cal}H_{cr,si}$ – elastic force due to rotation of the building, $^{cal}H_{cr}$ – the total internal force in stiffening wall (elastic phase), $^{cal}H_{u,I}$ – force due to shear (nonlinear phase), $^{cal}H_{u,si}$ – force due to rotation of the building (nonlinear phase), $^{cal}H_u$ – the total internal force in a stiffening wall (nonlinear phase)

Table 5.15

Comparison of test results and analytical analysis

Model	Model wall	Elastic phase			Nonlinear phase		
		H_{cr}, kN	$^{cal}H_{cr}$, kN	$H_{cr} / {}^{cal}H_{cr}$	H_u, kN	$^{cal}H_u$, kN	$H_u / {}^{cal}H_u$
MB-AAC-010/2	A	24.81	22.56	1.10	34.62	31.48	1.10
	B	24.81	27.06	0.92	34.62	37.77	0.92
MB-AAC-010/3	A	32.64	29.10	1.12	37.02	33.67	1.10
	B	31.37	34.91	0.90	37.02	40.38	0.92
MB-AAC-010/4	A	34.37	31.25	1.10	42.43	38.58	1.10
	B	34.37	37.49	0.92	42.43	46.28	0.92
MB-AAC-010/5	A	25.73	23.40	1.10	43.77	39.80	1.10
	B	25.73	28.06	0.92	43.77	47.73	0.92
MB-AAC-010/6	A	28.25	25.69	1.10	37.26	33.89	1.10
	B	28.25	30.82	0.92	37.26	40.64	0.92
MB-AAC-010/7	A	26.02	23.66	1.10	33.35	30.32	1.10
	B	26.02	28.38	0.92	33.35	36.37	0.92
MB-AAC-010/8	A	26.44	24.04	1.10	32.76	29.79	1.10
	B	26.44	28.83	0.92	32.76	35.73	0.92

* signs of internal forces in absolute value

The results indicate a redistribution of internal forces between the stiffening walls. The difference between the theoretical values and those obtained in the tests is not more than 12%.

5.3. The procedure for calculations of the coordinates of the rotation center

The proposed procedure applies to a situation where the uncertainty of a single measurement of displacements of measurement points is not specified. The solution should take into account the uncertainty transfer principle. As a result of the external load, the building is rotated relative to the center of torsion (also called RC – rotation center) and simultaneously displaced (translation). The coordinates of the assumed measurement points before and after loading are known. The coordinates of the center of torsion (x_{RC}, y_{RC}), the angle of rotation (α) and the translation parallel to the load

direction (ΔT) are not known. Figure 5.22 shows the layout of the building before and after loading in the direction of the X-axis. The load point (LC) is located at the intersection of the load directions. Points "a", "b", "c", "d" are in the corners, and point "e", is located at the intersection of the axes of the walls and the direction of the applied load.
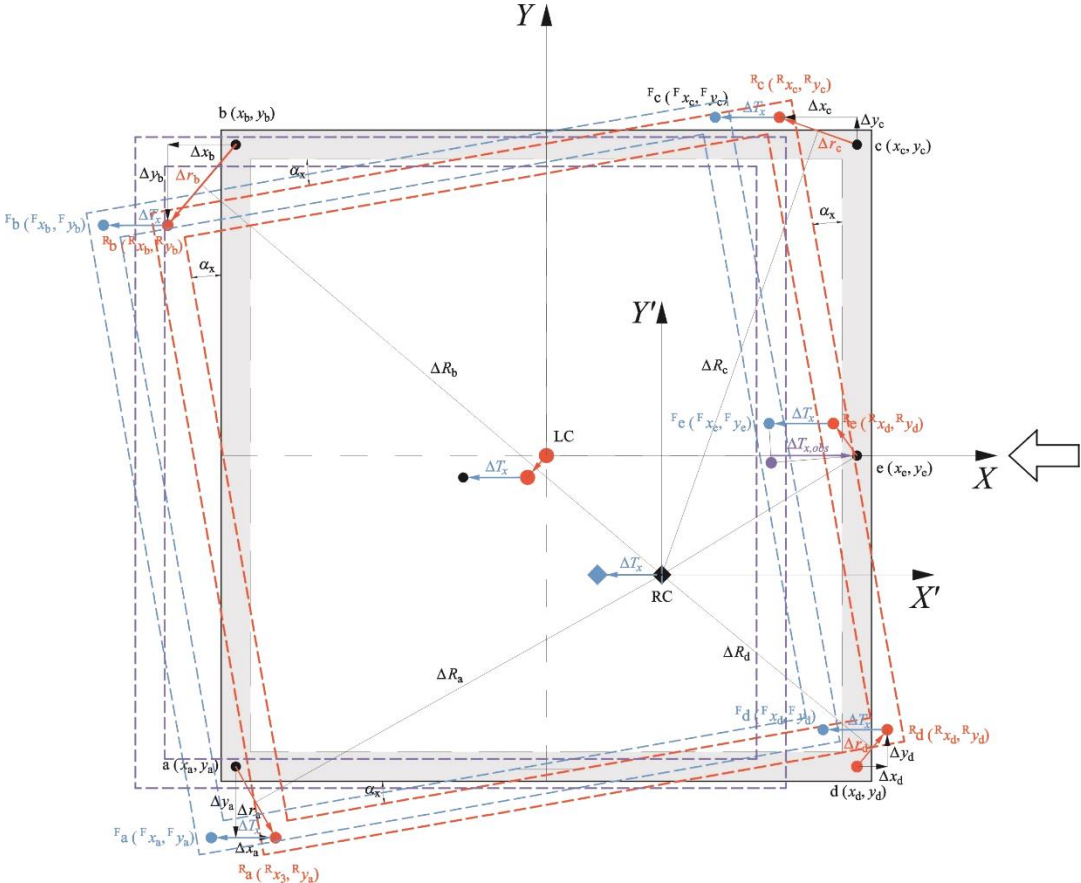

Fig. 5.22 Layout of the building before and after loading in the direction of the X-axis

Two coordinate systems are introduced LC-X-Y associated with the load center and RC-X'-Y' at the center of rotation (RC) – Fig. 5.23. The kinematics of all available measurement points should be considered to determine four unknowns. In the general solution, the coordinates of the considered point defined in the LC-X-Y coordinate system (related to the assumed load point) are equal to (5.25):

$$A\,(x, y) \tag{5.25}$$

In the coordinate system associated with the center of rotation RC-X'-Y', the coordinates are (5.26):

$$A\,(x', y') \tag{5.26}$$

123

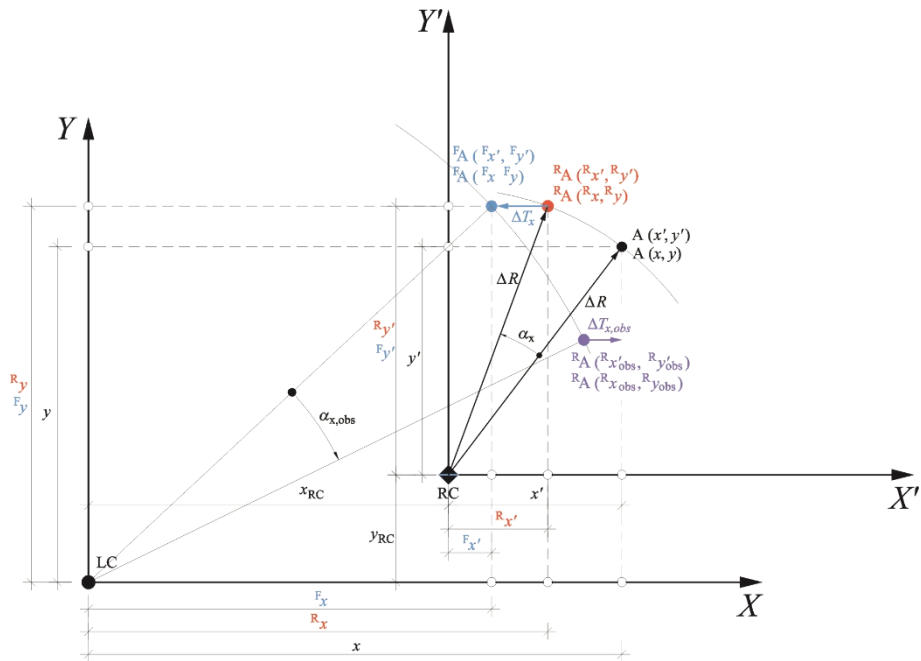The coordinates can be calculated according to (5.27) and (5.28):

$$x' = x - x_{RC} \qquad (5.27)$$

$$y' = y - y_{RC} \qquad (5.28)$$

where:

x_{RC}, y_{RC} – the coordinates of the RC point relative to the LC-X-Y system.
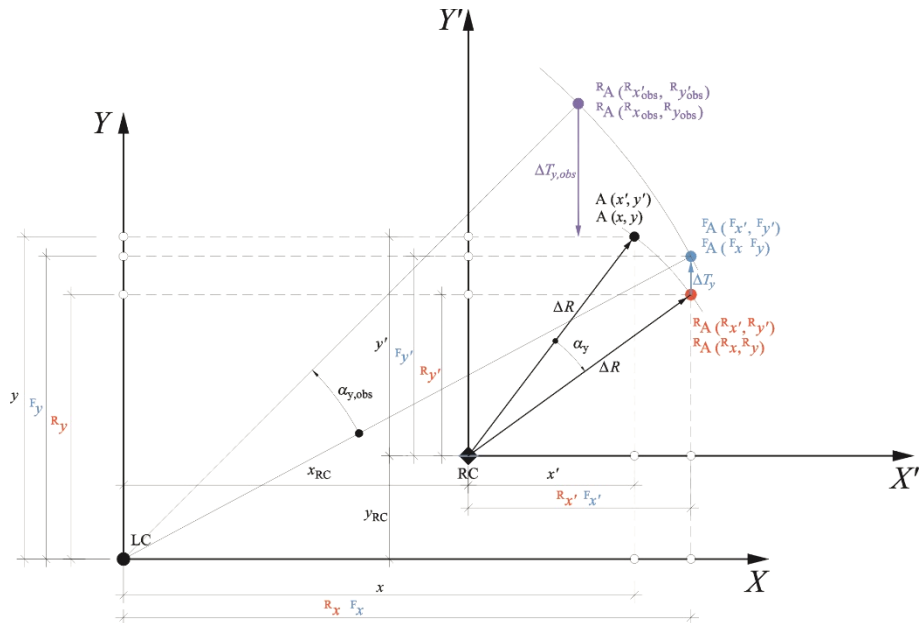
a)

b)

Fig. 5.23 Changes in the position of the RC point: a) as a result of rotation by the angle α and translation in the X-direction, b) as a result of rotation by the angle α and translation in the Y-direction

Due to the specificity of the load, each of the directions can be considered separately. When the load acts in the direction of the X-axis (Fig. 5.23a), the building will rotate relative to the RC-X'-Y' coordinate system by the angle α_x. The coordinates of point A in the rotated coordinate system will be (5.29) and (5.30):

$$^R x' = x' \cos \alpha_x - y' \sin \alpha_x \qquad (5.29)$$

$$^R y' = x' \sin \alpha_x - y' \cos \alpha_x \qquad (5.30)$$

In the LC-X-Y coordinate system, the coordinates are equal to (5.31) and (5.32):

$$^R x = {}^R x' + x_{RC} \qquad (5.31)$$

$$^R y = {}^R y' + y_{RC} \qquad (5.32)$$

In addition to the rotation, the building will be translated by distance ΔT_x. The coordinates in the RC-X'-Y' and LC-X-Y coordinate systems are equal to (5.33) – (5.36):

$$^F x' = {}^R x' + \Delta T_x \qquad (5.33)$$

$$^F y' = {}^R y' \qquad (5.34)$$

$$^F x = {}^R x + \Delta T_x \qquad (5.35)$$

$$^F y = {}^R y \qquad (5.36)$$

The measurement of displacements of the building slab is made about the LC-X-Y system, and the coordinates are equal to (5.37):

$$A \, (^F x, \, {}^F y) \qquad (5.37)$$

The corresponding relative displacements of the point coordinates in the LC-X-Y coordinate system (directly determined in tests) are (5.39) – (5.40):

$$\Delta x = {}^F x, - x \qquad (5.39)$$

$$\Delta y = {}^F y, - y \qquad (5.40)$$

125

When the load acts in the direction of the Y-axis (Fig. 5.23b), the building will rotate relative to the RC-X'-Y' coordinate system by the angle α_{y}. The coordinates of point A in the rotated coordinate system can be determined according to formulas (5.29) and (5.30). In the LC-X-Y coordinate system, the coordinates of point A can be calculated according to formulas (5.31) and (5.32).

Similarly, the building will be translated by the distance ΔT_y, and the coordinates in the RC-X'-Y' and LC-X-Y coordinate systems are equal (5.41) – (5.44):

$$^{F}x' = {}^{R}x' \tag{5.41}$$

$$^{F}y' = {}^{R}y' + \Delta T_y \tag{5.42}$$

$$^{F}x = {}^{R}x \tag{5.43}$$

$$^{F}y = {}^{R}y + \Delta T_y \tag{5.44}$$

The value of translation is crucial. Without knowing the displacement of the RC point, it is impossible to determine the position of the RC. The assumption is that this RC point displacement corresponds to the horizontal load application point displacement. In the direction of the load acting parallel to the Y-axis, the coordinates of point A relative to the LC-X-Y coordinate system are (5.45):

$$A(\,^{F}x,\,{}^{F}y) \tag{5.45}$$

Similarly, the relative displacements of the coordinates of the point in the LC-X-Y coordinate system are (5.46) – (5.47):

$$\Delta x = {}^{F}x - x \tag{5.46}$$

$$\Delta y = {}^{F}y - y \tag{5.47}$$

A minimum of three points must be defined on the slab to determine the coordinates of the center of the building torsion. However, it is better to take points located in the corners of the slab at the intersection of the wall axes (points: "a", "b", "c", "d") and the intersection of the wall axes and the direction of the load (point: "e"). The unknowns in the load direction parallel to the X-axis (in the LC-X-Y system) are the angle of rotation of the building α_x, the translation of the building ΔT_x and the x_{RC} and y_{RC} coordinates.

The unknowns in the load direction parallel to the Y-axis are the angle of rotation of the building α_y, the translation of the building ΔT_y and the x_{RC} and y_{RC} coordinates. The joint (independent) unknowns are the coordinates of the x_{RC} and y_{RC} centers of rotation. The building rotation angles α_x, α_y and the values of translations ΔT_x and ΔT_y are dependent unknown. Each direction can be analysed separably and reduce the number of unknowns. First, the angle of rotation of the building should be determined. For this purpose, it can consider any two points located initially in the load direction and then construct a straight line passing through these points in the post-load stage. The inclination angle of the straight line corresponding to the angle of rotation in the case of corners "b" and "c" (when the load is applied in the direction of the X-axis) is equal to (5.48):

$$\alpha_{x,cal} = \mathrm{actg}\left(\frac{^F y_{"b"} - \, ^F y_{"c"}}{^F x_{"b"} - \, ^F x_{"c"}} \right) \tag{5.48}$$

Next, the approximate slab translation should be determined. For this purpose, point "e" located at the intersection of the wall axis and the load direction can be used. The approximate displacement after the transformation of the coordinate system is (5.49):

$$\Delta T_{x,obs} = x - \, ^F x \cos \alpha_{x,cal} \tag{5.49}$$

Then, the coordinates of the points (corners) in the LC-X-Y system, caused only by the rotation, should be determined according to the following relations (5.50) and (5.51):

$$^R x_{cal} = \, ^F x - \Delta T_{x,obs} \tag{5.50}$$

$$^R y_{cal} = \, ^F y \tag{5.51}$$

In each corner, in addition to the coordinates before the deformation, there are coordinates after the deformation. Straight lines $y = a_1 x + b_1$ are drawn through these two points (straight lines "1", "2", "3", "4") in Fig. 5.24a. Directional coefficients of straight lines "a_1" in any corner can be determined according to the following relation (5.52):

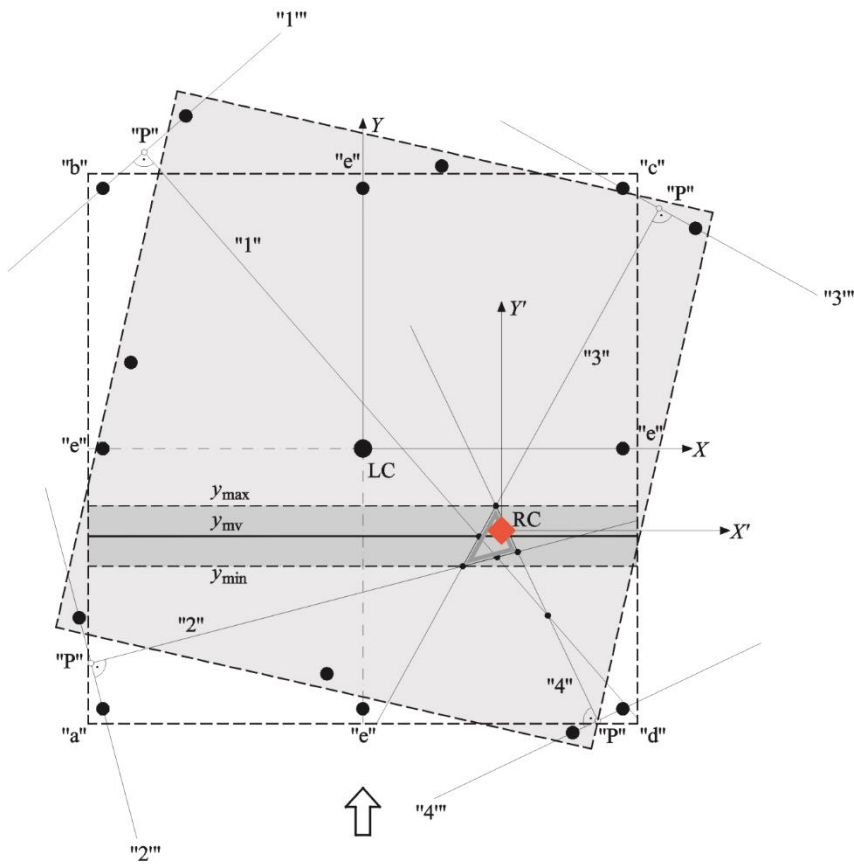$$a_1 = \frac{y - \, ^R y_{cal}}{x - \, ^R x_{cal}} \tag{5.52}$$
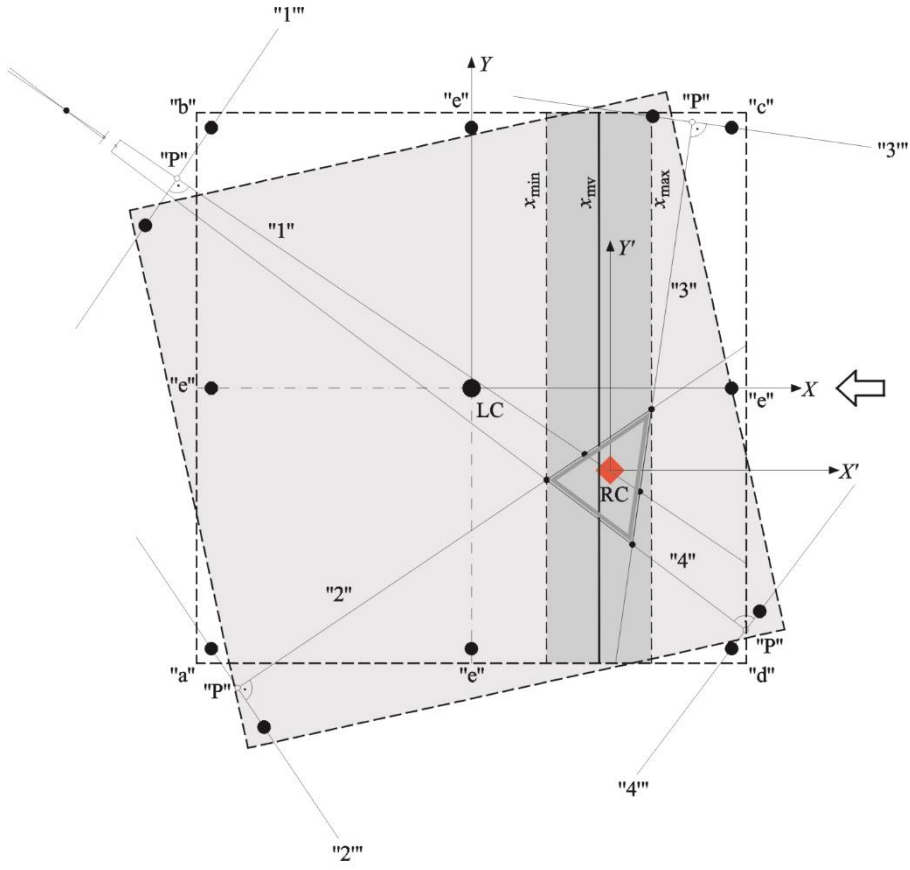
Fig. 5.24 Construction of lines used to determine the location of the center of rotation: a) when the load is applied in the direction of the X axis, b) when the load is applied in the direction of the Y axis

The intercept can be calculated according to the relation (5.53):

$$b_1 = {}^R y_{cal} - a_1 \, {}^R x_{cal} \tag{5.53}$$

Then, it is possible to determine the coordinates of the auxiliary point "P" located in the middle of the segment connecting the points before and after the rotation by equations (5.54) and (5.55):

$$x_p = \frac{1}{2}\left(x + {}^R x_{cal}\right) \tag{5.54}$$

$$y_p = \frac{1}{2}\left(y + {}^R y_{cal}\right) \tag{5.55}$$

Perpendicular lines ${}^P y = {}^P a_1 x + {}^P b_1$ (straight lines "1", "2", "3", "4" in Fig. 5.24a are constructed through this point to straight lines connecting points in the building corner before and after rotation. The slopes of the lines are equal to (5.56):

$$^P a_1 = -\frac{1}{a_1} \tag{5.56}$$

The intercepts are (5.57):

$$^P b_1 = y_p - {}^P a_1 \, {}^P x \tag{5.57}$$

A straight line from each corner can be drawn perpendicular to a line connecting the corner coordinates before and after the building rotation. It is enough to solve the system of equations of two straight lines formed from adjacent corners to determine the x_{RC} and y_{RC} coordinates. It is much more advantageous to solve all combinations occurring in individual corners. As a result, this gives $n = 6$ systems of equations to be solved:

- the straight line "1" – the straight line "2",
- the straight line "1" – the straight line "3",
- the straight line "1" – the straight line "4",
- the straight line "2" – the straight line "3",
- the straight line "2" – the straight line "4",
- the straight line "3" – the straight line "4".

From each of the systems of the equation, the coordinates $x_{RC,i}$ and $y_{RC,i}$ are obtained. The calculation results are the maximum, minimum, mean and median values. All values that do not make physical sense and significantly deviate from the others, confirmed by the Grubbs statistical test, should be omitted from the calculation. This approach allows determining the interval in which the coordinates occur with equal probabilities (rectangular distribution). Outlier analysis can be omitted when a robust approach is used, and then the median of the results should be sought. The same procedure is followed when the load acts in the direction parallel to the Y-axis. The angle of inclination of the straight line, corresponding to the angle of rotation, for the corners "b" and "c" (when the load acts in the direction of the Y-axis) is equal (5.58):

$$\alpha_{y,cal} = \operatorname{atan}\left(\frac{{}^F y_{"b"} - {}^F y_{"c"}}{{}^F x_{"b"} - {}^F x_{"c"}}\right) \tag{5.58}$$

The approximate translation is determined from the displacement of the point "e" located at the intersection of the wall axis and the load direction. The approximate displacement after the transformation of the coordinate system is (5.59):

$$\Delta T_{y,obs} = y - {}^F y \cos \alpha_{y,cal} \tag{5.59}$$

Then determine the coordinates of the points (corners) in the LC-X-Y alignment caused by rotation only, according to the following relationships (5.60) and (5.61):

$$^R x_{cal} = {}^F x \tag{5.60}$$

$$^R y_{cal} = {}^F y - \Delta T_{y,obs} \tag{5.61}$$

At each corner, straight lines are drawn between the points before and after the deformation (lines "1", "2", "3", and "4" in Fig. 5.24b). The constants in the equations of the straight lines are calculated according to (5.52) and (5.53). Then, an auxiliary point "P" is introduced. That point is located in the middle of the segment between the corners before and after the deformation. The point coordinates are determined using formulas (5.54) and (5.55). The constants of straight lines passing through the point "P" (straight lines "1", "2", "3", "4" in Fig. 5.24b) perpendicular to the lines connecting the corners before and with the deformation are calculated according to equation 5.56 and 5.57. Similarly to the action of the load in the X direction, it is possible to build $n = 6$

130

systems of equations and determine the six coordinates $x_{RC,i}$ and $y_{RC,i}$. The result of the calculation is the minimum, maximum and mean values.

If the rotation of the building for a load direction does not occur or is negligibly small, then the x_{RC} and y_{RC} coordinates have infinitely large values. Otherwise, when the rotation has a finite value and the translation is negligibly small, the exact position of the center of torsion is obtained. In the general case, there will be both a finite rotation and a finite translation. Then the coordinates of the center of torsion are obtained, which are between the minimum and maximum values. Considering that the value adopted for calculations in an analysed direction is not true and affects the calculated coordinate associated with such a direction, as a result of calculations, a coordinate not related to a given direction is obtained as credible. When the load is parallel to the X-axis, the plausible value is $x_{RC,cal}$, and when the load is parallel to the Y-axis, the plausible value is $y_{RC,cal}$.

After considering the confidence intervals of both coordinates, a rectangular area is obtained. The probability of the location of the center of torsion in such an area is identical (after standardization of the coordinates). If a robust approach is used, the RC coordinates are uniquely specified.

The results with greater error (the intersection of the lines is far beyond the slab contour, and each measurement inaccuracy generates greater uncertainty of the results) can be obtained by specifying the coordinates of the torsion center, ignoring the shift effect. Then the coordinates related to the direction of the load (parallel to the X-axis ($x_{RC,cal}$) and the Y-axis ($y_{RC,cal}$,) are calculated assuming the values $\Delta T_{x,obs} = 0$ and $\Delta T_{y,obs} = 0$. After determining the coordinates of the rotation center, it is possible to calculate the exact translation of the building under the action of the load in the direction of the X and Y axes. When the load is applied in the X-axis direction, the coordinates in the RC-X'-Y' coordinate system are first calculated from the following dependencies (5.62) and (5.63):

$$x_{obs}' = x - x_{RC,cal} \tag{5.62}$$

$$y_{obs}' = y - y_{RC,cal} \tag{5.63}$$

Then transform the points to the position before loading according to the relationship (5.64) and (5.65):

$$^{R}x'_{obs} = x'_{obs} \cos \alpha - y'_{obs} \sin \alpha \tag{5.64}$$

$$^{R}y'_{obs} = x'_{obs} \sin \alpha + y'_{obs} \cos \alpha \tag{5.65}$$

The next step is to express the coordinates in the LC-X-Y coordinate system according to the formula (5.66) and (5.67):

$$^{R}x_{obs} = {}^{R}x'_{obs} + x_{RC,cal} \tag{5.66}$$

$$^{R}y_{obs} = {}^{R}y'_{obs} + y_{RC,cal} \tag{5.67}$$

Finally, at each point (corner) the displacement value is calculated according to the relation (5.68):

$$\Delta T_{x,cal} = {}^{F}x - {}^{R}x_{obs} \tag{5.68}$$

The result of the calculation is the mean and standard deviation (5.69) and (5.70):

$$\Delta T_{x,cal} = \frac{1}{n} \sum_{i=1}^{6} \Delta T_{x,i} \tag{5.69}$$

$$s_{x} = \frac{1}{n-1} \sum_{i=1}^{6} \left(\Delta T_{x,i} - \Delta T_{x,cal}\right)^{2} \tag{5.70}$$

The same procedure is followed in the direction of the load in the Y-axis direction. Coordinates are transformed according to formulas (5.62) – (5.67). The value of the displacement at each corner is determined according to (5.71):

$$\Delta T_{y,cal} = {}^{F}y - {}^{R}y_{obs} \tag{5.71}$$

The result of the calculation is the mean and standard deviation (5.72) and (5.73):

$$\Delta T_{y,cal} = \frac{1}{n} \sum_{i=1}^{6} \Delta T_{y,i} \tag{5.72}$$

$$s_{y} = \frac{1}{n-1} \sum_{i=1}^{6} \left(\Delta T_{y,i} - \Delta T_{y,cal}\right)^{2} \tag{5.73}$$

6. CRACK MORPHOLOGY

The crack morphology analysis was divided into two stages. The first part concerns recognising the order in which successive cracks appear during the test (crack propagation) – section 6.1. The results from the DIC system and the macroscopic assessment of the tested buildings were collected in the second stage. The model damage was summarized as a crack pattern in section 6.2.

6.1. Digital image correlation results

The results from the DIC system enclose seven building models (no results for model MB-AAC-010/3). The results were presented as deformation maps ε_1 (principal strain), and the scales were adjusted to obtain the best crack propagation map.

6.1.1. Results for MB-AAC-010/1 model

Figure 6.1 presents the crack propagation maps for the MB-AAC-010/1 model. Stiffening wall A was analyzed. The order of damage was as follows:

- horizontal crack in the corner of the door opening and a small stepped crack in the upper left part of the wall,
- increasing the crack size within the door opening and progressing step cracking of the wall,
- the horizontal crack from the top edge of the wall connects to the crack at the opening,
- a step crack divides the vertical pier into two parts, and new step cracks are formed.
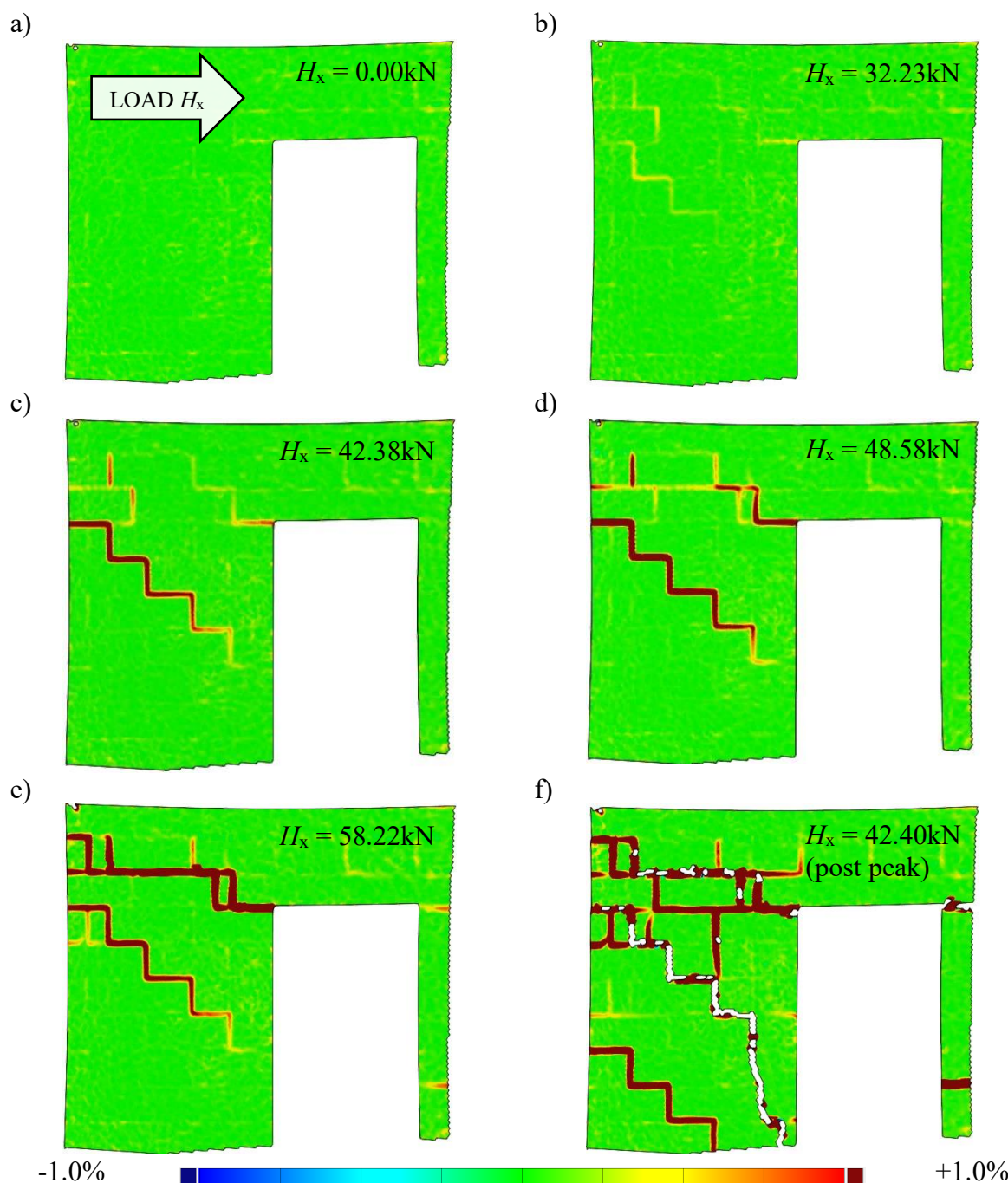
Fig. 6.1 Crack propagation of Wall A – model MB-AAC-010/1: a) analyzed area, b) crack pattern at H_x = 32.23 kN, c) crack pattern at H_x = 42.38 kN, d) crack pattern at H_x = 48.58 kN, e) crack pattern at H_x = 58.22kN, f) crack pattern at H_x = 42.40kN (post-peak)

Figures 6.2, 6.3 and 6.4 present the horizontal, vertical and out-of-plane deformation of stiffening wall A. The sliding failure occurs in the left vertical pier. The maximum horizontal deformation equals about 23.0 mm, and the vertical displacement is about 4.0 mm. The out-of-plane deformation indicates the rotation of the building.
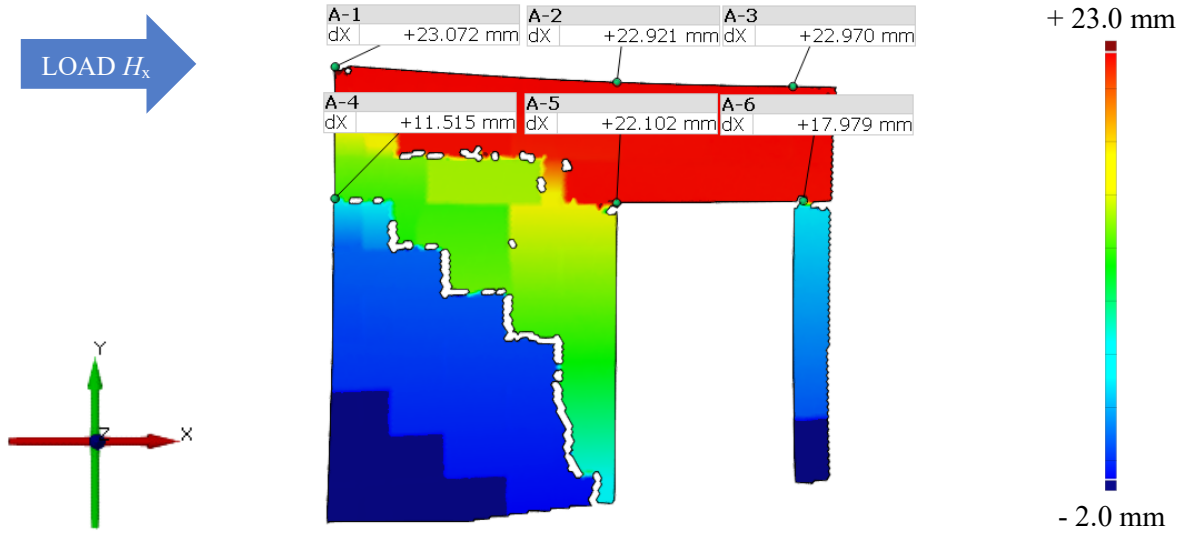
Fig. 6.2 Post peak in-plane horizontal deformation d_x with force $H_x = 42.40$ kN for Wall A
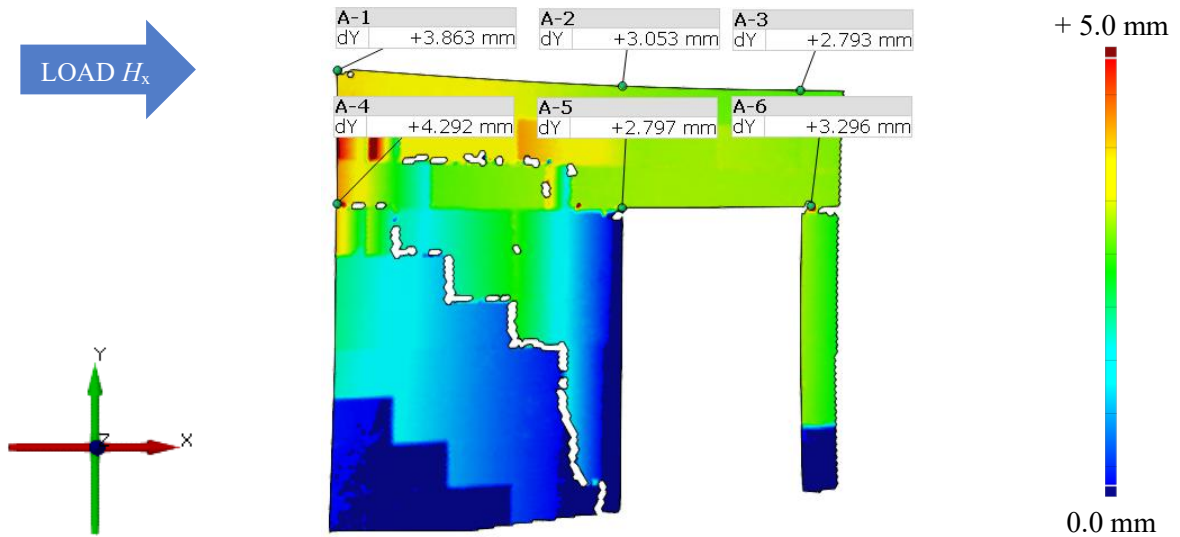
Fig. 6.3 Post peak in-plane vertical deformation d_y with force $H_x = 42.40$ kN for Wall A
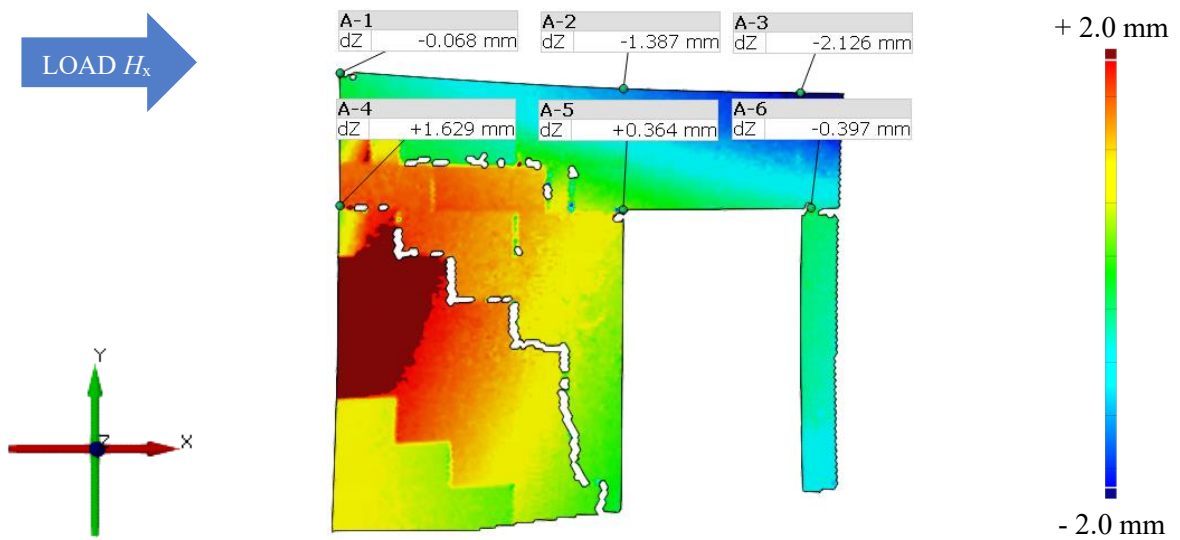
Fig. 6.4 Post peak in-plane out-of-plane deformation d_z with force $H_x = 42.40$ kN for Wall A

6.1.2. Results for MB-AAC-010/2 model

Figure 6.5 shows the crack propagation maps for the MB-AAC-010/2 model. Stiffening wall A was analyzed. The order of damage was as follows:

- a stepped crack formed in the corner of a door opening,
- increasing the crack size,
- formation of a stepped crack in the lower part of the wall,
- formation of new step cracks in the part of the wall from the side of the applied horizontal load,
- increasing the opening of the existing cracks,
- dividing the vertical pier into two parts.
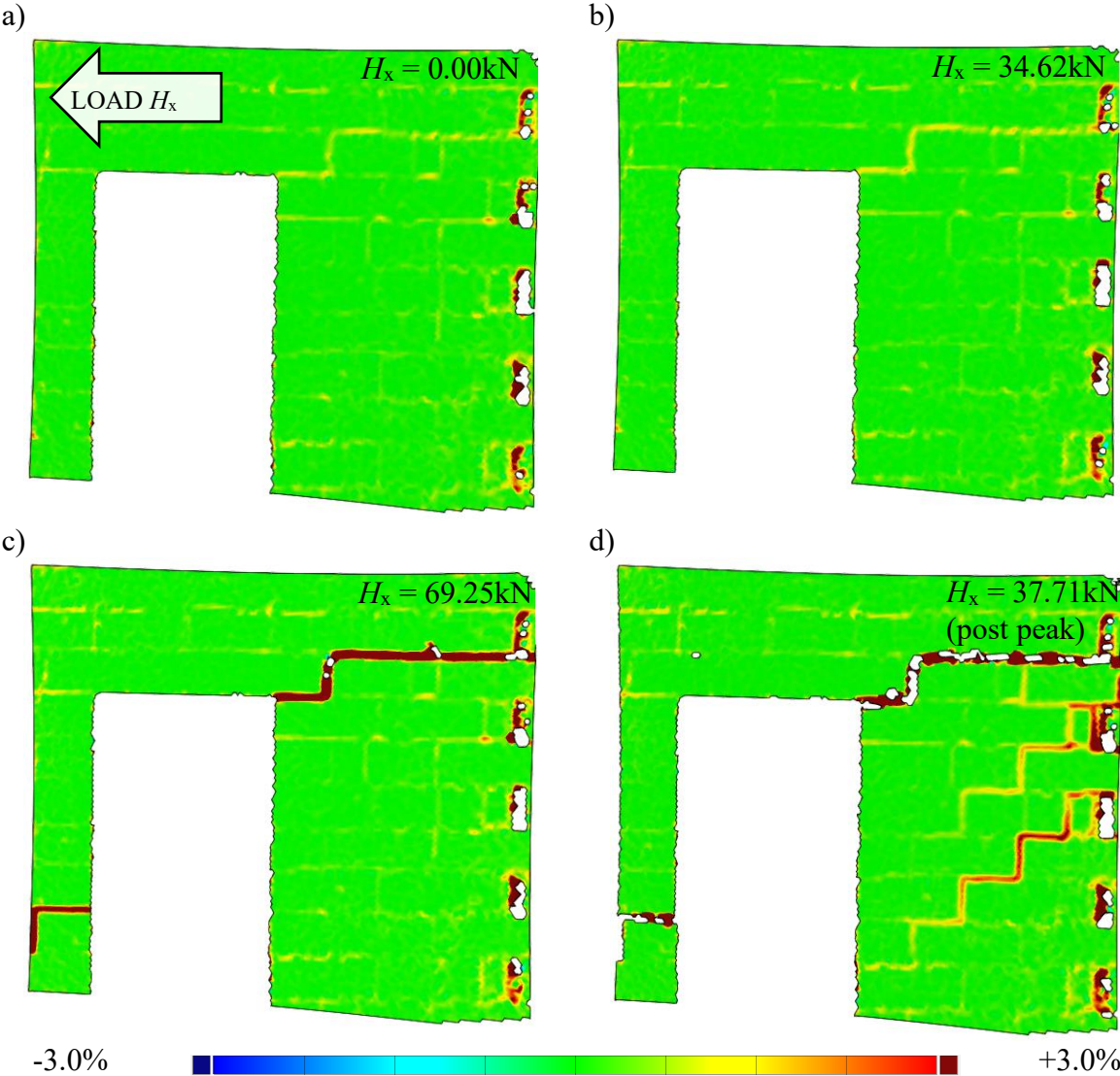
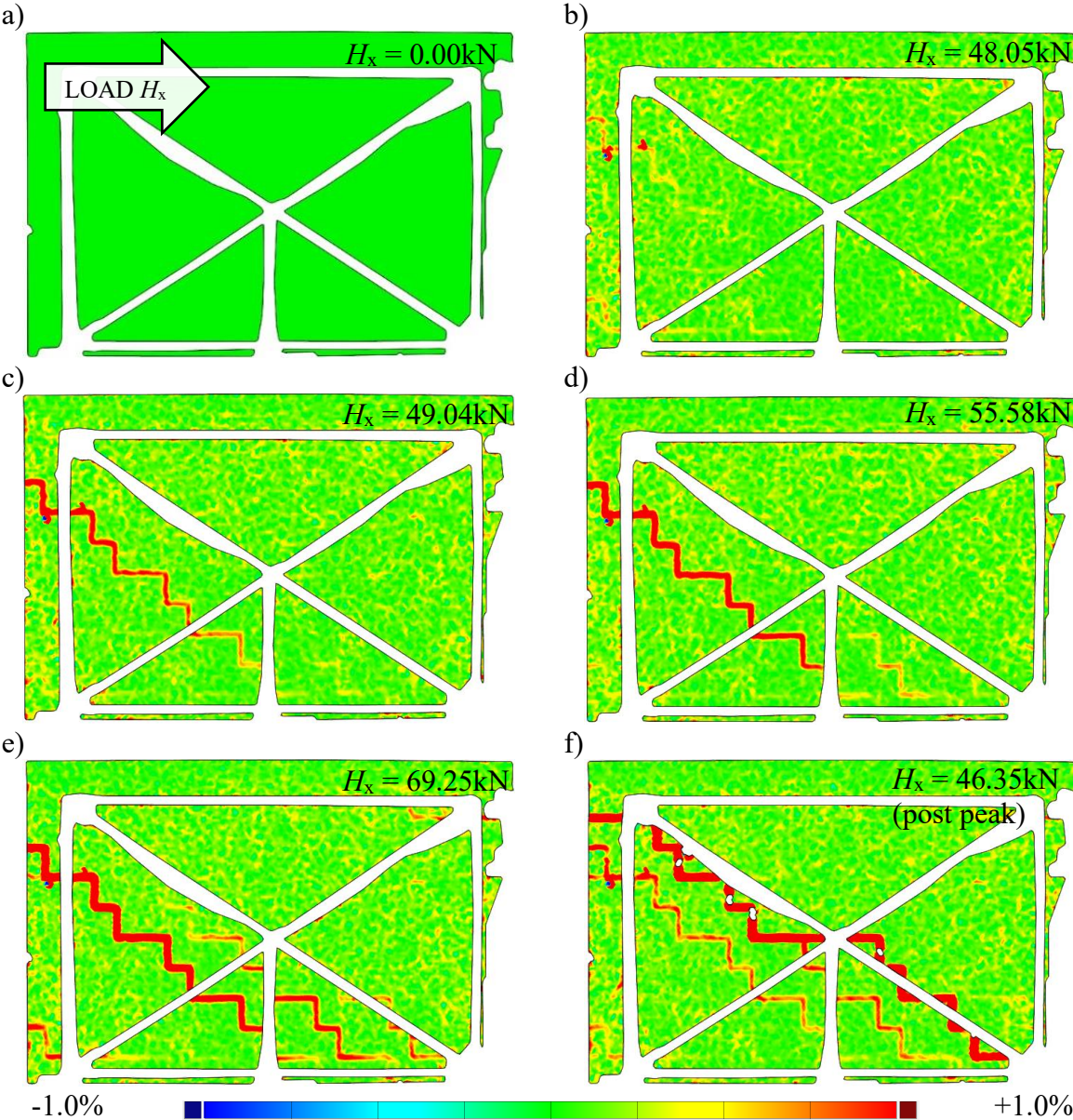Fig. 6.5 Crack propagation of Wall A - model MB-AAC-010/2: a) analyzed area, b) crack pattern at H_x = 34.62 kN, c) crack pattern at H_x = 69.25 kN, d) crack pattern at H_x = 37.71 kN

A similar DIC analysis was done for stiffening wall B; the results are presented in Fig. 6.6. As a wall without openings, the initial phase was not observed. The order of damage was:

- the first crack in the upper part of the wall from the side of the applied horizontal load,
- step cracks gradually widening from the top to the bottom of the wall,
- then new step cracks parallel to the existing one in the lower part of the wall,
- increasing the opening of the existing cracks,
- separating the wall into two parts with a diagonal step crack.

Fig. 6.6 Crack propagation of Wall B – model MB-AAC-010/2: a) analyzed area, b) crack pattern at H_x = 48.05 kN, c) crack pattern at H_x = 49.04 kN, d) crack pattern at H_x = 55.58 kN, e) crack pattern at H_x = 69.25kN, f) crack pattern at H_x = 46.35 kN (post-peak)

Figures 6.7 and 6.8 show the horizontal and vertical deformation at the post-peak phase of stiffening wall B. The measured horizontal displacement is about 19.6 mm, and the vertical one is equal to over 2.5 mm. A stepped crack divides the wall into two parts, and a wall fragment above the diagonal crack is prone to lifting. The diagonal crack is formed from the top edge of the wall, where the load is applied and proceeds diagonally to the wall base.

Figures 5.9 – 5.11 shows the displacement map for stiffening wall A at the same load level (the post-peak phase). The horizontal crack runs from the corner of the door opening to the edge of the wall. The values of horizontal displacements are greater than those of parallel wall B and are a maximum of 19.8 mm. The out-of-plane displacements are about 1.0 mm.
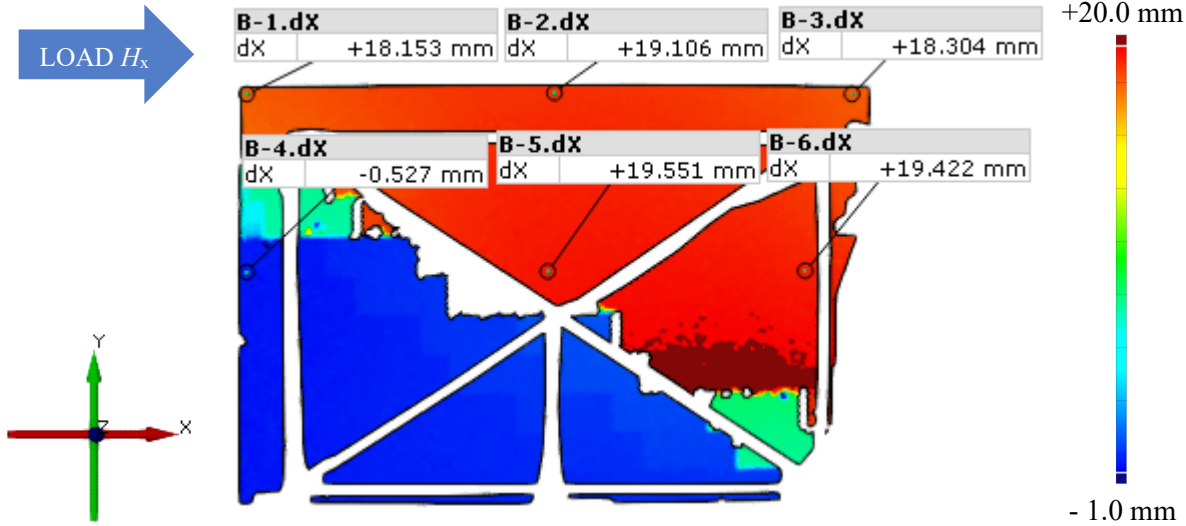

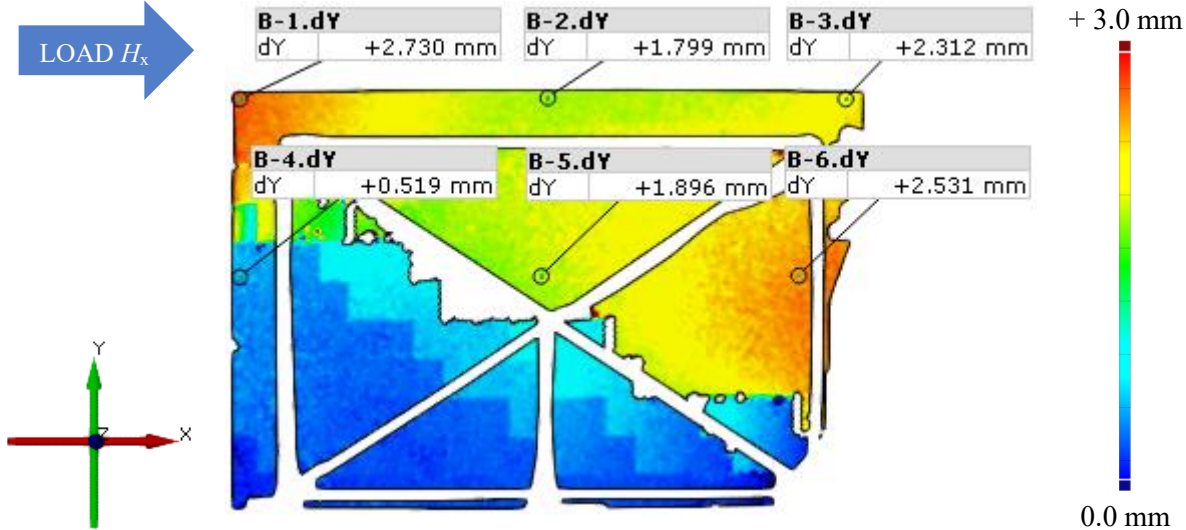Fig. 6.7 Post peak in-plane horizontal deformation d_x with force $H_x = 37.71$ kN for Wall B

Fig. 6.8 Post peak in-plane vertical deformation d_y with force $H_x = 37.71$ kN for Wall B
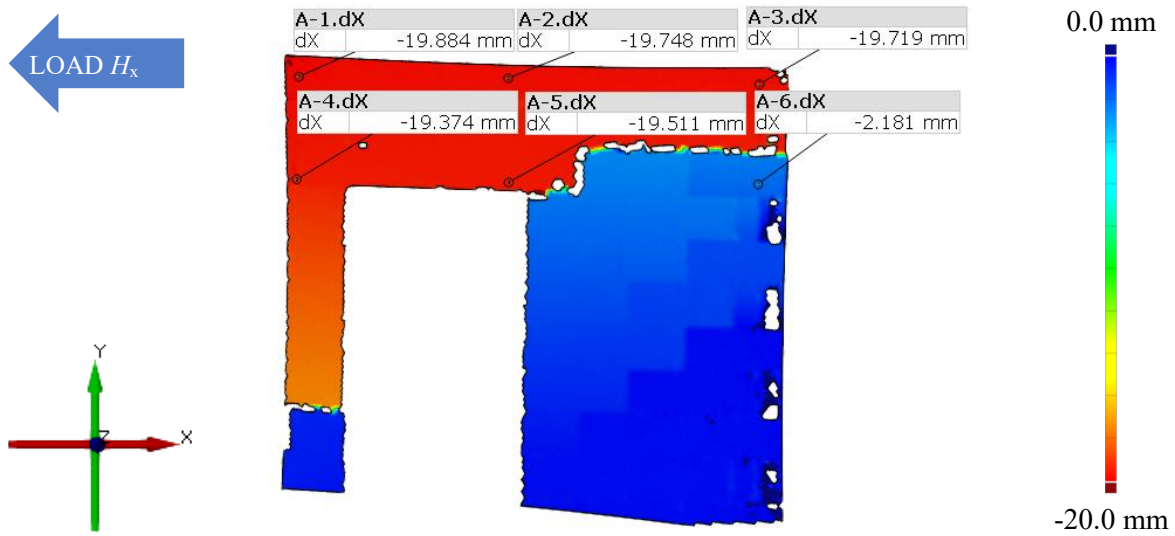
Fig. 6.9 Post peak in-plane horizontal deformation d_x with force $H_x = 37.71$ kN for Wall A
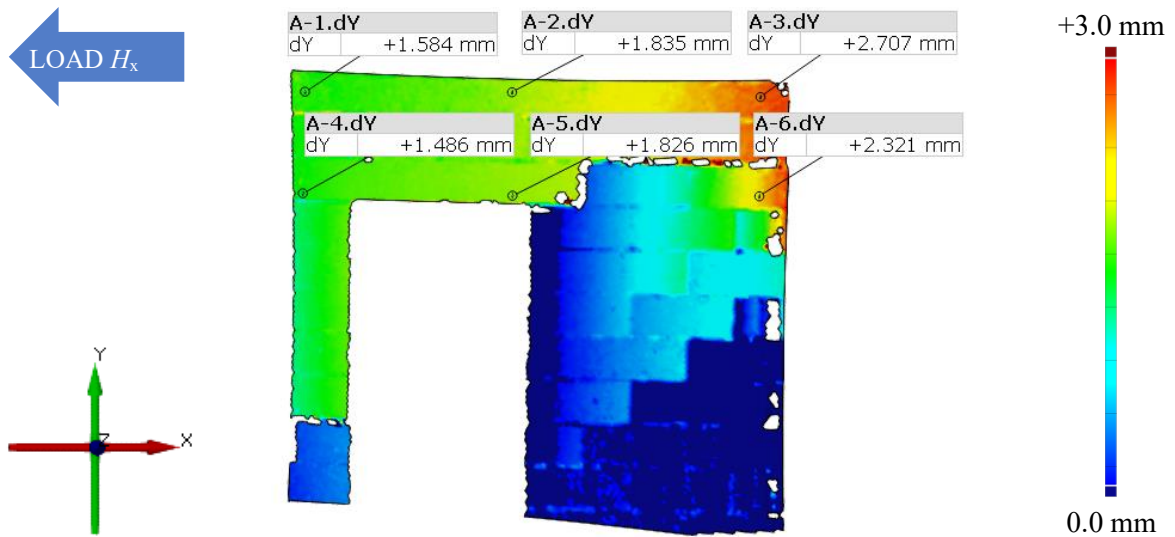

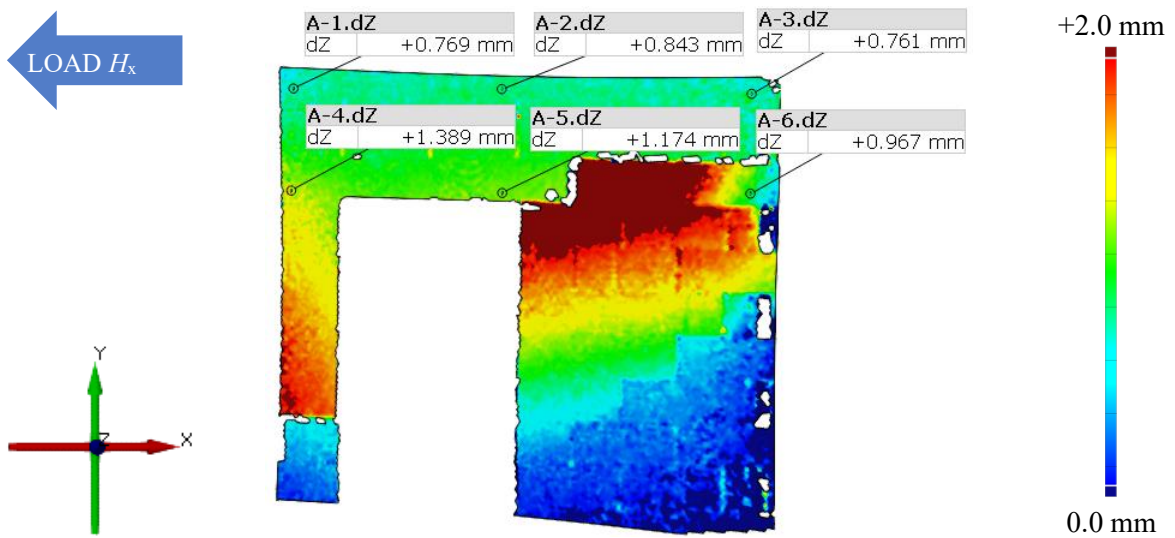Fig. 6.10 Post peak in-plane vertical deformation d_y with force $H_x = 37.71$ kN for Wall A

Fig. 6.11 Post peak in-plane out-of-plane deformation d_z with force $H_x = 37.71$ kN for Wall A

139

6.1.3. Results for MB-AAC-010/4 model

Figure 6.12 shows the crack propagation maps for the MB-AAC-010/4 model. Deformation maps of stiffening wall A were presented in Fig. 6.13 – 6.15.
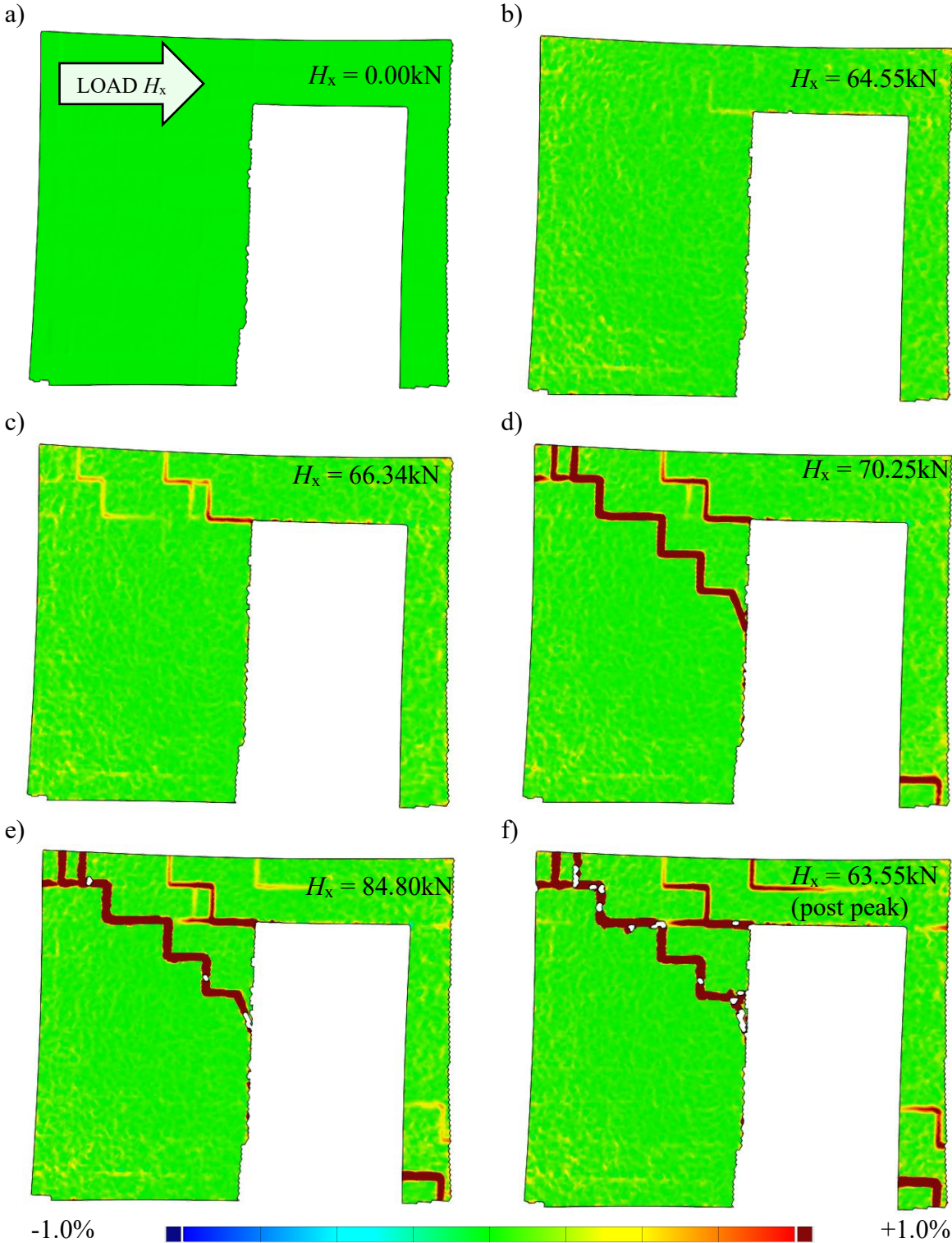

Fig. 6.12 Crack propagation of Wall A – model MB-AAC-010/4: a) analyzed area, b) crack pattern at $H_x = 64.55$ kN, c) crack pattern at $H_x = 66.34$ kN, d) crack pattern at $H_x = 70.25$ kN, e) crack pattern at $H_x = 84.80$kN, f) crack pattern at $H_x = 63.55$kN (post peak)
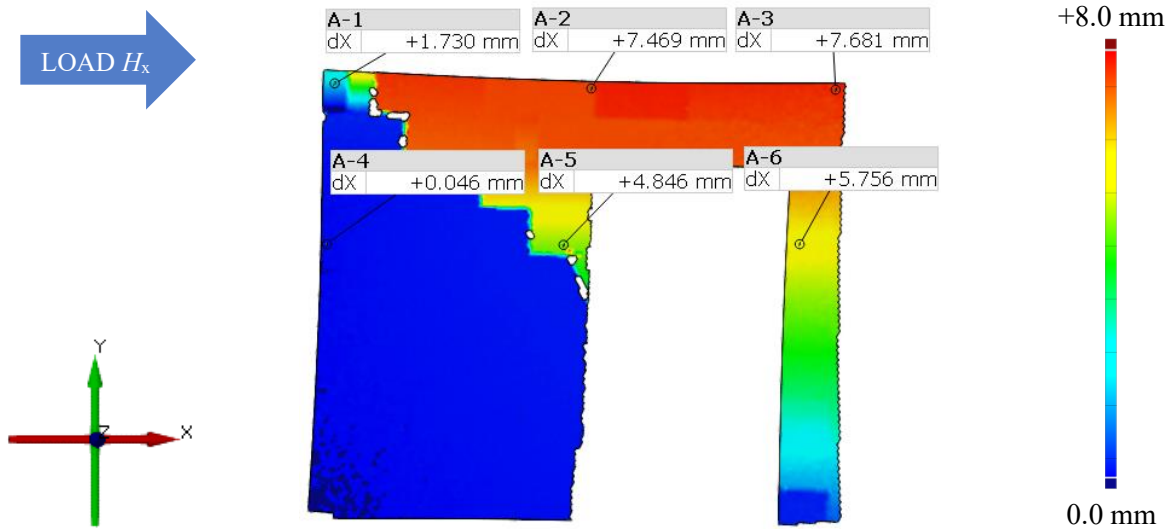
Fig. 6.13 Post peak in-plane horizontal deformation d_x with force $H_x = 63.55$ kN for Wall A
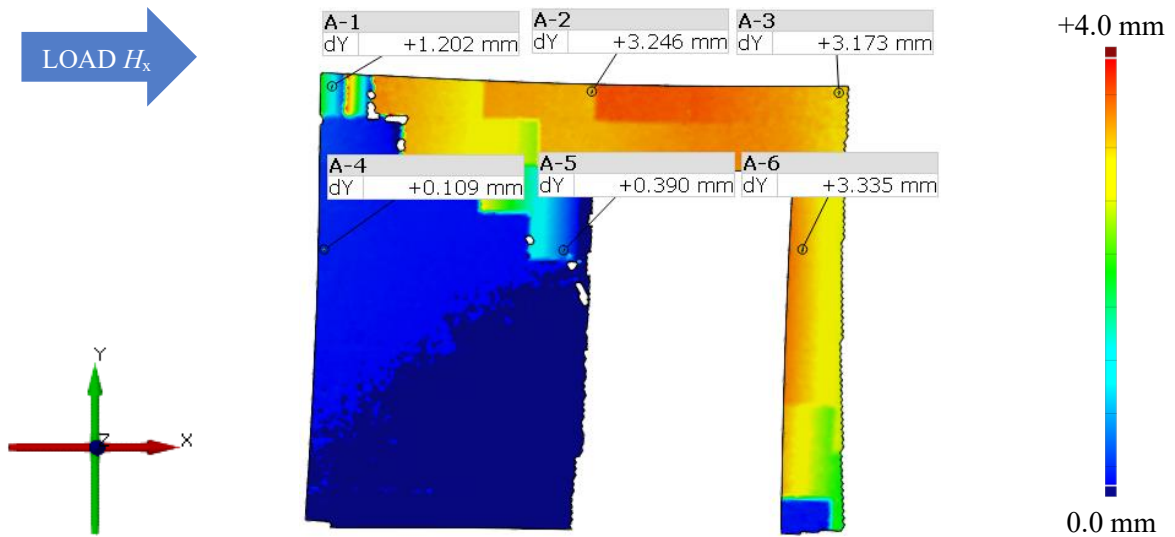

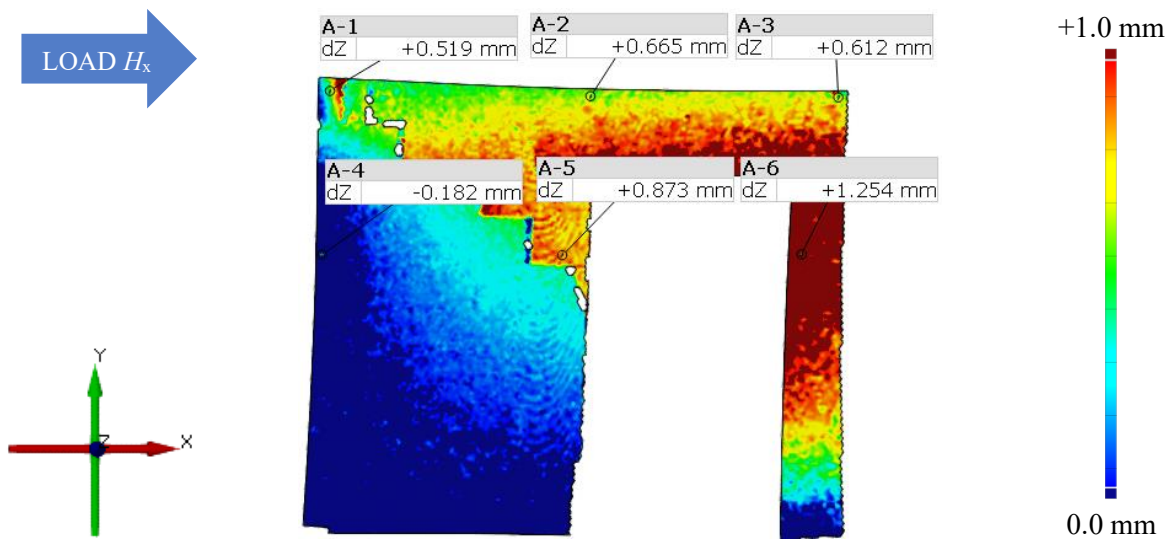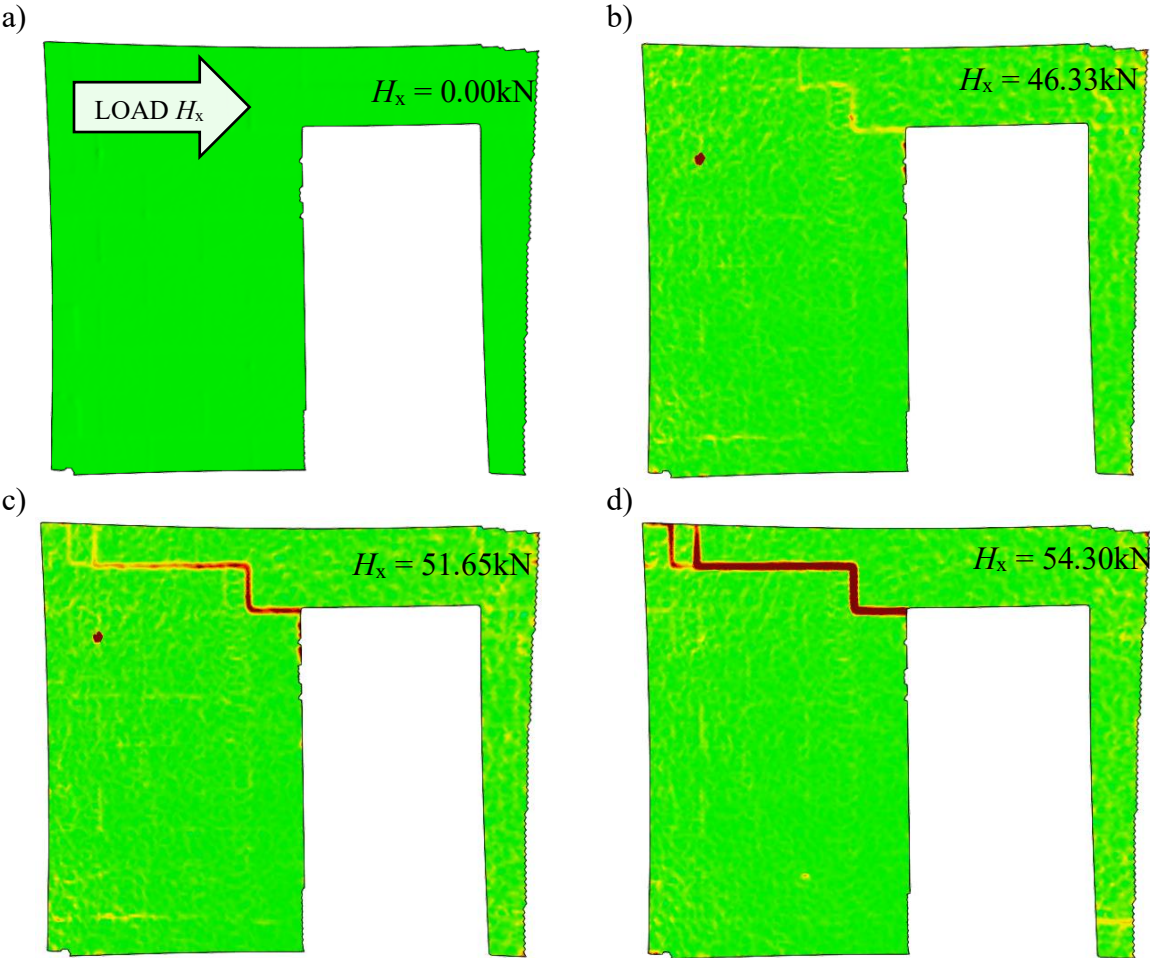Fig. 6.14 Post peak in-plane vertical deformation d_y with force $H_x = 63.55$ kN for Wall A

Fig. 6.15 Post peak in-plane out-of-plane deformation d_z with force $H_x = 63.55$ kN for Wall A

141

The crack morphology was similar to the previously analyzed walls. The first crack is located in the corner of the door opening. Then, with a slight increase in horizontal load - numerous step cracks appear. In the next stage, the size of the main step crack is increased. After exceeding the load capacity of the wall, there are no more new cracks. However, there are increasing displacements, and a sliding failure occurs. The maximum horizontal displacement was 7.7 mm, and the maximum vertical displacement was about 3.3 mm. The out-of-plane displacements were small and amounted to a maximum of 1.3 mm.

6.1.4. Results for MB-AAC-010/5 model

Figure 6.16 presents the crack propagation maps for stiffening wall A of the MB-AAC-010/5 model. The sequence of appearance of cracks in the wall with a door opening was identical to previous models, and the first crack occurred in the door opening corner. Figures 6.17 – 6.19 show maps of wall deformation at the nonlinear post-peak phase.

a)

LOAD H_x $H_x = 0.00\text{kN}$

b)

$H_x = 46.33\text{kN}$

c)

$H_x = 51.65\text{kN}$

d)

$H_x = 54.30\text{kN}$

Fig. 6.16 Crack propagation of Wall A – model MB-AAC-010/5: a) analyzed area, b) crack pattern at $H_x = 46.33$ kN, c) crack pattern at $H_x = 51.65$ kN, d) crack pattern at $H_x = 54.30$ kN, e) crack pattern at $H_x = 87.53$ kN, f) crack pattern at $H_x = 66.17$ kN (post-peak)
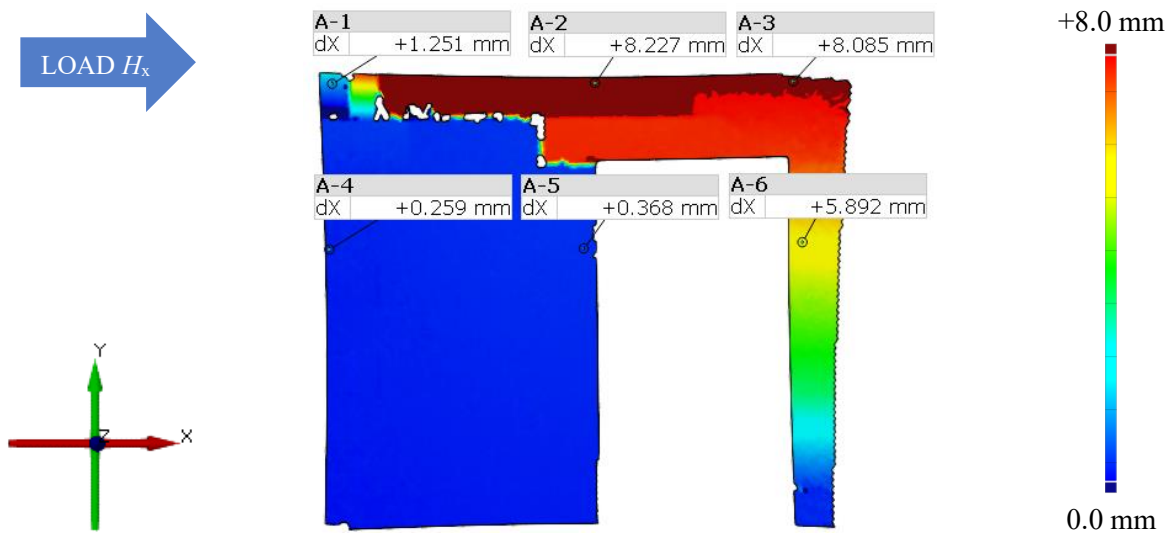
Fig. 6.17 Post peak in-plane horizontal deformation d_x with force $H_x = 66.17$ kN for Wall A
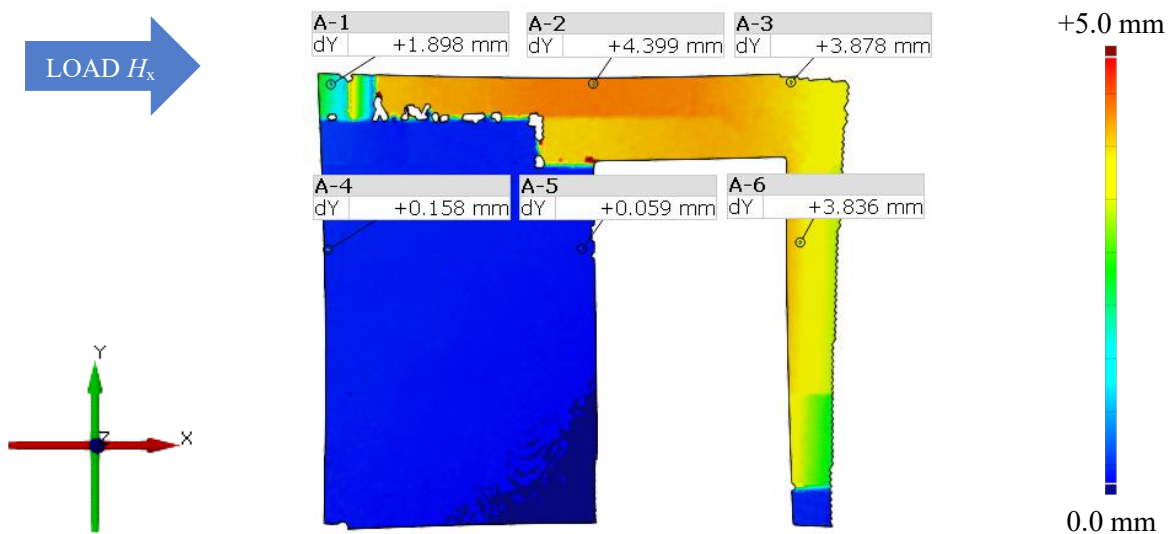
Fig. 6.18 Post peak in-plane vertical deformation d_y with force $H_x = 63.55$ kN for Wall A

143

Fig. 6.19 Post peak in-plane out-of-plane deformation d_z with force $H_x = 63.55$ kN for Wall A of MB-AAC-010/5 model

As in model MB-AAC-010/4, the horizontal displacements were small and reached a maximum of 8.2 mm. The corresponding maximum vertical displacement equals 4.4 mm, and the out-of-plane deformation does not over 1.0 mm.

6.1.5. Results for MB-AAC-010/6 model

The crack propagation maps for stiffening wall A of the MB-AAC-010/6 were presented in Fig. 6.20. As in other models, the first cracks appear within the window opening – the vertical crack below the opening and the horizontal one in a tensile corner. Then stepped cracks appeared on the left side of the wall from the side of the acting load. With increasing load, the cracks are connected and have a diagonal course. Finally, a diagonal step crack divides the wall into two parts.
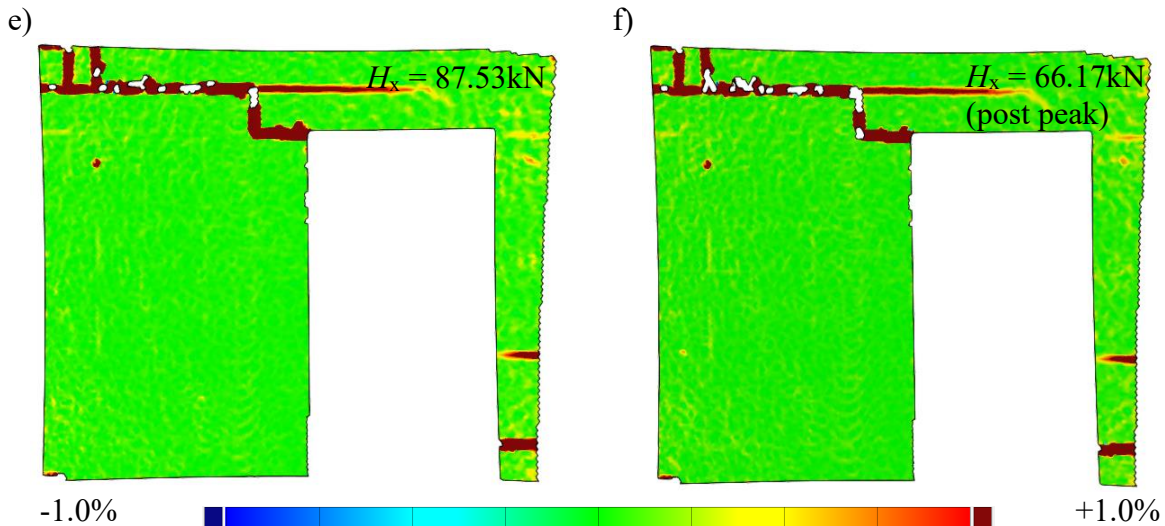
Fig. 6.20 Crack propagation of Wall A – model MB-AAC-010/6: a) analyzed area, b) crack pattern at $H_x = 46.28$ kN, c) crack pattern at $H_x = 56.60$ kN, d) crack pattern at $H_x = 57.25$ kN, e) crack pattern at $H_x = 74.53$kN, f) crack pattern at $H_x = 61.44$ kN (post-peak)

Figures 6.21 – 6.23 present the deformation maps of stiffening wall A at the post-peak phase.

Fig. 6.21 Post peak in-plane horizontal deformation d_x with force $H_x = 61.44$ kN for Wall A of MB-AAC-010/6 model

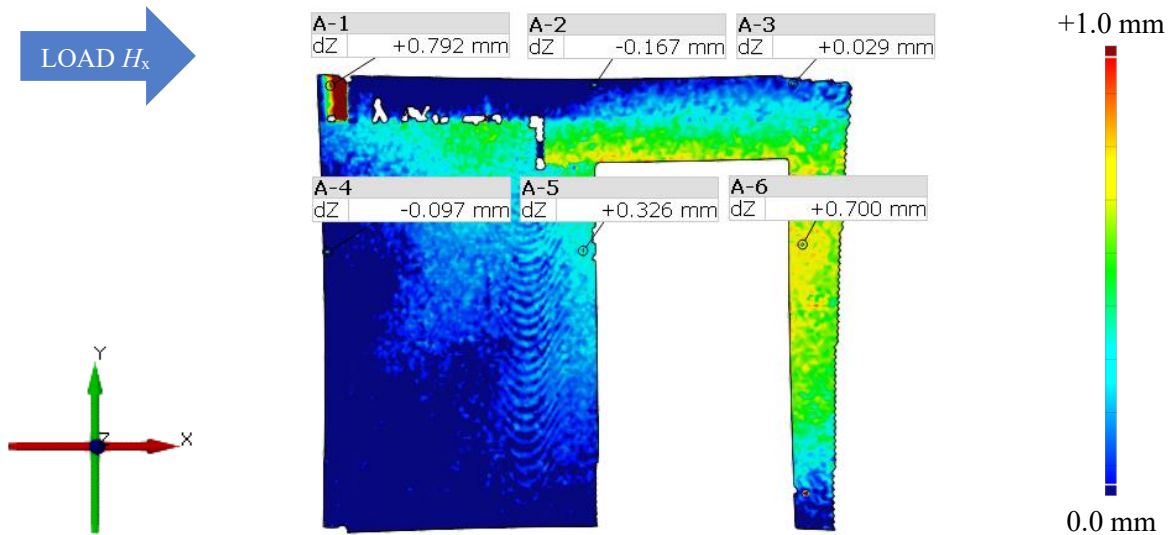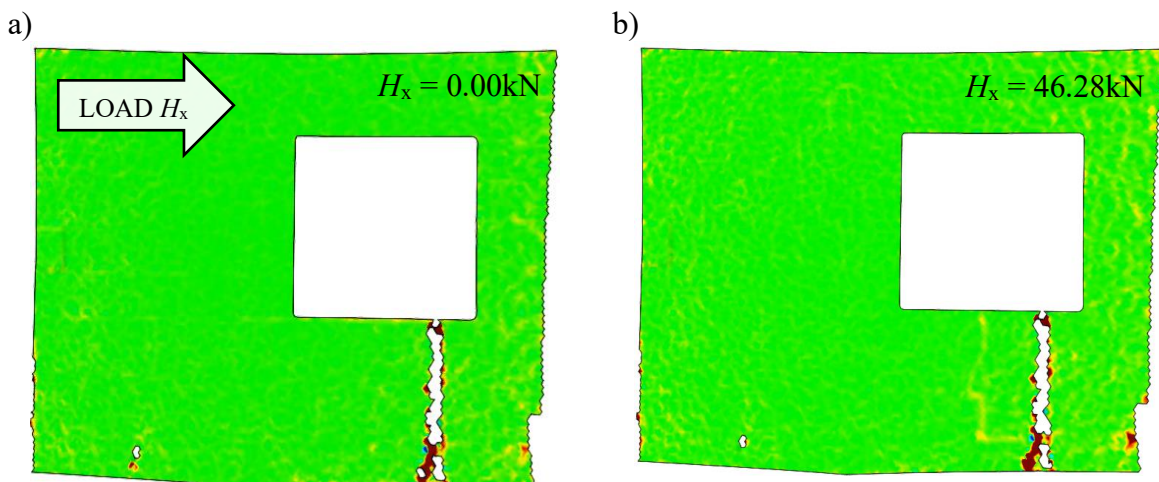Fig. 6.22 Post peak in-plane vertical deformation d_y with force $H_x = 61.44$ kN for Wall A of MB-AAC-010/6 model
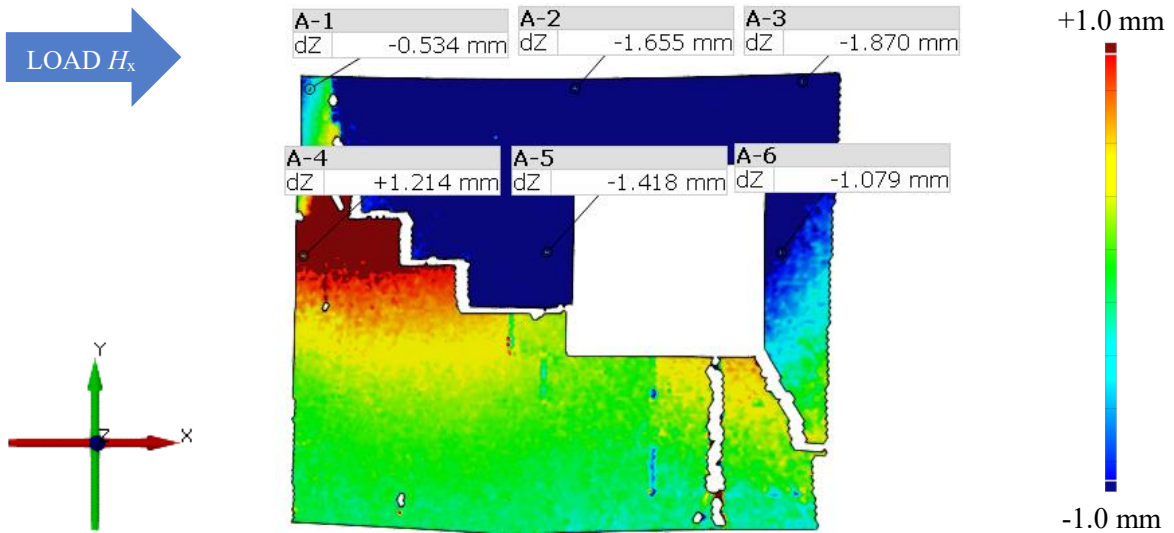
Fig. 6.23 Post peak in-plane out-of-plane deformation d_z with force $H_x = 61.44$ kN for Wall A of MB-AAC-010/6 model

The values of a maximum horizontal deformation are 36.9 mm. After dividing the wall with a diagonal crack, the part of the wall above the crack is horizontally displaced. The largest vertical displacement was measured in the corner of the wall from the side of the applied load – 5.0 mm, and the out-of-plane displacement reached almost 2.0 mm.

6.1.6. Results for MB-AAC-010/7 model

The damage propagation of wall A of the MB-AAC-010/7 is shown in Fig. 6.24. Similar to model MB-AAC-010/6, the first cracks appeared in the upper left corner of the window opening and the lower half of the opening. Successively, numerous stepped

146

cracks occur, which eventually run diagonally from the upper corner to the opposite lower corner. Figures 6.25 – 6.27 present the deformation maps. Significant out-of-plane displacements of almost 5.0 mm were recorded in the analysed model (Fig. 6.27).
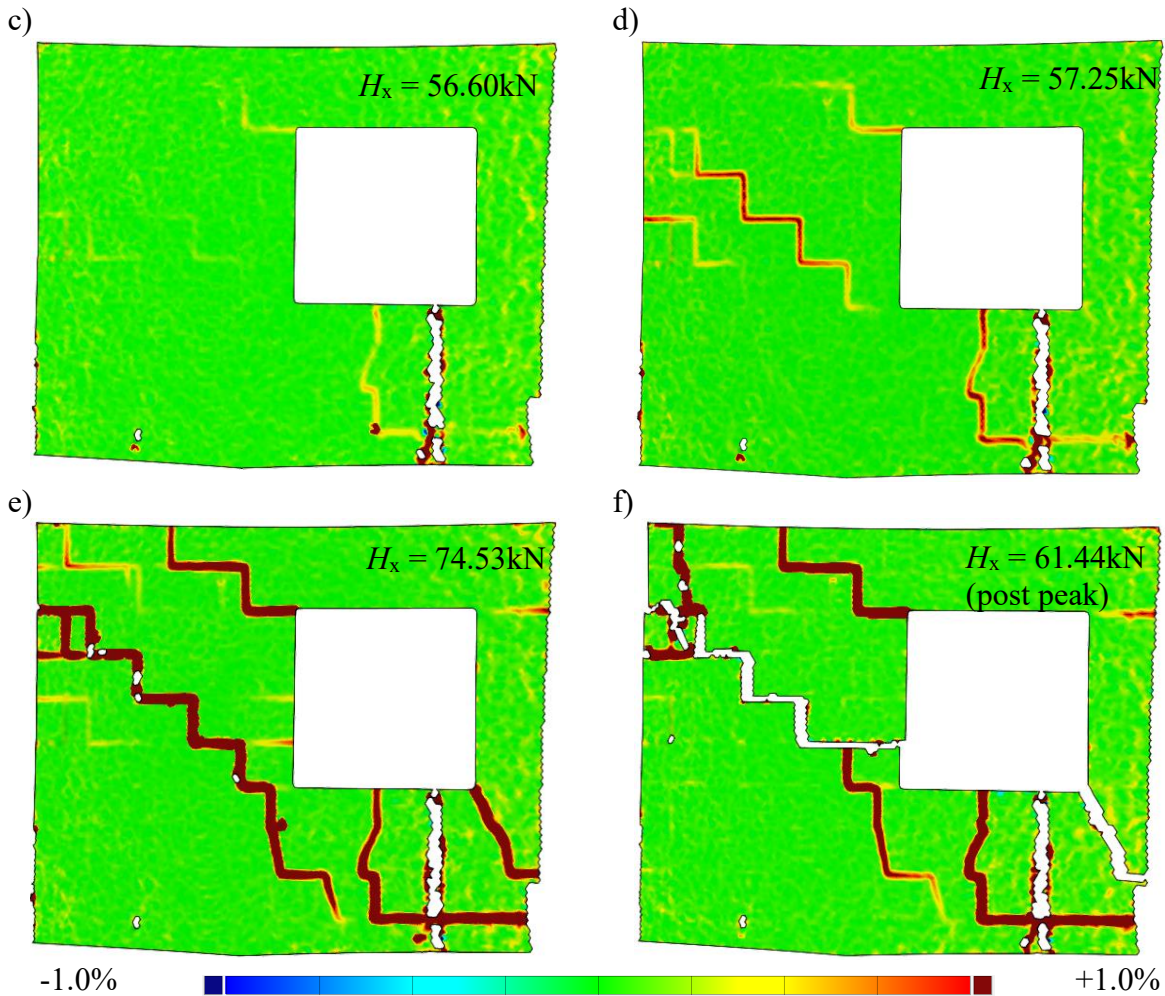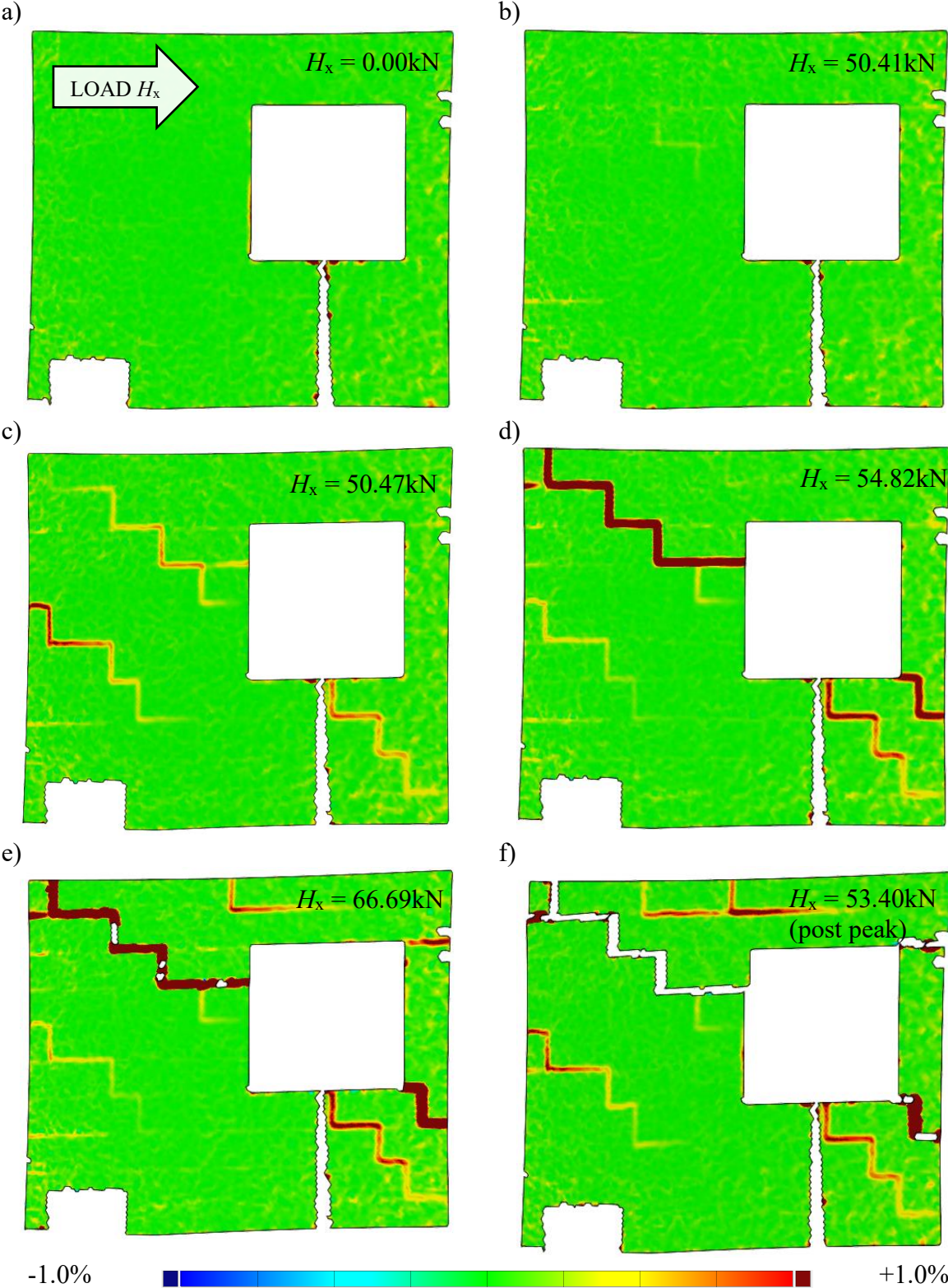

Fig. 6.24 Crack propagation of Wall A – model MB-AAC-010/7: a) analyzed area, b) crack pattern at H_x = 50.41 kN, c) crack pattern at H_x = 50.47 kN, d) crack pattern at H_x = 54.82 kN, e) crack pattern at H_x = 66.69 kN, f) crack pattern at H_x = 53.40 kN (post-peak)
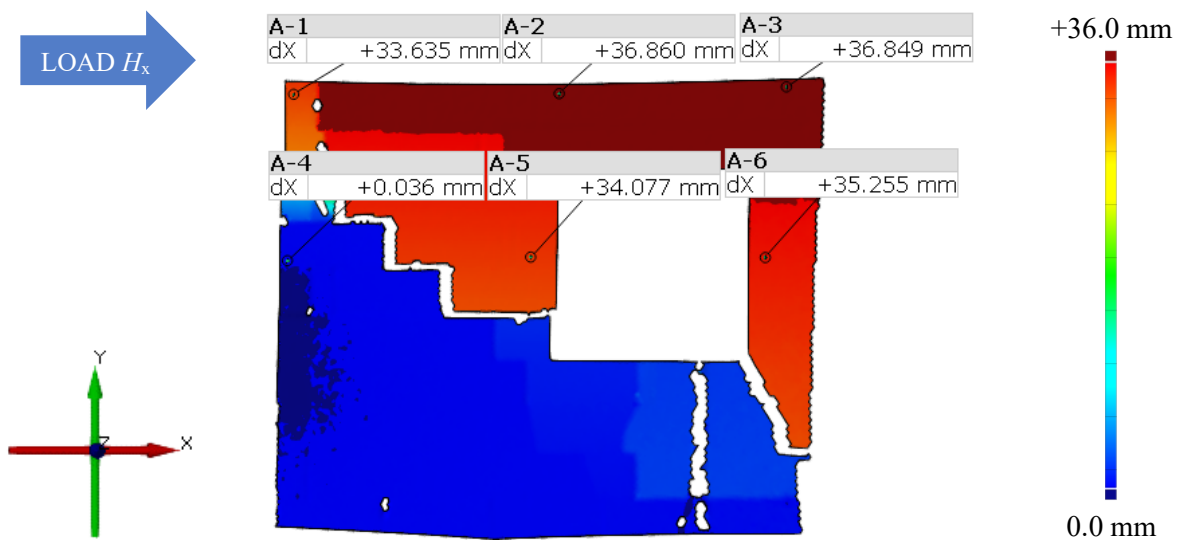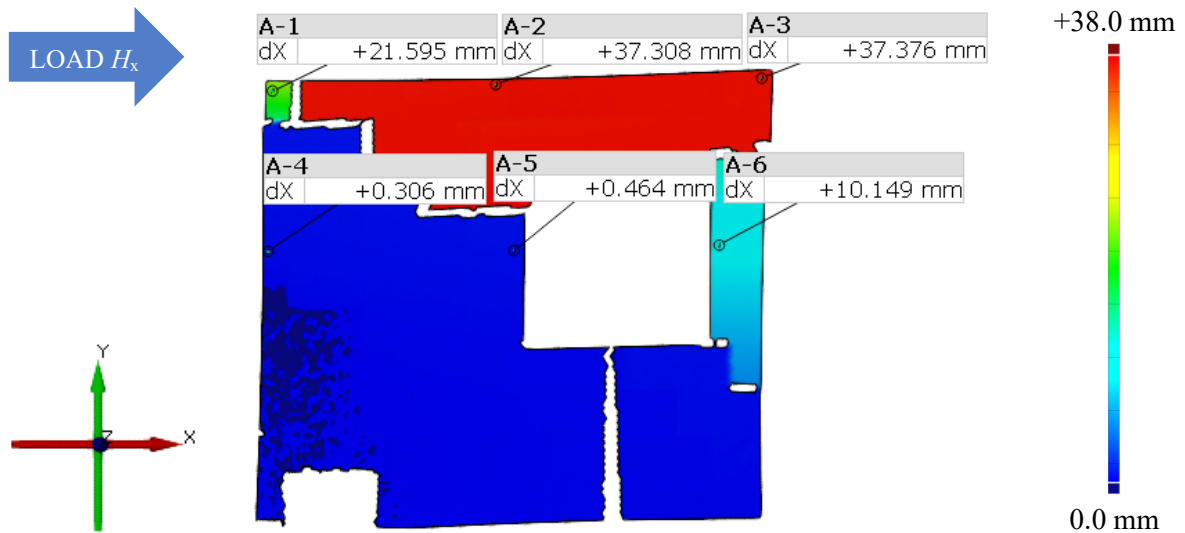
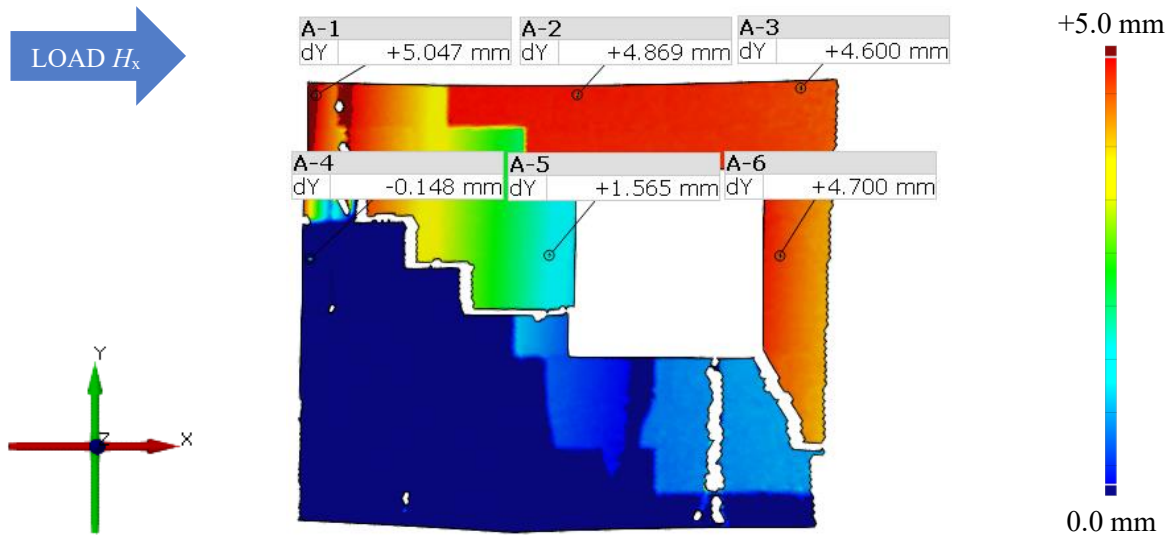Fig. 6.25 Post peak in-plane horizontal deformation d_x with force H_x = 53.40 kN for Wall A
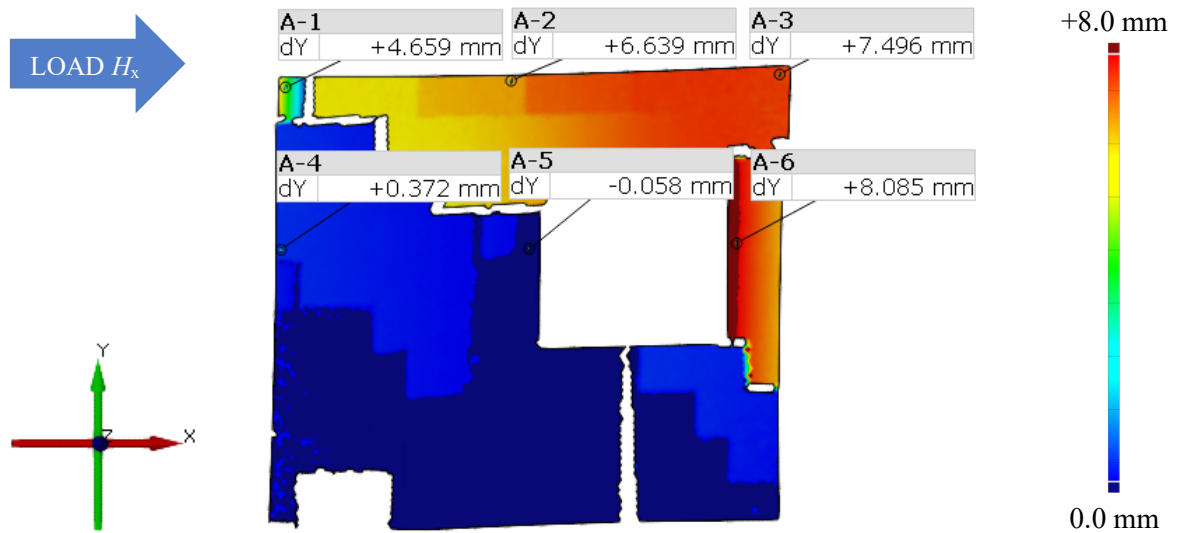
Fig. 6.26 Post peak in-plane vertical deformation d_y with force H_x = 53.40 kN for Wall A
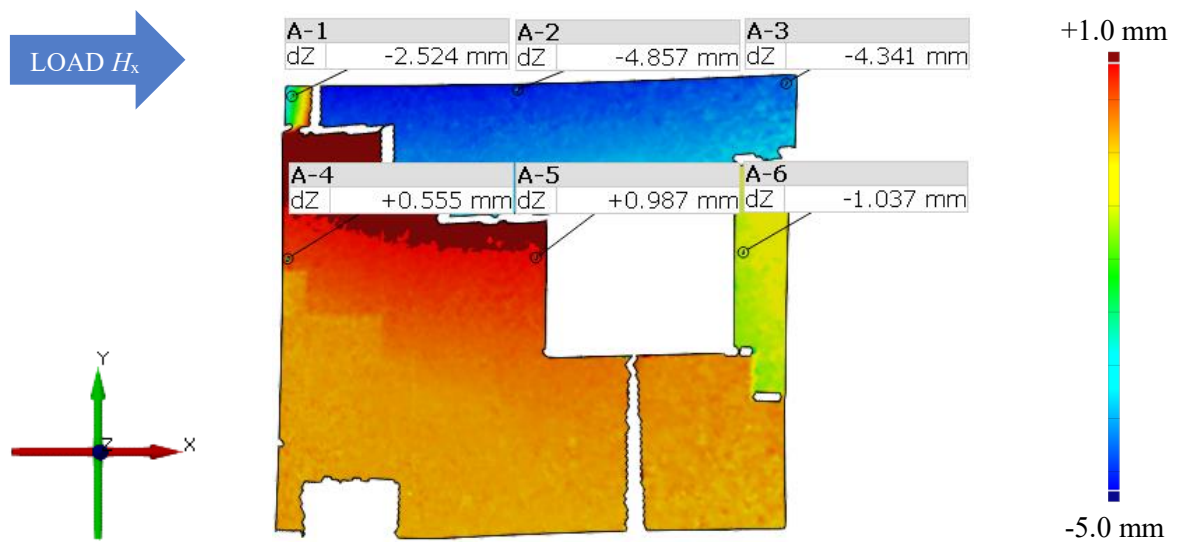
Fig. 6.27 Post peak in-plane out-of-plane deformation d_z with force H_x = 53.40 kN for Wall A

148

6.1.7. Results for MB-AAC-010/8 model

Stiffening wall A was observed in the reference model. The crack propagation is presented in Fig. 6.28, and the deformation maps in Fig. 6.29 – 6.31.
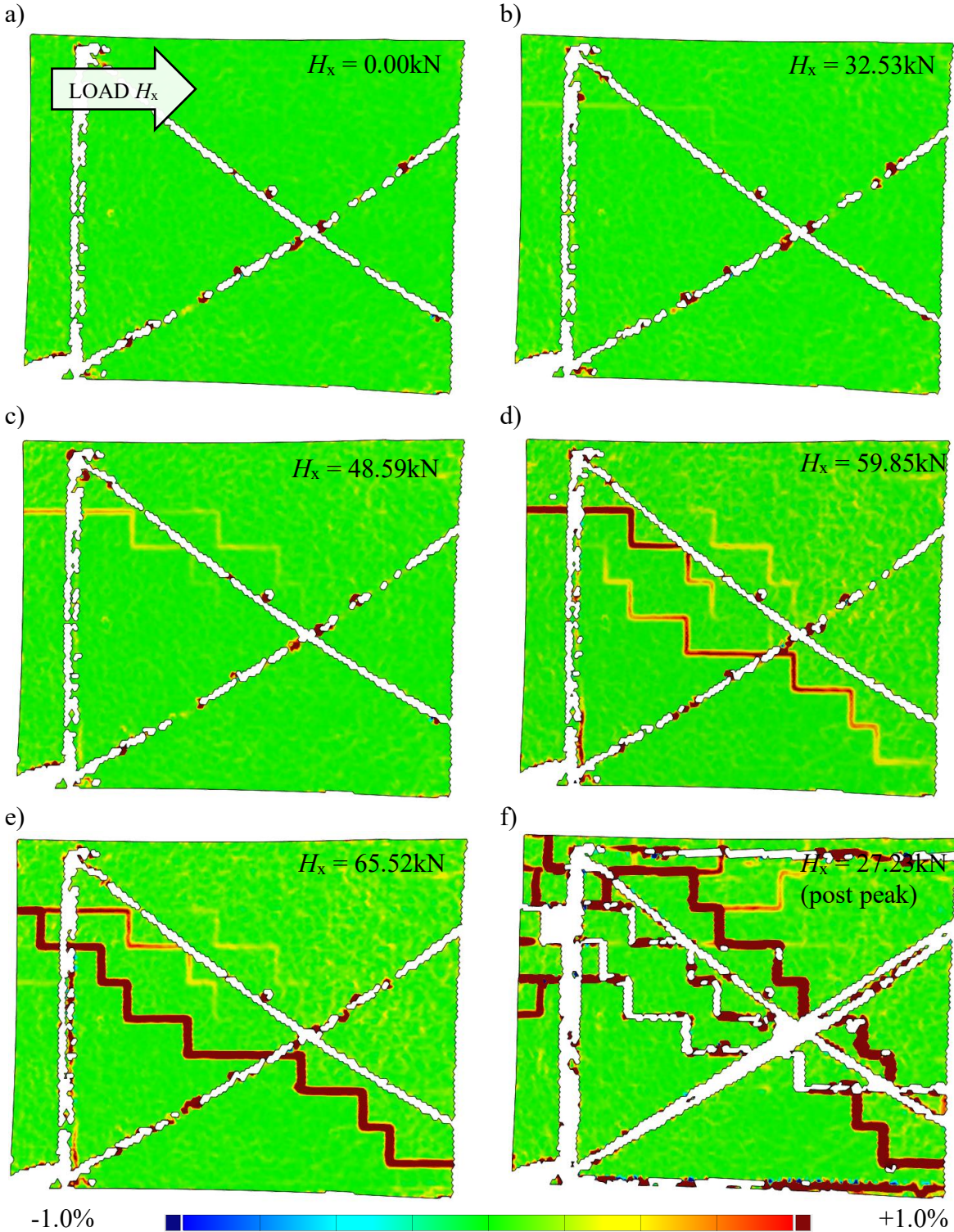
Fig. 6.28 Crack propagation of Wall A – model MB-AAC-010/8: a) analyzed area, b) crack pattern at H_x = 32.53 kN, c) crack pattern at H_x = 48.59 kN, d) crack pattern at H_x = 59.85 kN, e) crack pattern at H_x = 65.52 kN, f) crack pattern at H_x = 27.23 kN (post-peak)
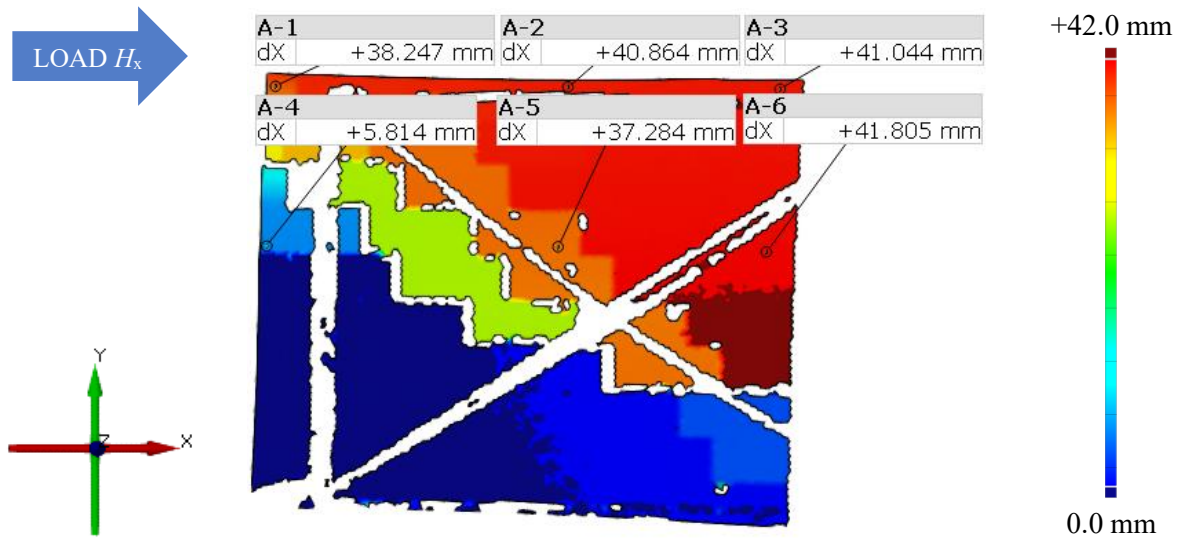
Fig. 6.29 Post peak in-plane horizontal deformation d_x with force $H_x = 27.23$ kN for Wall A
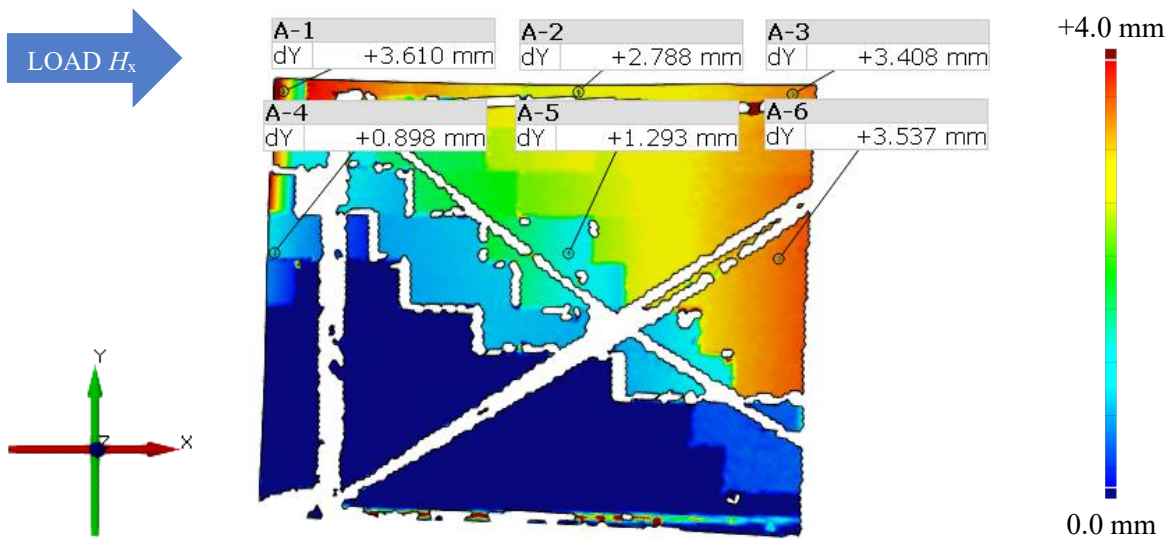
Fig. 6.30 Post peak in-plane vertical deformation d_y with force $H_x = 27.23$ kN for Wall A
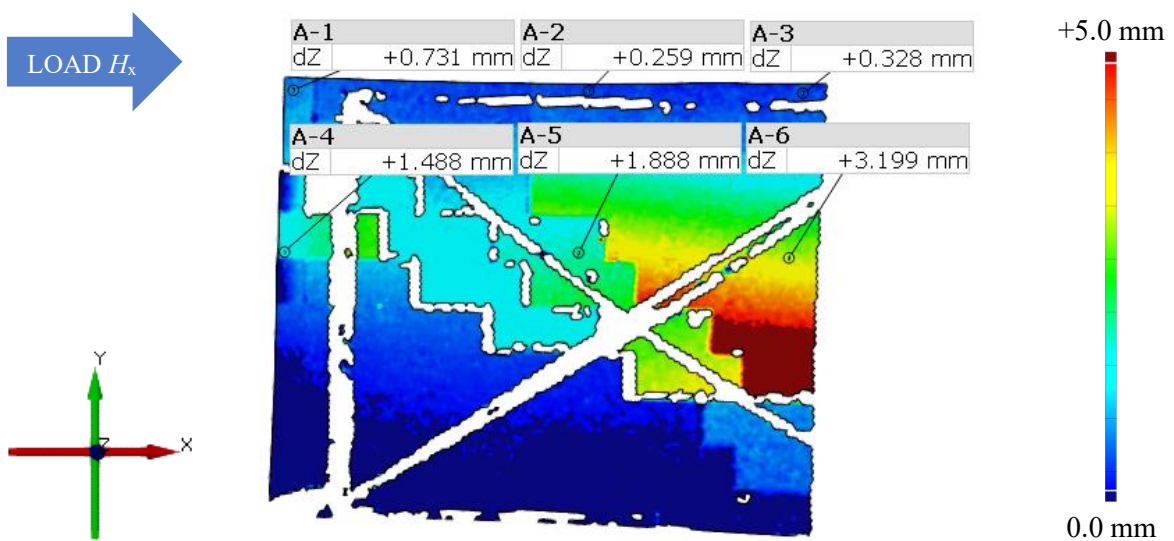
Fig. 6.31 Post peak in-plane out-of-plane deformation d_z with force $H_x = 27.23$ kN for Wall

150

The first crack appears in the upper part of the wall facing the applied load. With increasing load, a stepped diagonal crack appears, gradually increasing its width. Finally, a diagonal step crack divides the wall into two parts. The horizontal displacement at the post-peak phase equals 41.0 mm, and the maximum vertical one is 3.6 mm. The out-of-plane displacement was also recorded.

6.2. Crack patterns of tested buildings

The 3D drawings were prepared to show a detailed crack pattern of each model. Additionally, distinct types of cracks are documented with photos of the damage. The pattern is similar for each model, and common areas of failure can be distinguished. In stiffening walls, the cracks run diagonally from the side of the applied load to the wall base in the opposite corner. If there are openings in the walls (windows or doors), the initiation of cracks takes place in the tensile corner of the opening. Diagonal cracks divide the wall into two parts, and after reaching the load capacity of the wall, the part above the crack undergoes significant horizontal displacements (sliding failure). It should be added that in the tested models, the diagonal cracks had a stepped course. With greater compressive stresses of the walls, the diagonal cracks would also run through the masonry elements (a straight diagonal crack).

The damage pattern is different in the walls perpendicular to the stiffening walls. No diagonal cracks are observed, but only small areas of accumulated damage. There is a horizontal crack in half the height of the wall from the side of the applied load (wall assigned as wall 2). This damage is the result of tensile and lifting of the wall. The remaining damage accumulates in the upper part of the wall at its edges – they are local and small (small cracks or chipping of the surface of masonry units).

A similar damage pattern occurs on the opposite side of the building in the perpendicular wall marked as Wall 1. The damage does not accumulate in its corner if an opening is made in such a wall. The cracks occur in the lower part of the wall; the most damaged areas are the corners, which result from the concentration of compressive stresses in such areas. Figures 6.33 – 6.40 shows the observed crack patterns of tested masonry buildings. Cracks and damages are marked in red in the drawings.

Fig. 6.32 Crack pattern – model MB-AAC-010/1: a) view of the stiffening wall A with the door opening, b) view of the stiffening wall B without an opening

a)

4,59 kN/m²

1

MB-AAC-010/2

2

A

B

b)

4,59 kN/m²

2

MB-AAC-010/2

1

B

A

Fig. 6.33 Crack pattern – model MB-AAC-010/2: a) view of the stiffening wall A with the door opening, b) view of the stiffening wall B without an opening

a)

b)
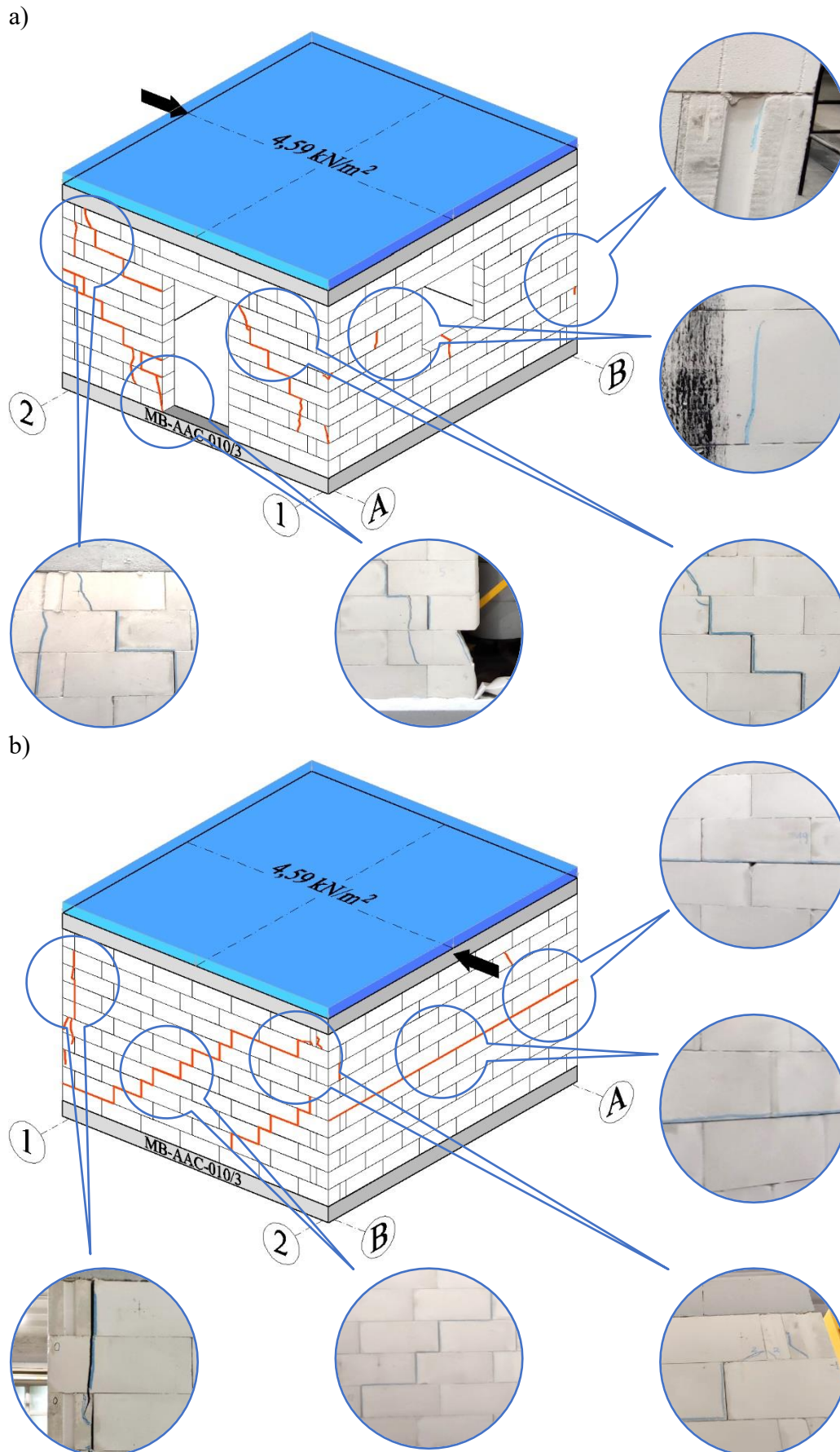
Fig. 6.34 Crack pattern – model MB-AAC-010/3: a) view of the stiffening wall A with the door opening, b) view of the stiffening wall B without an opening

a)

b)
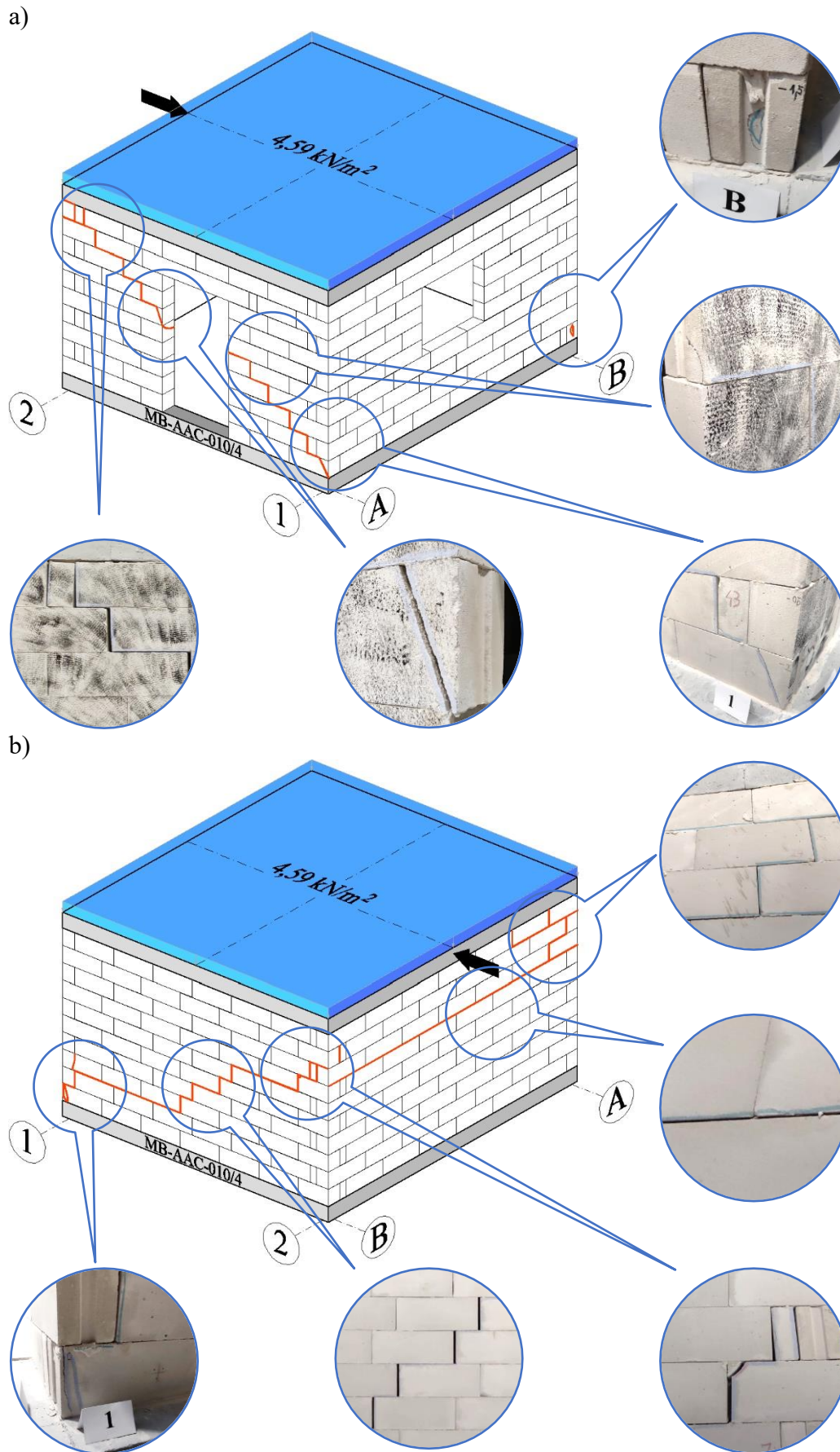
Fig. 6.35 Crack pattern – model MB-AAC-010/4: a) view of the stiffening wall A with the door opening, b) view of the stiffening wall B without an opening

a)

b)
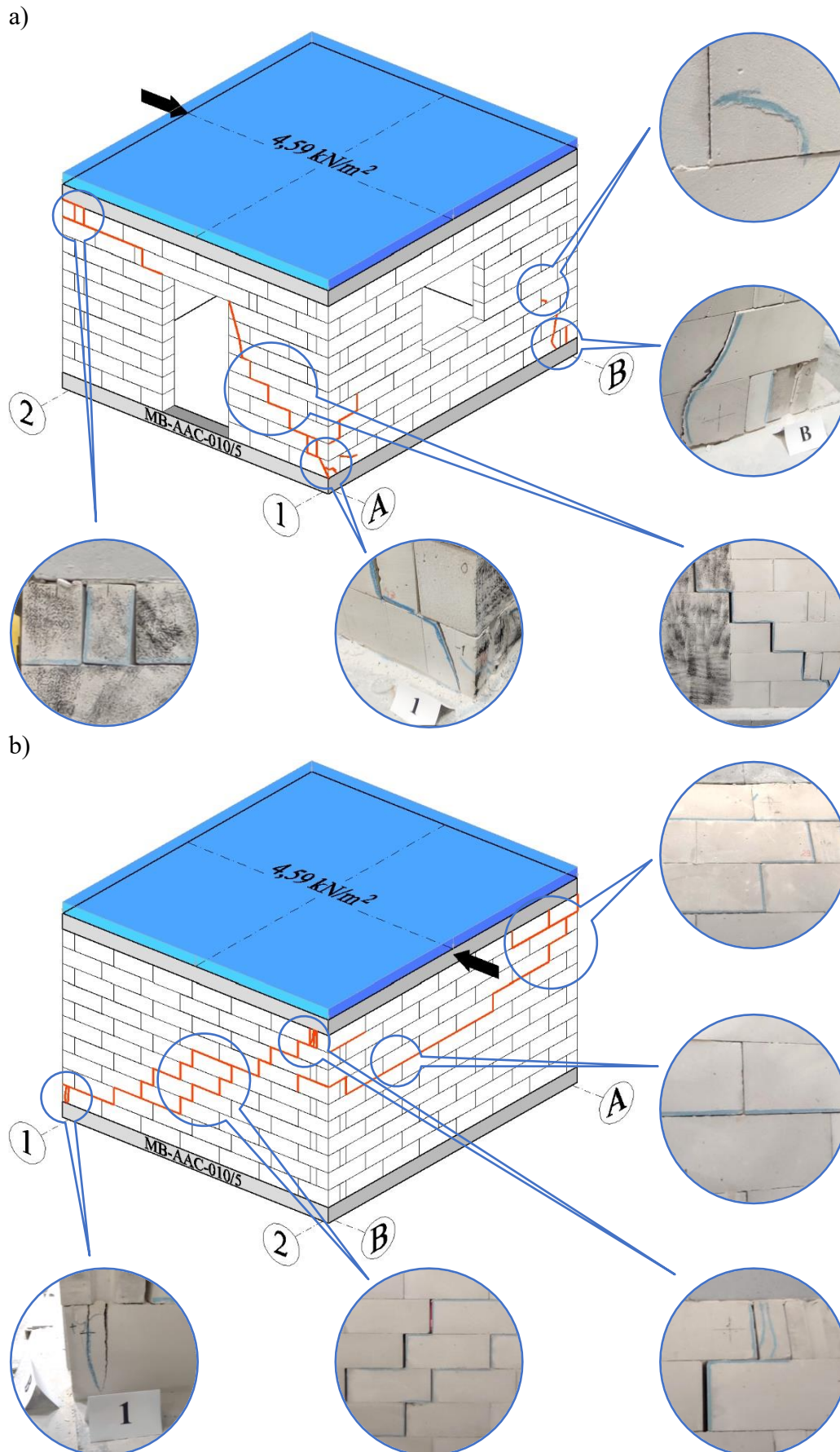
Fig. 6.36 Crack pattern – model MB-AAC-010/5: a) view of the stiffening wall A with the door opening, b) view of the stiffening wall B without an opening

Fig. 6.37 Crack pattern – model MB-AAC-010/6: a) view of the stiffening wall A with the window opening, b) view of the stiffening wall B with the door opening
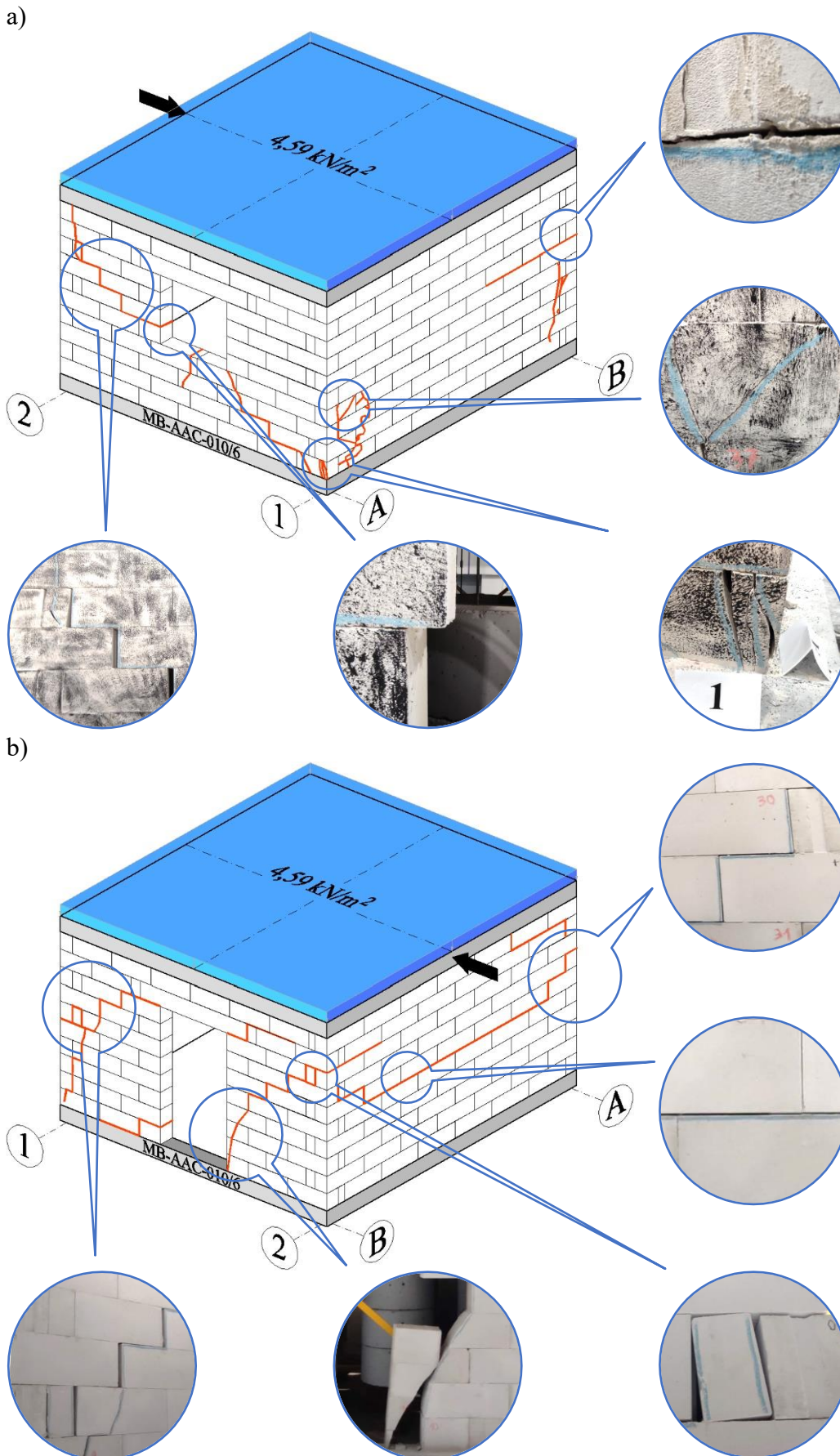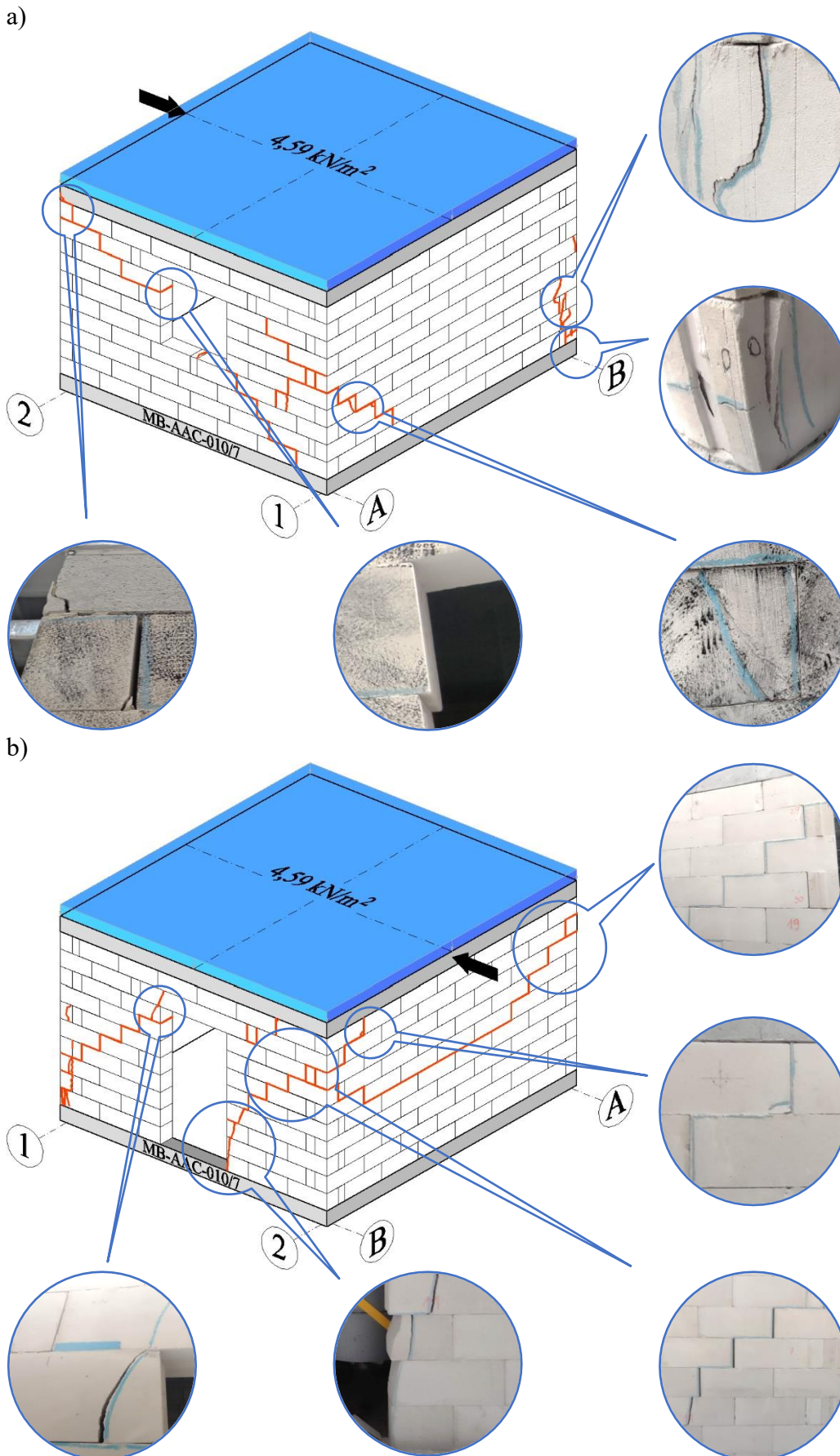
Fig. 6.38 Crack pattern – model MB-AAC-010/7: a) view of the stiffening wall A with the window opening, b) view of the stiffening wall B with the door opening
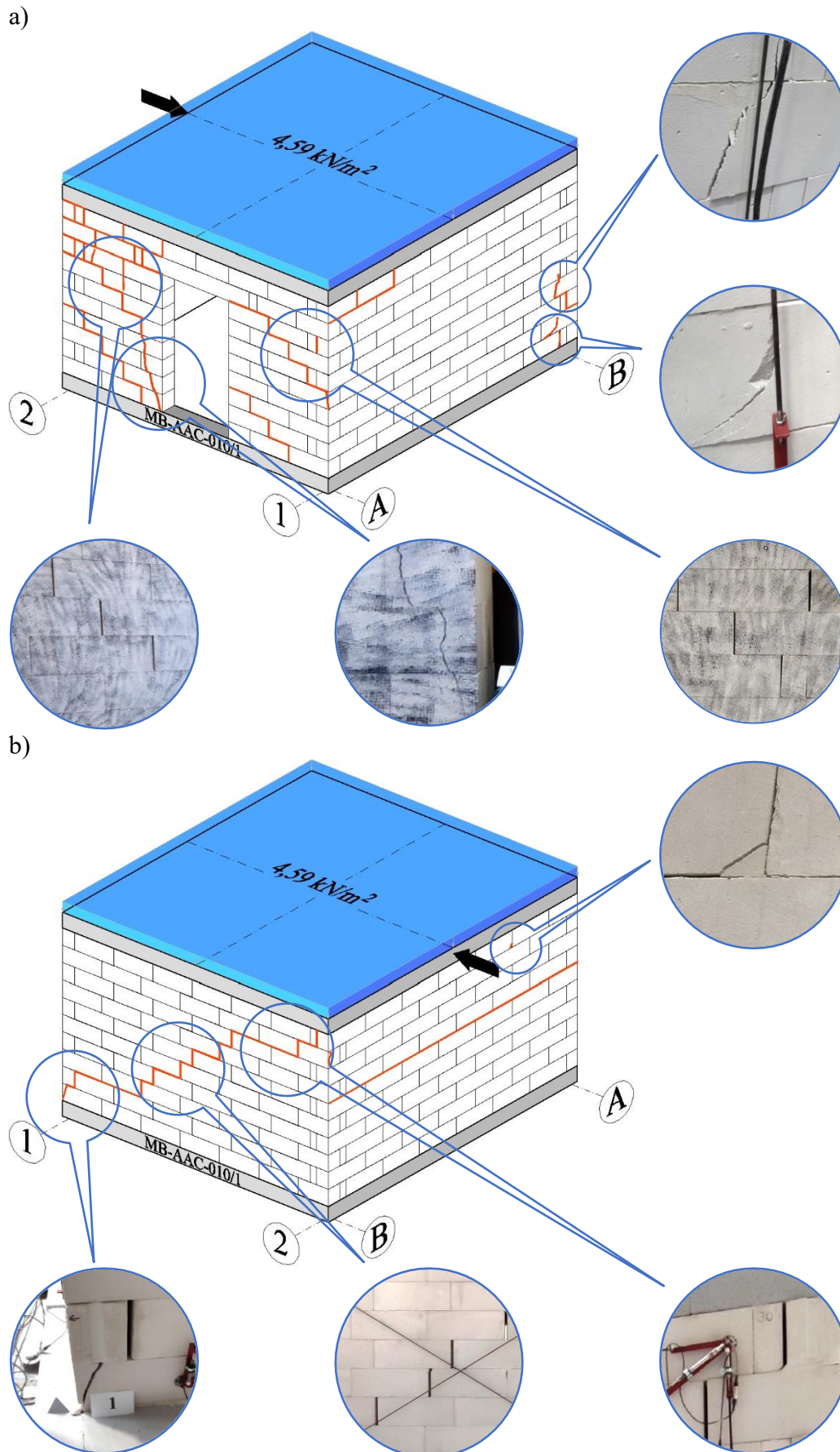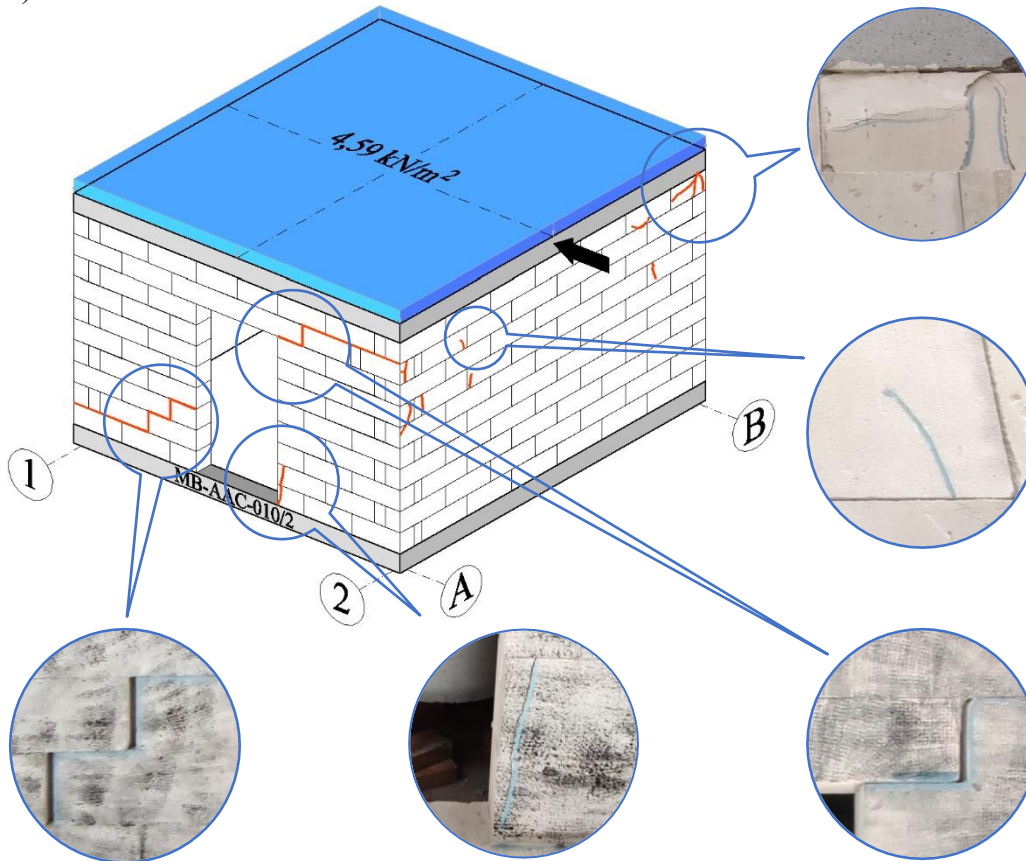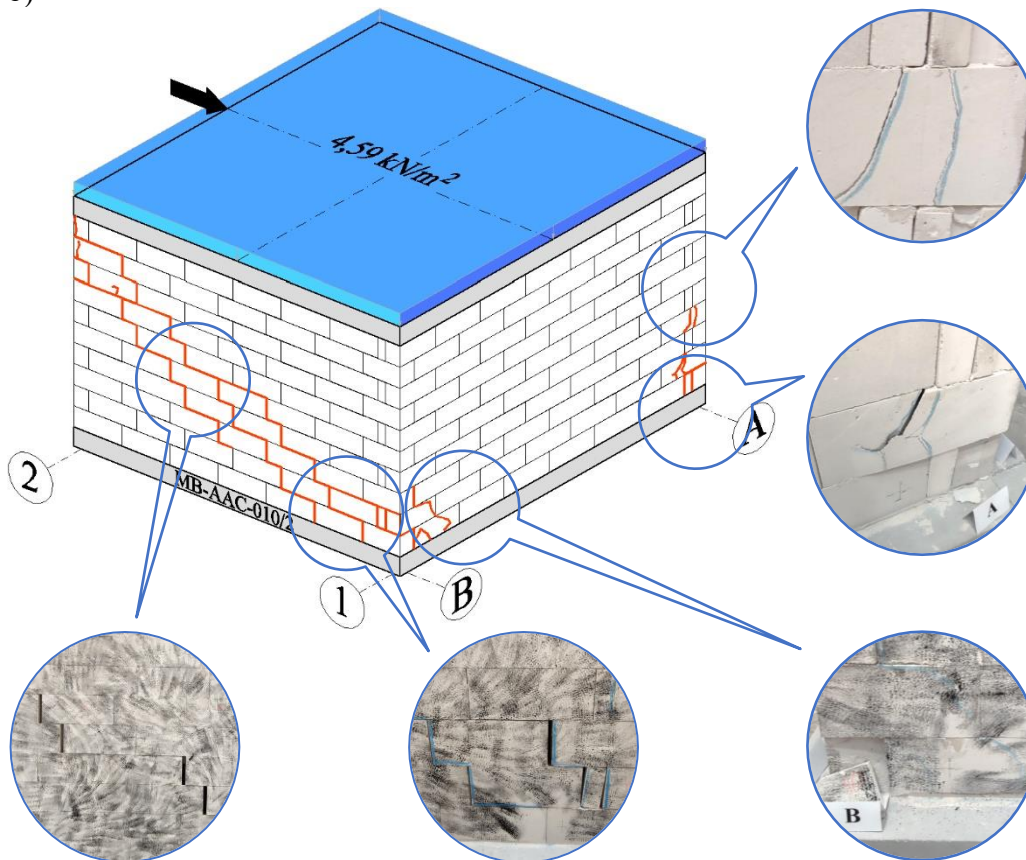
a)

b)
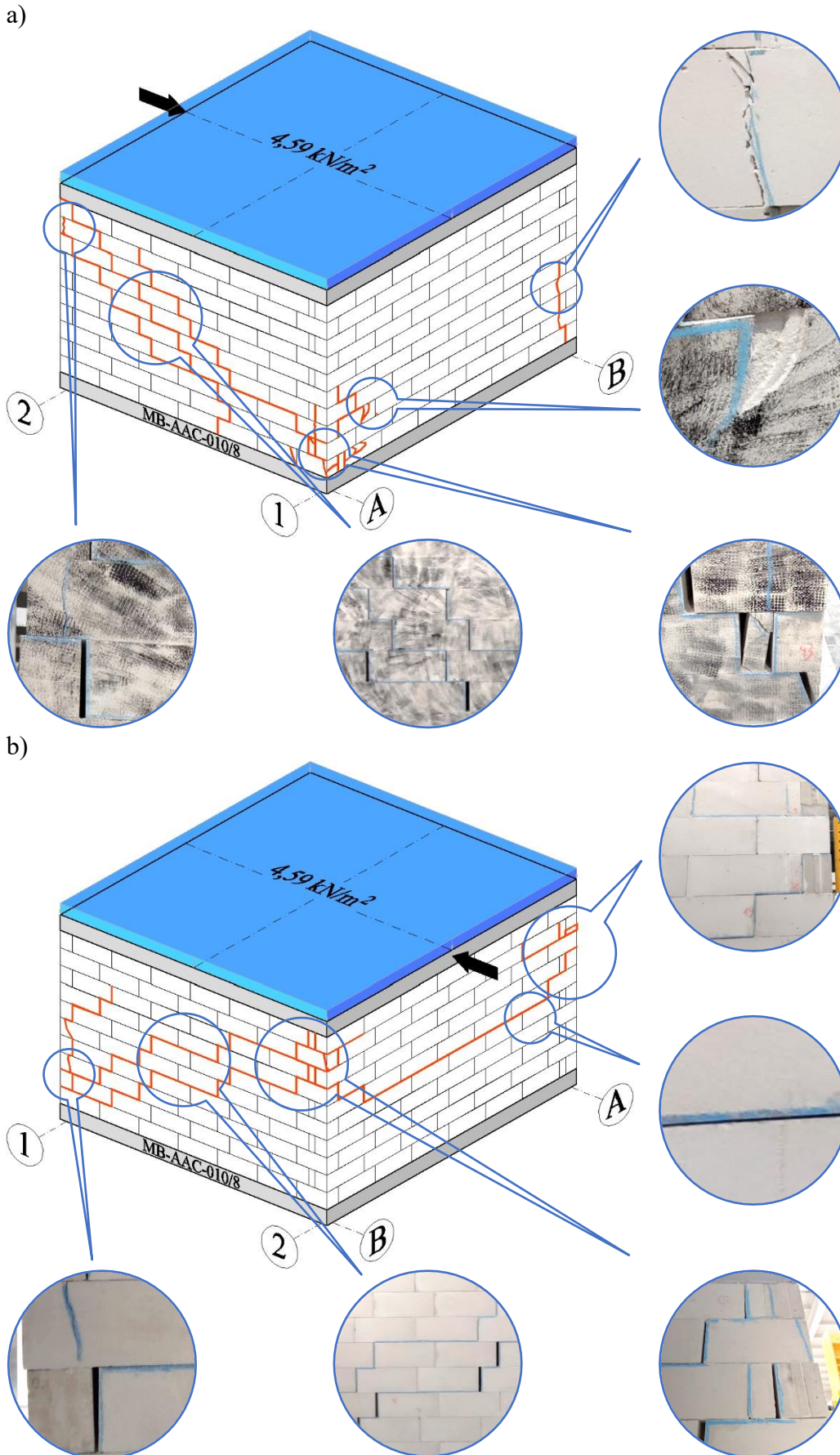
Fig. 6.39 Crack pattern – model MB-AAC-010/8: a) view of the stiffening wall A without an opening,
b) view of the stiffening wall B without an opening

7. NUMERICAL ANALYSIS

7.1. Empirical homogenization of the elasto-plastic model

7.1.1. Assumptions

Many homogenization methods show a good agreement between test results and numerical calculations. However, the practical and common applications of homogenization can be limited as they require many material tests on masonry units and mortar and are often performed at original test stands. Also, the test procedures are not standardized. Validation of individual non-linear parameters for the models can be troublesome as it was performed and tested on bigger elements under simple stress states. Therefore, it is necessary to develop a new procedure for the masonry homogenization approach. The biggest problem with the existing wall homogenization approach is the procedure's lack of repeatability. Thus, the own procedure for masonry homogenization was developed. The approach is based on the test results performed on models and according to procedures standardized following the current standards [67]. The proposed empirical homogenization fulfils the following assumptions:

- the method is developed for designing new buildings and provides the possibility for conducting a set of standard tests on masonry and its components while the in-situ tests using the NDT (non-destructive testing) or MDT (minor-destructive testing) methods were not required,
- a multi-stage validation could be performed on models developed and tested following the design standards for masonry structures [N1, N16],
- the masonry material was represented by a model of the isotropic material whose yield and failure surfaces depended on values of hydrostatic stress – similarly as in the case of concrete and rock,
- the presence of contact surfaces between the masonry units could be neglected.

7.1.2. Properties of masonry components

The own homogenization approach was developed based on the test results conducted in [131]. The masonry consists of autoclaved aerated concrete masonry units with a nominal density class of 600 kg/m³ and M5 class mortar for thin joints. The concrete masonry units had a length l_u = 590 mm, a height h_u = 240 mm, and a width t_u = 180 mm. Mechanical parameters of materials were tested on at least six specimens following the standard procedure. According to the user-defined procedure, the uniaxial compressive and tensile strength, modulus of elasticity, and Poisson's ratio were determined for cylinders of 60 mm diameter and 120 mm height. The basic mechanical parameters are presented in Table 7.1.

Table 7.1

Mechanical properties of masonry components

Material	Average parameter (coefficient of variation)						
	f_b, N/mm²	f_m, N/mm²	$f_{c,cyl}$, N/mm²	f_t, N/mm²	E, N/mm²	v	$G_{f,mv}$, MN/m
AAC	4.95 (7%)	--	4.25 (7.3%)	0.61 (14.0%)	2886 (10.5%)	0.20 (8.5%)	5.21·10⁻⁵ (15%)
Mortar	--	6.1 (6.2%)	5.64 (4.0%)	0.51 (22%)	6351 (9%)	0.18 (10%)	--
Procedure	EN 772-1:2015 [N8]	EN 1015-11:2020 [N5]	The tests were performed on cylinders Ø60×120 mm				RILEM [136]

f_b – standardized compressive strength,
f_m – compressive strength,
$f_{c,cyl}$ – uniaxial compressive strength,
f_t – uniaxial tensile strength,
E – modulus of elasticity,
v – Poisson's ratio,
$G_{f,mv}$ – cracking energy corresponding to cracking model I (bending test).

7.1.3. Masonry models used in the validation procedure

Following the made assumptions, the validation involved the normalized models in specifying the mechanical properties of the masonry in compression perpendicular and diagonal to planes of bed joints. The tests were conducted on walls having a size of 1180 x 1210 x 180 mm (*l* x *h* x *t*) as specified in the standards EN 1052-1:2000 [N16] and ASTM E519-81 [N1]. The walls were erected in a thin joint mortar with a thickness t_{bj} = 3 mm. The measuring frames were fixed to the test specimens to measure strains using linear variable differential transducers (LVDT). The frames fixed to axially

compressed walls were parallel and perpendicular to the load direction, while the (diagonally) shear walls had the frames arranged along their diagonals. All the models were tested after 28 days of concrete hardening under laboratory conditions (relative humidity 80%, average temperature 23°C, relative humidity of AAC at the time of testing $w = 3\%$ did not significantly impact the test results [77]). Figure 7.1 illustrates the test models and determines the relationship between stress and strains. The results are shown in Table 7.2.
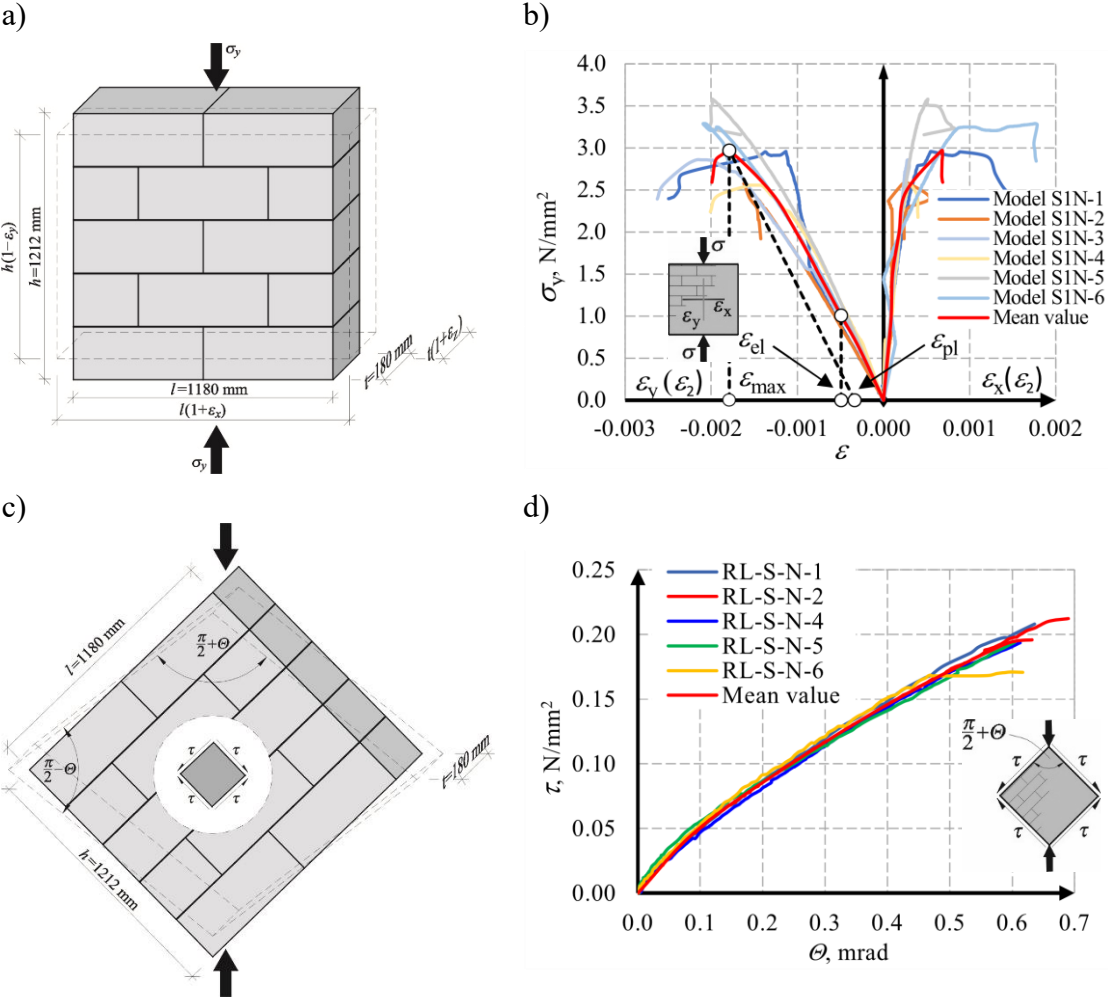
Fig. 7.1 The models and test results for test specimens used in the validation procedure: a) walls compressed in a perpendicular direction to the plane of bed joints according to the standard [N16], b) $\sigma_y - \varepsilon_x$, $\sigma_y - \varepsilon_x$ relationships for walls compressed in a perpendicular direction to the plane of bed joints, c) walls in diagonal compression tested according to the standard [N1], d) $\tau - \Theta$ relationships for walls in diagonal compression

Table 7.2

Properties of masonry used in the validation procedure

Loading	Average parameter (coefficient of variation)									
	f_c, N/mm^2	E_{obs}, N/mm^2	v	ε_{el} %	ε_{max} %	ε_{pl} %	f_{tm}, N/mm^2	$\Theta_{cr,obs}$ mrad	$\Theta_{cr,1/3}$ mrad	G, N/mm^2
Axial compression	2.97 (14%)	2041 (11%)	0.18 (15%)	-0.048	- 0.179 **	- 0.033 **	--	--	--	--
Diagonal compression	--	--	--	--	--	--	0.196 (8.3%)	0.587 (12.3%)	0.138 (15.4%)	475 (15.4%)
Procedure	EN 1052-1:2000 [N16]						ASTM E519-81 [N1]			

* – read from the averaged diagram of σ – ε relationships at $0.33f_{cm}= 0.33\sigma_{cm}$,

* – read from the averaged diagram of σ – ε relationships,

f_c – compressive strength of masonry,

E – modulus of elasticity,

v – Poisson's ratio,

ε_{max} – strain at the maximum stress,

ε_{pl} – plastic strain,

f_{tm} – diagonal compressive strength,

$\Theta_{cr,obs}$ – mean angle of shear strain determined at the time of formation of visible cracks,

$\Theta_{cr,1/3}$ – mean angle of shear strain determined at the level of $1/3f_t$,

G – shear modulus.

7.1.4. Material models

The procedure of homogenization included the elastoplastic model showing the M-W-3 degradation. The linear-elastic model defined by Hooke's law was also used as the auxiliary model. The M-W-3 model was developed to model brittle materials in which the shape of the boundary surface depended on average hydrostatic stresses. Constitutive relations, which were not the same in the hardening and softening phases, were used to specify the non-linear behavior of the model. This model combined two material models: the elastoplastic model with the Menétrey-William boundary surface and the elastic-brittle model with the Rankine boundary surface [34]. The boundary surfaces (failure surfaces) were defined for the reduced space of octahedral stresses. The space of principal stresses is described by principal stresses $\sigma_1, \sigma_2, \sigma_3$. The free parameters define the octahedral space specified by Haigh-Westergaard coordinates: the hydrostatic coordinator ξ, the deviatoric coordinator ρ, and the Lodge angle Θ. The Haigh-Westergaard coordinates – Fig. 7.2 are the functions of invariants (I_1, J_2, J_3) of principle stress tensors ($\sigma_1 > \sigma_2 > \sigma_3$). The following formulas (7.1) – (7.3) can describe the

definition of the space coordinators for boundary surfaces:

$$\zeta = \frac{I_1}{\sqrt{3}}$$ (7.1)

$$\rho = \sqrt{2I_2}$$ (7.2)

$$\Theta = \frac{1}{3}\mathrm{acos}\left(\frac{3\sqrt{3}}{2}\frac{I_3}{I_2^{3/2}}\right)$$ (7.3)

for which formulas express the stress tensor's invariants (7.4) – (7.6):

$$I_1 = \sigma_1 + \sigma_2 + \sigma_2$$ (7.4)

$$I_2 = \frac{[(\sigma_1 - \sigma_2)^2 + (\sigma_2 - \sigma_3)^2 + (\sigma_3 - \sigma_1)^2]}{6}$$ (7.5)

$$I_3 = (\sigma_1 - \tfrac{1}{3}I_1)(\sigma_2 - \tfrac{1}{3}I_1)(\sigma_3 - \tfrac{1}{3}I_1)$$ (7.6)
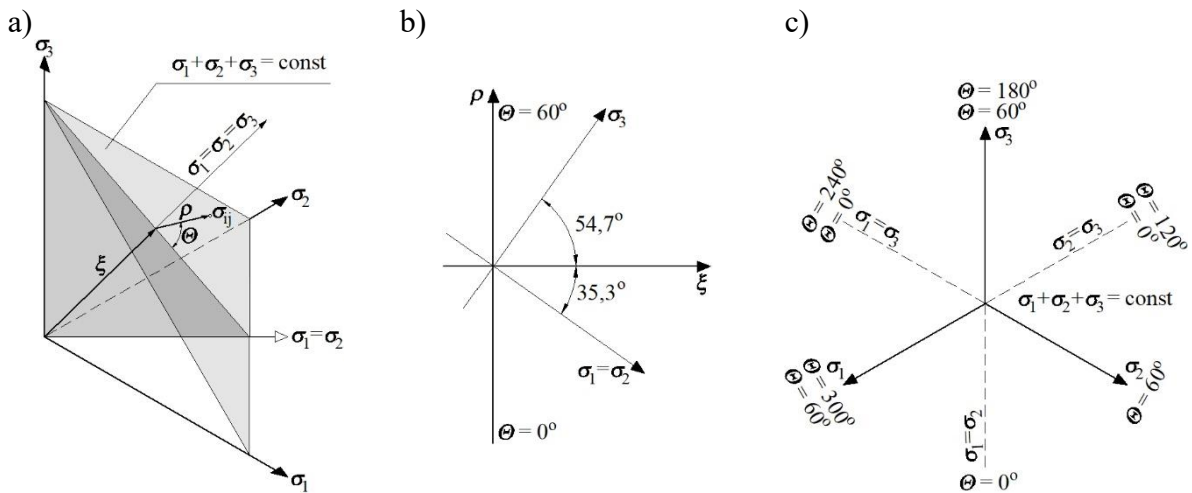
Fig. 7.2 The Haigh–Westergaard coordinates in space: a) the components of principal stress space, b) an axiatoric section, c) a deviatoric section

The Rankine criterion was used as the tension-induced failure condition. This criterion described the condition $\sigma_k \leq f_t$ (Fig. 7.3), in which each of three directions of principal stress ($k = 1, 2, 3$) could be described by the general form (7.7):

$$f_k^f = {}^t\sigma_{ij}n_i^k n_j^k - f_t \leq 0$$ (7.7)

at Haigh-Westergaard coordinates are (7.7):

$$f^f = \xi - \sqrt{2}\rho cos\Theta - \sqrt{3}f_t \leq 0 \qquad (7.7)$$

Fig. 7.3 The Rankine criterion in the Haigh-Westergaard space: a) view of principle stress space, b) view of axiatoric section, c) view of deviatoric section

The following relationship expresses strains on the Rankine surface (7.8):

$$d\varepsilon_{ij}^{rfk} = d\lambda^k \frac{\partial f_k^f}{\partial \sigma_{ij}} = d\lambda^k = \frac{{}^t\sigma_{ij}n_i^k n_j^k - f_t(w^k)}{D_{ijmn}n_i^k n_j^k n_m^k n_n^k} \qquad (7.8)$$

where: w^k is a crack width calculated from the relationship (7.9):

$$w^k = L^t(\hat{\varepsilon}_k^f + d\lambda^k) \qquad (7.9)$$

Equation (7.8) was satisfied after cracking while softening the cracked material depended on the cracking energy and the crack width [72] expressed by equation (7.9). The crack width in the direction k was calculated using the known strains $\hat{\varepsilon}_k^f$, and the specified length L_t (*crack band size*) of smeared cracks. The crack width in the discussed material model was calculated from the element's size projected into the direction k (Fig. 7.4).
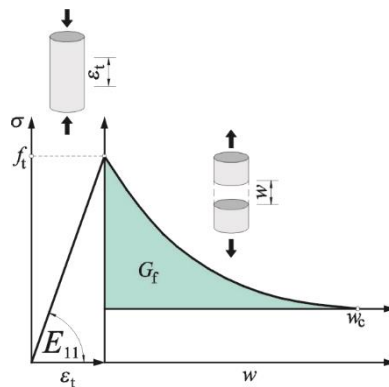
Fig. 7.4 The function of material softening expressed as the crack width

165

The elastoplastic model was described with the modified empirical model by Hoek and Brown [71] based on the concept of Menétrey and William [115], who expressed a three-parameter yield surface M-W-3 as follows (7.10):

$$f^\rho(\xi, \rho, \Theta) = \left(\sqrt{1,5}\frac{\rho}{k(\kappa)f_c}\right)^2 + m\left(\frac{\rho}{\sqrt{6}k(\kappa)f_c}r(\Theta, e) + \frac{\xi}{\sqrt{3}k(\kappa)f_c}\right) - c(\kappa) = 0 \quad (7.10)$$

where:

m - a parameter, an equivalent to cohesion equal to (7.11):

$$m = 3\frac{(k(\kappa)f_c)^2 - (\lambda_t f_t)^2}{k(\kappa)f_c\lambda_t f_t}\frac{e}{e+1} \quad (7.11)$$

r - an elliptical function (7.12):

$$r(\Theta, e) = \frac{4(1-e^2)cos^2\Theta + (2e-1)^2}{2(1-e^2)cos\Theta + (2e-1)\sqrt{4(1-e^2)cos^2\Theta + 5e^2 - 4e}} \quad (7.12)$$

in which:

e – eccentricity of the elliptical function taking values from the range $e \in (0.5; 1.0)$,
f_c, f_t – uniaxial compressive and tensile strength,
$\lambda_t \geq 1$ – scaling parameter for M-W-3 surface.

The surface defined by Menétrey and William (Fig. 7.5) comprised parabolic compressive meridians (visible in the axiatoric section – Fig. 7.5b) intercepting at a point corresponding to the triaxial tension. The M-W-3 surface in a deviatoric section was composed of three tangential curves along compressive meridians, whose shape was affected by the value of eccentricity e - Fig. 7.5c.

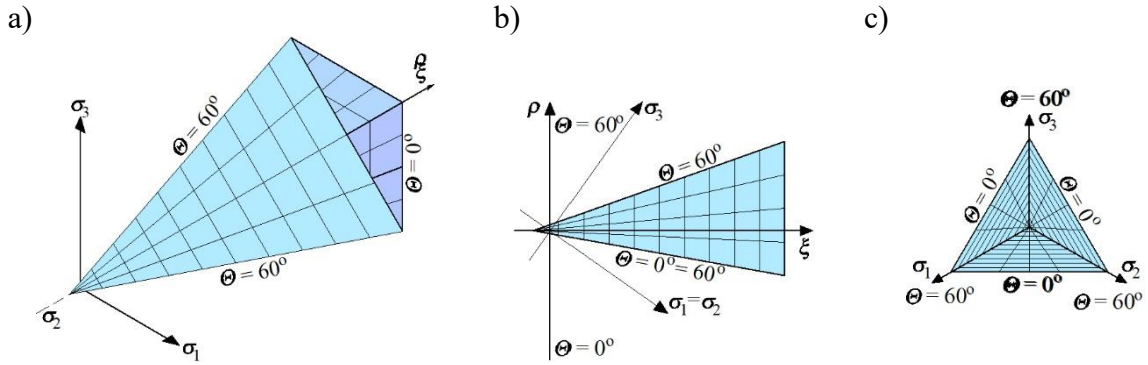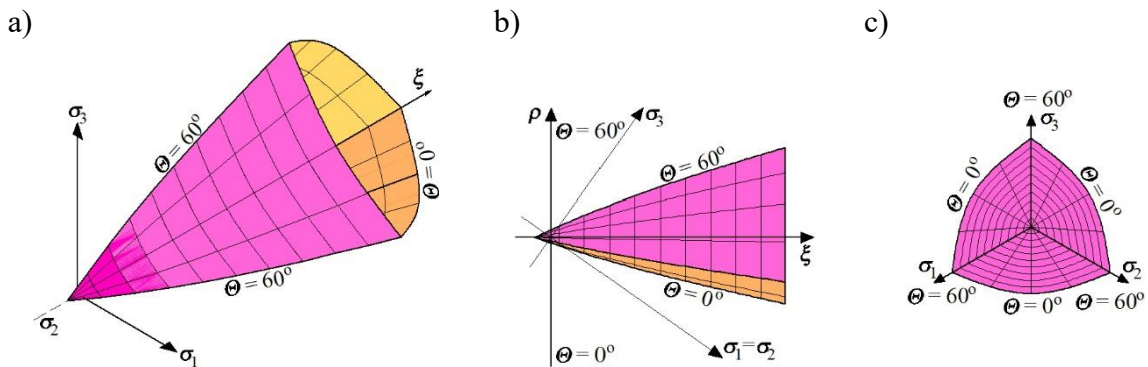Fig. 7.5 Menétrey-William criterion in the Haigh-Westergaard space: a) view of principal stress space, b) view of an axiatoric section, c) view of a deviatoric section

The eccentricity of the elliptical function determined the shape of the elliptical curve. The curves constituting the deviatoric section formed a circle at the eccentricity value of 1.0. When the eccentricity e equalled 0.5, the elliptical curve in the deviatoric section had a shape of an equilateral triangle. The intermediate values of the eccentricity changed the curves' shapes, forming an equilateral triangle with rounded corners. The surface matching parameter $\lambda_t > 1$ determined the relative positions of the M-W-3 and the Rankine surfaces – Fig. 7.6. If $\lambda_t = 1$, the yield surface was confined in the Rankine pyramid. For $\lambda_t = 2\lambda_t = 2$, the surfaces were intercepting from the side of hydrostatic tension and minor compression. The Rankine boundary surface was used to describe the stress states in that situation.
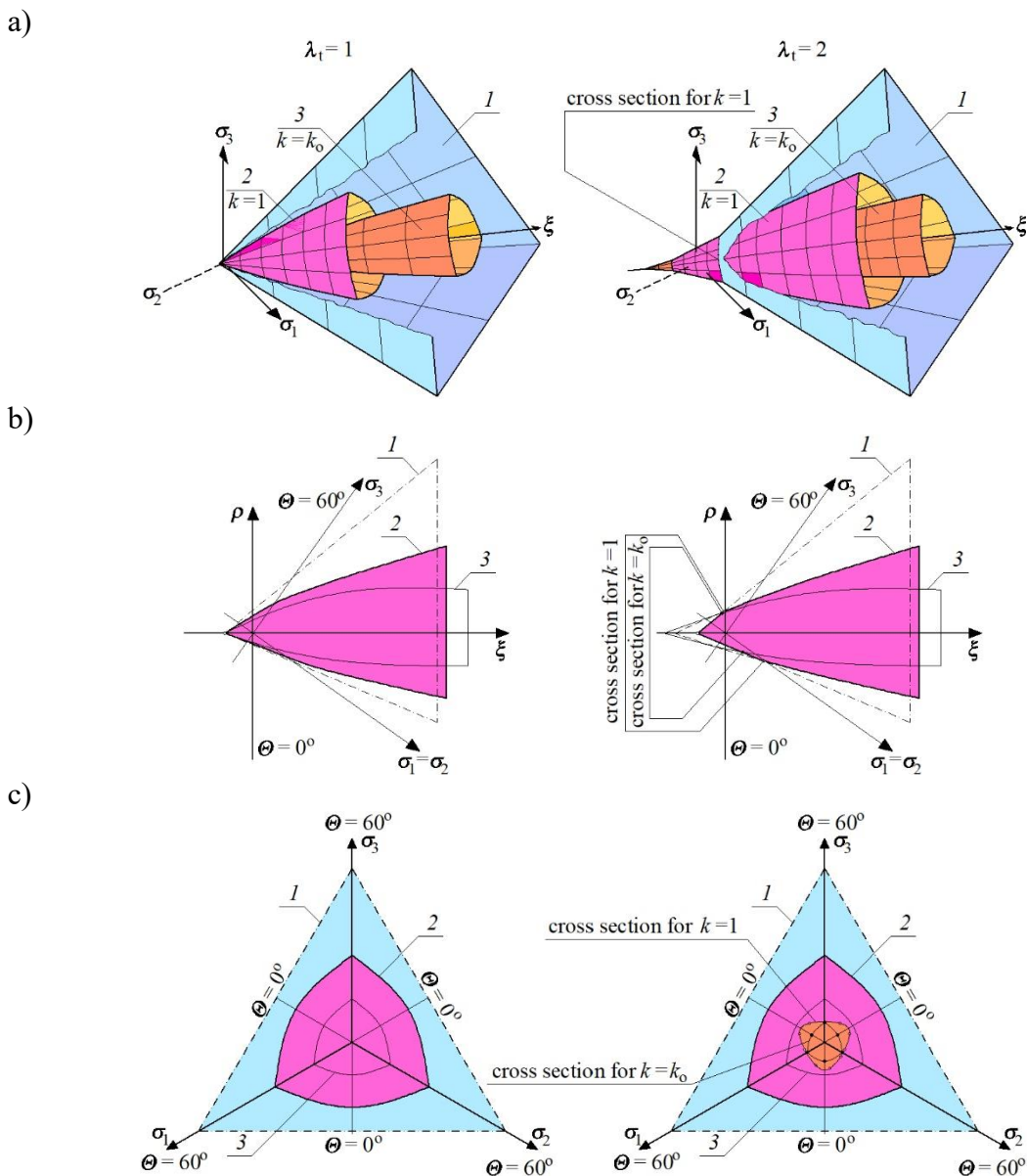
Fig. 7.6 Relative position of Rankine and M-W-3 surfaces: a) view of surfaces in principal stress space, b) axiatoric sections, c) deviatoric sections: 1 – Rankine Surface, 2 – M-W-3, the surface at k = 1 (yield strength), 3 – M-W-3 surface at k_0 (end of the elastic stage)

167

At higher values of hydrostatic compression, the failure was specified by the M-W-3 surface. Displacements of the M-W-3 surface along the hydrostatic axis were possible due to changes in the surface matching parameter λ_t by simulating the material hardening or softening stages. These stages were determined by the parameter κ related to plastic volumetric strains expressed by the following (7.13):

$$dκ = dε_V^p = dε_1^p + dε_2^p + dε_3^p \qquad (7.13)$$

The location of the M-W-3 surface and its temporary shape at the hardening stage was defined by the hardening function κ, which depended on the hardening and softening parameters. This function was included in the M-W-3 surface and was responsible for scaling the compressive strength f_c of the material. It had the elliptical form [66] defined by the following formula (7.14):

$$k(κ) = k\left(ε_V^p\right) = k_0 + (1 - k_0)\sqrt{1 - \left(\frac{ε_{V,t}^p - ε_V^p}{ε_{V,t}^p}\right)^2} \qquad (7.14)$$

where:

$ε_V^p$ – plastic strain at the highest compressive stress obtained from uniaxial compression tests,

$ε_{V,t}^p$ – plastic volumetric strain obtained from uniaxial compression tests (the beginning of softening),

k_0 – the value defining an initial yield surface that limited the elastic state (the beginning of plastic behavior).

At the end of the hardening stage, the function reached the constant value, and the material entered the softening phase specified by the softening function c. That function simulated decohesion by shifting the yield surface towards a negative part of the hydrostatic axis. That function (7.15) in the uniaxial compression had the following form [156]:

$$c(κ) = c\left(ε_V^p\right) = \left(1 / \left[1 + \left(\frac{n_1 - 1}{n_2 - 1}\right)^2\right]\right)^2 \qquad (7.15)$$

where:

$$n_1 = \frac{\varepsilon_V^p}{\varepsilon_{V,t}^p} \tag{7.16}$$

$$n_2 = (\varepsilon_{V,t}^p + t)\varepsilon_{V,t}^p \tag{7.17}$$

The parameter t, describing the volumetric strain, controlled the slope of the softening function. The value of the softening function c was equal to 1 at the hardening stage. The complete softening of the material with decohesion c was observed at a value equal to 0. The function's behavior for material hardening k and softening c is illustrated in Fig. 7.7.
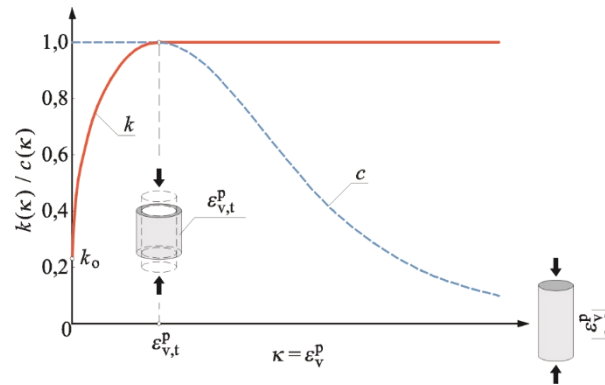
Fig. 7.7 Shape of hardening/softening function

7.1.5. Strategy for calibrating mechanical parameters

Following the assumptions, homogenization was based on the results obtained from the standard tests for the masonry models in diagonal compression. The material parameters for the Rankine and M-W-3 surfaces were validated by step-by-step changes in the values of the selected mechanical parameters. The results were verified by comparing the stress-vertical strain and the standard stress-horizontal strain relationships for the compressed walls. In the case of the walls in diagonal compression, the verification was based on the relationships between shear stress and an angle of shear strain. Apart from that, the crack images were compared. They were the images obtained by calculating the crack morphology from the tested models. Individual stages of the validation procedure for the homogeneous model for the masonry are presented in Fig. 7.8.

INPUT DATA: $G, v, f_c, f_t, G_f, \varepsilon_{cp}$
WITH ACCORDANCE TO STANDRD TESTS

STAGE I
CALCULATION OF THE MODULUS OF ELASTICITY
PARAMETER - E_{init}

STAGE II
CALIBRATION OF THE MODULUS OF ELASTICITY
$E_{init} \rightarrow E_{cal}$
ELASTIC MATERIAL MODEL
DIAGONAL COMPRESSED WALL

STAGE III
CALIBRATION OF THE MODULUS OF ELASTICITY
$E_{init} \rightarrow E_{cal}$
ELASTIC MATERIAL MODEL
COMPRESSED WALL

STAGE IV
CALIBRATION OF THE TENSILE STRENGTH
$f_t \rightarrow f_{t,cal}$
ELASTIC-PLASTIC MODEL WITH DEGRADATION
DIAGONAL COMPRESSED WALL

STAGE IV-A
CALIBRATION OF THE FRACTURE ENERGY
$G_f \rightarrow G_{f,cal}$
ELASTIC-PLASTIC MODEL WITH DEGRADATION
DIAGONAL COMPRESSED WALL

STAGE IV-B
CALIBRATION OF THE PLASTIC STRAIN
$\varepsilon_{cp} \rightarrow \varepsilon_{cp,cal}$
ELASTIC-PLASTIC MODEL WITH DEGRADATION
DIAGONAL COMPRESSED WALL

STAGE V
CALIBRATION OF THE COMPRESSIVE STRENGTH
$f_c \rightarrow f_{c,cal}$
ELASTIC-PLASTIC MODEL WITH DEGRADATION
COMPRESSED WALL

OUTPUT DATA: $E_{cal}, v, f_{c,cal}, f_{t,cal}, G_{f,cal}, \varepsilon_{cp,cal}$

Fig. 7.8 Stages of the validation procedure for mechanical parameters for the homogeneous model

Stage I of the calibration was to determine the masonry's input modulus of elasticity E_{init}. This value was used as the input parameter for the calibration. In stage II, the 2D linear elastic models of a wall in diagonal compression (the plane stress state) were developed. Values of the input modulus of elasticity E_{init} were changed to reach the modulus value E_{cal}. Stage III was to verify the value of the modulus of elasticity E_{cal} calibrated in stage II against the masonry model in diagonal compression. The

procedure was the same as the previous one. Values of the modulus E_{cal} were changed in such a way as to ensure the best match between the stress-vertical strain relationship and the test results. The material's tensile strength in the diagonally compressed model f_t was calibrated in stage IV. Cracking energy $G_{f,cal}$ was calibrated in stage IV-A, and plastic strain $\varepsilon_{cp,cal}\varepsilon_{cp}$ in stage IV-B. In stage V, compressive strength $f_{c,cal}$ of the masonry was calibrated against the masonry parameters that had been calibrated in the previous stages.

7.1.6. Results of the validation of parameters for the homogeneous finite element model

Stage I - determination of the input value of the modulus of elasticity for the masonry – the elastic model

The input modulus of elasticity was calculated based on the tests on diagonally compressed models using the known relationship $E_{init} = 2(1+v)G$ and the masonry parameters from Table 7.2. At Poisson's ratio $v = 0.18$ and shear modulus $G = 475$ N/mm², the elasticity modulus reached the value $E_{init} = 1121$ N/mm².

Stage II - calibration of the elasticity modulus E for diagonally compressed walls – the elastic model

The modulus of elasticity was calibrated during stage II at the constant value of Poisson's ratio using the 2D linear-plastic, isotropic models of finite elements. The masonry and steel elements of the test stand, which were arranged along the diagonal in the wall corners, were modelled separately. The contact elements were introduced between the test stand elements and the masonry. The cohesion between these introduced elements was $c = 0$, and the friction coefficient was $\mu = 0.1$. All the models were loaded under the same scheme, which included vertical displacements of the upper supports equal to the constant value $\Delta = -10$ mm. Each loading step, at which the calculated results were read, was 0.001Δ. The bottom of the steel elements of the test stand was placed on hinge supports. The numerical models of finite elements in the masonry structures in diagonal compression are shown in Fig. 7.9. The values of shear strain angle $\Theta_{cal} = \Theta_{el}$ were taken as the conformance criterion for shear stress equal to $0.33\tau_{max}$ (the representative range of elastic behavior of the wall) and $\Theta_{cal} = \Theta_{max}$ for the stress τ_{max}. The results obtained from calibrating the modulus of elasticity for the models of walls subjected to diagonal compression are presented in Table 7.3 and illustrated in graphs of the relationships $\tau - \Theta$ (Fig. 10a) and $\Theta_{cal}/\Theta_{obs.} - E_{cal}/E_{init}$ Fig. 10b.

Fig. 7.9 The numerical 2D model for diagonally compressed masonry structures: 1 – the macro-model of homogenized masonry units made of autoclaved aerated concrete, 2 – steel elements of the test machine, 3 – the contact elements representing the connection between the masonry and steel elements of the test stand

Table 7.3

Results for validation of the elasticity modulus in stage II

Model	E_{cal}, N/mm^2	E_{cal}/E_{init}	Θ_{el}, mrad	Θ_{el}/Θ_{obs}	Θ_{max}, mrad	$\Theta_{max}/\Theta_{obs}$
S1	1121	1.000	0.212	1.50	0.626	0.99
S2	**1110**	**0.990**	**0.212**	**1.50**	**0.632**	**1.00**
S3	1612	1.438	0.147	1.04	0.435	0.69
S4	1630	1.454	0.146	1.03	0.430	0.68
S5	1670	1.490	0.142	1.00	0.420	0.67
S6	1675	1.494	0.142	1.00	0.419	0.66
S7	**1676**	**1.495**	**0.142**	**1.00**	**0.418**	**0.66**

a)   b)
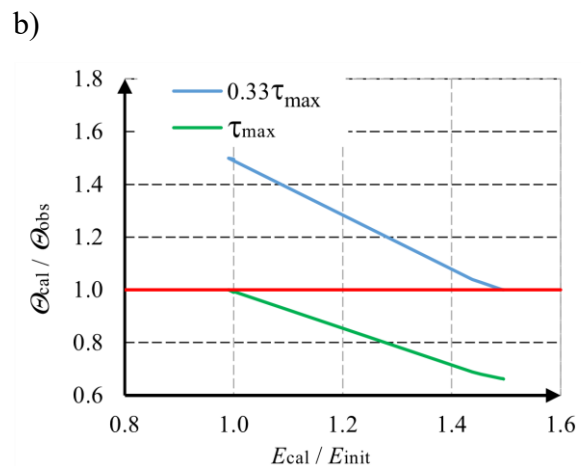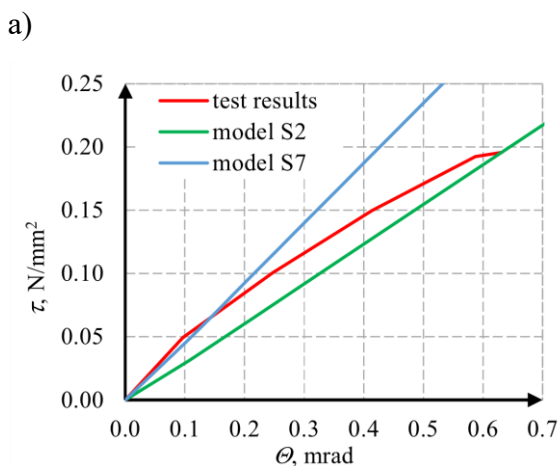
Fig. 7.10 Calibration results for stage II: a) comparison of shear stress – deformation angle relationship for test results and numerical calculations, b) analysis of the sensitivity of the change in the elasticity modulus E to the value of the deformation angle

172

The test results for shear walls indicated the non-linear behavior of the masonry even at a low-stress level. Thus, it was impossible to obtain the modulus of elasticity, which could be a reliable representation of the actual differences in the behavior of the stressed masonry. The deformation was consistent at the level of $0.33\tau_{max}$ for model S7 and the elasticity modulus $E = 1676$ N/mm^2, and at the level τ_{max} for the model S2 and the modulus $E = 1110$ N/mm^2. Differences in the modulus of elasticity exceeded 50%. According to the calculations, changes in the modulus of elasticity caused nearly proportional changes in the angle of shear strain. Some change in the direction of graphs representing changes in the shear strain (Fig. 10b) was observed only at the reduced modulus of elasticity. Eventually, the modulus of elasticity $E_{cal} = 1676$ N/mm^2 at Θ_{el} and $E_{cal} = 1110$ N/mm^2 at Θ_{max} were taken for the calculations made in the subsequent stage.

Stage III - calibration of the elasticity modulus E for axially compressed walls – the elastic model

Stage III was to verify the values of the modulus of elasticity calibrated in stage II against the behavior of the wall under axial compression. The numerical models of finite elements were the same as in stage I, apart from an obvious boundary and loading conditions change. The masonry and steel slabs of the test machine were modelled separately. The contact elements were introduced between the test stand elements and the masonry. The cohesion between these introduced elements was $c = 0$, and the friction coefficient was $\mu = 0.1$. All the models were loaded under the same scheme, which included the vertical displacement of the top slabs of the test machine equal to the constant value $\Delta = -10$ mm. Each loading step, at which the calculated results were read, was 0.001Δ. The bottom of the steel slabs of the test machine was placed on hinge supports. The numerical FEM models of the wall subjected to axial compression are shown in Fig. 7.11.

The results were analysed by comparing horizontal $\varepsilon_{x,cal}$ and vertical $\varepsilon_{y,cal}$ strains at two levels of standard stress $0.33\sigma_{max}$ (the representative range of elastic behavior of the wall) and maximum stress σ_{max}. The modulus of elasticity of the masonry was changed as in stage I. The numerical calculations with reference to the test results are presented in Tables 7.4 and 7.5.
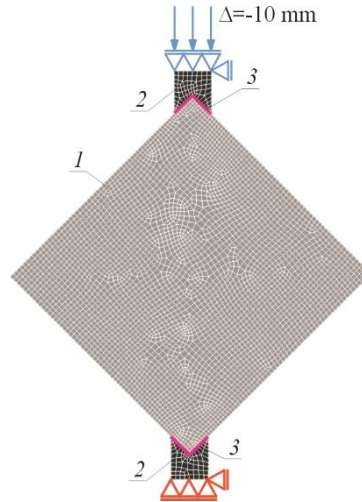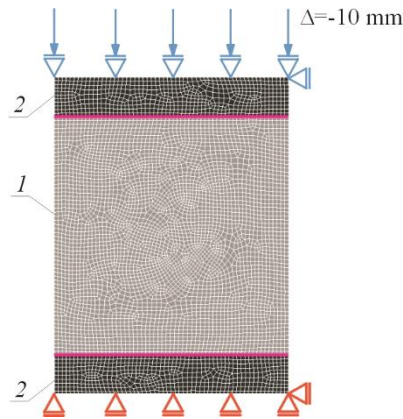
Fig. 7.11 The numerical 2D models for axially compressed masonry structures: 1 – the macro-model of homogenized masonry units made of autoclaved aerated concrete, 2 – steel elements of the test machine, 3 – the contact elements representing the connection between the masonry and steel elements of the test stand

For the elasticity modulus $E_{cal} = 1676$ N/mm^2, which was calibrated during stage II and at the phase of elastic behavior, horizontal strains in compressed walls differed by 32% for horizontal strains and 23% for vertical ones. A similar situation was found for maximum stress values and the elasticity modulus $E_{cal} = 1110$ N/mm^2. In that case, the difference in horizontal strains about the test results was 72%, and in the vertical strains – 52%.

Table 7.4

Results for validation of the elasticity modulus E in stage III – horizontal strains

Model	E_{cal}, N/mm^2	E_{cal}/E_{init}	$\varepsilon_{x,el}$ $(0.33\sigma_{max})$	$\varepsilon_{x,el} / \varepsilon_{x,obs}$	$\varepsilon_{x,max}$ (σ_{max})	$\varepsilon_{x,max} / \varepsilon_{x,obs}$
C1	1100	0.98	$1.57 \cdot 10^{-4}$	1.80	$4.83 \cdot 10^{-4}$	0.72
C2	1121	1.00	$1.55 \cdot 10^{-4}$	1.78	$4.66 \cdot 10^{-4}$	0.69
C3	1140	1.02	$1.53 \cdot 10^{-4}$	1.75	$4.69 \cdot 10^{-4}$	0.69
C4	1500	1.34	$1.24 \cdot 10^{-4}$	1.42	$3.76 \cdot 10^{-4}$	0.56
C5	1650	1.47	$1.16 \cdot 10^{-4}$	1.33	$3.53 \cdot 10^{-4}$	0.52
C6	1667	1.49	$1.16 \cdot 10^{-4}$	1.33	$3.50 \cdot 10^{-4}$	0.52
C7	1668	1.49	$1.16 \cdot 10^{-4}$	1.33	$3.54 \cdot 10^{-4}$	0.52
C8	**1669**	**1.49**	**$1.15 \cdot 10^{-4}$**	**1.32**	**$3.51 \cdot 10^{-4}$**	**0.52**
C9	1676	1.50	$1.15 \cdot 10^{-4}$	1.32	$3.54 \cdot 10^{-4}$	0.52
C10	1690	1.51	$1.14 \cdot 10^{-4}$	1.31	$3.51 \cdot 10^{-4}$	0.52
C11	1700	1.52	$1.14 \cdot 10^{-4}$	1.30	$3.52 \cdot 10^{-4}$	0.52
C12	**2069**	**1.85**	**$9.94 \cdot 10^{-5}$**	**1.14**	**$3.03 \cdot 10^{-4}$**	**0.45**
C13	2070	1.85	$1.24 \cdot 10^{-4}$	1.42	$3.03 \cdot 10^{-4}$	0.45

Table 7.5

Results for validation of the elasticity modulus E in stage III – vertical strains

Model	E_{cal}, N/mm^2	E_{cal}/E_{init}	$\varepsilon_{y,el}$ (0.33σ_{max})	$\varepsilon_{y,el}$ / $\varepsilon_{y,obs}$	$\varepsilon_{y,max}$ (σ_{max})	$\varepsilon_{y,max}$ / $\varepsilon_{y,obs}$
C1	1100	0.98	-8.99·10^{-4}	1.88	-2.71·10^{-3}	1.52
C2	1121	1.00	-8.82·10^{-4}	1.85	-2.66·10^{-3}	1.49
C3	1140	1.02	-8.68·10^{-4}	1.82	-2.62·10^{-3}	1.46
C4	1500	1.34	-6.59·10^{-4}	1.38	-1.99·10^{-3}	1.11
C5	1650	1.47	-5.99·10^{-4}	1.25	-1.81·10^{-3}	1.01
C6	1667	1.49	-5.93·10^{-4}	1.24	-1.79·10^{-3}	1.00
C7	1668	1.49	-5.93·10^{-4}	1.24	-1.79·10^{-3}	1.00
C8	**1669**	1.49	-5.92·10^{-4}	**1.24**	**-1.79·10^{-3}**	**1.00**
C9	1676	1.50	-5.90·10^{-4}	1.23	-1.78·10^{-3}	0.99
C10	1690	1.51	-5.85·10^{-4}	1.22	-1.77·10^{-3}	0.99
C11	1700	1.52	-5.82·10^{-4}	1.22	-1.76·10^{-3}	0.98
C12	**2069**	1.85	-4.78·10^{-4}	**1.00**	**-1.45·10^{-3}**	**0.81**
C13	2070	1.85	-4.78·10^{-4}	1.00	-1.45·10^{-3}	0.81

The values of the modulus of elasticity calibrated in stage I against the models of diagonally compressed walls did not provide a reliable estimation of the behavior of axially compressed walls. Therefore, another calibration was performed. It included a change in the value of the elasticity modulus E_{cal} to match the values of vertical deformations to the test results at the stress level equal to 0.33σ_{max} and σ_{max}. The agreement between the vertical strains and the test results at the level of normal stress equal to 0.33σ_{max} was found for model C12 at the modulus E_{cal} = 2069 N/mm^2 – Fig. 7.12a. The difference in the horizontal strains was 14%. Thus, the modulus of elasticity increased by 23% compared to the calibrated modulus of elasticity E_{cal} = 1676 N/mm^2 of the model subjected to diagonal compression. The vertical strains of model C8 at E_{cal} = 1669 N/mm^2 agreed with the test results at the stress level σ_{max}. Differences in horizontal strains determined from the numerical calculations and the tests were equal to 52% at the stress level σ_{max} – Fig. 7.12b. In that case, the modulus of elasticity E_{cal} increased by 52% compared to the calibrated modulus of elasticity E_{cal} = 1110 N/mm^2 of the models subjected to diagonal compression. Fig. 7.13 compares how changes in the modulus of elasticity affected the changes in vertical and horizontal strains at different normal stresses. The obtained relationships were clearly non-linear. At the stress level of 0.33σ_{max}, the curves representing horizontal and vertical strains intercepted at the point representing the elasticity modulus which increased by 18% regarding the value E_{init}. Then, the error in representing the horizontal and vertical strains would be at the same level of ca. 60%.
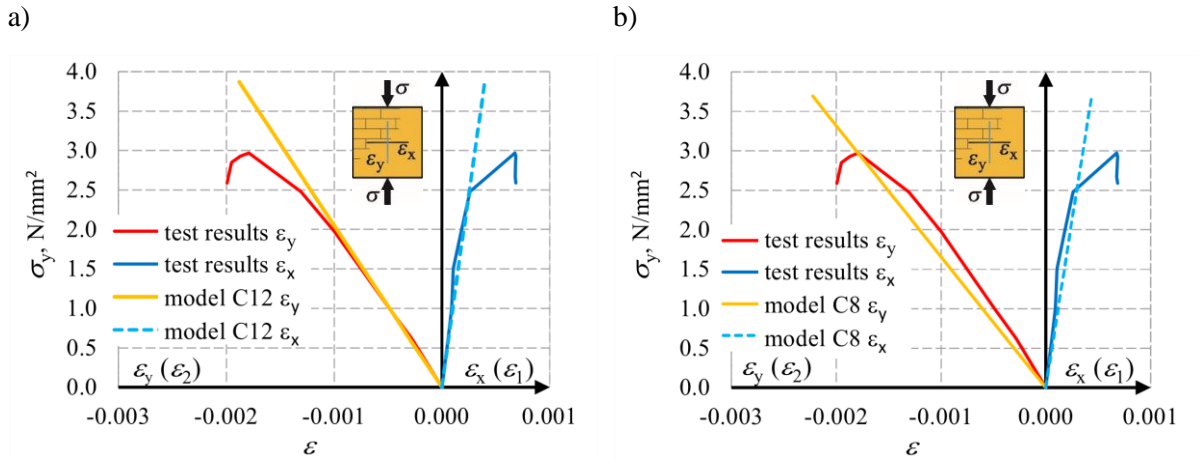
Fig. 7.12 Comparison of normal stress-horizontal and vertical deformation relationships for test results and numerical calculations: a) calibration of vertical deformation at $0.33\sigma_{max}$, b) calibration of vertical deformation at σ_{max}
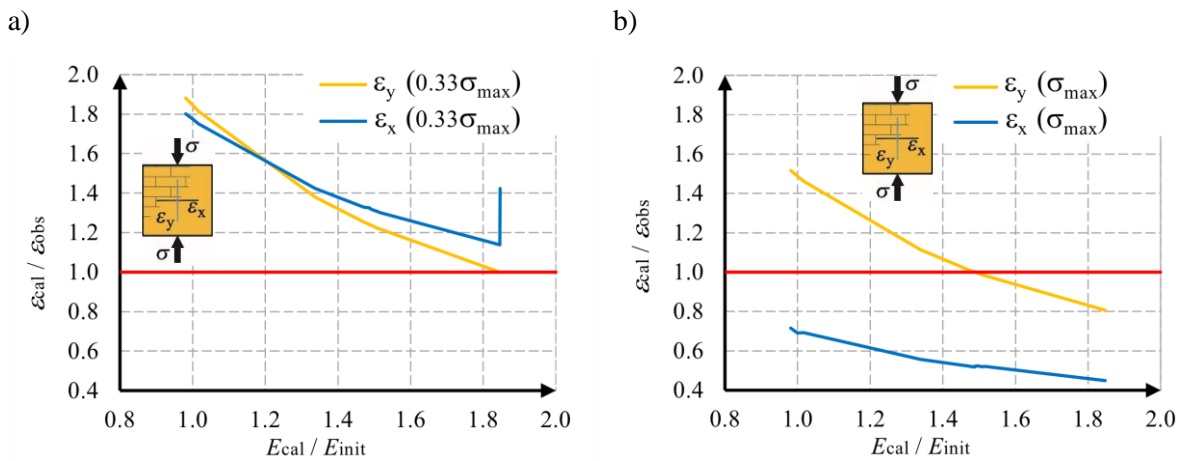
Fig. 7.13 The sensitivity analysis of the change in the elasticity modulus E to the value of the horizontal and vertical deformation: a) at $0,33\sigma_{max}$, b) at σ_{max}

At the normal stress σ_{max} within the analysed range of changes of the modulus of elasticity E, the curves were non-linear and clearly divergent. No value of the modulus E could be determined, at which the estimating error for horizontal and vertical strains would be at the same level. The curves also had different slope angles – a change in the modulus of elasticity caused a more rapid change in the vertical strains than the horizontal ones.

Stage IV – calibration of the tensile strength f_t of the diagonally compressed walls – the elasto-plastic damage model

The linear-plastic damage model was used in the subsequent stages of the calibration. The parameters shown in Table 7.6 were taken for further calculations. The value $E_{cal} = 2069$ N/mm^2 was assumed as the representative value of the elasticity modulus.

This parameter was calibrated for the wall models subjected to axial compression by matching the vertical strains to the test results at the level of standard stress equal to $0.33\sigma_{max}$.

<div align="right">Table 7.6</div>

Material parameters – elasto-plastic damage model in stage IV

No.	Parameter	Based on:	Value
1	Modulus of elasticity E, N/mm^2	Calibration stage III – Table 7.5	2069
2	Uniaxial compressive strength f_c, N/mm^2	Tests on compressed walls – Table 7.2	2.97
3	Plastic strain under compression ε_{pl}	Tests on compressed walls – Table 7.2	$3.33 \cdot 10^{-4}$
4	Uniaxial tensile strength f_t, N/mm^2	Tests on cylindrical AAC specimens (Ø60×x120mm) – Table 7.1	0.61
5	Poisson's ratio	Tests on compressed walls – Table 7.2	0.18
6	Fracture energy G_f, MN/m	Tests on AAC specimens – Table 7.1	$5.21 \cdot 10^{-5}$
7	Softening function in tension	Softening described by the exponential function	-
8	Ultimate displacement in compression w_d, m	Constant value	0.0005
9	Displacement w_c in tension, m	Calculated based on the cracking energy from the relationship $w_c = 5.14(G_f/f_t)$	-
10	Reduced compressive strength in the direction parallel to cracks	Default value	0.8
11	Coefficient of stiffness reduction coefficient in shearing	Constant value as for ordinary concrete	20
12	Crack spacing, m	Constant value	0.0005
13	The average size of aggregate, mm	Determined based on macroscopic observations of the masonry units	2.0
14	Eccentricity of elliptical function e	Determined from triaxial tests	0.52
15	Direction of plastic flow β	Taken as for incompressible material	0

The procedure of calibration in stage IV consisted in changing the tensile strength. The strength of a masonry unit determined from the cylindrical specimens Ø60×120 mm and equal to $f_t = 0.61$ N/mm^2 was taken as the reference value. The calculations were made for the models for shear walls (in diagonal compression), and their results are presented in Table 7.7.

Table 7.7

Shear wall calculation results - elasto-plastic damage model in stage IV

Model	$f_{t,cal}$, N/mm^2	$f_{t,cal}/f_t$	Θ_{el}, mrad	Θ_{el}/Θ_{obs}	Θ_{max}, mrad	$\Theta_{max}/\Theta_{obs}$
S20	0.610	1.000	0.115	0.81	0.339	0.54
S21	0.087	0.143	0.115	0.81	0.516	0.82
S22	0.078	0.128	0.115	0.81	0.613	0.97
S23	**0.076**	**0.125**	**0.115**	**0.81**	**0.637**	**1.01**
S24	0.075	0.123	0.115	0.81	0.655	1.03
S25	0.074	0.121	0.115	0.81	0.662	1.05
S26	0.070	0.115	0.115	0.82	0.692	1.10
S27	0.061	0.100	0.118	0.83	0.826	1.31
S28	**0.038**	**0.062**	**0.146**	**0.99**	**1.293**	**2.05**
S29	0.037	0.061	0.144	1.02	1.331	2.11
S30	0.0061	0.010	1.389	9.81	-	-

Due to a change in the tensile strength, the values of shear strain were matched to the test results for stress levels $0.33\tau_{max}$ and τ_{max} (the models S28 and S23). However, the shape of the curve representing the $\tau - \Theta$ relationship was not convergent, considering the complete range of shear stress values. The behavior of individual numerical models and the related test results are compared in Fig. 7.14.
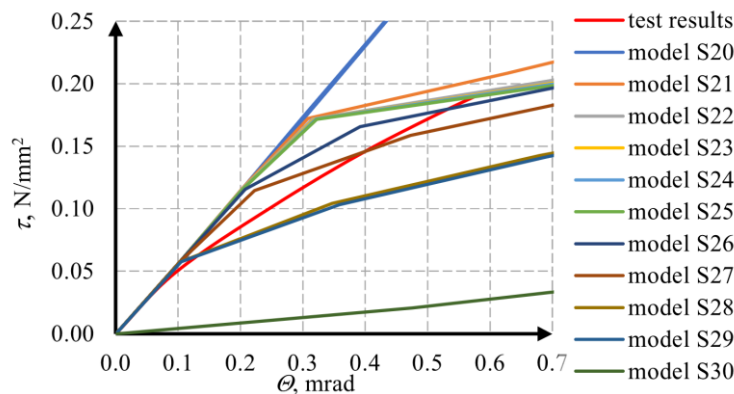
Fig. 7.14 Comparison of shear stress – deformation angle relationships for test results and numerical calculations in stage IV of calibration

By matching the angle of shear strain for model S28 at the stress level of $0.33\tau_{max}$, a huge discrepancy in the test results exceeding 200% was generated at the level of the failure stress. In model S23, whose tensile strength was reduced to 0.125 of the value f_t, the convergence of an angle of shear strain was reached at the level of ultimate stresses. At this tensile strength value, the shear strain estimation error was equal to 19% at the stress level of $0.33\tau_{max}$.

The sensitivity analysis of changes in tensile strength that affected the relationships between calculated results for an angle of shear deformation and the test results was conducted. This comparison was performed independently at two levels of shear stress. A change in the tensile strength had a non-linear effect on the behavior of the masonry subjected to shear loading. The calculations showed that there was no strength value $f_{t,cal}$, which could represent the behavior of the actual model in shear within the full range of stresses. The angle of shear deformation was precisely determined at ultimate stresses for the model S23, for which the best agreement was found between numerical calculations and test results. The calibrated tensile strength $f_{t,cal} = 0.076$ N/mm^2 was used in further calculations. Maps of maximum principal strains of the models S23 and S28 at stress levels $0.33\tau_{max}$ and τ_{max} are shown in Fig. 7.15, and charts for sensitivity analysis are shown in Fig. 7.16.
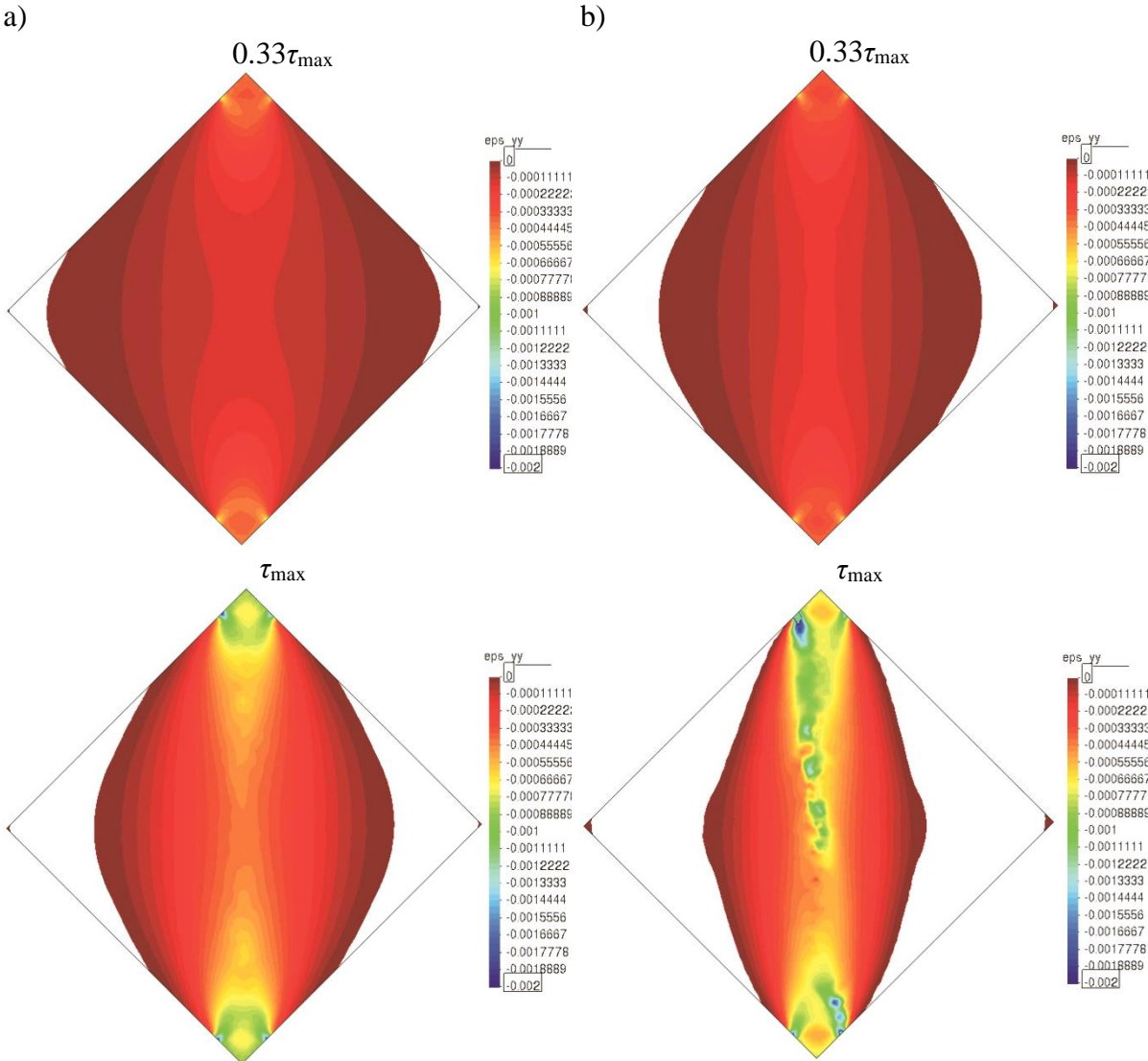

Fig. 7.15 Principal minimum strain of the selected numerical models: a) S23, b) S28
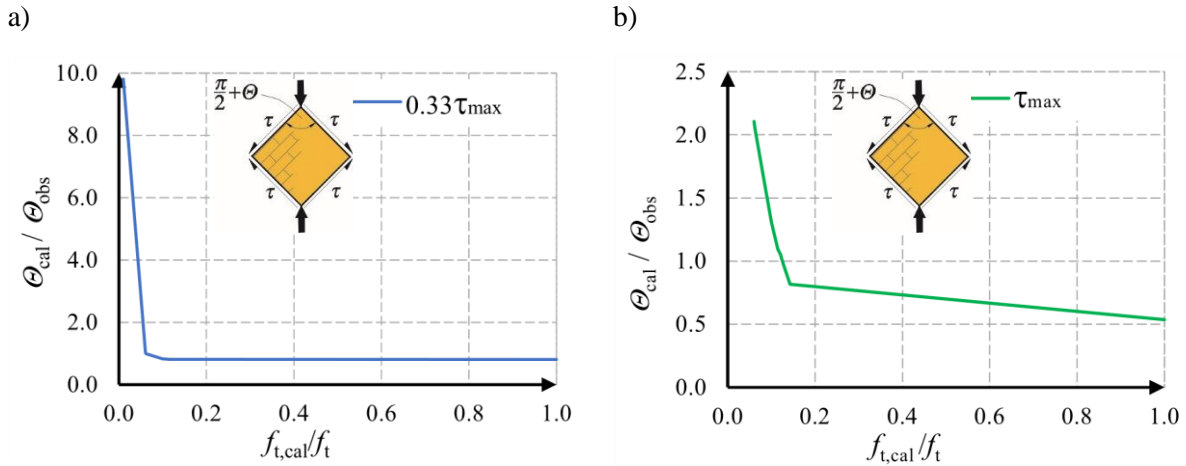
179

Fig. 7.16 Sensitivity analysis of the change in the tensile strength to the value of the strain angle: a) at $0.33\tau_{max}$, b) at τ_{max}

Stage IV-A - calibration of cracking energy G_f of walls in diagonal compression – the elasto-plastic damage model

The subsequent stages of the calibration verified the effect of the remaining mechanical parameters on the behavior of numerical models for shear walls. The tensile strength value $f_{t,cal} = 0.076$ N/mm^2, calibrated in stage IV, was taken in stage IV-A. The values of cracking energy G_f were changed by referring them to the reference value obtained from the masonry unit tests (Table 7.1). The results from numerical calculations are compared in Table 7.8.

Table 7.8

Shear wall calculation results - elasto-plastic damage model in stage IV -A

Model	$G_{f,cal}$ MN/m	$G_{f,cal}/G_f$	Θ_{el}, mrad	Θ_{el}/Θ_{obs}	Θ_{max}, mrad	$\Theta_{max}/\Theta_{obs}$
S31	$5.210 \cdot 10^{-3}$	100	0.1149	0.81	0.636	1.01
S32	$5.210 \cdot 10^{-4}$	10	0.1149	0.81	0.636	1.01
S23	$5.210 \cdot 10^{-5}$	1.00	0.1149	0.81	0.637	1.01
S33	$5.210 \cdot 10^{-6}$	0.10	0.1149	0.81	0.655	1.04
S34	$5.210 \cdot 10^{-7}$	0.01	0.1149	0.81	1.115	1.77
S35	$5.210 \cdot 10^{-8}$	0.001	0.1945	1.37	-	-

A change in the parameter G_f did not affect the angle of shear strain in the linear stage (at the value of shear stress equal to $0.33\tau_{max}$. An increase in the parameter by 10 and 100 times did not cause an increase in shear strains within the analysed range at the stress level of failure τ_{max}. A significant reduction of cracking energy intensified the model vulnerability at the post-elastic phase. The behavior of shear walls in the calibration stage IV-A is compared in Fig. 7.17. Figures 7.17a and 7.17b show the sensitivity analysis of the numerical models to the change in the analysed parameter.
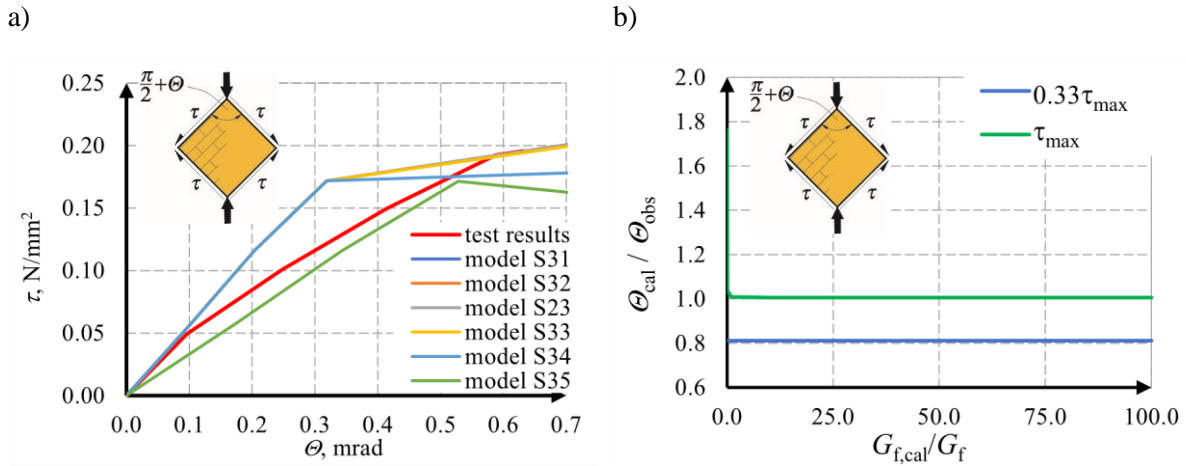
Fig. 7.17 Calibration results for stage IV-A: a) comparison of shear stress – deformation angle relationships for test results and numerical calculations, b) analysis of the sensitivity of the change in fracture energy to the value of the deformation angle at $0.33\tau_{max}$ and at τ_{max}

Stage IV-B - calibration of cracking energy G_f of walls in diagonal compression – the elasto-plastic damage model

A similar procedure of calibration was applied in stage IV-B. The elasticity modulus $E_{cal} = 2069$ N/mm^2 that was calibrated in stage III and tensile strength $f_{t,cal} = 0.076$ N/mm^2 from stage IV were used in these calculations. The impact of changes in plastic strain ε_{cp}, which was equated to plastic strain ε_{pl} of the wall in axial compression presented in Table 7.2, was tested against the results from numerical calculations. Following the calculations performed in stage IV-A, the calibrated cracking energy took the value $G_{f,cal} = G_f = 5.21 \cdot 10^{-5}$ MN/m shown in Table 7.1. The test results are presented in Table 7.9.

Table 7.9

Shear wall calculation results – elasto-plastic damage model in stage IV-B

Model	$\varepsilon_{cp,cal}$	$\varepsilon_{cp,cal} / \varepsilon_{cp}$	Θ_{el}, mrad	Θ_{el}/Θ_{obs}	Θ_{max}, mrad	$\Theta_{max}/\Theta_{obs}$
S36	$-3.330 \cdot 10^{-2}$	100	0.115	0.81	-	-
S37	$-3.330 \cdot 10^{-3}$	10	0.115	0.81	0.808	1.28
S23	$-3.330 \cdot 10^{-4}$	1.00	0.115	0.81	0.637	1.01
S38	$-3.330 \cdot 10^{-5}$	0.10	0.115	0.81	0.622	0.96
S39	$-3.330 \cdot 10^{-6}$	0.01	0.115	0.81	0.606	0.960

A change in the plastic strain did not affect the angle of shear strain at the level of representative cracking stress $0.33\tau_{max}$. The model stiffness in the non-linear regime decreased as the parameter decreased. However, matching the shape of the curve $\tau – \Theta$ to the test results was impossible despite the calibration of the analysed parameter – Fig. 18. Due to the validation, the value $\varepsilon_{cp,cal} = \varepsilon_{pl}$ was used in further calculations.
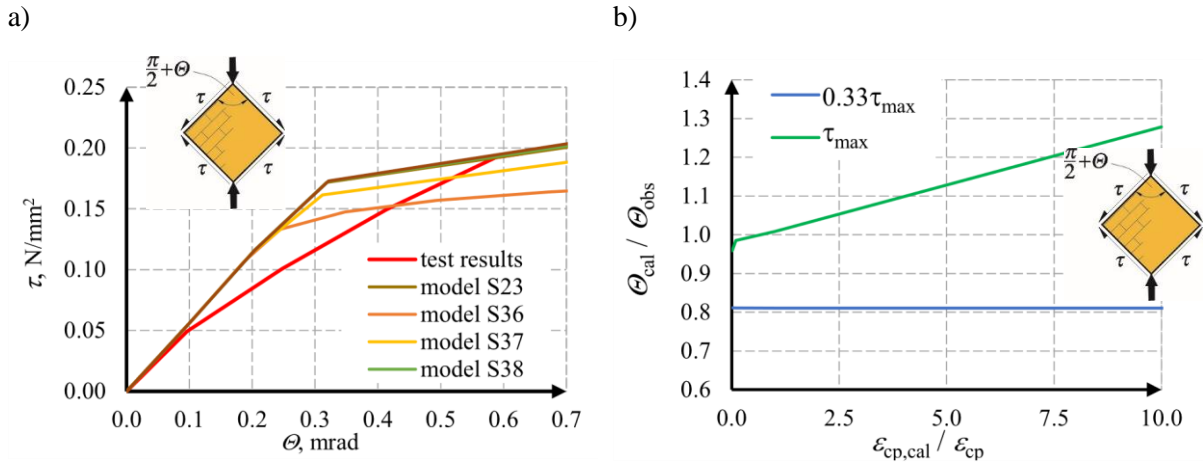
Fig. 7.18 Calibration results for stage IV-B: a) comparison of shear stress – deformation angle relationships for test results and numerical calculations, b) analysis of the sensitivity of the change in plastic deformation ε_{cp} to the value of the deformation angle at 0.33 τ_{max} and at τ_{max}

Stage V – calibration of compressive strength f_c of the wall model in axial compression – the elasto-plastic damage model

The tensile strength of the masonry in compression was calibrated in stage V. The following values were used in the calculations: elasticity modulus $E_{cal} = 2069$ N/mm², cracking energy $G_{f,cal} = G_f = 5.21 \cdot 10^{-5}$ MN/m, plastic strain $\varepsilon_{cp,cal} = \varepsilon_{pl} = -3.330 \cdot 10^{-3}$ (cf Table 7.2), and tensile strength $f_{t,cal} = 0.076$ N/mm². The numerical calculations for shear walls were based on these assumptions, and three different values of compressive strength $f_{c,cal}$ were used – Table 7.10.

Table 7.10

Calculation results for compressed wall – elasto-plastic damage model in stage V
(comparison of horizontal and vertical deformations)

Model	$f_{c,cal}$, N/mm²	$f_{c,cal}/f_c$	σ_{max}/f_{cm}	$\varepsilon_{x,el}$ (0.33σ_{max})	$\varepsilon_{x,el} / \varepsilon_{x,obs}$	$\varepsilon_{y,el}$ (0.33σ_{max})	$\varepsilon_{y,el} / \varepsilon_{y,obs}$
C20	2.82	0.95	0.95	$1.02 \cdot 10^{-4}$	1.16	$-4.84 \cdot 10^{-4}$	1.01
C21	2.97	1.00	0.94	$1.02 \cdot 10^{-4}$	1.16	$-4.83 \cdot 10^{-4}$	1.01
C22	3.12	1.05	0.99	$1.01 \cdot 10^{-4}$	1.16	$-4.82 \cdot 10^{-4}$	1.01

A difference in the determined maximum stress values σ_{max} did not exceed 5% for all the numerical models with changed compressive strength of the masonry. The best agreement was found for model C22, for which the difference did not exceed 1% compared to the empirical value. For the horizontal strains determined at the level of 0.33σ_{max}, the calculated strains were greater by 16%, and a negligible difference was obtained for the vertical strains. The numerical calculations for the homogeneous model for the masonry can take the value of compressive strength equal to the average compressive strength determined from the tests $f_{c,cal} = f_c$. The comparison of stress-strain

relationships for the models C20, C21, and C22 is illustrated in Fig. 7.19. Maps of maximum principal strains of the models C21 and C22 at stress levels $0.33\tau_{max}$ and τ_{max} are shown in Fig. 7.20.
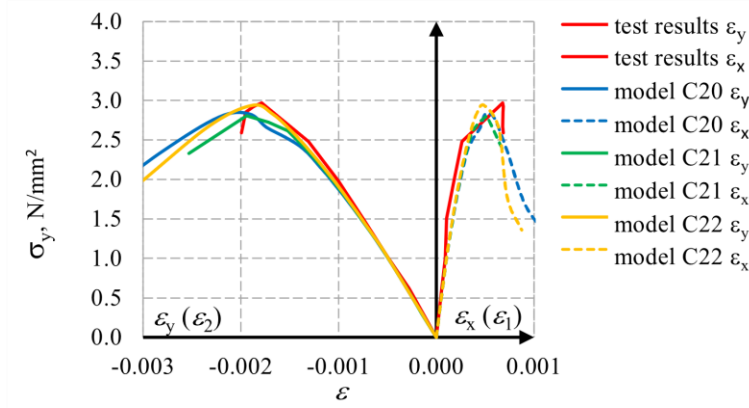

Fig. 7.19 Calibration results for stage V - comparison of normal stress – horizontal and vertical deformation relationships for test results and numerical calculations
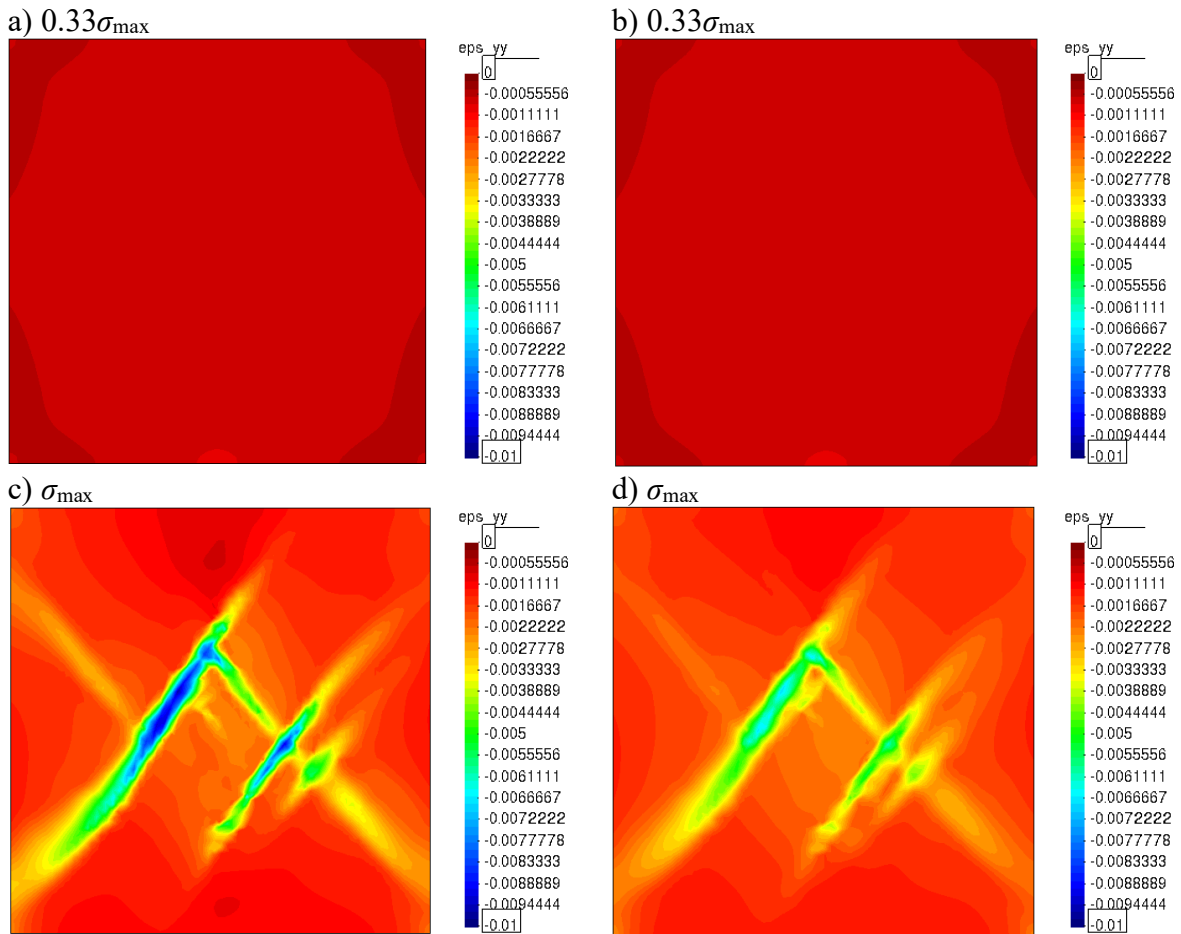
a) $0.33\sigma_{max}$

b) $0.33\sigma_{max}$

c) σ_{max}

d) σ_{max}

Fig. 7.20 Principal minimum strain of the selected numerical models: a) C21, b) C22

Comparison of crack images

The last analysed factor included images of the element cracking under the highest compressive stresses. Compared results from tests and calculations are shown in Fig. 21. Cracks in the numerical models for the walls in axial compression were developed diagonally from the base towards the centre. They formed two pyramids connected at their tops– Fig. 21a. The similar cracks were found in the test models at failure. However, the predominant cracks were running vertically in the extended head joints – Fig. 21b. Considering the numerical models for the walls in diagonal compression – Fig. 21c; the cracks cumulated in their central part. The test models – Fig. 21d had cohesive cracks that developed in the head and bed joints. The masonry units were also cracked with certain exceptions. To sum up, the images of cracks in the numerical models for masonry containing the homogeneous material were convergent only for compressed walls. The crack images showed only a certain tendency for the complex stress states with predominate shear stresses.
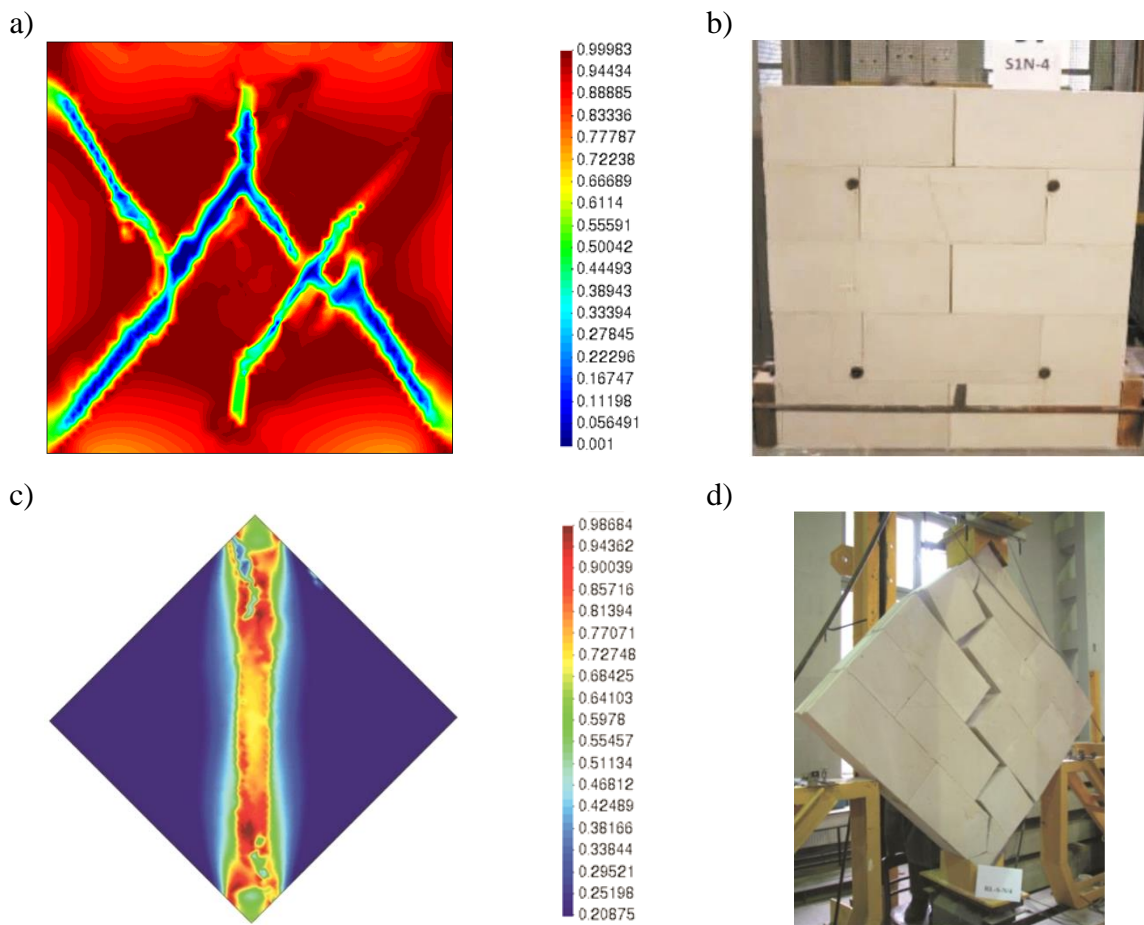
a)

b)

c)

d)

Fig. 7.21 Comparison of empirical images of cracking and images of cracking in calibrated numerical models: a) cracks in the numerical model C22 for the wall in axial compression, b) real images of cracking in the wall in axial compression, c) cracks in the numerical model S23 for the wall in diagonal compression, d) real images of cracks in the wall in diagonal compression

Discussion of calculated results

The proposed homogenization procedure for the AAC masonry was based on another approach than recommended in the literature. Instead of calculating the resultant parameters for the homogeneous model, the results obtained from the standardized tests on masonry models in axial and diagonal compression were taken as the reference level. Based on the tests on walls in diagonal compression, the initial value of the elasticity modulus for the masonry was determined in stage I. The correctness of the parameter used in the linear-elastic FEM models was verified in stage II.

Then, the elasticity modulus $E_{cal} = 2069$ N/mm^2 was calibrated against the linear-elastic FEM model for the compressed walls in stage III (there was an agreement between vertical strains in the axially compressed model with the standard tests at the level of cracking stresses). The determined value of the elasticity modulus was slightly higher than the empirical elasticity modulus for axially compressed wall equal to $E_{obs} = 2041$ N/mm^2 (cf Table 7.2). The elasticity modulus for the numerical calculation in the linear stage can take the value $E_{cal} = 1.01 E_{obs}$. It should be noted that the inverse approach was possible. It could be based on taking in stage I the value of the masonry elasticity, which was determined in the tests on axially compressed walls with the subsequent calibration against the walls in diagonal compression.

Stages IV and V verified the taken value of tensile strength for the elasticity modulus calibrated for the axially compressed model. The agreement of the vertical strains was found at the level of stresses $0.33\sigma_{max}$. In that case, the tensile strength of the AAC block equal to $f_{t,cyl} = 0.61$ N/mm^2, was assumed to be the trigger value (cf Table 7.1). This approach was very reasonable as the subject of the tests included the walls with thin joints at the minimum mortar content. Based on the conducted calibration of the models for diagonally compressed walls, the determined tensile strength was $f_{cal} = 0.076$ N/mm^2. Following the proposed homogenization method, the tensile strength could be determined from the equation $f_{t,cal} = 0.125 f_t$.

Regarding the diagonal compression strength of the masonry (cf Table 7.2), this relation was expressed as $f_{cal} = 0.39 f_{tm}$. The additional analysis was conducted in stages IV-A and IV-B. The sensitivity analysis of cracking energy Gf was in line with the cracking model I and plastic strains in compression ε_{cp}. The analyses were performed on the models in axial and diagonal compression. No significant effect on the obtained test results was found in both case. The developed approach seemed rather reliable for predicting strain and stress values in the state specified as the linear range of the wall behavior at maximum standard and shear stresses. Compressive strength $f_{c,cal}$ of the masonry was calibrated in stage V. The calculated and test results show the agreement

when $f_{c,cal} = f_c = 2.97$ N/mm^2. The final results of calibrating the linear and non-linear parameters for the masonry as the relationship between the stress-strain of the walls in diagonal and linear compression are presented in Fig. 7.22.

a)   b)
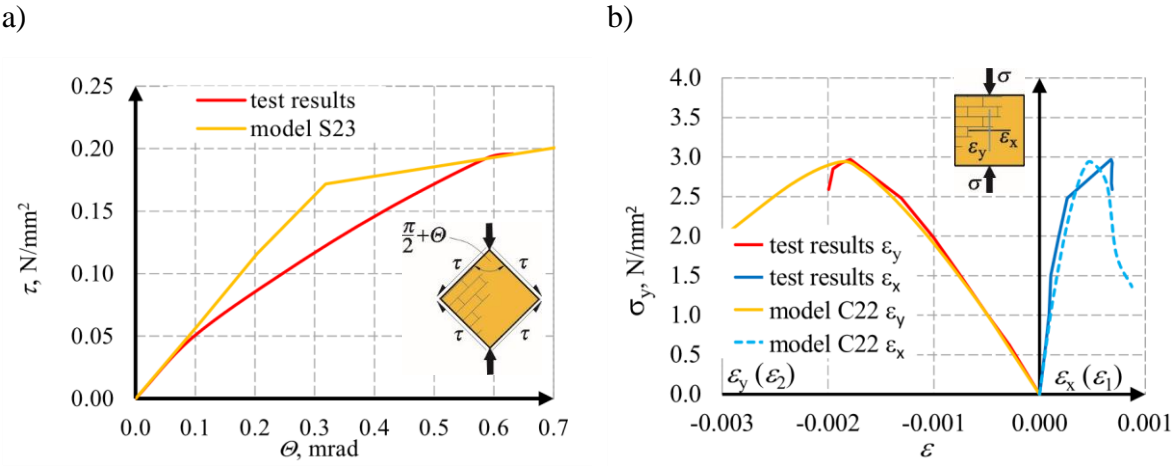

Fig. 7.22 Compared calculated and test results: a) comparison of shear stress-strain angle relationship for walls in diagonal compression, b) comparison of normal stress – a horizontal and vertical strain of compressed walls

The differences in results between the tests and calculations were at ±10%. It was possible to obtain a better agreement between these results providing that the model for the orthotropic material with adequate failure surfaces was used. However, this approach would be considerably beyond the range of the standard tests on masonry. The highest reliability of results was obtained for the crack pattern at failure. The numerical crack patterns in the compressed walls agreed with the test results. This effect was caused by softening of the masonry units, which predominate during the compression and are induced by the compression of AAC blocks. A different situation was observed for the walls in diagonal compression, for which the calculated images of cracks showed the trend observed during the tests. These findings resulted from neglecting the contact effects in the homogeneous model, which were noticed in the tests. Such imperfections of this model could not be eliminated and were identified as the main weaknesses of this approach. The conversion factors for the mechanical parameters of the homogeneous model intended for the practical application are presented in Table 7.11.

Table 7.11

Summary of empirical results for the masonry homogenization

Parameter	Test results		Parameter for the homogeneous model (FEM)	Conversion coefficient of the parameter	
	Tests on AAC block (AAC)	Tests on masonry (M)		$\dfrac{FEM}{AAC}$	$\dfrac{FEM}{M}$
Modulus of elasticity E, N/mm^2	2886	2041	2069	0.72	1.01
Tensile strength f_t, N/mm^2	0.61	0.196	0.076	0.12	0.39
Fracture energy G_f, MN/m	$5.21 \cdot 10^{-5}$	--	$5.21 \cdot 10^{-5}$	1.0	--
Plastic strain ε_{cp}	--	$-3.330 \cdot 10^{-3}$	$-3.330 \cdot 10^{-3}$	--	1.0
Compressive strength f_c, N/mm^2	4.95	2.97	2.97	0.60	1.00

Conclusions

The own empirical approach to calibrating the mechanical parameters for the homogeneous model for the masonry made of AAC masonry units was developed. At first, the elasticity modulus of the masonry was calibrated using the models of axially and diagonally compressed walls. They were linear-elastic FEM models. The elasticity modulus of the masonry, which correctly specified the vertical strains in axial compression, could be assumed as $E_{cal} = E_{obs}$. Other parameters were calibrated against the elasto-plastic FEM models with the combined Rankine and Menétrey-William boundary surfaces. The tensile strength of the masonry units was the most crucial parameter affecting the calculated results for the walls in axial and diagonal compression. Hence, the obtained empirical value used to calculate the tensile strength of the masonry model was expressed as $f_{cal} = 0.125 \, f_t$. Other parameters that controlled the material behavior in the softening phase in tension (cracking energy) and compression (plastic strain and compressive strength) had a minor effect on the masonry behavior. The values of stress and strain in compression and tension could be successfully determined using the procedure of empirical homogenization. However, the crack images would only agree if the compressive stresses predominated. To sum it up, the advantages of the described method of homogenization are as follows:

- easy determination of parameters for the masonry using the normalized models in axial and diagonal compression,
- simple development of the 2D FEM model with calibrated parameters for the masonry. The contact elements between the masonry units and mortar were neglected,
- the possible application of the homogeneous model to predict the relationship between stress and strain of the masonry in the complex state of stresses. The maximum error could be of the order of $\pm 10\%$,
- the adequate estimation of the masonry behavior in the elastic and post-elastic phase,
- and the adequate estimation of a crack pattern of the masonry mainly subjected to compressive stresses.

The obvious weaknesses of this procedure include:
- its limitation to the masonry made of solid elements with similar mechanical parameters of the orthotropic nature,
- incorrect specification of crack pattern for the walls that are mainly subjected to tensile stresses.

7.2. Full-scale nonlinear analysis

A full-scale numerical model was made to verify the empirical homogenization based on axial and diagonal wall compression tests. The building with a door opening in the stiffening wall A was analyzed. The main assumptions of the numerical model are:
- a spatial model of the building (Fig. 7.23) with a mesh size of 9.0 cm,
- the geometry of the numerical model was consistent with the research model MB-AAC-010/2,
- the model was fixed on the bottom surface of the walls – Fig. 7.24,
- the horizontal load was applied at the gravity center of the slab, as in the tests,
- the elastic material model represents the slab (concrete class C30/37) – Fig. 7.25,
- the elastoplastic material model with degradation represents the masonry walls, model parameters following Table 7.12,
- individual elements of the model are connected (inseparability of displacements).

Table 7.12

Parameters of the elasto-plastic material model (first calculation approach)

| No.	Parameter	Value
1	Modulus of elasticity E, N/mm^2	2069
2	Uniaxial compressive strength f_c, N/mm^2	2.97
3	Plastic strain under compression ε_{pl}	$3.33 \cdot 10^{-4}$
4	Uniaxial tensile strength f_t, N/mm^2	0.076
5	Poisson's ratio	0.18
6	Fracture energy G_f, MN/m	$5.21 \cdot 10^{-5}$
7	Softening function in tension	-
8	Ultimate displacement in compression w_d, mm	0.05
9	Displacement w_c in tension, m	-
10	Reduced compressive strength in the direction parallel to cracks	0.8
11	Coefficient of stiffness reduction coefficient in shearing	20
12	Crack spacing, m	0.0005
13	The average size of aggregate, mm	2.0
14	Eccentricity of elliptical function e	0.52
15	Direction of plastic flow β	0
16	Onset of crushing, MPa	0.16
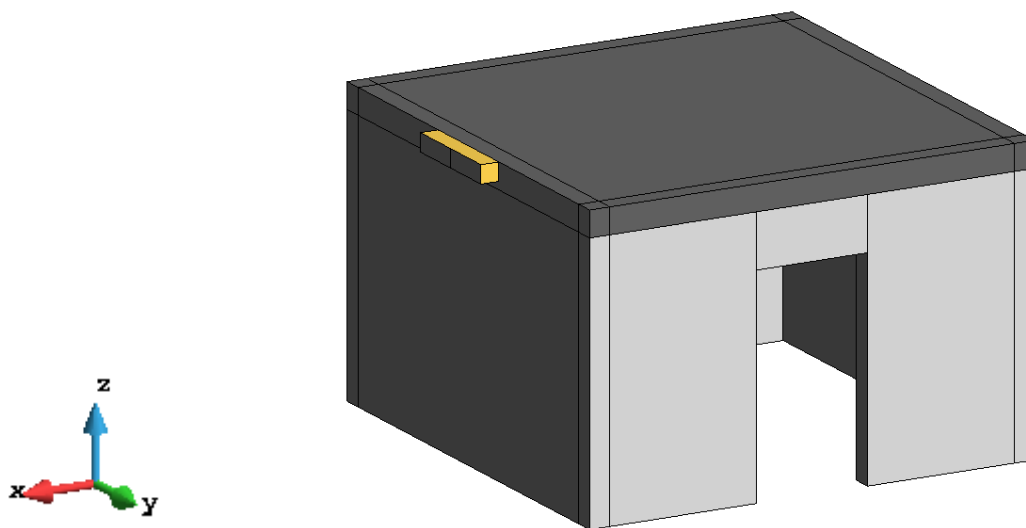
Fig. 7.23 Numerical model view (3D volume model) with the coordinate system
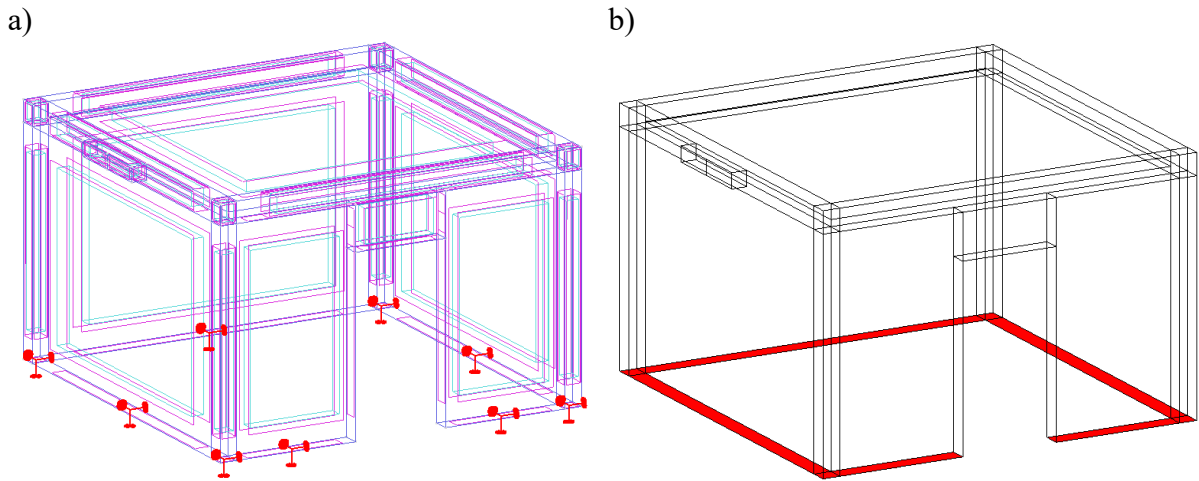
Fig. 7.24 Support boundary conditions: a) locked displacements in all directions, b) surface view of locked displacements

concrete
elastic material model

steelmaterial
elastic material model

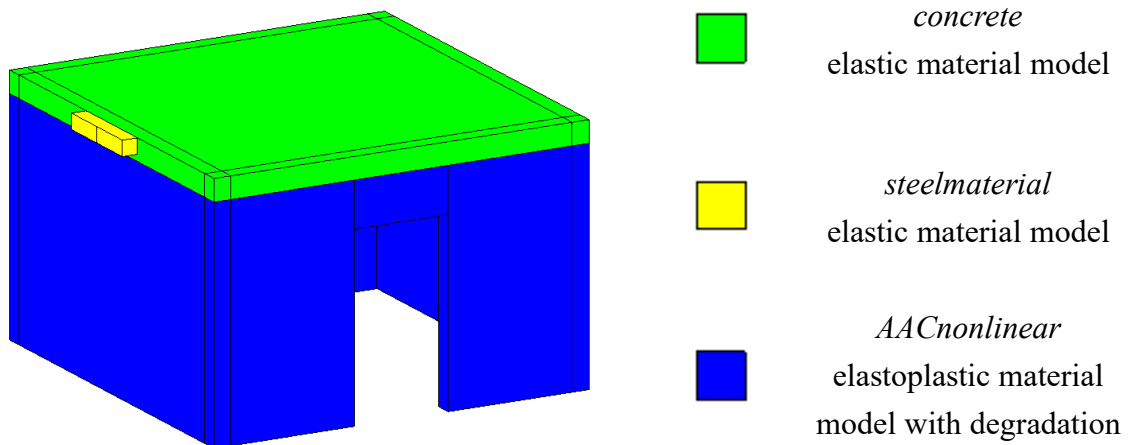AACnonlinear
elastoplastic material
model with degradation

Fig. 7.25 Material models for particular parts of the calculation building model

Loads were applied in stages in three sequences. A self-weight of walls and slab was applied in the first sequence – Fig. 7.26, and in the second sequence, the load corresponding to the weight of the finishing layers and the live load was set – Fig. 7.27. Load values were recalculated and applied to volumetric elements – Table 7.13. The horizontal load was applied at the end as a displacement for point – Fig. 7.28. After that, the model was divided into finite elements with a mesh size of 9.0 cm. The view of the 3D model with the FEM mesh is shown in Fig. 7.29.

Table 7.13

Load values in the calculation model

Types of load	Description	Value, kN	Weight for volume, kN/m^3
Dead-load	Self-weight of slab	57.00	26.888
Dead-load	Self-weight of walls	-	6.000
Live load	Live-load for floor	73.44	34.643

*volume of the slab in the calculation model: 3.64 m x 3.64 m x 0.16 m = 2.12 m^3

| | Weight of slab
-26.888 kN/m^3 |
| | Weight of walls
-6.00 kN/m^3 |
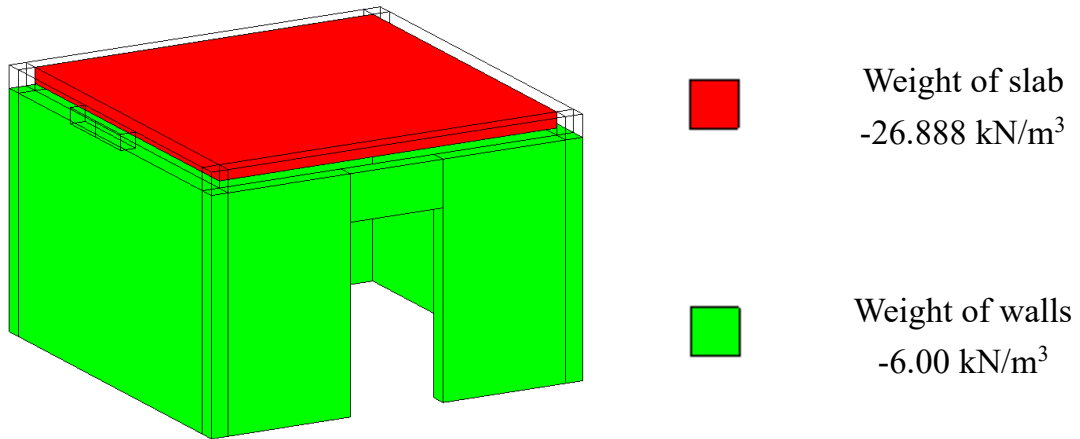
Fig. 7.26 First load sequence – self-weight of slab and masonry walls

| | Live load
-34.643 kN/m^3 |
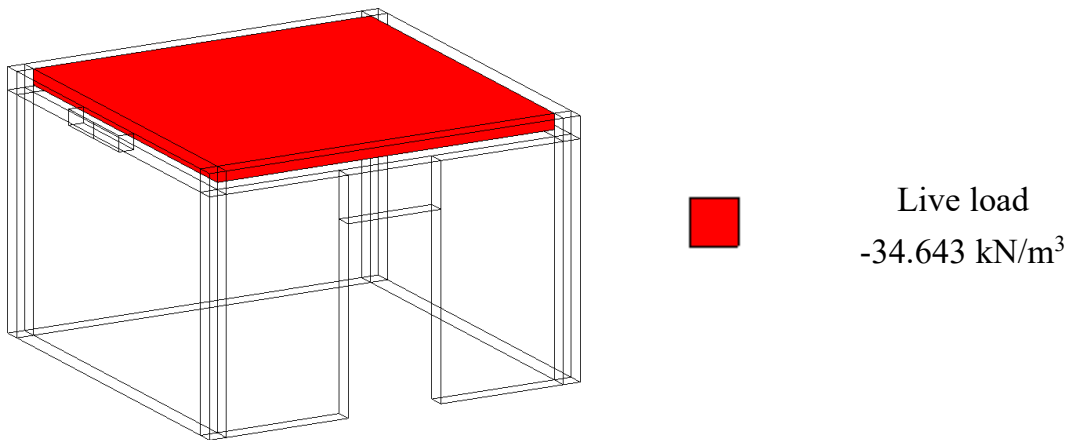
Fig. 7.27 Second load sequence – live load of a floor
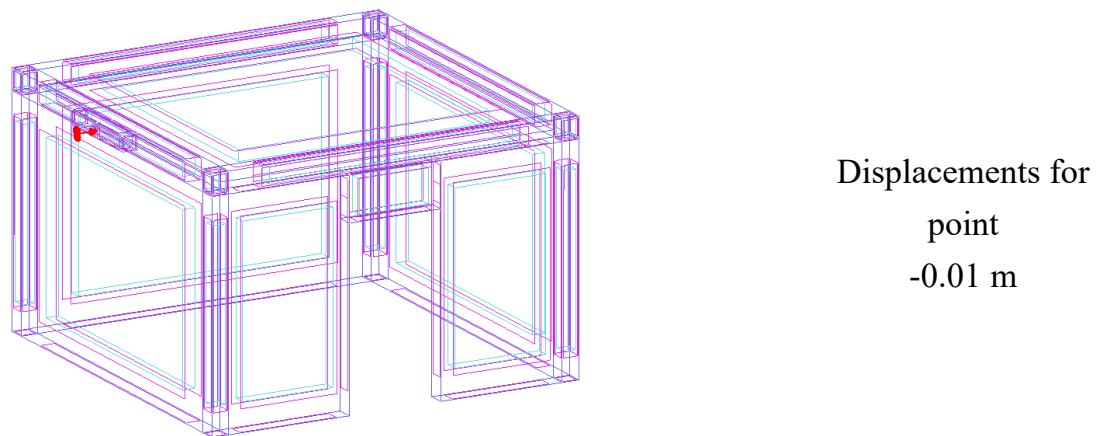

Displacements for
point
-0.01 m

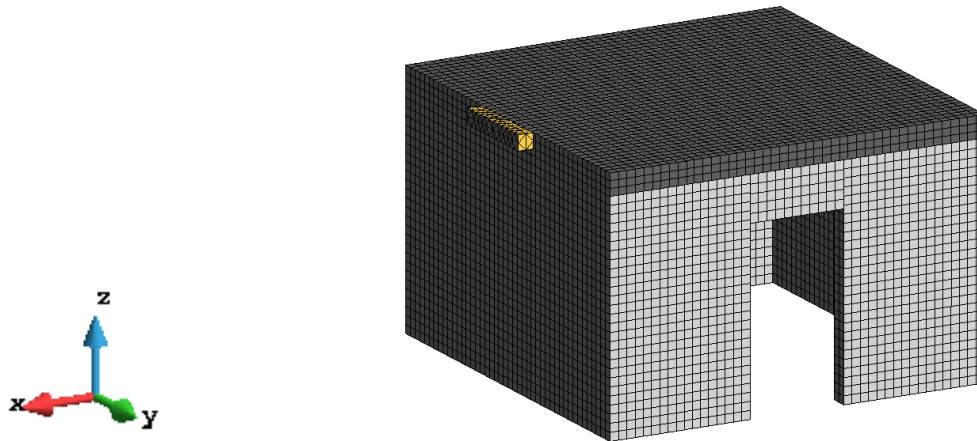Fig. 7.28 Third load sequence – horizontal load

Fig. 7.29 Mesh of finite elements with a mesh size of 9.0 cm

Calculation results were compared with the test results of the MB-AAC-010/2 model. The model validation criteria were established as follows:

- criterion A – the global behavior of the building expressed by the dependency $H_x – u_x$ (horizontal load – horizontal displacements of the stiffening walls A and B),
- criterion B – crack pattern

7.2.1. First calculation approach

The numerical calculations in the first approach do not agree with the test results. The maximum force of the numerical model was 214.78 kN, and the corresponding one in the test results was 69.25 kN – Table 7.14. The numerical model was also characterized by lower initial stiffness than the tested model. Fig. 7.30 compares the results, and Fig. 7.31 shows the values of horizontal displacements in the X-direction.

Table 7.14

Comparison of total forces between numerical and test results

Model		Nonlinear phase					
		$H_u,$ kN	$^{num}H_u,$ kN	$H_u / ^{num}H_u$	$u_u,$ mm	$^{cal}u_u,$ mm	$u_u / ^{num}u_u$
MB-AAC-010/2	Wall A	69.25	214.78	0.32	4.97	9.20	0.54
	Wall B				1.99	6.74	0.30

192
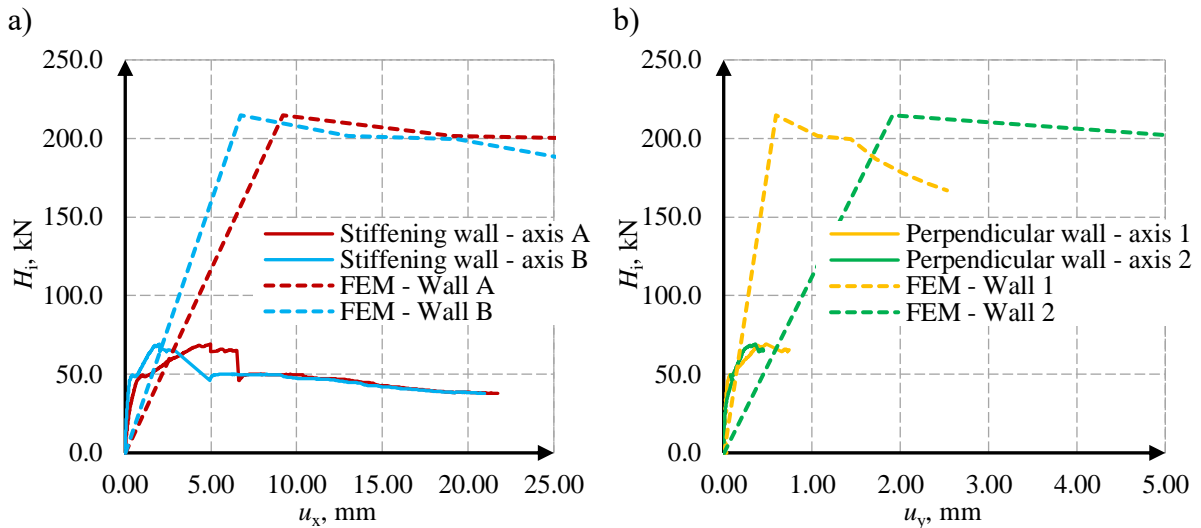
Fig. 7.30 First calculation approach - comparison of numerical calculations and test results: a) results for A and B walls, b) for 1 and 2 walls
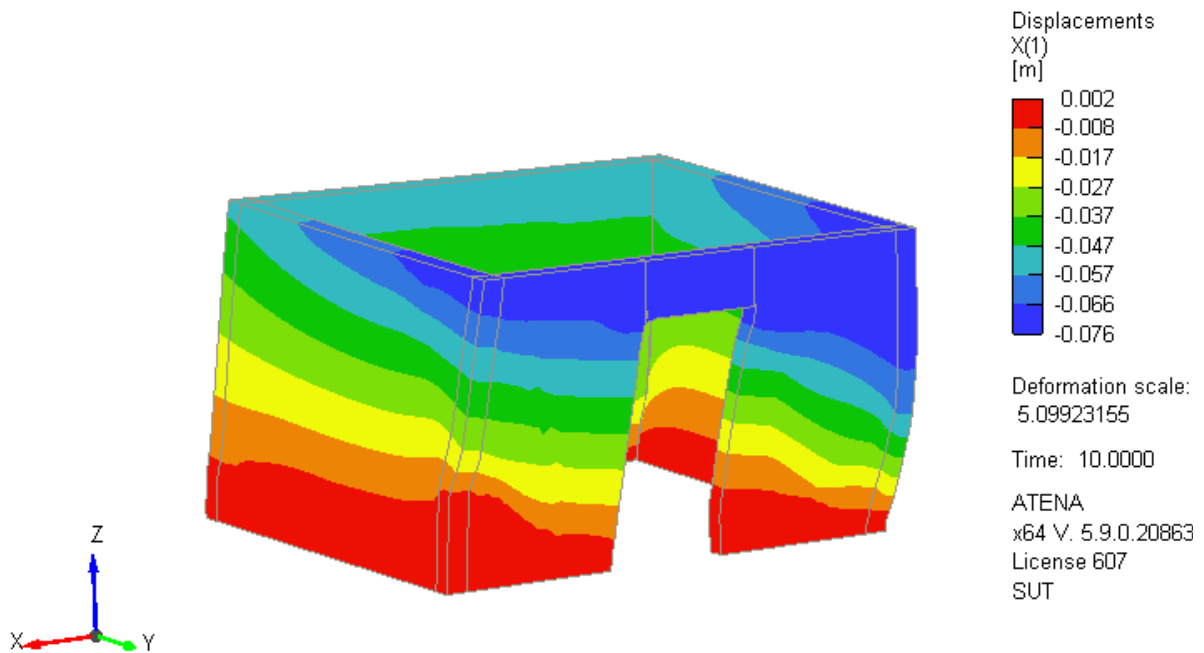
Fig. 7.31 Horizontal displacements in the X-direction of a nonlinear numerical model (first approach)

Furthermore, the analysis of criterion B showed that the crack pattern does not coincide with the test result. No cracks were obtained in the homogeneous numerical model. Therefore, instead of cracks, areas of material softening – (7.14) and (7.15) – are shown in Fig. 7.32 and Fig. 7.33. The crack pattern obtained in the calculations is diffuse - without dominant diagonal damage in the stiffening walls, as was in the test.

193

Fig. 7.32 Softening of the material – view of walls A and 2 of a nonlinear numerical model (first approach)

Fig. 7.33 Softening of the material – view of walls B and 1 of a nonlinear numerical model (first approach)

As the material model is isotropic and the real masonry behaves orthotopically, calibration of the homogeneous model is required (even if the model was calibrated on

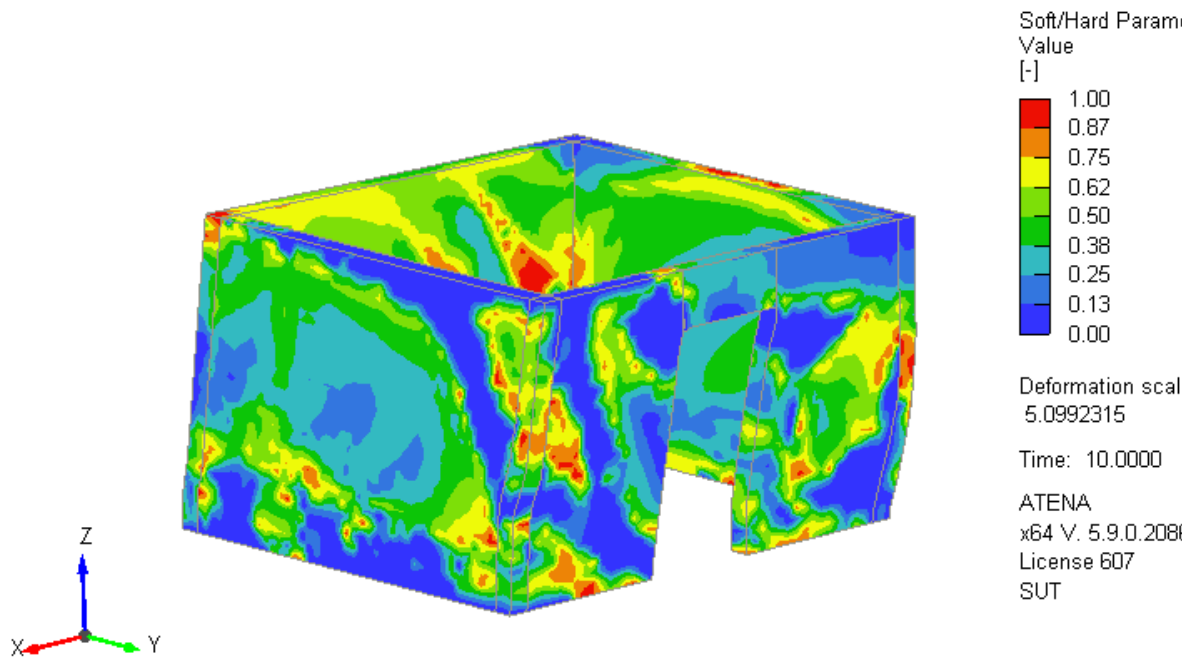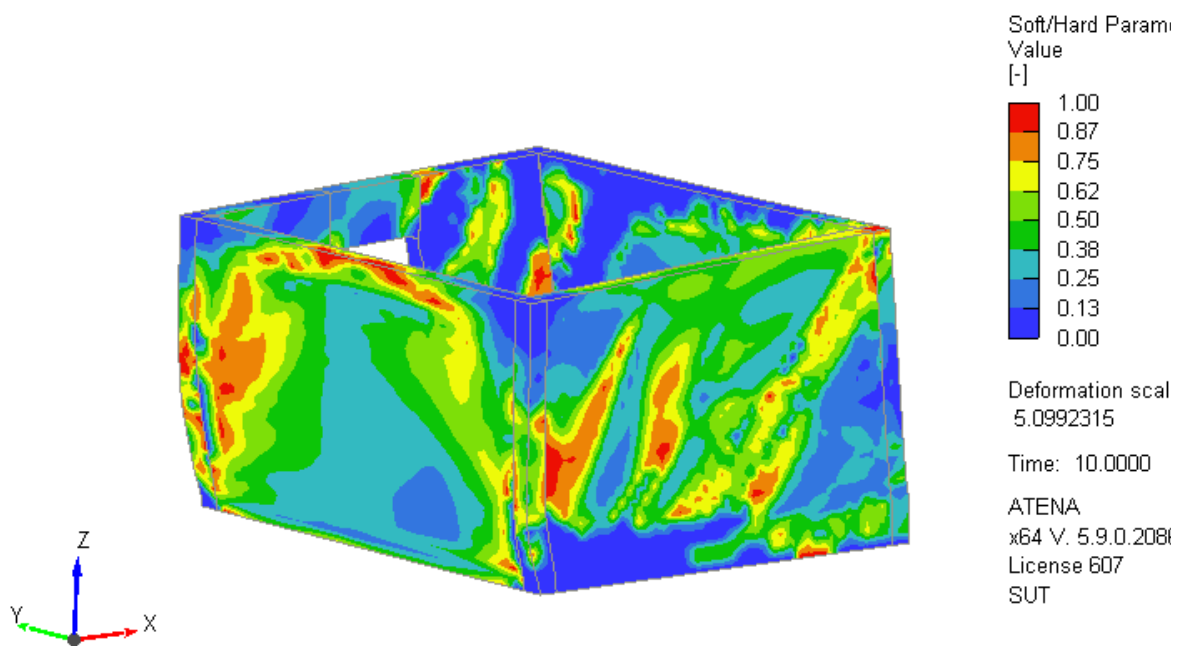walls with smaller geometry). Calibration of the tensile strength (second approach), fracture energy (third approach) and a combined model (fourth approach) in which both parameters were modified was analysed. When the tensile strength f_t was changed, the onset of crushing was also corrected as $-2.1f_t$. Table 7.15 shows the values of changed parameters.

The values of calibrated parameters in particular computational approaches

Calcula-tion ap-proach	Parameter	Test results		Parameter for the ho-mogeneous model (FEM)	Conversion coefficient of the parameter	
		Tests on AAC block (AAC)	Tests on masonry (M)		$\dfrac{FEM}{AAC}$	$\dfrac{FEM}{M}$
1	Tensile strength f_t, N/mm^2	0.61	0.196	0.076	0.12	0.39
	Fracture energy G_f, MN/m	$5.21 \cdot 10^{-5}$	-	$5.21 \cdot 10^{-5}$	1.00	-
2	Tensile strength f_t, N/mm^2	0.61	0.196	$1.00 \cdot 10^{-4}$	$1.64 \cdot 10^{-4}$	$5.10 \cdot 10^{-4}$
	Fracture energy G_f, MN/m	$5.21 \cdot 10^{-5}$	-	$5.21 \cdot 10^{-5}$	1.00	-
3	Tensile strength f_t, N/mm^2	0.61	0.196	0.076	0.12	0.39
	Fracture energy G_f, MN/m	$5.21 \cdot 10^{-5}$	-	$5.21 \cdot 10^{-10}$	$1.00 \cdot 10^{-5}$	-
4	Tensile strength f_t, N/mm^2	0.61	0.196	0.010	0.02	0.05
	Fracture energy G_f, MN/m	$5.21 \cdot 10^{-5}$	-	$5.21 \cdot 10^{-10}$	$1.00 \cdot 10^{-5}$	-

7.2.2. Second calculation approach

In the second calculation approach, the tensile strength was significantly reduced to the value $f_t = 1.00 \cdot 10^{-4}$ N/mm^2 (Table 7.15). The onset of crushing was adjusted to the value of $2.10 \cdot 10^{-4}$ N/mm^2. A better convergence of the maximum force value was

obtained; however, the horizontal displacements of the numerical model were greater than the real ones. Numerical stiffening wall A moved horizontally at maximum force by 10.37 mm and wall B by 5.66 mm – Table 7.16. In addition, the numerical models showed significantly lower stiffness than the tested building – Fig. 7.34.

Table 7.16

Comparison of total forces between numerical and test results

Model		Nonlinear phase					
		H_u, kN	$^{num}H_u$, kN	$H_u / ^{num}H_u$	u_u, mm	$^{cal}u_u$, mm	$u_u / ^{num}u_u$
MB-AAC-010/2	Wall A	69.25	85.90	0.81	4.97	10.37	0.48
	Wall B				1.99	5.66	0.35

Fig. 7.34 Second calculation approach - comparison of numerical calculations and test results: a) results for A and B walls, b) for 1 and 2 walls

The significant weakening of the masonry tensile strength resulted in a change in the damage to the building. The softening of the material was more concentrated in points (small areas) – Fig. 7.35. The nature of the damage to the stiffening wall B was similar to the test results - diagonal softening of the material – Fig. 7.36. At the intersection of the stiffening wall A and the perpendicular wall 1 (the lower part of the corner), material softening was indicated as it was in the tests.

Fig. 7.35 Softening of the material – view of walls A and 2 of a nonlinear numerical model (second approach)

Fig. 7.36 Softening of the material – view of walls A and 2 of a nonlinear numerical model (second approach)

7.2.3. Third calculation approach

The third approach concerned the reduction of the fracture energy - the tensile strength was the same as in the first approach (Table 7.15). This led to significant discrepancies between actual and numerical displacements – Table 7.17. Only the maximum force was similar to the test results – Table 7.18; the corresponding displacements differed significantly. The analyzed numerical model had lower initial stiffness than the tested building. The global behavior is presented in Fig. 7.37. The softening of the material is shown in Fig. 7.38 and Fig. 7.39.

Table 7.17

Comparison of total forces between numerical and test results – linear phase

Model		Nonlinear phase					
		H_{cr}, kN	$^{num}H_{cr}$, kN	H_{cr} / $^{num}H_{cr}$	u_{cr}, mm	$^{cal}u_{cr}$, mm	u_{cr} / $^{num}u_{cr}$
MB-AAC-010/2	Wall A	49.62	150.43	0.33	1.02	9.90	0.10
	Wall B				0.43	6.17	0.07

Table 7.18

Comparison of total forces between numerical and test results – nonlinear phase

Model		Nonlinear phase					
		H_u, kN	$^{num}H_u$, kN	H_u / $^{num}H_u$	u_u, mm	$^{cal}u_u$, mm	u_u / $^{num}u_u$
MB-AAC-010/2	Wall A	69.25	164.69	0.81	4.97	29.90	0.17
	Wall B				1.99	18.69	0.11
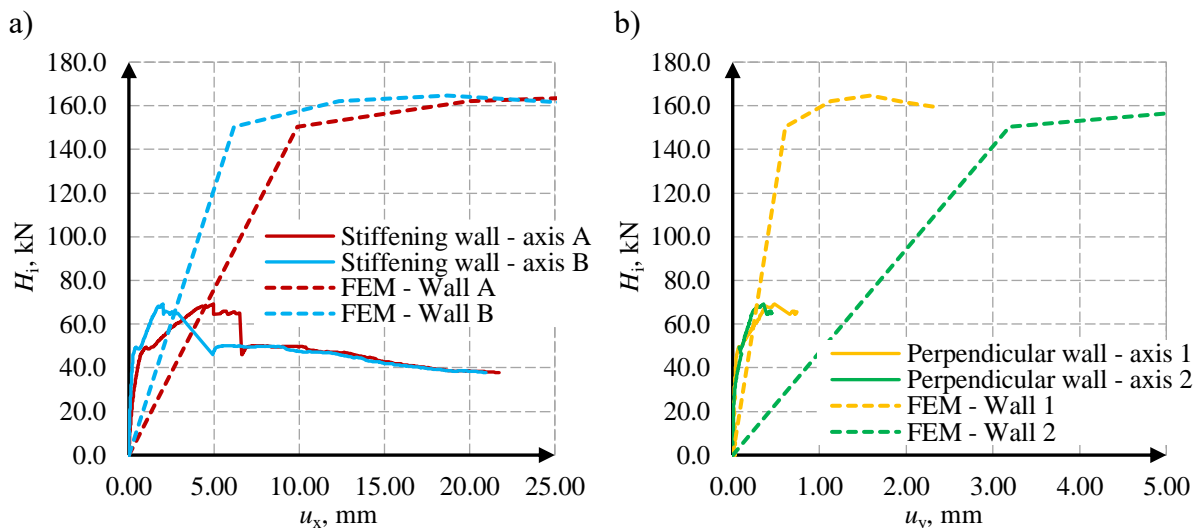
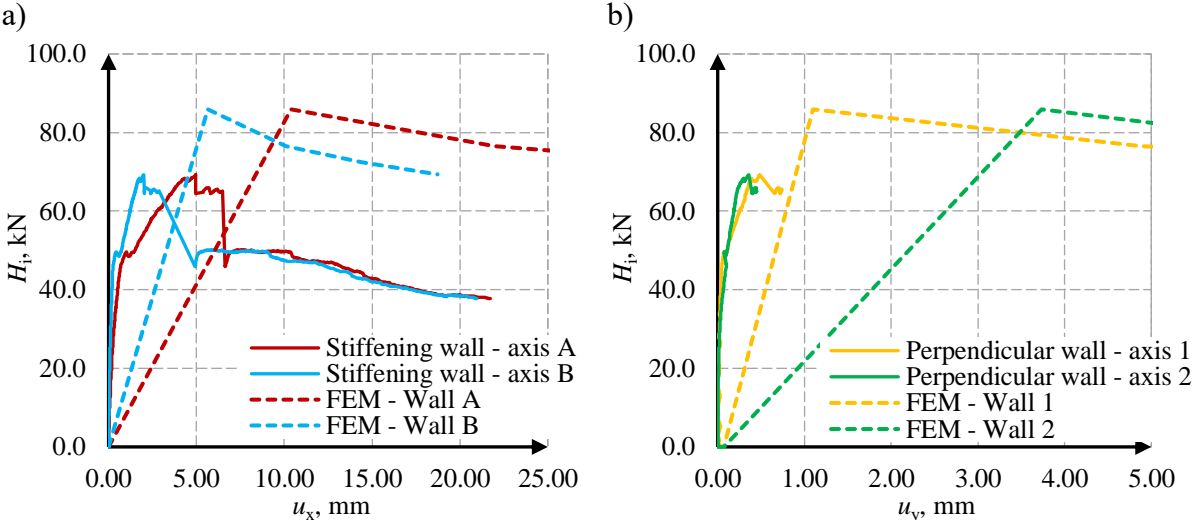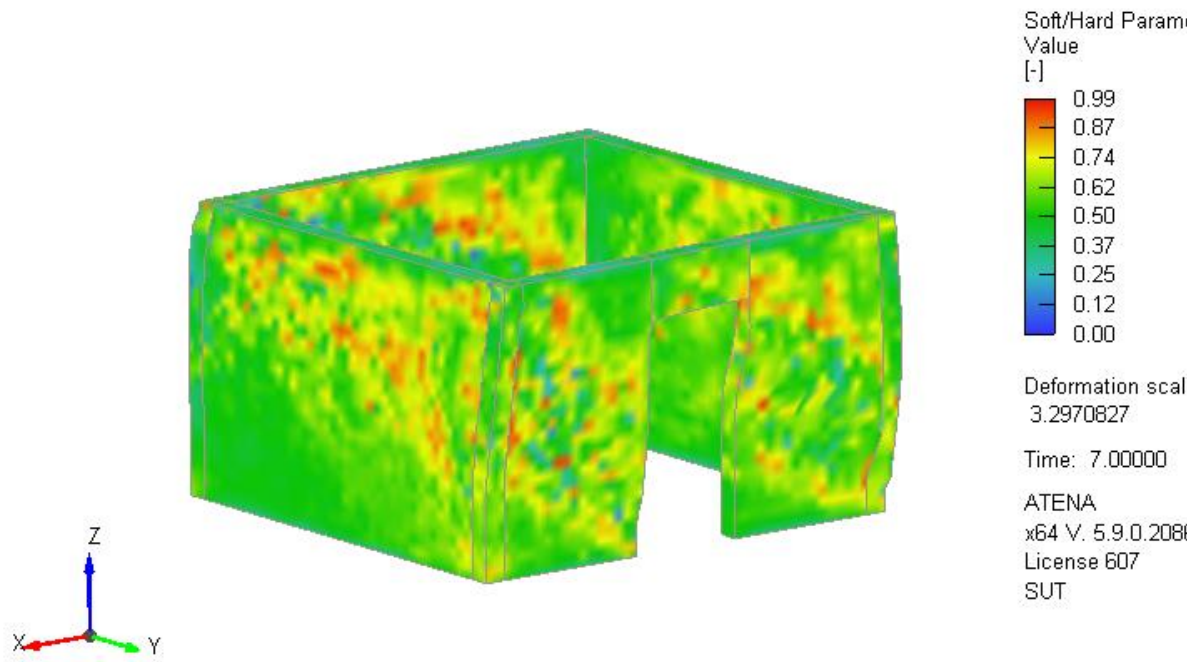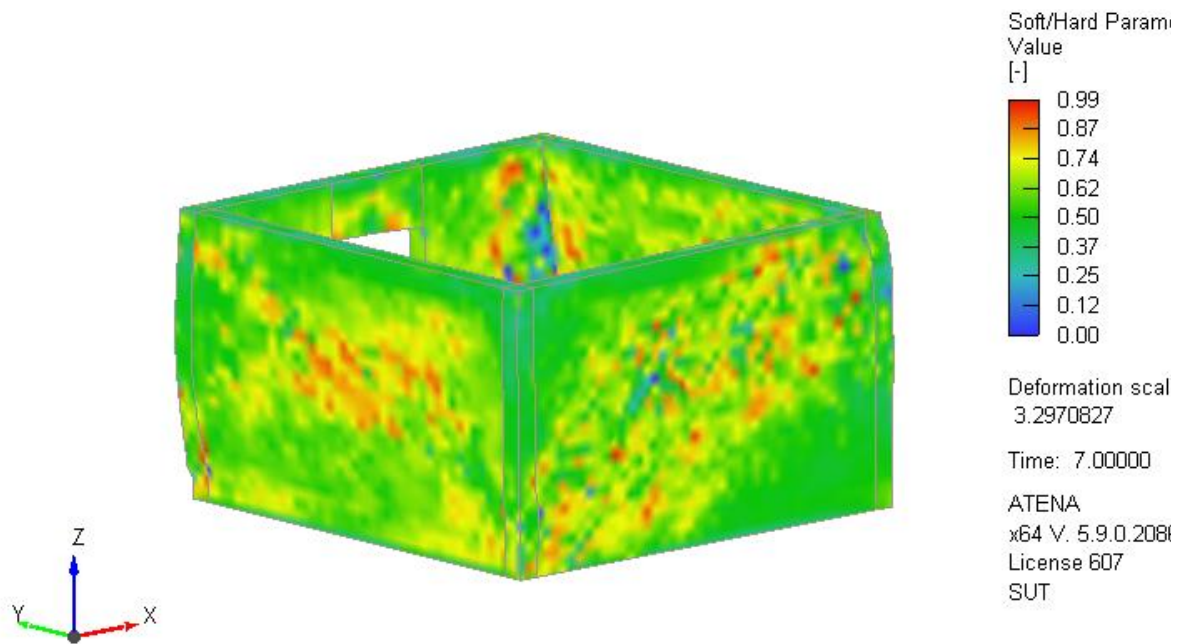Fig. 7.37 Third calculation approach - comparison of numerical calculations and test results: a) results for A and B walls, b) for 1 and 2 walls
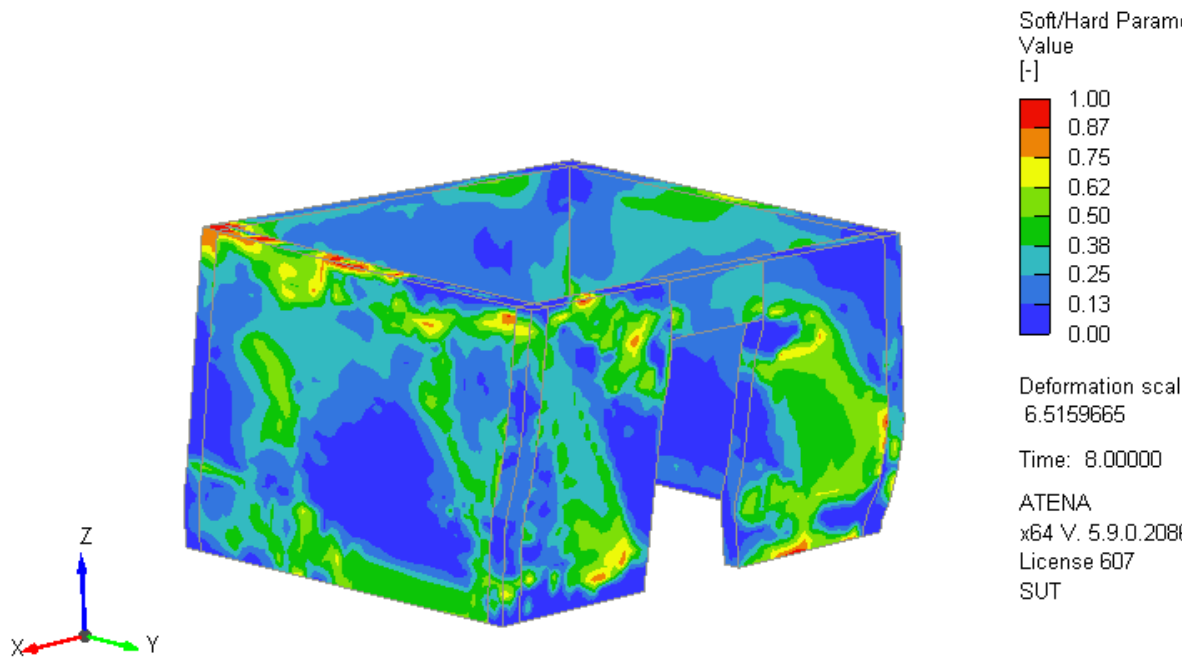
Fig. 7.38 Softening of the material – view of walls A and 2 of a nonlinear numerical model (third approach)
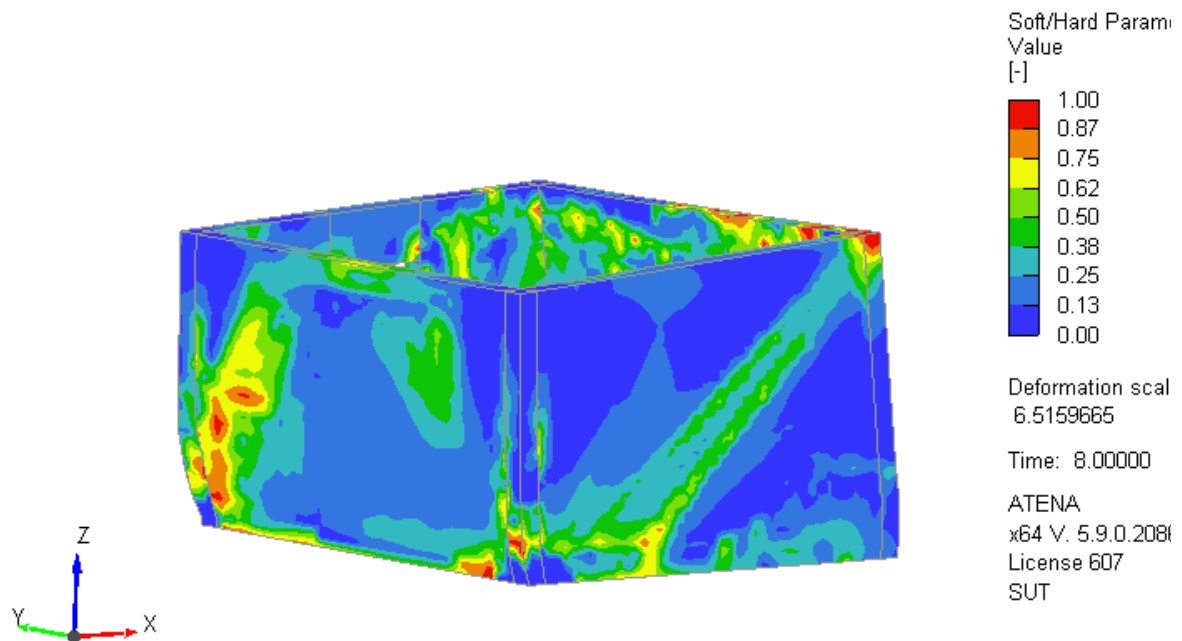
Fig. 7.39 Softening of the material – view of walls A and 2 of a nonlinear numerical model (third approach)

Although the cracking and maximum forces differed from the test results, a convergent crack pattern was obtained. The homogeneous model showed the formation of diagonal damage in walls A and B and local concentrations in the corners.

7.2.4. Fourth calculation approach

The fourth approach is a combined model in which the fracture energy (as in approach 3) and the tensile strength are reduced to value $f_t = 0.01$ N/mm^2 (the onset of crushing was 0.021 N/mm^2). The discrepancies in the horizontal displacements of the walls were significant both in the linear – Table 7.19 and nonlinear phases – Table 7.20. Reducing parameters lowers the initial stiffness (Fig. 7.40) - higher values lead to overestimating the structure's load capacity (maximum force).

Table 7.19

Comparison of total forces between numerical and test results – linear phase

Model		Nonlinear phase					
		H_{cr}, kN	$^{num}H_{cr}$, kN	H_{cr} / $^{num}H_{cr}$	u_{cr}, mm	$^{cal}u_{cr}$, mm	u_{cr} / $^{num}u_{cr}$
MB-AAC-010/2	Wall A	49.62	97.48	0.51	1.02	9.23	0.11
	Wall B				0.43	6.79	0.06

Table 7.20

Comparison of total forces between numerical and test results – nonlinear phase

| Model		Nonlinear phase					
		H_u, kN	$^{num}H_u$, kN	H_u / $^{num}H_u$	u_u, mm	$^{cal}u_u$, mm	u_u / $^{num}u_u$
MB-AAC-010/2	Wall A	69.25	116.28	0.60	4.97	28.56	0.17
	Wall B				1.99	19.78	0.10
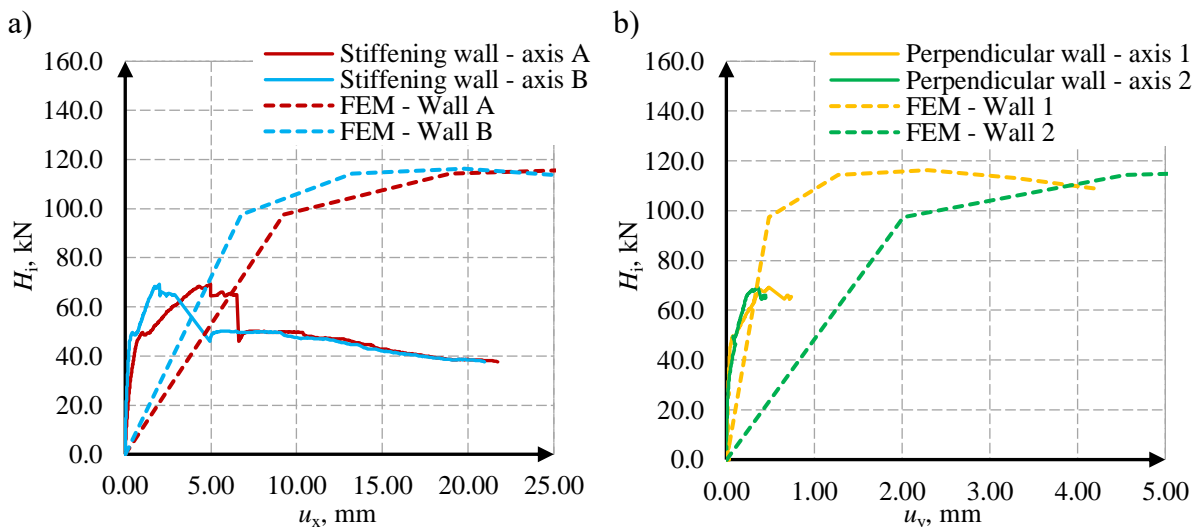
Fig. 7.40 Fourth calculation approach - comparison of numerical calculations and test results: a) results for A and B walls, b) for 1 and 2 walls

Changing the parameters also affects the crack pattern obtained – Fig. 7.41 and Fig. 7.42. In the fourth approach, the cracks (softening of the material in the numerical calculation) consistent with the test results were not obtained.
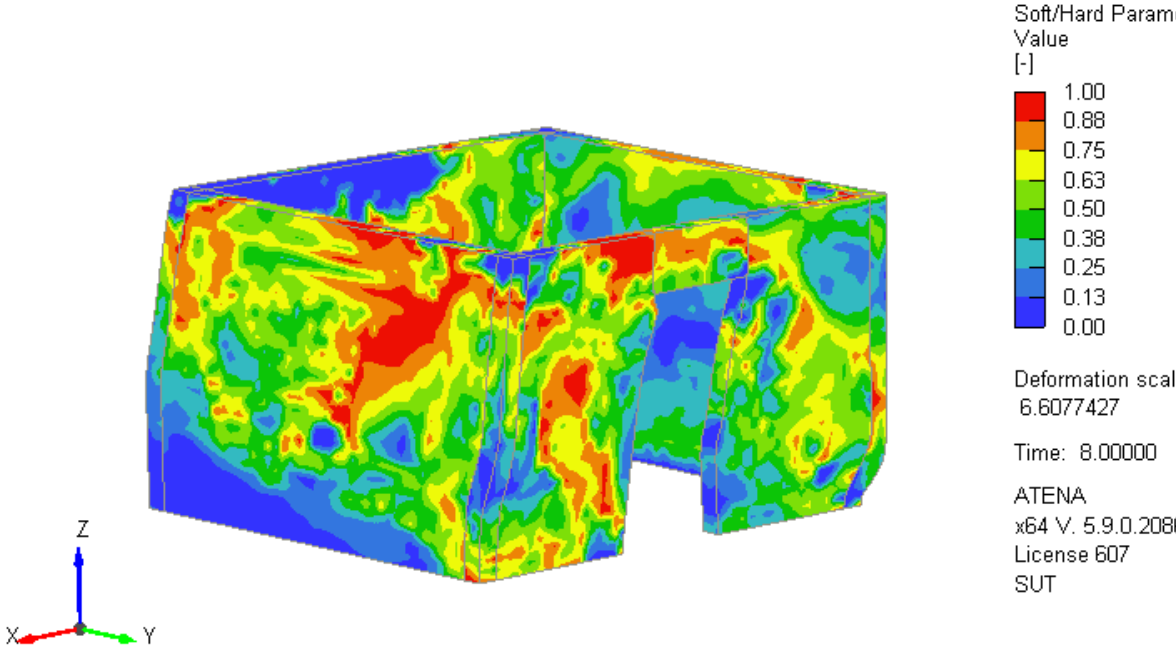
Fig. 7.41 Softening of the material – view of walls A and 2 of a nonlinear numerical model (fourth approach)

Fig. 7.42 Softening of the material – view of walls A and 2 of a nonlinear numerical model (fourth approach)

In conclusion, non-linear, full-scale numerical analyzes of the building with a door opening in the stiffening wall A were carried out. Validations were performed based on the results of testing the MB-AAC-010/2 model. Two criteria for verification of numerical models have been proposed: comparison of horizontal displacements (criterion A) and crack pattern (criterion B). The calculation results of four selected models are presented:

- the first approach – model with mechanical parameters calibrated on standard models,
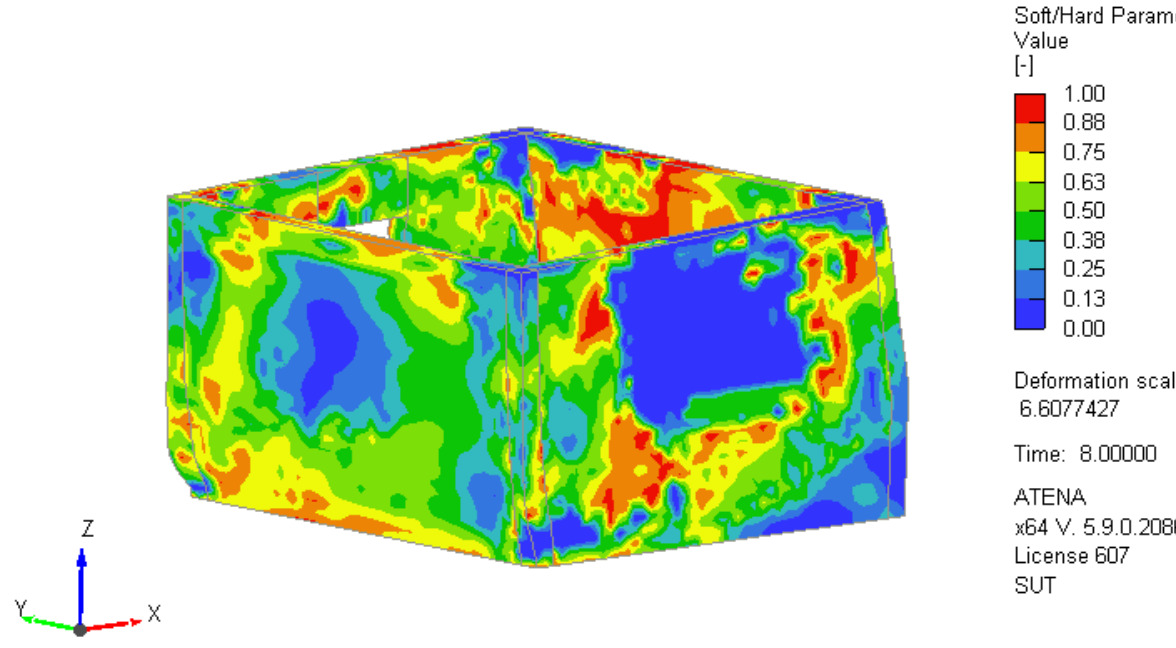- the second approach – model with reduced tensile strength ($f_t = 1.00 \cdot 10^{-4}$ N/mm^2),
- the third approach – model with reduced fracture energy ($G_f = 5.21 \cdot 10^{-10}$ MN/m),
- the fourth approach – combined model with reduced fracture energy as in approach third and reduced the tensile strength ($f_t = 0.010$ N/mm^2).

Calibration of the tensile strength reduced the models' load capacity - although no convergence with the test results was obtained. The reduction of the fracture energy G_f allowed for accurate representing of damage in the lack of convergence of criterion A. It should be added that the calculations were carried out on an isotropic, homogeneous model, which is a significant simplification of the masonry structure characterized by anisotropic behavior. Introducing contact surfaces (calculations on the micromodel) would allow for a better representation of stiffening masonry behavior.

The above calculations should be continued in a scheme similar to section 7.1 as a multi-stage calibration of mechanical parameters until the results converge based on criteria A and B. Complete solutions should also include an analysis of the sensitivity of parameter changes to validation criteria. The parameter correction β is expected to soften the masonry model and validate the numerical results. Another approach is introducing contact elements in the crack zones, e.g. in the tensile corner of the opening. Nevertheless, the calculated results indicate that validation based on relevant test findings is essential to advance nonlinear numerical calculations.

8. DISCUSSION

The behavior of stiffening walls is a complex issue consisting of multi-stage phases (initial phase, linear and nonlinear and residual one). Numerical simulations using advanced material models (e.g. elasto-plasic with degradation) allow for partially representing masonry behavior. However, this approach is time-consuming and labor-intensive. Multi-parameter models require structural tests and validation of the model each time, which is impractical and unfeasible from the engineering point of view. In addition, modelling all openings in the building may not be justified for designing the structure.

A significant simplification of calculations using elastic models without openings is proposed. Instead of modelling the openings in the numerical model, it can be replaced with a solid wall with reduced stiffness. This solution speeds up modelling and allows getting correct calculation results. Two approaches were analysed.

In the first model, the wall stiffness was the same as in the test results based on standards (uncalibrated model). In the second approach, the modulus of elasticity was calibrated (reduced) – Table 8.1.

Table 8.1

Results for calibrating the elastic modulus of numerical models

Model (approach)		Parameter	Test results		Parameter for the elastic model (FEM)	Conversion coefficient of the parameter	
			Tests on AAC block (AAC)	Tests on masonry (M)		$\dfrac{FEM}{AAC}$	$\dfrac{FEM}{M}$
1	Wall A	Modulus of elasticity E, N/mm^2	2886	2041	2041	0.71	1.00
	Walls B, 1, 2				2041	0.71	1.00
2	Wall A	Modulus of elasticity E, N/mm^2	2886	2041	35	0.01	0.02
	Walls B, 1, 2				1200	0.42	0.59

Vertical loads were omitted from the analysis because the reduction of the modulus of elasticity would lead to an incorrect estimation of slab deflections due to excessive vertical displacements of the wall. For this reason, the proposed approach applies only to the analysis of horizontal displacements under an acting lateral load. The numerical model was based entirely on the elastic material model – Fig. 8.1. Stiffening wall A with a door opening has been replaced with a solid wall.

concrete
elastic material model
steelmaterial
elastic material model
AACall
elastic material model
AACwallA
elastic material model
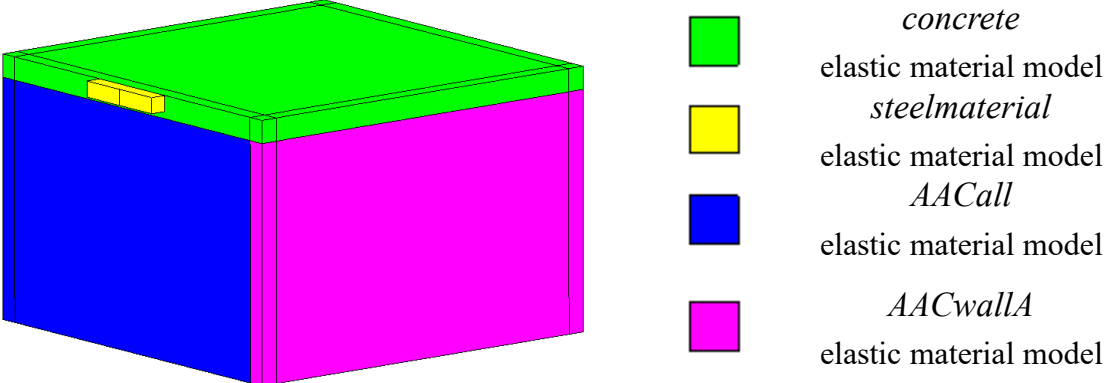
Fig. 8.1 Material models for particular parts of the calculation building model

The uncalibrated model was characterized by greater stiffness than the test results of the MB-AAC-010/2 model – Fig. 8.2. Moreover, the rotation of the building was not obtained (no displacements in the direction perpendicular to the acting load). Because the stiffness of all the walls was the same, only translation occurred. The values of horizontal displacements are presented as a map of displacements in Fig. 8.3.

Fig. 8.2 Comparison of numerical calculations and test results (elastic model 1): a) results for A and B walls, b) for 1 and 2 walls

Fig. 8.3 Horizontal displacements in the X-direction of a numerical model (elastic model 1)

In the second model, in which the wall stiffnesses were reduced, the correct values of stiffnesses were estimated - matched to the initial stiffnesses of the tested building (Fig. 8.4).

In addition, the rotation of the building resulting from the difference in stiffness of the walls was also indicated – Fig. 8.5. The calibration of numerical models can be done by reducing the modulus of elasticity or by reducing the wall thickness, depending on the chosen approach.
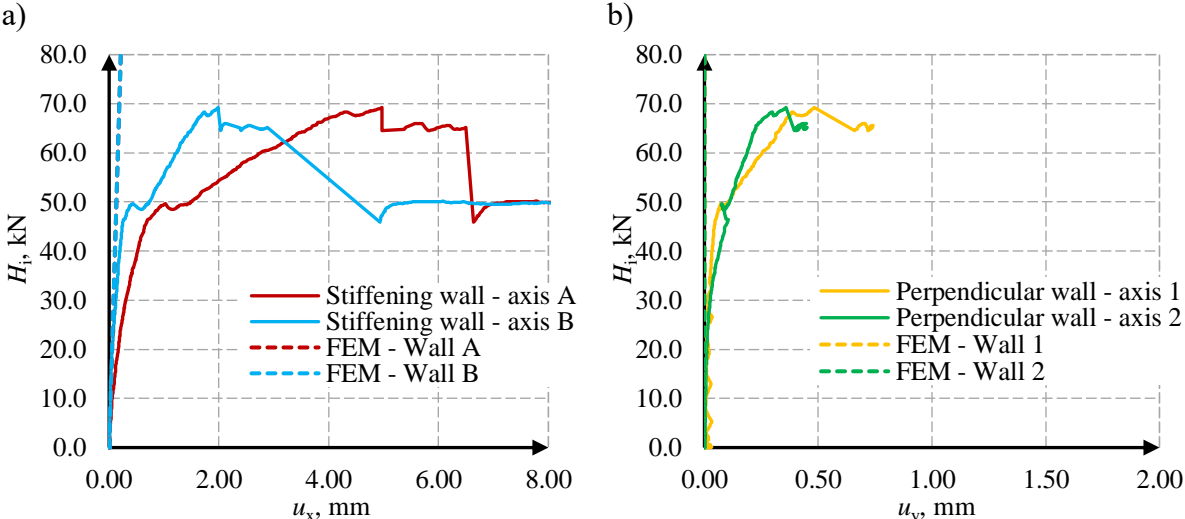

Fig. 8.4 Comparison of numerical calculations and test results (elastic model 2): a) results for A and B walls, b) for 1 and 2 walls

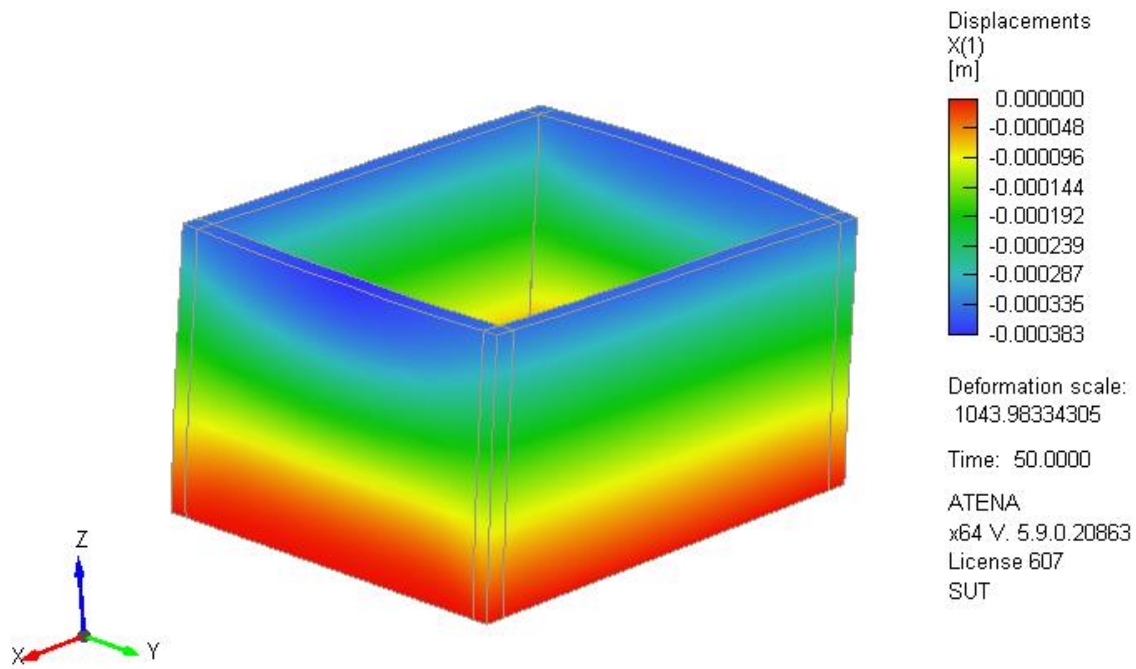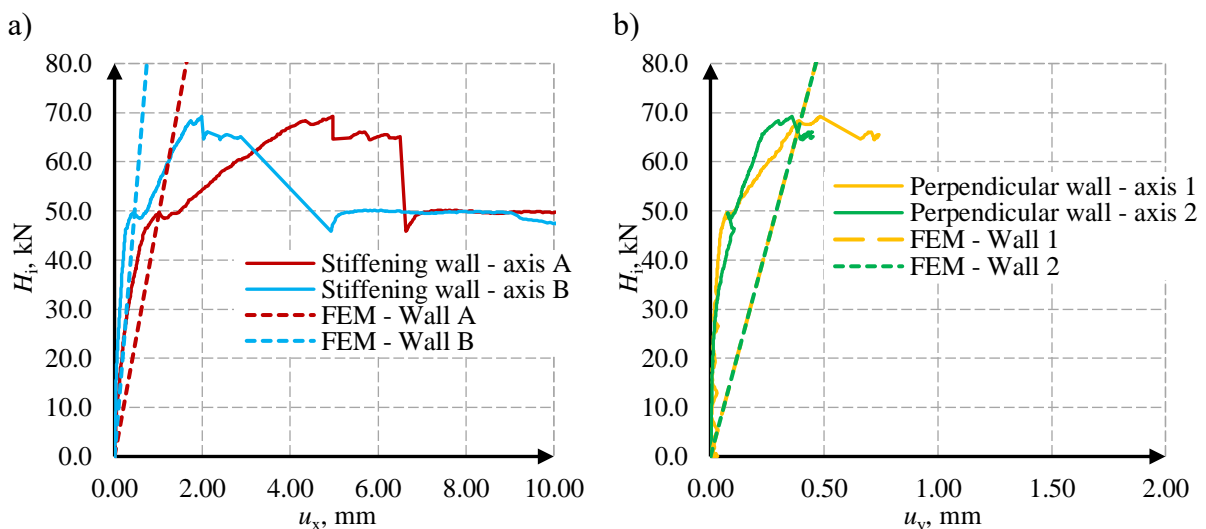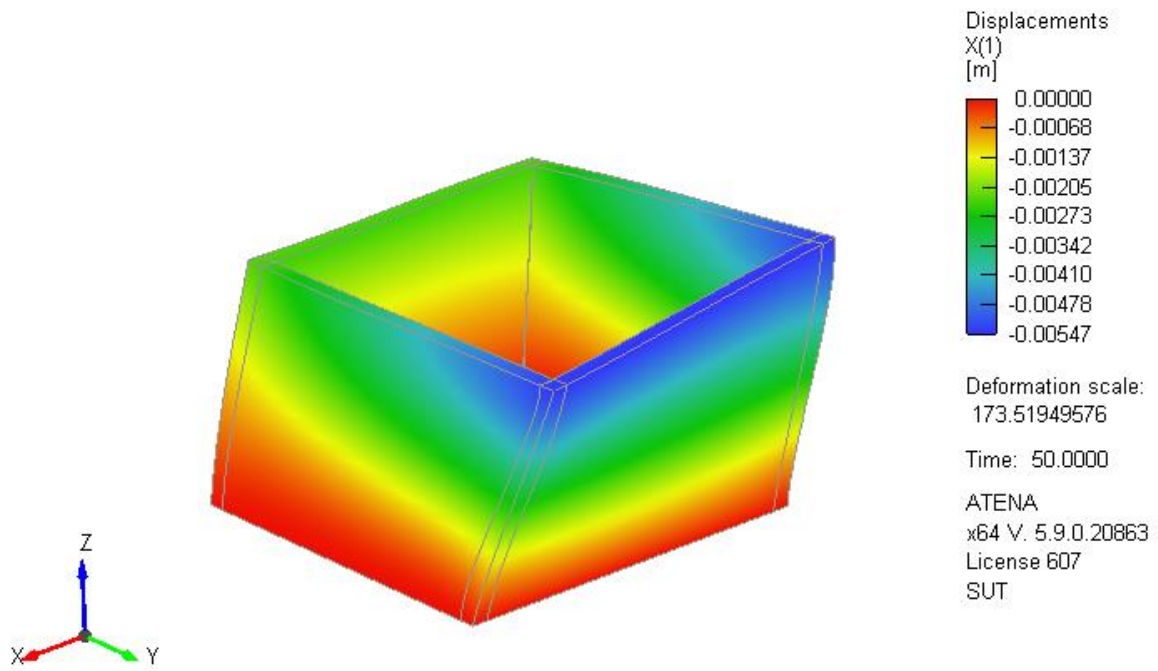Fig. 8.5 Horizontal displacements in the X-direction of a numerical model (elastic model 2)

The approaches to calculating stiffness presented in this dissertation are subject to some assumptions. The adopted static scheme of the wall or its components determines the final result in the total stiffness method. Table 8.2 show the stiffness calculation results for a stiffening wall with a door opening, assuming the wall is restrained on both sides (double-fixed static scheme).

Table 8.2

Stiffness of wall A with door opening for double-fixed piers

Wall or component		Moment of inertia I, m^4	Static scheme	Distance GC-LC a, m	Stiffness K, kN/mm	
A	A'	1.59	F		592.75	81.46
	C	0.09	F	1.91	47.22	
	D	0.09	F		47.22	

For such assumptions, the stiffness of the masonry wall is 81.46 kN/mm. Assuming that the piers between the opening behave in the static cantilever scheme, the stiffness of the wall is lower by 28% and amounts to 58.5 – Table 8.3. This significant difference has consequences in changing the location of the torsion center. Assuming the double-fixed piers, the coordinates of the torsion center are $x_r = 0.00$ m and $y_r = -0.32$ m. The coordinates of the torsion center in the static cantilever scheme of piers are $x_r = 0.00$ m and $y_r = -0.61$ m – Table 8.4.

Table 8.3

Stiffness of wall A with door opening for cantilever piers

Wall or component		Moment of inertia I, m^4	Static scheme	Distance GC-LC a, m	Stiffness K, kN/mm	
A	A'	1.59	F		592.75	
	C	0.09	C	1.91	32.45	58.49
	D	0.09	C		32.45	

Table 8.4

The coordinates of the torsion center

Static scheme of piers	Coordinates of torsion center	
	x_r, m	y_r, m
double-fixed	0.00	-0.32
cantilever	0.00	-0.61

In the engineering approach of replacing a wall with an opening with a solid wall of reduced stiffness, the total stiffness method can be used to calculate the cracking phase. As shown in chapter 6 – cracks change the geometry of the piers between the openings, and considering this fact makes it possible to calculate the reduced stiffness of the wall – Fig. 8.6.
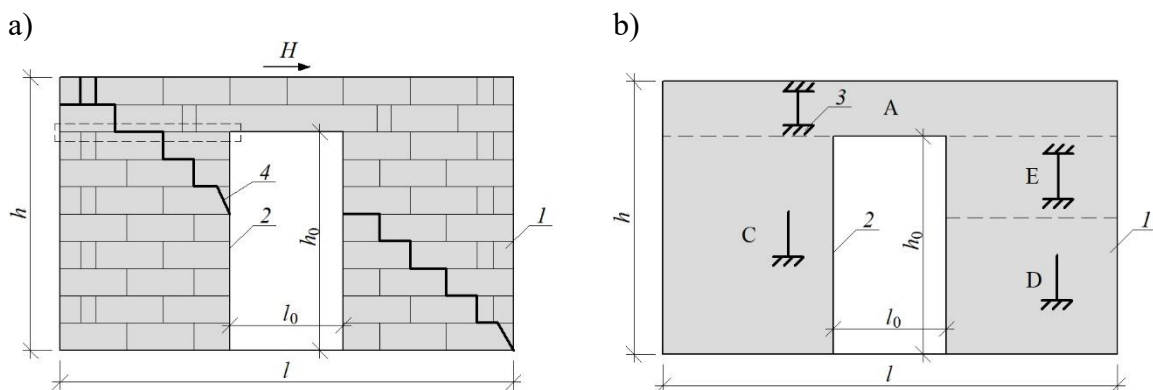
Fig. 8.6 Division of the wall into components: a) cracked wall, b) calculation model: 1 – masonry wall, 2 – door opening, 3 – static scheme, 4 – cracks

The stiffness of a wall with a door opening (and a window opening) can be calculated by adopting a modulus of elasticity calibrated in a numerical model and piers geometry following Fig. 8.6. The boundary conditions of the structure influence the assuming static schemes of individual wall parts. The calculation results for the wall with the door opening, taking into account the cracking, are presented in Table 8.5.

This approach allows for a safe estimation of the behavior of the wall in the post-

elastic phase. A reduced stiffness is shown as a green line in Fig. 8.7.

Stiffness of cracked wall A with door opening

Wall or component		Moment of inertia I, m^4	Static scheme	Distance GC-LC a, m	Stiffness K, kN/mm	
A	A'	1.59	F		540.71	
	C	0.09	C	1.91	4.9	1.53
	D	0.09	C		5.15	
	E	0.09	F		30.86	

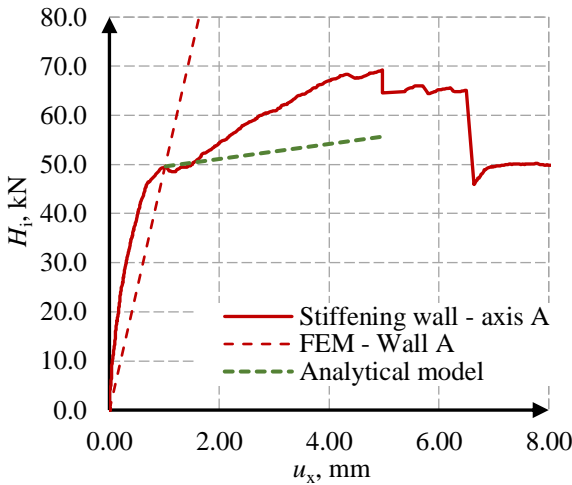* a reduced modulus of elasticity was assumed: $E = 35.0$ MPa (Table 8.1).

Fig. 8.7 Behavior phases of stiffening wall A

The wall stiffness differs both in the initial phase due to the openings and in the non-linear phase due to progressive cracking. This phenomenon causes the building's center of torsion to be constantly changing. Digital image correlation (DIC) was used to measure the displacements of slab corners to prove that the coordinates of the torsion center changed within the loading process. Vectors of resultant displacements and values of horizontal and vertical displacements were analysed. The measurements were made in all behavior phases of the stiffening walls.

Analysis of displacement vectors showed that in the initial phase, when the stiffness of the building is the highest, the building rotates – Fig. 8.9 and Fig. 8.9. As the load increases, the walls crack, and the internal forces redistribute. The equalization of internal forces between the walls makes the rotation give way to the translation of the building in the subsequent phases – Fig. 8.10. In the residual phase, the rotation is marginal, and the horizontal displacement, consistent with the action of the lateral load, dominates – Fig. 8.11.

a)
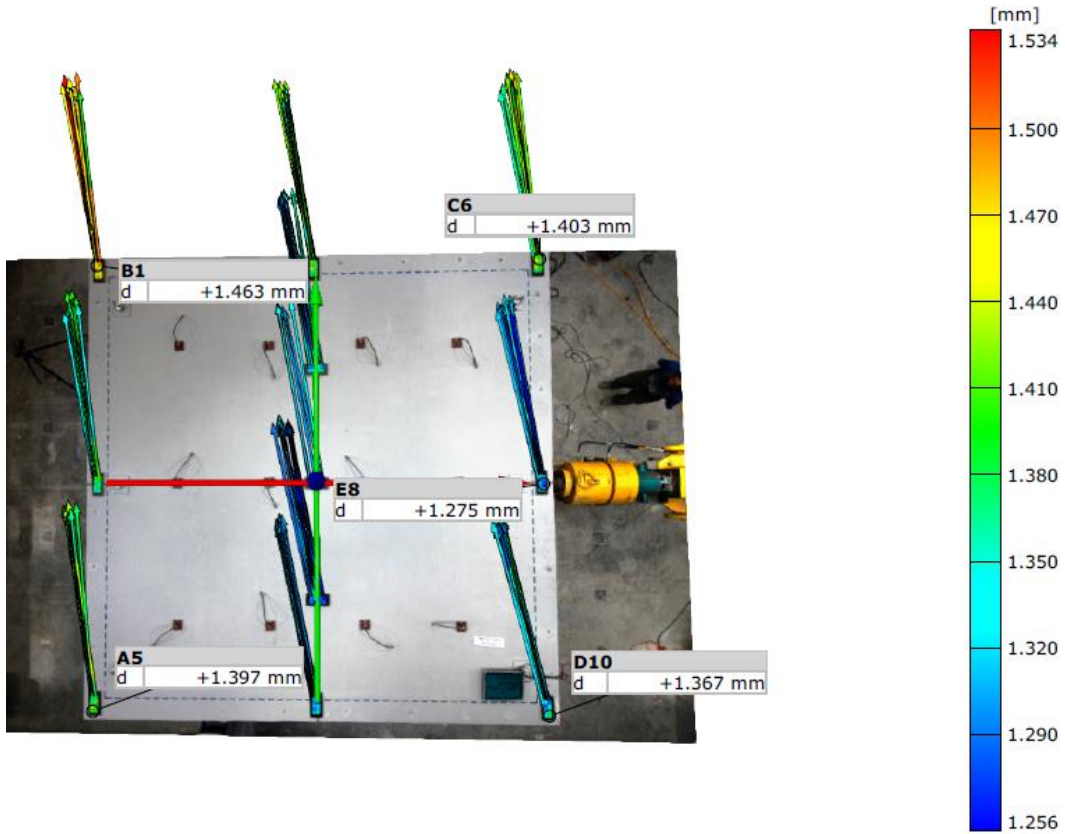
b)
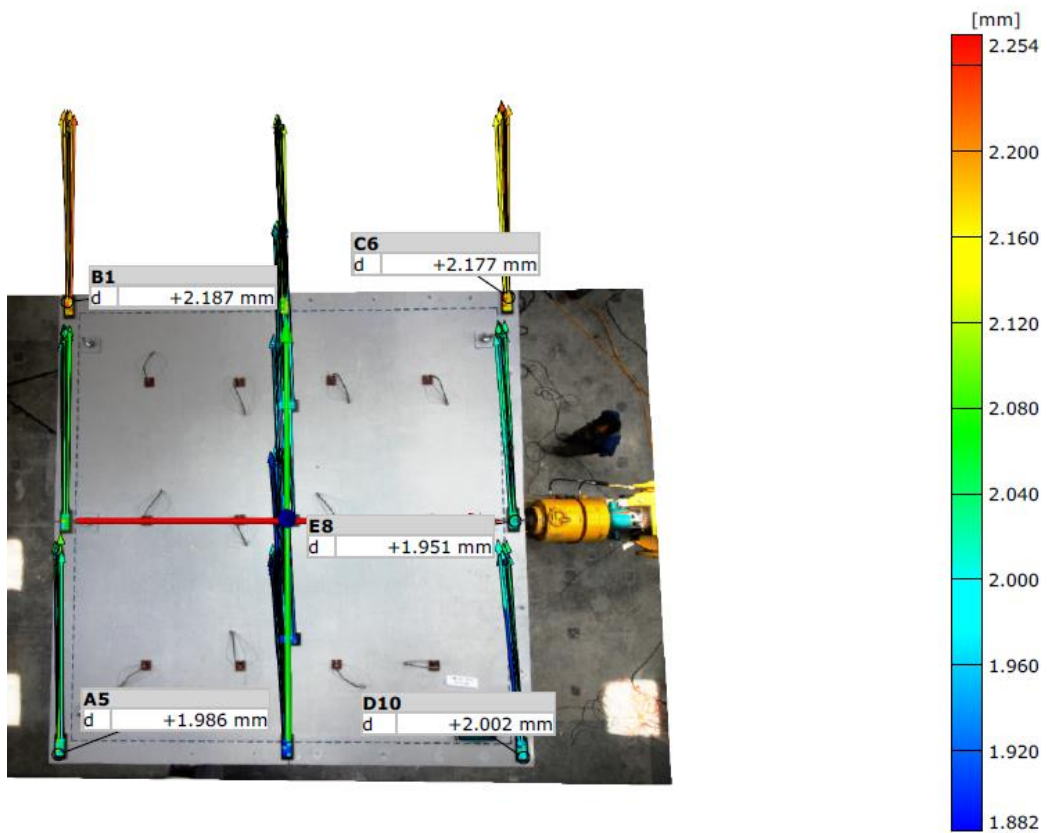
Fig. 8.8 The horizontal displacement vectors in the elastic phase: a) at force H_x = 16.826 kN, b) at force H_x = 20.693 kN

a)
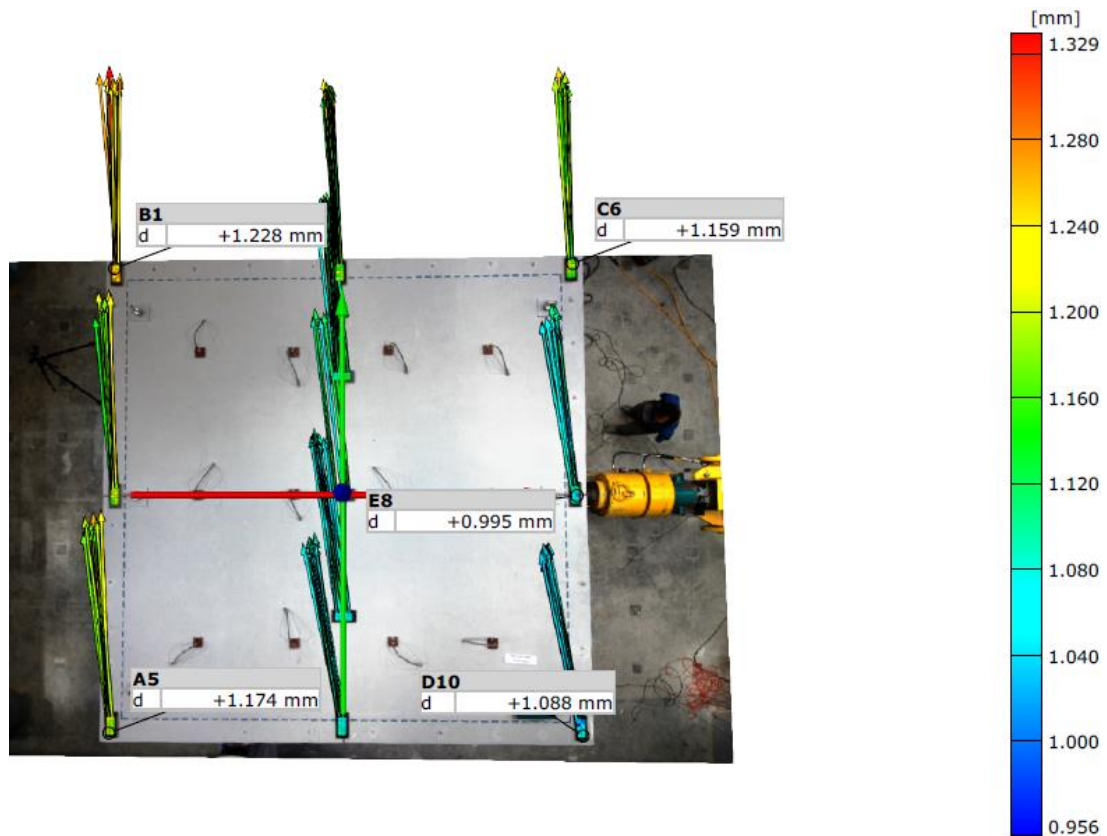
b)

Fig. 8.9 The horizontal displacement vectors: a) at force H_x = 29.519 kN, b) at force H_x = 34.854 kN

Fig. 8.10 The horizontal displacement vectors: a) at force H_x = 49.328 kN, b) at force H_x = 69.247 kN

a)

b)

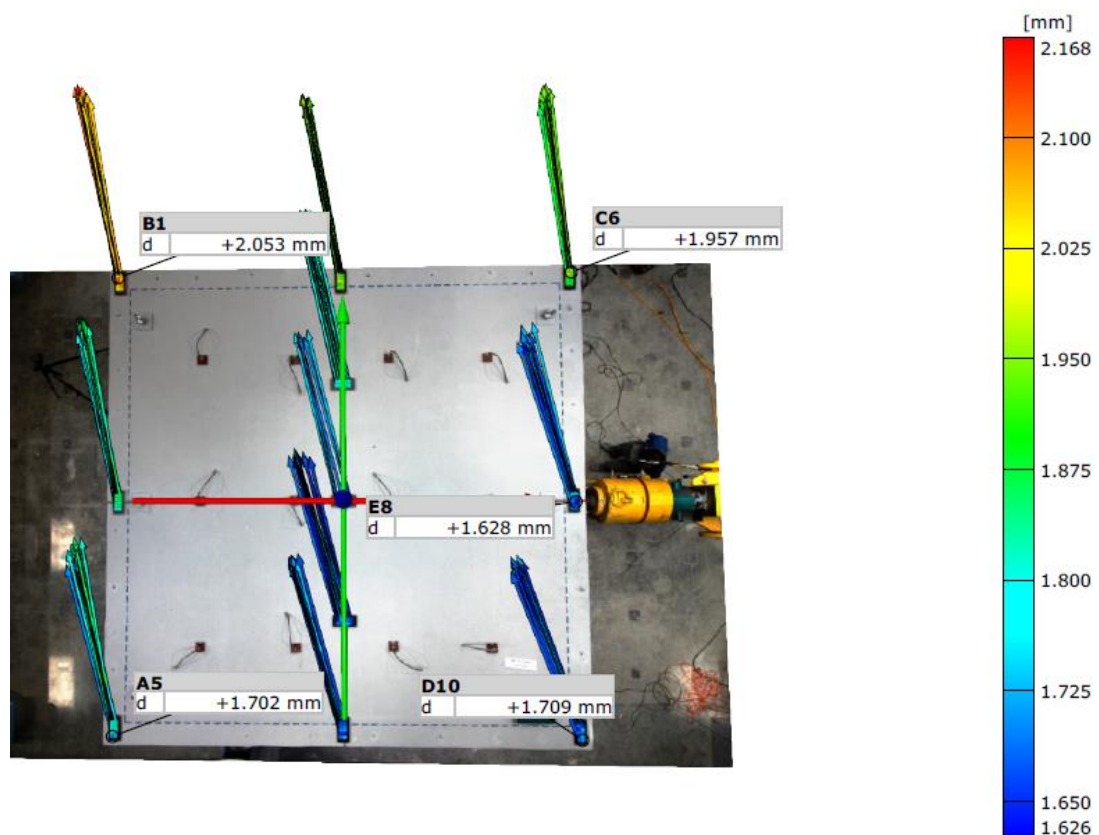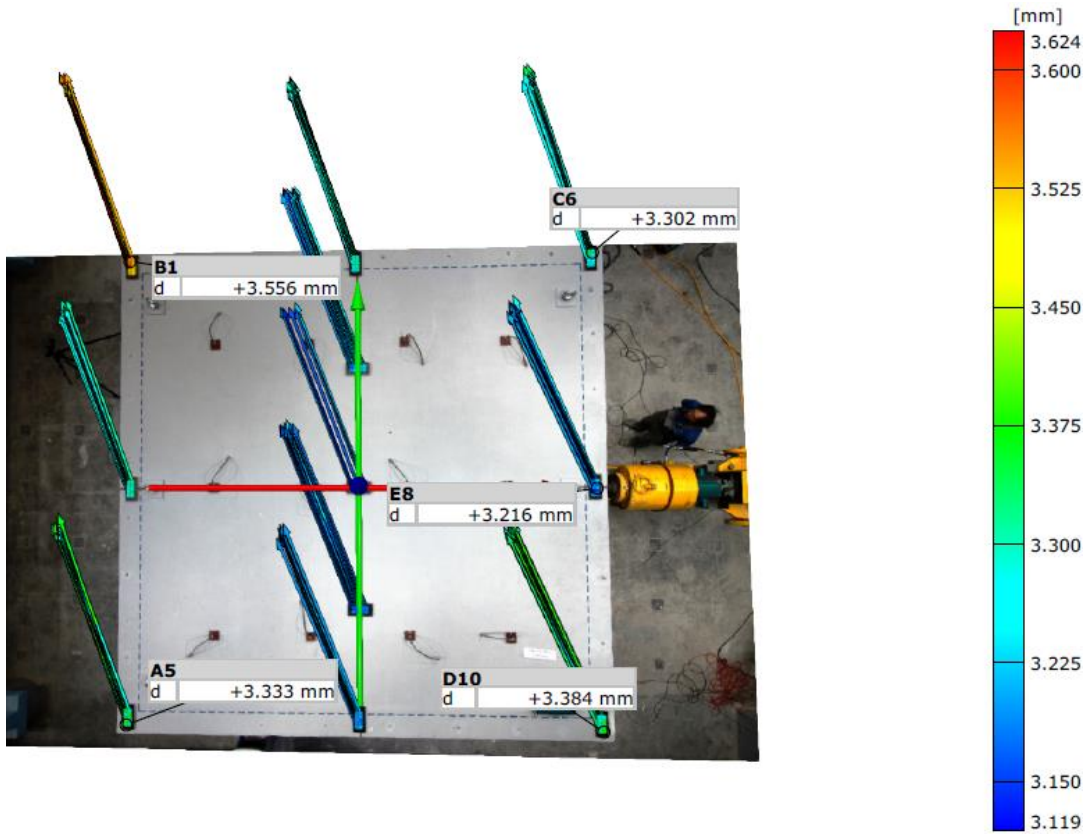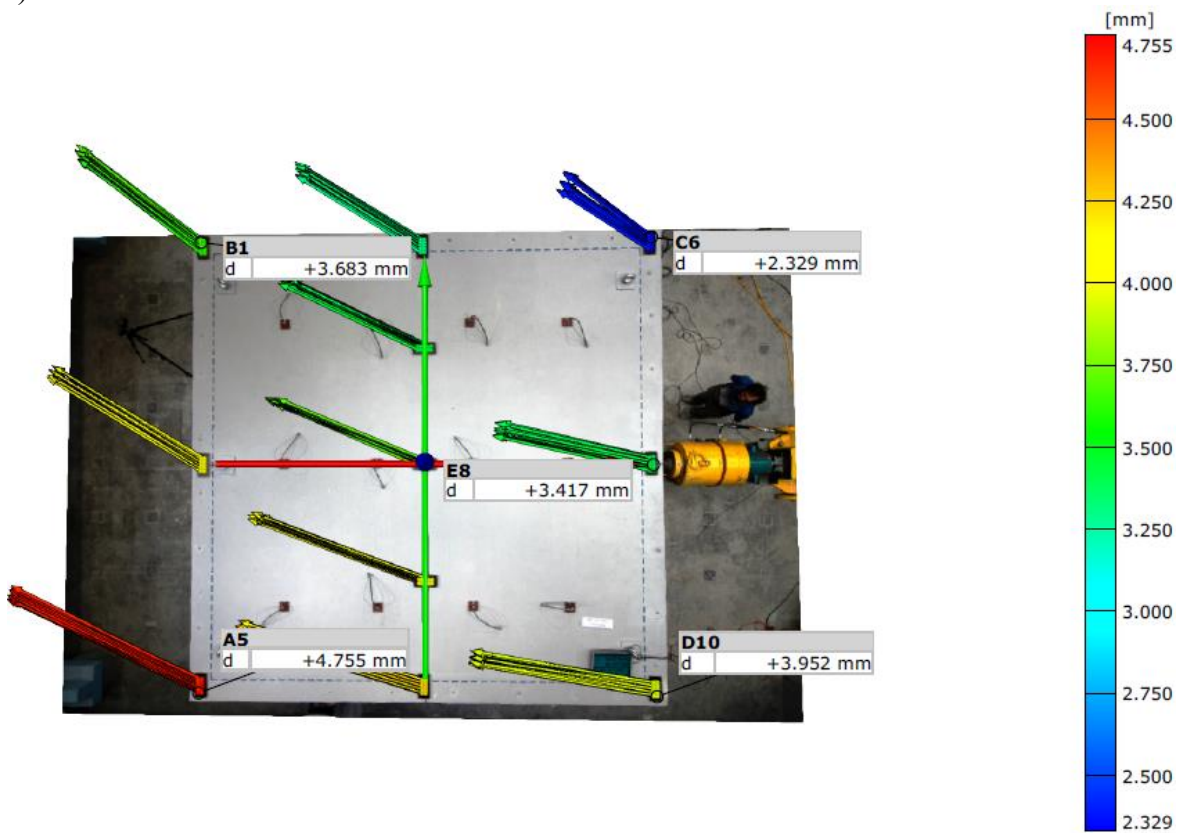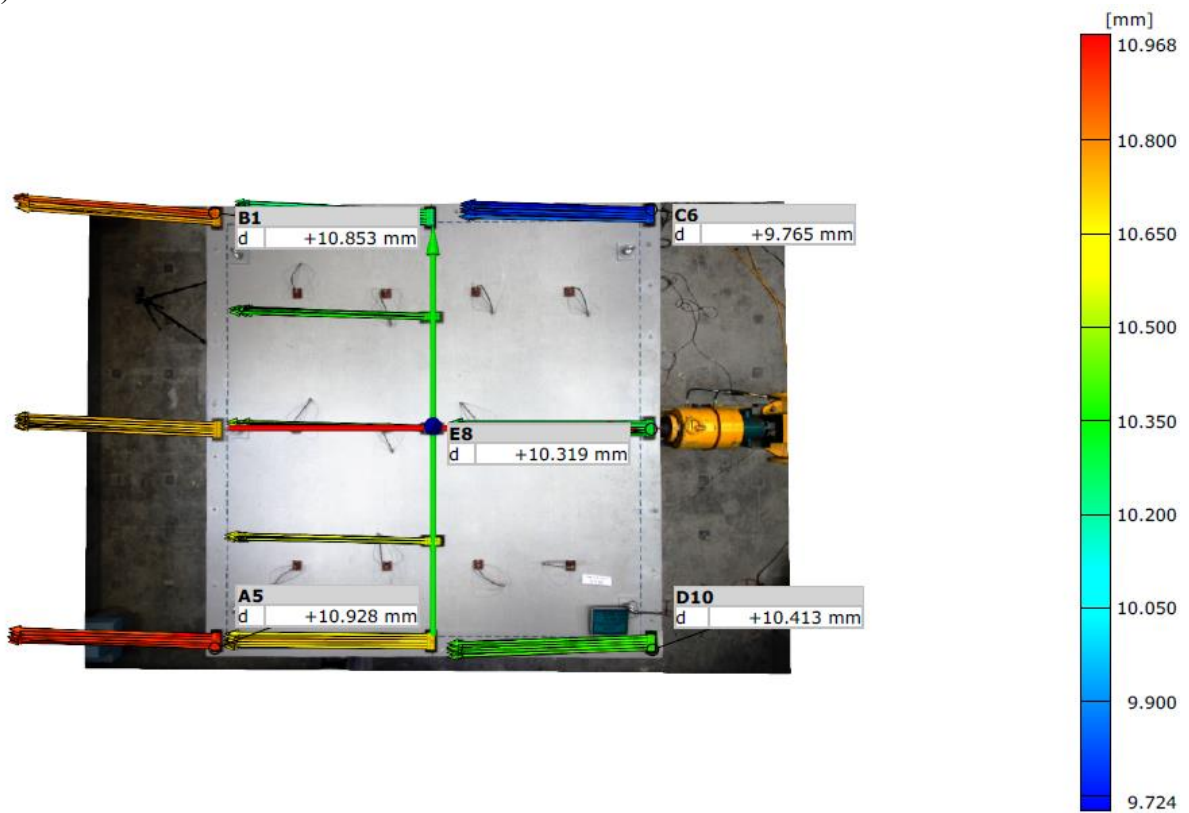

Fig. 8.11 The horizontal displacement vectors in residual phase: a) at force H_x = 64.494 kN, b) at force H_x = 46.850 kN

The procedure described in section 5.3 and the results of displacement measurements in the X and Y directions (Table 8.6) were used to calculate the torsion center (RC). Different coordinates were obtained for each load level – Table 8.7. Moreover, the results indicate that the torsion center of the building is constantly changing due to the changing stiffness of the building's structural elements. A similar verification was carried out for the elastic numerical model (approach 2). Based on the slab corners' displacements, the torsion centre's location was calculated – Table 8.8. The coordinates of the torsion center calculated on the calibrated elastic model were close to the residual phase of the MB-AAC-010/2 model. Moreover, the changing position of the RC determines the change in the distribution of internal forces. In the walls transverse to the stiffening ones, the internal forces are caused by the torsion effect of the structure.

Table 8.6

The horizontal corners displacements of slab for the MB-AAC-010/2 model

Horizontal force, H_x, kN	The horizontal displacements of slab corners, mm									
	Point a		Point b		Point c		Point d		Point e	
	$d_{x.a}$	$d_{y.a}$	$d_{x.b}$	$d_{y.b}$	$d_{x.c}$	$d_{y.c}$	$d_{x.d}$	$d_{y.d}$	$d_{x.e}$	$d_{y.e}$
16.826	-0.191	1.384	-0.243	1.443	-0.201	1.389	-0.291	1.336	-0.270	1.246
20.693	-0.059	1.985	-0.097	2.185	0.007	2.177	-0.077	2.001	-0.105	1.948
29.519	-0.180	1.161	-0.076	1.226	-0.043	1.158	-0.180	1.073	-0.107	0.990
34.854	-0.493	1.629	-0.471	1.999	-0.198	1.947	-0.564	1.613	-0.476	1.557
49.328	-1.236	3.095	-1.286	3.316	-0.947	3.163	-1.394	3.083	-1.277	2.951
69.247	-4.320	1.987	-2.898	2.273	-1.814	1.461	-3.902	0.623	-3.351	0.672
64.494	-4.967	2.036	-3.322	2.410	-2.269	1.366	-4.625	0.521	-3.911	0.578
46.850	-10.925	0.238	-10.812	0.946	-9.756	0.415	-10.404	-0.430	-10.319	-0.082

Table 8.7

The coordinates of the torsion center of the MB-AAC-010/2 model based on research

Horizontal force, H_x, kN	Coordinates of torsion center	
	x_r, m	y_r, m
16.826	-216.31	13.52
20.693	-113.16	-0.98
29.519	26.81	0.97
34.854	147.68	0.02
49.328	-65.31	-0.15
69.247	4.71	1.04
64.494	3.56	0.70
46.850	-0.48	0.70

Table 8.8

The coordinates of the torsion center of the MB-AAC-010/2 FEM elastic model
(approach 2)

Horizontal force, H_x, kN	Coordinates of torsion center	
	x_r, m	y_r, m
26.47	-0.05	0.72
37.05	-0.05	0.72
47.64	-0.05	0.72
68.81	-0.05	0.71

The analysis shows that the center of torsion in a real building changes its position with increasing load. The proper design of elements stiffening masonry buildings should ensure the geometric invariability of the structure both in terms of horizontal displacement of the building and its rotation.

9. CONCLUSIONS

This doctoral thesis is devoted to masonry stiffening walls. The modern trend in the construction industry to optimize the structure (reducing the cross-sections of load-bearing elements) does not always go hand in hand with the correct calculation verification. The lack of a comprehensive method for calculating the stiffness of stiffening walls, localization of the torsion center and a deep understanding of the behavior of such elements prompted the author to consider the topic from theoretical and experimental points of view.

Chapter 1 is a short introduction describing the current economic situation and market-related to the construction industry. Chapter 2 includes the justification for taking up the subject of shear walls as well as the goals, theses (statements) and scope of the work. Chapter 3 analyzes the state of knowledge regarding standard regulations and scientific publications in domestic (polish) and foreign literature. Selected results of masonry structures tests, calculation procedures and methods of wall homogenization used in numerical calculations are presented. Chapter 4 concerns the own experimental program of testing full-scale models of masonry buildings, the description of the test stand and the measurement methods used. Chapter 5 presents the main test results and a determination of the behavior phases of the stiffening walls in the elastic and non-linear range. Chapter 6 contains the results of analyzes of the propagation of cracks and wall damage. Chapter 7 covers numerical calculations. Chapter 8 encloses a discussion of the research results in the field of the stiffness of walls, taking into account the cracking process, the location of the torsion center, and a proposal for an engineering method of numerical analysis of walls.

Based on the analysis of state of the art, the twelve most important issues regarding shear walls were defined:

1. The tests of monotonically loaded stiffening walls are rare.
2. Most analyses of unreinforced shear walls involve cyclic loads.
3. The horizontal displacement of the walls consists of a component due to shear

and due to bending (flexural deformation).

4. The contribution of shear displacements depends not on the initial compressive stress but, above all, on the wall geometry.

5. The initial prestressing of the wall influences shear load capacity – higher compressive stress determines the shear resistance increase.

6. Compressive stress changes the crack morphology of the wall. At low levels of compressive stresses, shear cracking is stepped. When the wall is highly prestressed, the cracks run diagonally through the masonry units.

7. Perpendicular fragments of the stiffening walls (flanged walls) participate in transferring horizontal loads.

8. The stiffness of unreinforced shear walls and lateral load capacity decreases significantly due to wall openings.

9. The openings affect the crack pattern change and the pillars' actual geometry between the openings.

10. The different stiffness of the shear walls caused by the openings determines the building to twist.

11. The method of numerical masonry homogenization should be adapted to the size of the analyzed structure and the purpose of the calculations (representation accuracy).

12. Advanced material models require many input parameters - physical and empirical, and few works provide their values adopted in the calculations.

The unique test stand was constructed to identify the stiffening walls experimentally. The research was designed so that it was possible to apply a monotonic horizontal load while inducing initial compressive stresses. Full-scale testing concerned eight masonry buildings erected on a square plan of 4.0x4.0 m. The studies analyzed the values of the forces acting on the particular walls and the shear deformation angles (and strain angle in the linear phase). Measurement techniques included measuring displacements using LVDT sensors and a digital image correlation (DIC) system for crack morphology analysis. Based on the results, the behavior phases of the stiffening walls with (Fig. 9.1) and without openings (Fig. 9.2) were determined:

- the initial phase (cracks in the tensile corner): 0 - $H_{cr,1}$,
- elastic phase (cracks in the wall without opening): $H_{cr,1}$ - H_{cr},
- nonlinear phase (up to maximum horizontal force): H_{cr} - H_u,
- post-peak residual phase (decrease the horizontal force and stabilization of shear deformations): H_u - H_{res}.
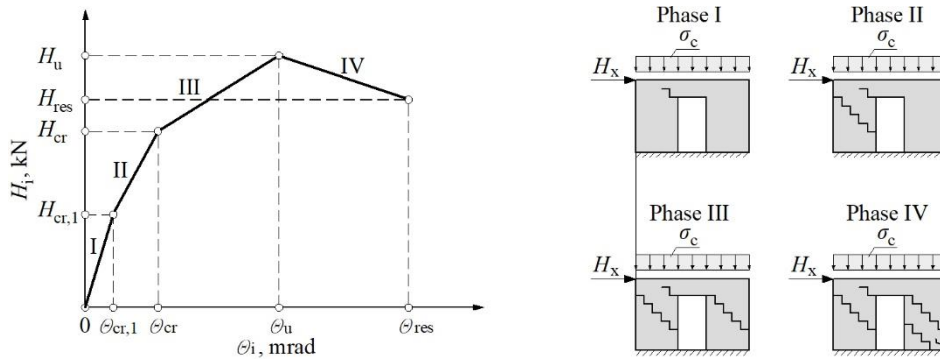
216

Fig. 9.1 Behavior phases of stiffening walls with door opening: I – initial phase, II – elastic phase, III – nonlinear phase, IV – post-peak residual phase
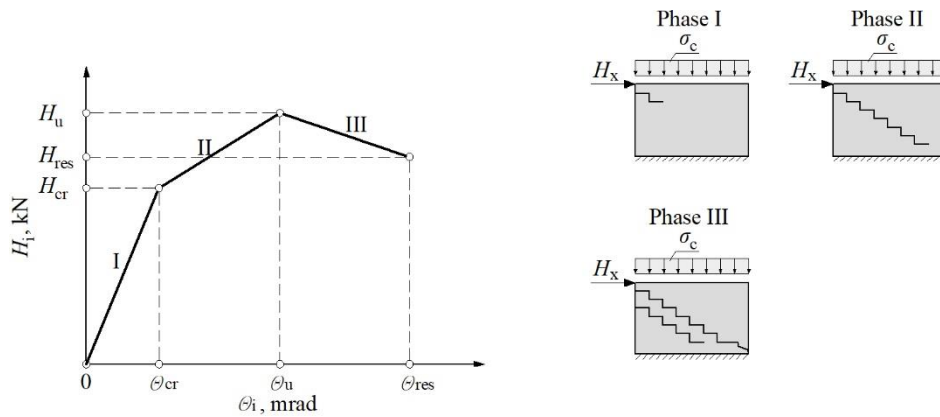

Fig. 9.2 Behavior phases of solid stiffening walls: I – elastic phase, II – nonlinear phase, III – post-peak residual phase

It has been shown that there is no initial phase in walls without openings, which consists of cracking the tensile opening corners. The behavior of walls with openings is more complex than the corresponding solid wall. The range of elastic behavior of walls with a door opening is 29% (mean value) of the maximum force, 38% for walls with a window opening, and 78% for solid walls. Large openings may lead to the non-linear behavior of the structure even at low shear loads due to cracking of the walls within the openings. Subsequent cracks cause significant degradation of wall stiffness and an uncontrolled increase in horizontal displacements.

Moreover, two approaches to the determination of forces in stiffening walls have been proposed:

- empirical approach - based on empirical proportions between the deformation angles of the walls,
- analytical approach - based on determining the stiffness of each wall component.

Comparing forces in both methods enabled the redistribution of internal forces in the walls estimation at a maximum of 12%.

The analysis of horizontal displacements of the slab corners showed that the building undergoes both translation and rotation. In the elastic phase, the building tends to rotate; as the horizontal load increases, the walls are cracked, and the stiffness decreases. In the post-peak phase, translation dominates with marginal importance of torsion of the building. As part of the work, numerical calculations were also carried out on an elastic-plastic model with degradation. The need to validate the model based on the calibration of the mechanical parameters of the wall was demonstrated. Based on the research and calculations, it is concluded that the theses formulated at the beginning of the work can be considered trustworthy – Table 9.1.

Table 9.1

Verification of the veracity of theses of the dissertation

Number	Statement	Verification
1	The stiffness of individual parts of the structure determines the distribution of internal forces in masonry buildings.	true
2	The linear behavior of an unreinforced masonry structure subjected to horizontal shear is small and ends at approximately 30% of the maximum force.	true
3	The lateral load of the building causes a significant decrease in the structure's stiffness.	true
4	A building with asymmetric stiffness distribution, subjected to horizontal shear, undergoes rotation and translation.	true
5	The location of the building torsion center results from the stiffness distribution of the structural elements.	true
6	The selection method of the masonry homogenization affects the accuracy and reliability of the numerical representation of the stiffening walls.	true

The author is aware of the inexhaustibility of the subject and treats the research presented within the dissertation as exploratory. Further work should include the following:

- numerical analyses on micromodels of the wall allowing for an accurate representation of the shear masonry and comparison of the internal forces with test results,
- repetition of tests on scale models to verify the results of full-scale studies,
- extension of the research campaign with scale models of buildings with increased vertical load (higher precompression of walls),
- systematization of procedures for calculating the stiffness of stiffening walls.

10. BIBLIOGRAPHY

Publications

1. Abdelwahab A., Bedeir H., Shedid M., Okail H., Abdelrahman A.: Simplified mechanics-based approach for modeling of flexurally dominated reinforced masonry structural wall systems subjected to lateral load, Eng Struct 210, 110351, 2020. https://doi.org/10.1016/j.engstruct.2020.110351

2. Adesina A.: Recent advances in the concrete industry to reduce its carbon dioxide emissions, Environ Challenges 1, 100004, 2020. https://doi.org/10.1016/j.envc.2020.100004

3. Aksogan O., Bikce M., Emsen E., Arslan HM.: A simplified dynamic analysis of multi-bay stiffened coupled shear walls, Adv Eng Softw 38, 2007, p. 552–560. https://doi.org/10.1016/j.advengsoft.2006.08.019

4. Aksogan O., Turker HT., Oskouei AV.: Stiffening of coupled shear walls at arbitrary number of heights, 1993.

5. Aksogan O., Turkozer CD., Emsen E., Resatoglu R.: Dynamic analysis of non-planar coupled shear walls with stiffening beams using Continuous Connection Method, Thin-Walled Struct 82, 2014, p. 95–104. https://doi.org/10.1016/j.tws.2014.03.018

6. Al-Ahdal A., Aly N., Galal K.: Simplified analytical models for partially grouted reinforced masonry shear walls, Eng Struct 252, 113643, 2022. https://doi.org/10.1016/j.engstruct.2021.113643

7. Alfaiate J., De Almeida J.: Modelling Discrete Cracking on Masonry Walls, Mason Int 83–93, 2004.

8. Ali SS., Page A.: Finite Element Model for Masonry Subjected to Concentrated Loads, J Struct Eng 114, 1988, p. 1761–1784

9. Angelillo M., Lourenço PB., Milani G.: Masonry behaviour and modelling, Mechanics of Masonry Structures, 2014, p. 1–26.

10. Angelosanti M., Currà E., Sabato A.: BIM oriented applications of structural health monitoring based on magnified digital image correlation point-clouds, Autom Constr 148, 2023. https://doi.org/10.1016/j.autcon.2023.104754

11. Aşıkoğlu A., Vasconcelos G., Lourenço PB., Pantò B.: Pushover analysis of unreinforced irregular masonry buildings: Lessons from different modeling approaches, Eng Struct 218, 2020. https://doi.org/10.1016/j.engstruct.2020.110830

12. Asteris PG., Plevris V., Sarhosis V., Papaloizou L., Mohebkhah A., Komodromos P., Lemos JV.: Numerical modeling of historic masonry structures, Chapter 7 of Handbook of Research on Seismic Assessment and Rehabilitation of Historic Structures, A volume in the Advances in Civil and Industrial Engineering (ACIE) Book Series, 2015, p. 213-256.

13. Baloevic G., Radnic J., Matesan D., Grgic N., Banovic I.: Comparison of developed numerical macro and micro masonry models for static and dynamic analysis of masonry-infilled steel frames, Lat Am J Solids Struct 13, 2016, p. 2251–2265. https://doi.org/10.1590/1679-78252520

14. Baraldi D., Cecchi A.: Three-dimensional nonlinear behaviour of masonry walls modelled with discrete elements, ECCOMAS Congr 2016 - Proc 7th Eur Congr Comput Methods Appl Sci Eng 3, 2016, p. 5248–5261. https://doi.org/10.7712/100016.2177.10185

15. Barattucci S., Sarhosis V., Bruno AW., D'Altri AM., de Miranda S., Castellazzi G.: An experimental and numerical study on masonry triplets subjected to monotonic and cyclic shear loadings, Constr Build Mater 254, 119313, 2020. https://doi.org/10.1016/j.conbuildmat.2020.119313

16. Beconcini ML., Croce P., Formichi P., Landi F., Puccini B.: Experimental evaluation of shear behavior of stone masonry wall, Materials (Basel) 14, 2021. https://doi.org/10.3390/ma14092313

17. Bedeir H., Shedid M., Okail H., Hamdy O.: Numerical modeling of a two story third-scale reinforced masonry shear wall building subjected to quasi-static lateral loading, Eng Struct 181, 2019, p. 310–323. https://doi.org/10.1016/j.engstruct.2018.12.010

18. Benedetti A., Steli E.: Analytical models for shear-displacement curves of unreinforced and FRP reinforced masonry panels, Constr Build Mater 22, 2008, p. 175–185. https://doi.org/10.1016/j.conbuildmat.2006.09.005

19. Bergmans J., Nielsen P., Snellings R., Broos K.: Recycling of autoclaved aerated concrete in floor screeds: Sulfate leaching reduction by ettringite formation, Constr Build Mater 111, 2016, p. 9–14. https://doi.org/10.1016/j.conbuildmat.2016.02.075

20. Binda L., Pina-Henriques J., Anzani A., Fontana A., Lourenço PB.: A contribution for the understanding of load-transfer mechanisms in multi-leaf masonry walls: Testing and modelling, Eng Struct 28, 2006, p. 1132–1148. https://doi.org/10.1016/j.engstruct.2005.12.004

21. Bolhassani M., Hamid AA., Johnson C., Schultz AE.: Shear strength expression for partially grouted masonry walls, Eng Struct 127, 2016, p. 475–494. https://doi.org/10.1016/j.engstruct.2016.09.001

22. Bolhassani M., Hamid AA., Lau ACW., Moon F.: Simplified micro modeling of partially grouted masonry assemblages, Constr Build Mater 83, 2015, p. 159–173. https://doi.org/10.1016/j.conbuildmat.2015.03.021

23. Brodsky A., Yankelevsky DZ., Rabinovitch O.: Shearing of infill masonry walls under lateral and vertical loading, J Build Eng 38, 2021. https://doi.org/10.1016/j.jobe.2021.102147

24. Calderón S., Milani G., Sandoval C.: Simplified micro-modeling of partially-grouted reinforced masonry shear walls with bed-joint reinforcement: Implementation and validation, Eng Struct 234, 2021. https://doi.org/10.1016/j.engstruct.2021.111987

25. Calderón S., Sandoval C., Arnau O.: Shear response of partially-grouted reinforced masonry walls with a central opening: Testing and detailed micro-modelling, Mater Des 118, 2017, p. 122–137. https://doi.org/10.1016/j.matdes.2017.01.019

26. Caliò I., Marletta M., Pantò B.: A new discrete element model for the evaluation of the seismic behaviour of unreinforced masonry buildings, Eng Struct 40, 2012, p. 327–338. https://doi.org/10.1016/j.engstruct.2012.02.039

27. Casolo S.: Macroscale modelling of microstructure damage evolution by a rigid body and spring model, Mech Mater Struct 4 (3), 2009.

28. Casolo S.: Modelling in-plane micro-structure of masonry walls by rigid elements, Int J Solids Struct 41, 2004, p. 3625–3641. https://doi.org/10.1016/j.ijsolstr.2004.02.002

29. Castellazzi G., Ciancio D., Ubertini F.: A simplified micro-modeling approach for Historical Stone Masonry Walls, Key Eng Mater 624, 2015, p. 74–79. https://doi.org/10.4028/www.scientific.net/KEM.624.74

30. Cecchi A., Milani G., Tralli A.: Validation of analytical multiparameter homogenization models for out-of-plane loaded masonry walls by means of the finite element method, J Eng Mech 131, 2005, p. 185–198. https://doi.org/10.1061/(ASCE)0733-9399(2005)131:2(185)

31. Cecchi A., Sab K.: A multi-parameter homogenization study for modeling elastic masonry, Eur J Mech A/Solids 21, 2002, p. 249–268. https://doi.org/10.1016/S0997-7538(01)01195-0

32. Celano T., Argiento LU., Ceroni F., Casapulla C.: In-plane behaviour of masonry walls: Numerical analysis and design formulations, Materials (Basel) 14, 2021. https://doi.org/10.3390/ma14195780

33. Celano T., Argiento LU., Ceroni F., Casapulla C.: Literature review of the in-plane behavior of masonry walls: Theoretical vs. experimental results, Materials (Basel) 14, 2021. https://doi.org/10.3390/ma14113063

34. Červenka J., Papanikolaou VK.: Three dimensional combined fracture-plastic material model for concrete, Int J Plast 24, 2008, p. 2192–2220. https://doi.org/10.1016/j.ijplas.2008.01.004

35. Chaimoon K., Attard MM.: Modeling of unreinforced masonry walls under shear and compression, Eng Struct 29, 2007, p. 2056–2068. https://doi.org/10.1016/j.engstruct.2006.10.019

36. Chen X., Chan A.: Soft impact responses of laminated glass simulated with the combined finite-discrete element method, Eng Comput (Swansea, Wales) 35, 2018, p. 1460–1480. https://doi.org/10.1108/EC-10-2017-0386

37. Chen X., Chan AHC., Yang J.: Simulating the breakage of glass under hard body impact using the combined finite-discrete element method, Comput Struct 177, 2016, p. 56–68. https://doi.org/10.1016/j.compstruc.2016.08.010

38. Chen X., Chan AHC.: Modelling impact fracture and fragmentation of laminated glass using the combined finite-discrete element method, Int J Impact Eng 112, 2018, p. 15–29. https://doi.org/10.1016/j.ijimpeng.2017.10.007

39. Chen X., Wang H., Chan AHC., Agrawal AK., Cheng Y.: Collapse simulation of masonry arches induced by spreading supports with the combined finite–discrete element method, Comput Part Mech 8, 2020, p. 721–735. https://doi.org/10.1007/s40571-020-00366-x

40. Chen X., Wang H.: Slope failure of noncohesive media modelled with the combined finite-discrete element method, Appl Sci 9, 2019, p. 1–13. https://doi.org/10.3390/app9030579

41. Choudhury T., Milani G., Kaushik HB.: Experimental and numerical analyses of unreinforced masonry wall components and building, Constr Build Mater 257, 119599, 2020. https://doi.org/10.1016/j.conbuildmat.2020.119599

42. Chu TC., Ranson WF., Sutton MA.: Applications of digital-image-correlation techniques to experimental mechanics, Exp Mech 25, 1985, p. 232–244. https://doi.org/10.1007/BF02325092

43. Coull A., Subedi NK.: Coupled shear walls with two and three bands of openings, Build Sci 7, 1972, p. 81–86. https://doi.org/10.1016/0007-3628(72)90043-6

44. Croce P., Beconcini ML., Formichi P., Cioni P., Landi F., Mochi C., De Lellis F., Mariotii E., Serra I.: Shear modulus of masonry walls: A critical review, Procedia Struct Integr 11, 2018, p. 339–346. https://doi.org/10.1016/j.prostr.2018.11.044

45. Curt J., Capaldo M., Hild F., Roux S.: An algorithm for structural health monitoring by digital image correlation: Proof of concept and case study, Opt Lasers Eng 151,106842, 2022. https://doi.org/10.1016/j.optlaseng.2021.106842

46. D'Altri AM., Sarhosis V., Milani G., Rots J., Cattari S., Lagomarsino S., Sacco E., Tralli A., Castellazzi G., De Miranda S.: Modeling Strategies for the Computational Analysis of Unreinforced Masonry Structures: Review and Classification, Archives of Computational Methods in Engineering 27(4), 2019, p. 1153-1185. https://doi.org/10.1007/s11831-019-09351-x

47. Da Porto F., Guidi G., Garbin E., Modena C.: In-Plane Behavior of Clay Masonry Walls: Experimental Testing and Finite-Element Modeling, J Struct Eng 136, 2010, p. 1379–1392. https://doi.org/10.1061/(asce)st.1943-541x.0000236

48. De Wolf C., Cordella M., Dodd N., Byers B., Donatello S.: Whole life cycle environmental impact assessment of buildings : Developing software tool and database support for the EU framework Level(s), Resour Conserv Recycl 188, 106642, 2023. https://doi.org/10.1016/j.resconrec.2022.106642

49. Dhanasekar M., Haider W.: Explicit finite element analysis of lightly reinforced masonry shear walls, Comput Struct 86, 2008, p. 15–26. https://doi.org/10.1016/j.compstruc.2007.06.006

50. Dhanasekar M.: Shear in reinforced and unreinforced masonry: Response, design and construction, Procedia Eng 14, 2011, p. 2069–2076. https://doi.org/10.1016/j.proeng.2011.07.260

51. Di Nino S., Zulli D.: Homogenization of ancient masonry buildings: A case study, Appl Sci 10, 2020. https://doi.org/10.3390/APP10196687

52. Drougkas A., Roca P., Molins C.: Analytical micro-modeling of masonry periodic unit cells - Elastic properties, Int J Solids Struct 69–70, 2015, p. 169–188. https://doi.org/10.1016/j.ijsolstr.2015.04.039

53. Drougkas A., Roca P., Molins C.: Experimental analysis and detailed micro-modeling of masonry walls subjected to in-plane shear, Eng Fail Anal 95, 2019, p. 82–95. https://doi.org/10.1016/j.engfailanal.2018.08.030

54. Drougkas A.: Macro-modelling of orthotropic damage in masonry: Combining micro-mechanics and continuum FE analysis, Eng Fail Anal 141, 106704, 2022, https://doi.org/10.1016/j.engfailanal.2022.106704

55. Elmeligy O., Aly N., Galal K.: Sensitivity analysis of the numerical simulations of partially grouted reinforced masonry shear walls, Eng Struct 245, 112876, 2021. https://doi.org/10.1016/j.engstruct.2021.112876

56. El-Sokkary H., Galal K.: Material Quantities of Reinforced Masonry versus Reinforced Concrete Shear Walls, Structures 27, 2020, p. 767–779. https://doi.org/10.1016/j.istruc.2020.06.020

57. Ferretti F., Mazzotti C., Esposito R., Rots JG.: Shear-sliding behavior of masonry: Numerical micro-modeling of triplet tests, Comput Model Concr Struct - Proc Conf Comput Model Concr Concr Struct EURO-C 2018, p. 941–954. https://doi.org/10.1201/9781315182964-109

58. Furtado A., Rodrigues H., Arêde A., Varum H.: Simplified macro-model for infill masonry walls considering the out-of-plane behaviour, Earthq Eng Struct Dyn 45, 2016, p. 507–524. https://doi.org/10.1002/eqe.2663

59. Galasco A., Lagomarsino S., Penna A.: Non linear macro-element dynamic analysis of masonry buildings, ECCOMAS Thematic Conference on Computational Methods in Structural Dynamics and Earthquake Engineering M. Papadrakakis, D.C. Charmpis, N.D. Lagaros, Y. Tsompanakis (eds.) Rethymno, Crete, Greece, 13–16 June 2007.

60. Gehri N., Mata-Falcón J., Kaufmann W.: Refined extraction of crack characteristics in Large-scale concrete experiments based on digital image correlation, Eng Struct 251, 2022. https://doi.org/10.1016/j.engstruct.2021.113486

61. Ghiassi B., Soltani M., Tasnimi AA.: A simplified model for analysis of unreinforced masonry shear walls under combined axial, shear and flexural loading, Eng Struct 42, 2012, p. 396–409. https://doi.org/10.1016/j.engstruct.2012.05.002

62. Gioffrè M., Cavalagli N., Gusella V., Pepi C.: Confined vs. unreinforced masonry: Construction and shaking table tests of two-storey buildings, Constr Build Mater 333, 126961, 2022. https://doi.org/10.1016/j.conbuildmat.2022.126961

63. Gonen S., Pulatsu B., Erdogmus E., Lourenço PB., Soyoz S.: Effects of spatial variability and correlation in stochastic discontinuum analysis of unreinforced masonry walls, Constr Build Mater 337, 127511, 2022. https://doi.org/10.1016/j.conbuildmat.2022.127511

64. Gooch LJ., Masia MJ., Stewart MG.: Application of stochastic numerical analyses in the assessment of spatially variable unreinforced masonry walls subjected to in-plane shear loading, Eng Struct 235, 112095, 2021. https://doi.org/10.1016/j.engstruct.2021.112095

65. Gourav K., Nanjunda Rao K., Reddy BVV.: Prediction of Out-of-plane Flexural Behaviour of FaL-G Brick Masonry using Simplified Micro-modelling Approach, J Int Mason Soc 33, 2020, p. 1–14

66. Grassl P., Lundgren K., Gylltoft K.: Concrete in compression: A plasticity theory with a novel hardening law, Int J Solids Struct 39, 2002, p. 5205–5223. https://doi.org/10.1016/S0020-7683(02)00408-0

67. Grzyb K., Jasiński R.: Parameter estimation of a homogeneous macromodel of masonry wall made of autoclaved aerated concrete based on standard tests, Structures 38, 2022, p. 385–401. https://doi.org/10.1016/j.istruc.2022.02.005

68. Haach VG., Ramalho MA., Corrêa MRS.: Parametrical study of unreinforced flanged masonry walls subjected to horizontal loading through numerical modeling, Eng Struct 56, 2013, p. 207–217. https://doi.org/10.1016/j.engstruct.2013.05.009

69. Hendry AW., Sinha BP., Davies SR.: Design of Masonry Structures, Third edit. Taylor & Francis e-Library, Edinburgh, 2004.

70. Herbert DM., Gardner DR., Harbottle M., Thomas J., Hughes TG.: The development of a new method for testing the lateral load capacity of small-scale masonry walls using a centrifuge and digital image correlation, Constr Build Mater 25, 2011, p. 4465–4476. https://doi.org/10.1016/j.conbuildmat.2011.02.002

71. Hoek E., Brown ET.: Empirical strength criterion for rock masses, J. Geotech. Eng. Div. ASCE 106, 1980, p. 1013–1035.

72. Hordijk D.A.: Local Approach to Fatigue of Concrete, PhD dissertation, Delft University of Technology, 1991.

73. Howlader MK., Masia MJ., Griffith MC.: Digital image correlation for the analysis of in-plane tested unreinforced masonry walls, Structures 29, 2021, p. 427–445. https://doi.org/10.1016/j.istruc.2020.11.051

74. Huang YH., Liu L., Sham FC., Chan YS., Ng SP.: Optical strain gauge vs. traditional strain gauges for concrete elasticity modulus determination, Optik (Stuttg) 121, 2010, p. 1635–1641. https://doi.org/10.1016/j.ijleo.2009.03.002

75. Hwang SH., Kim S., Yang KH.: In-plane lateral load transfer capacity of unreinforced masonry walls considering presence of openings, J Build Eng 47, 103868, 2022. https://doi.org/10.1016/j.jobe.2021.103868

76. Janaraj T., Dhanasekar M.: Finite element analysis of the in-plane shear behaviour of masonry panels confined with reinforced grouted cores, Constr Build Mater 65, 2014, p. 495–506. https://doi.org/10.1016/j.conbuildmat.2014.04.133

77. Jasiński R., Drobiec Ł., Mazur W.: Validation of Selected non-destructive methods for determining the compressive strength of masonry units made of autoclaved aerated concrete, Materials (Basel) 12, 2019. https://doi.org/10.3390/ma12030389

78. Jasiński R., Drobiec Ł.: Comparison Research of Bed Joints Construction and Bed Joints Reinforcement on Shear Parameters of AAC Masonry Walls, J Civ Eng Archit 10, 2016, p. 1329–1343. https://doi.org/10.17265/1934-7359/2016.12.004

79. Jasinski R., Grzyb K.: Adaptation of the total stiffness method to the load distribution of stiffening masonry walls according to Eurocode 6, Arch Civ Eng 68, 2022, p. 255–274. https://doi.org/10.24425/ace.2022.140167

80. Jasiński R., Stebel K., Domin J.: Application of the dic technique to remote control of the hydraulic load system, Remote Sens 12, 2020, p. 1–24. https://doi.org/10.3390/rs12213667

81. Jasiński R.: Comparisons of confined and different types of reinforcement on the behavior of masonry shear walls, ce/papers, 2018, p. 353–365. https://doi.org/10.1002/cepa.873

82. Jasiński R.: Research on the influence of bed joint reinforcement on strength and deformability of masonry shear walls, Materials (Basel) 12, 2019. https://doi.org/10.3390/ma12162543

83. Jasiński R.: Simple equilibrium models of masonry shear walls – experimental verification (in polish), Mater Bud 2016, p. 224–228. https://doi.org/10.15199/33.2016.06.93

84. Jasiński R.: Size effect of monotonically sheared masonry walls made of AAC masonry units, Ce/Papers 2, E12–E25, 2018. https://doi.org/10.1002/cepa.900

85. Jin G., Chung P.: An advanced digital speckle correlation method for strain measurement and nondestructive testing, 1997, p. 572–577.

86. Kalpana M., Mohith S.: Study on autoclaved aerated concrete: Review, Mater Today Proc 22, 2020, p. 894–896. https://doi.org/10.1016/j.matpr.2019.11.099

87. Kamrava AR., Najafgholipour MA., Fathi F., Dehghan SM.: An experimental study on the in-plane behavior of unreinforced masonry walls with an opening strengthened using steel fiber reinforced concrete overlays, J Build Eng 36, 102084, 2021. https://doi.org/10.1016/j.jobe.2020.102084

88. Kayırga OM., Altun F.: Investigation of earthquake behavior of unreinforced masonry buildings having different opening sizes: Experimental studies and numerical simulation, J Build Eng 40, 102666, 2021. https://doi.org/10.1016/j.jobe.2021.102666

89. Kim SC., White DW.: Linear static analysis of low-rise buildings with flexible diaphragms using the structural separation method, Eng Struct 26, 2004, p. 83–93. https://doi.org/10.1016/j.engstruct.2003.08.013

90. Kita A., Cavalagli N., Masciotta MG., Lourenço PB., Ubertini F.: Rapid post-earthquake damage localization and quantification in masonry structures through multidimensional non-linear seismic IDA, Eng Struct 219, 110841, 2020. https://doi.org/10.1016/j.engstruct.2020.110841

91. Knox CL., Dizhur D., Ingham JM.: Experimental study on scale effects in clay brick masonry prisms and wall panels investigating compression and shear related properties, Constr Build Mater 163, 2018, p. 706–713. https://doi.org/10.1016/j.conbuildmat.2017.12.149

92. Koo KK., Cheung YK.: The static analysis of multi-bay coupled shear walls, Build Environ 19, 1984, p. 93–99. https://doi.org/10.1016/0360-1323(84)90034-9

93. Korswagen PA., Longo M., Rots JG.: High-resolution monitoring of the initial development of cracks in experimental masonry shear walls and their reproduction in finite element models, Eng Struct 211, 110365, 2020. https://doi.org/10.1016/j.engstruct.2020.110365

94. Kuang JS., Chau CK.: Dynamic behaviour of stiffened coupled shear walls with flexible bases, Comput Struct 73, 1999, p. 327–339. https://doi.org/10.1016/S0045-7949(98)00261-2

95. Le DB., Tran SD., Torero JL., Dao VTN.: Application of digital image correlation system for reliable deformation measurement of concrete structures at high temperatures, Eng Struct 192, 2019, p. 181–189. https://doi.org/10.1016/j.engstruct.2019.05.009

96. Lewis JP.: Fast Template Matching, Vision Interface 95, Canadian Image Processing and Pattern Recognition Society, Quebec City, Canada, May 15-19, 1995, p. 120–123.

97. Li Z., Jin Z., Gao Y., Zhao T., Wang P., Li Z.: Coupled application of innovative electromagnetic sensors and digital image correlation technique to monitor corrosion process of reinforced bars in concrete, Cem Concr Compos 113, 103730, 2020. https://doi.org/10.1016/j.cemconcomp.2020.103730

98. Liberatore L., Noto F., Mollaioli F., Franchin P.: In-plane response of masonry infill walls: Comprehensive experimentally-based equivalent strut model for deterministic and probabilistic analysis, Eng Struct 167, 2018, p. 533–548. https://doi.org/10.1016/j.engstruct.2018.04.057

99. Lishak VI., Yagust VI., Yankelevsky DZ.: 2-D Orthotropic failure criteria for masonry. Eng Struct 36, 2012, p. 360–371. https://doi.org/10.1016/j.engstruct.2011.11.033

100. Lopez J., Oller S., Oñate E., Lubliner J.: A homogeneous constitutive model for masonry, Int J Numer Methods Eng 46, 1999, p. 1651–1671. https://doi.org/10.1002/(sici)1097-0207(19991210)46:10<1651::aid-nme718>3.3.co;2-u

101. Lourenço PB., Barros JO., Oliveira JT.: Shear testing of stack bonded masonry, Constr Build Mater 18, 2004, p. 125–132. https://doi.org/10.1016/j.conbuildmat.2003.08.018

102. Lourenço PB., Milani G., Tralli A., Zucchini A.: Analysis of masonry structures: Review of and recent trends in homogenization techniques, Can J Civ Eng 34, 2007, p. 1443–1457. https://doi.org/10.1139/L07-097

103. Lourenço PB., Oliveira DV., Roca P., Orduña A.: Dry Joint Stone Masonry Walls Subjected to In-Plane Combined Loading, J Struct Eng 131, 2005, p. 1665–1673. https://doi.org/10.1061/(asce)0733-9445(2005)131:11(1665)

104. Lourenco PB., Rots J., Blaauwendraad J.: Assessment of a strategy for the detailed analysis of masonry structures, DIANA Comput Mech '84, 1994, p. 359–369. https://doi.org/10.1007/978-94-011-1046-4

105. Lourenço PB., Rots JG., Blaauwendraad J.: Two approaches for the analysis of masonry structures: micro and macro-modeling, Heron 40, 1995, p. 313–340.

106. Lourenço PB.: An anisotropic macro-model for masonry plates and shells: implementation and validation, Delf University of Technology and University of Minho, 1997.

107. Lourenco PB.: Computational Strategy for Masonry Structures, Doctoral thesis, Delft University Press, The Netherlands, 1996.

108. Ma S., Jin G.: New correlation coefficients designed for digital speckle correlation method (DSCM), Opt Technol Image Process Fluids Solids Diagnostics 2002 5058, 25, 2003. https://doi.org/10.1117/12.509382

109. Marques R., Lourenço PB.: Unreinforced and confined masonry buildings in seismic regions: Validation of macro-element models and cost analysis, Eng Struct 64, 2014, p. 52–67. https://doi.org/10.1016/j.engstruct.2014.01.014

110. Massart TJ., Peerlings RHJ., Geers MGD.: A dissipation-based control method for the multi-scale modelling of quasi-brittle materials, Comptes Rendus - Mec 333, 2005, p. 521–527. https://doi.org/10.1016/j.crme.2005.05.003

111. Massart TJ., Peerlings RHJ., Geers MGD.: Mesoscopic modeling of failure and damage-induced anisotropy in brick masonry, Eur J Mech A/Solids 23, 2004, p. 719–735. https://doi.org/10.1016/j.euromechsol.2004.05.003

112. Mata-Falcón J., Haefliger S., Lee M., Galkovski T., Gehri N.: Combined application of distributed fibre optical and digital image correlation measurements to structural concrete experiments, Eng Struct 225, 2020. https://doi.org/10.1016/j.engstruct.2020.111309

113. Medeiros KAS., Parsekian GA., Shrive NG., Fonseca FS.: Shear load capacity prediction of unperforated and perforated partially grouted masonry walls, Eng Struct 256, 113927, 2022. https://doi.org/10.1016/j.engstruct.2022.113927

114. Meftah SA., Tounsi A., El Abbas AB.: A simplified approach for seismic calculation of a tall building braced by shear walls and thin-walled open section structures, Eng Struct 29, 2007, p. 2576–2585. https://doi.org/10.1016/j.engstruct.2006.12.014

115. Menétrey P. WK.: Triaxial failure criterion for concrete and its generalization, ACI Struct J 3, 1995, p. 311 – 318

116. Minaie E., Moon FL., Hamid AA.: Nonlinear finite element modeling of reinforced masonry shear walls for bidirectional loading response, Finite Elem Anal Des 84, 2017, p. 44–53. https://doi.org/10.1016/j.finel.2014.02.001

117. Mughal UA., Qazi AU., Ahmed A., Abbas W., Abbas S., Salmi A., Sayed MM.: Impact of Openings on the In-Plane Strength of Confined and Unconfined Masonry Walls: A Sustainable Numerical Study, Sustainability 14 (12), 7467, 2022. https://doi.org/10.3390/su14127467

118. Narayanan N., Ramamurthy K.: Structure and properties of aerated concrete: A review, Cem Concr Compos 22, 2000, p. 321–329. https://doi.org/10.1016/S0958-9465(00)00016-0

119. Ngeljaratan L., Moustafa MA.: Structural health monitoring and seismic response assessment of bridge structures using target-tracking digital image correlation, Eng Struct 213, 110551, 2020. https://doi.org/10.1016/j.engstruct.2020.110551

120. Nghiem HL., Al Heib M., Emeriault F.: Method based on digital image correlation for damage assessment in masonry structures, Eng Struct 86, 2015, p. 1–15. https://doi.org/10.1016/j.engstruct.2014.12.021

121. Nollet MJ., Smith BS.: Stiffened-story wall-frame tall building structure, Comput Struct 66, 1998, p. 225–240.

122. Pantò B., Caliò I., Lourenço PB.: Seismic safety evaluation of reinforced concrete masonry infilled frames using macro modelling approach, Bull Earthq Eng 15, 2017, p. 3871–3895. https://doi.org/10.1007/s10518-017-0120-z

123. Pantò B., Raka E., Cannizzaro F., Camata G., Caddemi S., Spacone E., Caliò I.: Numerical macro-modeling of unreinforced masonry structures: A critical appraisal, Civil-Comp Proc, 2015. https://doi.org/10.4203/ccp.108.81

124. Pegon P., Anthoine A.: Numerical strategies for solving continuum damage problems with softening: Application to the homogenization of masonry, Comput Struct 64, 1997, p. 623–642. https://doi.org/10.1016/S0045-7949(96)00153-8

125. Peng B., Wang D., Zong G., Zhang Y.: Homogenization strategy for brick masonry walls under in-plane loading, Constr Build Mater 163, 2018, p. 656–667. https://doi.org/10.1016/j.conbuildmat.2017.12.133

126. Petracca M., Pelà L., Rossi R., Zaghi S., Camata G., Spacone E.: Micro-scale continuous and discrete numerical models for nonlinear analysis of masonry shear walls, Constr Build Mater 149, 2017, p. 296–314. https://doi.org/10.1016/j.conbuildmat.2017.05.130

127. Pirsaheb H., Javad Moradi M., Milani G.: A Multi-Pier MP procedure for the nonlinear analysis of in-plane loaded masonry walls, Eng Struct 212, 110534, 2020. https://doi.org/10.1016/j.engstruct.2020.110534

128. Qu X., Zhao X.: Previous and present investigations on the components, microstructure and main properties of autoclaved aerated concrete – A review, Constr Build Mater 135, 2017, p. 505–516. https://doi.org/10.1016/j.conbuildmat.2016.12.208

129. Radhi H.: Viability of autoclaved aerated concrete walls for the residential sector in the United Arab Emirates, Energy Build 43, 2011, p. 2086–2092. https://doi.org/10.1016/j.enbuild.2011.04.018

130. Radosław J.: Experimental Verification of Same Simple Equilibrium Models of Masonry Shear Walls, IOP Conf Ser Mater Sci Eng 245, 2017. https://doi.org/10.1088/1757-899X/245/3/032044

131. Radosław Jasiński: Research and modelling of masonry shear walls, PhD DsC Thesis. (in polish), Silesian University of Technology, 2017.

132. Rafiza AR., Fazlizan A., Thongtha A., Asim N., Noorashikin MS.: The Physical and Mechanical Properties of Autoclaved Aerated Concrete (AAC) with Recycled AAC as a Partial Replacement for Sand, Buildings 12, 2022. https://doi.org/10.3390/buildings12010060

133. Rahgozar A., Hosseini A.: Experimental and numerical assessment of in-plane monotonic response of ancient mortar brick masonry, Constr Build Mater 155, 2017, p. 892–909. https://doi.org/10.1016/j.conbuildmat.2017.08.079

134. Ramos T., Furtado A., Eslami S., Alves S., Rodrigues H., Arêde A., Tavares P., Moreira PMGP.: 2D and 3D Digital Image Correlation in Civil Engineering -

Measurements in a Masonry Wall, Procedia Eng 114, 2015, p. 215–222. https://doi.org/10.1016/j.proeng.2015.08.061

135. Riddington JR., Naom NF.: Finite element prediction of masonry compressive strength, Comput Struct 52, 1994, p. 113–119. https://doi.org/10.1016/0045-7949(94)90261-5

136. RILEM Committee on Fracture Mechanics of Concrete – Test Methods: Determination of the Fracture Energy of Mortar and Concrete by Means of Three-Point Bend Tests on Notched Beams, Materials and Structures 1985, 18, p. 285 – 290, Mater. Struct. 18, 484.

137. Robazza BR., Brzev S., Yang TY., Elwood KJ., Anderson DL., McEwen B.: Seismic behaviour and design code provisions for predicting the capacity of ductile slender reinforced masonry shear walls, Eng Struct 222, 110992, 2020. https://doi.org/10.1016/j.engstruct.2020.110992

138. Roca P.: Assessment of masonry shear-walls by simple equilibrium models, Constr Build Mater 20, 2006, p. 229–238. https://doi.org/10.1016/j.conbuildmat.2005.08.023

139. Röchert D., Shahi GK., Neubaum G., Ross B., Stieglitz S.: The Networked Context of COVID-19 Misinformation: Informational Homogeneity on YouTube at the Beginning of the Pandemic, Online Soc Networks Media 26, 100164 2021. https://doi.org/10.1016/j.osnem.2021.100164

140. Romeo E.: Two-dimensional digital image correlation for asphalt mixture characterisation: interest and limitations, Road Mater Pavement Des 14, 2013, p. 747–763. https://doi.org/10.1080/14680629.2013.815128

141. Ruiz DM., Barrera N., Reyes JC., Restrepo M., Alvarado YA., Lozada M., Vacca HA.: Strengthening of historical earthen constructions with steel plates: Full-scale test of a two-story wall subjected to in-plane lateral load, Constr Build Mater 363, 129877, 2023. https://doi.org/10.1016/j.conbuildmat.2022.129877

142. Sahoo DSK.: An Efficient Approach for Optimization of Nonlinearity Response in Linear Variable Differential Transformer, CVR J Sci Technol 17, 2019, p. 115–119. https://doi.org/10.32377/cvrjst1720

143. Sajid HU., Ashraf M., Ali Q., Sajid SH.: Effects of vertical stresses and flanges on seismic behavior of unreinforced brick masonry, Eng Struct 155, 2018, p. 394–409. https://doi.org/10.1016/j.engstruct.2017.11.013

144. Sandoval C., Arnau O.: Experimental characterization and detailed micro-modeling of multi-perforated clay brick masonry structural response, Mater Struct Constr 50 (34), 2017. https://doi.org/10.1617/s11527-016-0888-3

145. Sayed-Ahmed EY., Shrive NG.: Nonlinear Finite-Element Model of Hollow Masonry, J Struct Eng 122, 1996, p. 683–690. https://doi.org/10.1061/(asce)0733-9445(1996)122:6(683)

146. Senthivel R., Lourenço PB.: Finite element modelling of deformation characteristics of historical stone masonry shear walls, Eng Struct 31, 2009, p. 1930–1943. https://doi.org/10.1016/j.engstruct.2009.02.046

147. Shabani A., Kioumarsi M.: A novel macroelement for seismic analysis of unreinforced masonry buildings based on MVLEM in OpenSees, J Build Eng 49, 104019, 2022. https://doi.org/10.1016/j.jobe.2022.104019

148. Shabdin M., Zargaran M., Attari NKA.: Experimental diagonal tension (shear) test of Un-Reinforced Masonry (URM) walls strengthened with textile reinforced mortar (TRM), Constr Build Mater 164, 2018, p. 704–715. https://doi.org/10.1016/j.conbuildmat.2017.12.234

149. Shedid MT., El-Dakhakhni WW., Drysdale RG.: Behavior of fully grouted reinforced concrete masonry shear walls failing in flexure: Analysis, Eng Struct 31, 2009, p. 2032–2044. https://doi.org/10.1016/j.engstruct.2009.03.006

150. Shi Q-X., Wang B.: Simplified calculation of effective flange width for shear walls with flange, Struct Des Tall Spec Build 25, 2015, p. 558–577. https://doi.org/10.1002/tal.1272

151. Smoljanović H., Živaljić N., Nikolić Ž., Munjiza A.: Numerical analysis of 3D dry-stone masonry structures by combined finite-discrete element method, Int J Solids Struct 136–137, 2018, p. 150–167. https://doi.org/10.1016/j.ijsolstr.2017.12.012

152. Solution FD.: Analysis of Multi-Bay Coupled, Build Sci 8, 1973, p. 153–157.

153. Sreejith PP., Sivan PP., Praveen A., Gajendran C., Nisha V.: Simplified Method for Shear Strength Prediction of Confined Masonry Walls Subjected to in Plane Loads, Procedia Technol 24, 2016, p. 155–160. https://doi.org/10.1016/j.protcy.2016.05.022

154. Tripathy D., Singhal V.: Estimation of in-plane shear capacity of confined masonry walls with and without openings using strut-and-tie analysis, Eng Struct 188, 2019, p. 290–304. https://doi.org/10.1016/j.engstruct.2019.03.002

155. Trojanek R., Gluszak M.: Short-run impact of the Ukrainian refugee crisis on the housing market in Poland, Financ Res Lett 50, 103236, 2022. https://doi.org/10.1016/j.frl.2022.103236

156. Van Gysel A., Taerwe L.: Analytical formulation of the complete stress-strain curve for high strength concrete, Mater Struct Constr 29, 1996, p. 529–533. https://doi.org/10.1007/bf02485952

157. Vargas L., Sandoval C., Bertolesi E., Calderón S.: Seismic behavior of partially grouted masonry shear walls containing openings: Experimental testing, Eng Struct 278, 2023. https://doi.org/10.1016/j.engstruct.2022.115549

158. Vasconcelos G., Lourenço PB.: Experimental characterization of stone masonry in shear and compression, Constr Build Mater 23, 2009, p. 3337–3345. https://doi.org/10.1016/j.conbuildmat.2009.06.045

159. Vasconcelos GFM.: Experimental investigations on the mechanics of stone masonry: Characterization of granites and behavior of ancient masonry shear walls. PhD Thesis, 2005

160. Volk R., Steins JJ., Kreft O., Schultmann F.: Life Cycle Assessment of Post-Demolition Autoclaved Aerated Concrete (Aac) Recycling Options, SSRN Electron J 188, 106716, 2022. https://doi.org/10.2139/ssrn.4127305

161. Wang RT., Hu HS., Guo ZX.: Analytical study of stiffened multibay planar coupled shear walls, Eng Struct 244, 112770, 2021. https://doi.org/10.1016/j.engstruct.2021.112770

162. Wdowicki J., Wdowicka E.: Three-dimensional analysis of asymmetric shear wall structures with connecting and stiffening beams, Eng Struct 42, 2012, p. 362–370. https://doi.org/10.1016/j.engstruct.2012.04.038

163. Xu C., Xiangli C., Bin L.: Modeling of influence of heterogeneity on mechanical performance of unreinforced masonry shear walls, Constr Build Mater 26, 2012, p. 90–95. https://doi.org/10.1016/j.conbuildmat.2011.05.007

164. Xu X., Jin Z., Yu Y., Li N.: Damage source and its evolution of ultra-high performance concrete monitoring by digital image correlation and acoustic emission technologies, J Build Eng 65, 105734, 2023. https://doi.org/10.1016/j.jobe.2022.105734

165. Yi-Qiu T., Lei Z., Meng G., Li-Yan S.: Investigation of the deformation properties of asphalt mixtures with DIC technique, Constr Build Mater 37, 2012, p. 581–590. https://doi.org/10.1016/j.conbuildmat.2012.07.046

166. Zeman J., Šejnoha M.: From random microstructures to representative volume elements, Model Simul Mater Sci Eng 15, 2007. https://doi.org/10.1088/0965-0393/15/4/S01

167. Zucchini A., Lourenço PB.: A micro-mechanical homogenisation model for masonry: Application to shear walls, Int J Solids Struct 46, 2009, p. 871–886. https://doi.org/10.1016/j.ijsolstr.2008.09.034

Standards

N1. ASTM E519-81 Standard Test Method for Diagonal Tension (Shear) of Masonry Assemblages. American Society for Testing and Materials West Conshohocken, PA, United States of America; 2000.

N2. BS 5628-1:2005 Code of Practice for the Use of Masonry. Part 1: Structural Use of Unreinforced Masonry.

N3. Building Code Requirements for Masonry Structures. ACI 530-05/ASCE 5-05/TMS 402-05.

N4. Canadian Standards Associations CSA S304-14.

N5. CEN 1999 EN 1015-11: Methods of Test for Mortar for Masonry - Part 11: Determination of Flexural and Compressive Strength of Hardened Mortar. Eur. Comm. Stand. 1999, 12.

N6. DIN 1053-100:2006-08 Masonry – Part 100: Calculation Based on the Semi-Probabilistic Risk Concept (Mauerwerk – Teil 100: Berechnung Auf Der Grundlage Des Semiprobabilistischen Sicherheitskonzepts - in german).

N7. EN 1996-1-1:2005 Eurocode 6: Design masonry structures - Part 1-1: General rules for reinforced and unreinforced masonry structures.

N8. EN 772-1:2015 Methods of Test for Masonry Units - Part 1: Determination of Compressive Strength.

N9. GB50003-2011. National Standard of the People's Republic of China. Code for Design of Masonry Structures.

N10. IS:1905-1987 Indian Standard. Code of Practice for Structural Use of Unreinforced Masonry.

N11. National Building Code of Canada (NBCC) 2005.

N12. PN-B-03002:1987 Masonry structures. Static calculations and design (Konstrukcje murowe. Obliczenia statyczne i projektowanie - in polish).

N13. PN-B-03002:1989 Masonry structures. Static calculations and design (Konstrukcje murowe. Obliczenia statyczne i projektowanie - in polish).

N14. PN-B-03002:1999 Masonry structures. Design and calculation (Konstrukcje Murowe. Projektowanie i obliczanie - in polish).

N15. PN-B-03002:2007 Masonry structures. Design and calculation (Konstrukcje murowe. Projektowanie i obliczanie - in polish).

N16. PN-EN 1052-1:2000 Methods of Tests for Masonry. Part 1: Determination of Compression Strength. Polish Committee for Standardization (PKN): Warsaw, Poland, 2000, (in polish).

N17. PN-EN 1052-3:2004 Methods of Tests for Masonry. Part 3: Determination of Initial Shear Strength. Polish Committee for Standardization (PKN): Warsaw, Poland, 2004 (in polish).

N18. PrEN 1996-1-1:2017 Eurocode 6: Design of masonry structures - Part 1-1: General rules for reinforced and unreinforced masonry structures.

N19. SIA 266:2003 Masonry. Swiss Society of Civil Engineers Ans Architects, Zürich.

N20. SNiP II-22-81:2000 КАМЕННЫЕ И АРМОКАМЕННЫЕ. Design of Stone and Reinforced Stone (in Russian).

N21. TM 5-809-3/NAVFAC DM-2.9/AFM 88-3, Chap. 3. Masonry Structural Design for Buildings. Departments of the Army, the Navy and the Air Force.

ZACHOWANIE SIĘ MUROWANYCH ŚCIAN USZTYWNIAJĄCYCH NA PODSTAWIE BADAŃ PEŁNOSKALOWYCH

Streszczenie

Zadaniem murowanych ścian usztywniających jest zapewnienie geometrycznej niezmienności budynku, ograniczenie poziomych przemieszczeń konstrukcji oraz zapewnienie ogólnego komfortu użytkowania budowli. Elementy usztywniające przenoszą obciążenia poziome, oddziaływujące w płaszczyźnie ściany. Mogą być one wywołane przez oddziaływanie wiatru, nierównomierne osiadanie podłoża czy też mogą wynikać z negatywnych wpływów eksploatacji górniczej (wstrząsy, odkształcenia podłoża). Choć rola murowanych ścian usztywniających jest niezwykle ważna z punktu widzenia zarówno projektowania jak i użytkowania budynków – brakuje spójnego opracowania dotyczącego specyfiki tych elementów.

Niniejsza praca doktorska stanowi zatem wkład w usystematyzowanie wiedzy na temat murowanych usztywnień budynków. W ramach opracowania przeprowadzono wnikliwe studium literaturowe obejmujące krajowe i zagraniczne przepisy normowe oraz publikacje naukowe wraz z krytyczną analizą stanu wiedzy. Przeprowadzono badania pełnoskalowe jednokondygnacyjnych budynków murowanych z elementów murowanych z autoklawizowanego betonu komórkowego o różnej geometrii otworów w ścianach. Analizy te pozwoliły na określenie faz pracy ścian usztywniających z określeniem zakresu pracy sprężystej i nieliniowej. Wykonano szczegółowe obserwacje propagacji uszkodzeń oraz morfologii rys z wykorzystaniem technologii cyfrowej korelacji obrazu. Wykazano zmianę geometrii filarków międzyotworowych i wpływ tego fenomenu na sztywność konstrukcji. Zaproponowano dwie metody szacowania sztywności ścian usztywniających – metodę całkowitej sztywności oraz metodę empiryczną. Przedstawiono ponadto propozycję obliczania środka skręcania budynku na podstawie pomiaru przemieszczeń naroży budynku. Na podstawie porównania wyników teoretycznych i wyników badań określono wartości sił wewnętrznych.

Ponadto opracowano autorską procedurę numerycznej homogenizacji konstrukcji murowej w oparciu o badania normowe i kalibrację parametrów mechanicznych. Przeprowadzono stosowne pełnoskalowe analizy numeryczne w oparciu o sprężysto-plastyczny model materiałowy z degradacją. Wykazano wpływ zmiany energii pękania oraz wytrzymałości na rozciąganie muru na wyniki obliczeń numerycznych. Zaproponowano również inżynierskie podejście do analizy murowanych ścian usztywniających w oparciu o sprężyste modele numeryczne o skorygowanej sztywności ścian. Wyznaczono również dalsze kierunku prac badawczych i teoretycznych dotyczących przedmiotu rozprawy.

THE BEHAVIOR OF MASONRY STIFFENING WALLS BASED ON THE FULL-SCALE RESEARCH

Abstract

The role of the masonry stiffening walls is to ensure the geometric invariability of the building, to limit the horizontal displacements and to ensure the overall comfort of use of the building. Stiffeners transfer horizontal loads acting in the plane of the wall. Lateral loads may be caused by wind and uneven ground subsidence or may result from the adverse effects of mining (shocks, ground deformations). Although the masonry stiffening walls is crucial from the design and use of buildings' point of view, there is no consistent study on the specificity of these elements.

This doctoral thesis contributes to the systematization of knowledge about masonry stiffeners of buildings. A thorough literature study was carried out, including domestic and foreign standard regulations and scientific publications, along with a critical analysis of the state of knowledge. Full-scale tests of single-storey masonry buildings made of masonry elements made of autoclaved aerated concrete (AAC) with different geometry of openings in the walls were carried out. These analyses made it possible to determine the behavior phases of the stiffening walls, specifying the range of elastic and non-linear behavior. Detailed damage propagation and crack morphology observations were made using digital image correlation (DIC) technology. The change in the vertical piers geometry and the effect of this phenomenon on the stiffness was demonstrated. Two methods of estimating the stiffness of stiffening walls have been proposed - the total stiffness method and the empirical method. In addition, a proposal for calculating the torsion center of the building based on the measurement of slab corner displacements has been presented. The values of internal forces were determined based on comparing theoretical and test results.

In addition, an original procedure for numerical homogenization of the masonry structure was developed based on standard tests and calibration of mechanical parameters. Appropriate full-scale numerical analyzes were performed based on an elastic-plastic material model with degradation. The impact of changes in the cracking energy and tensile strength of the wall on the results of numerical calculations was indicated. An engineering approach to the analysis of stiffening masonry walls using numerical elastic models with corrected stiffness of the walls was also proposed. Further research directions and theoretical work on the dissertation subject were also set.

ZACHOWANIE SIĘ MUROWANYCH ŚCIAN USZTYWNIAJĄCYCH NA PODSTAWIE BADAŃ PEŁNOSKALOWYCH

Poszerzone streszczenie

Zadaniem murowanych ścian usztywniających jest zapewnienie geometrycznej niezmienności budynku, ograniczenie poziomych przemieszczeń konstrukcji oraz zapewnienie ogólnego komfortu użytkowania budowli. Elementy usztywniające przenoszą obciążenia poziome, oddziaływujące w płaszczyźnie ściany. Mogą być one wywołane przez oddziaływanie wiatru, nierównomierne osiadanie podłoża czy też mogą wynikać z negatywnych wpływów eksploatacji górniczej (wstrząsy, odkształcenia podłoża).

Konstrukcja murowa jest strukturą anizotropową, której cechy mechaniczne nie są prostym odzwierciedleniem parametrów mechanicznych składowych części muru – elementów murowych i zaprawy. Ponadto złożony stan naprężeń w murowanej ścianie usztywniającej wynika z jednoczesnego oddziaływania obciążenia poziomego i pionowego. Ściana usztywniająca jest jednocześnie ściskana, ścinana i zginana w swojej płaszczyźnie – co znacząco utrudnia badania eksperymentalne. Choć rola tych elementów jest niezwykle ważna z punktu widzenia zarówno projektowania jak i użytkowania budynków – brakuje spójnego opracowania dotyczącego specyfiki tychże usztywnień. Ten fakt skłonił autora do podjęcia rozprawy doktorskiej poświęconej zagadnieniu murowanych ścian sztywniących.

Celem pracy jest teoretyczne i eksperymentalne rozpoznanie przedmiotu pracy, motywowane następującymi czynnikami:

- brakiem spójnych procedur projektowania ścian usztywniających przy tendencji rynkowej do optymalizacji konstrukcji (zmniejszania przekroju poprzecznego ścian),
- niejasne i nieprecyzyjne sformułowania normowe dotyczące ścian usztywniających,
- nieznana rzeczywista wielkość redystrybucji sił wewnętrznych w murowanych ścianach usztywniających – w Eurokodzie 6 dopuszczono redystrybucję sił do 15% bez uzasadnienia takich regulacji,
- brak spójnych metod określania sztywności ścian usztywniających i rozdziału obciążeń poziomych na poszczególne ściany,
- brak metod wyznaczania położenia środka skręcania budynku i uwzględniania obrotu budynku w obliczeniach,
- nieznany wpływ perforacji ścian na sztywność konstrukcji,
- niedostateczne rozpoznanie badawcze przedmiotowej tematyki na modelach pełnoskalowych.

Głównym zagadnieniem badawczym pracy jest zachowanie się ścian usztywniających wykonanych z elementów murowych z autoklawizowanego betonu komórkowego (ABK) zarówno w fazie sprężystej jak i nieliniowej. Celami pracy są:

- analiza stanu wiedzy w literaturze krajowej i zagranicznej dotyczącej murowanych ścian usztywniających,
- przegląd ustaleń normowych,
- rozdział obciążeń na ściany usztywniające,
- określenie rzeczywistej redystrybucji sił wewnętrznych,
- analiza propagacji zarysowań i morfologii rys,
- propozycja metody wyznaczania położenia środka skręcania budynku,
- określenie faz pracy murowanych ścian usztywniających w zakresie sprężystym i post-sprężystym.

W ramach rozprawy sformułowano następujące tezy pracy:
1. Sztywność poszczególnych części konstrukcji determinuje wielkość redystrybucji sił wewnętrznych w budynku murowanym.
2. Sprężysty zakres pracy konstrukcji murowej jest niewielki i stanowi ok. 30% nośności.
3. Ściany usztywniające poddane ścinaniu ulegają znacznej degradacji swojej sztywności.
4. Położenie środka skręcania budynku wynika z rozkładu sztywności poszczególnych elementów konstrukcyjnych (ścian).
5. Budynek, w którym występuję niesymetryczny rozdział sztywności elementów usztywniających, na skutek działania obciążenia poziomego, ulega przesunięciu (translacji) oraz skręceniu (obrotowi).
6. Dobór metody homogenizacji konstrukcji murowej wpływa na dokładność numerycznego odwzorowania pracy konstrukcji.

Do weryfikacji postawionych tez przedsięwzięto analizy eksperymentalne i teoretyczne niezbrojonych konstrukcji murowych, poddanych działaniu monotonicznego obciążenia poziomego. Zakresem pracy objęto:

- przegląd literatury,
- własny program badań eksperymentalnych,
- analizy numeryczne z wykorzystaniem Metody Elementów Skończonych (MES),
- propozycję analitycznej metody wyznaczania sztywności ścian usztywniających i położenia środka skręcania budynku,
- dyskusję i główne wnioski.

Rozdział 1 rozprawy stanowi krótki wstęp opisujący aktualną sytuację gospodarczą i rynkową dotyczącą branży budowlanej – w okresie, w którym powstawała niniejsza praca. Rozdział 2 obejmuje uzasadnienie podjęcia tematu ścian usztywniających oraz cele, tezy i zakres pracy. Rozdział 3 obejmuje analizę stanu wiedzy w ujęciu przepisów normowych oraz publikacji naukowych w literaturze krajowej i zagranicznej. Przedstawiono wybrane wyniki badań konstrukcji murowych, procedury obliczeniowe i metody (techniki) homogenizacji muru, stosowane w obliczeniach numerycznych. Rozdział 4 dotyczy własnego programu badań pełnoskalowych modeli budynków murowanych, opis stanowiska badawczego opis oraz wykorzystywanych metod pomiarowych. W rozdziale 5 zaprezentowano główne wyniki badań i opis faz zachowania się ścian usztywniających w zakresie sprężystym i nieliniowym. W rozdziale 6 zawarto rezultaty analiz propagacji zarysowań i uszkodzeń ścian. Rozdział 7 obejmuje obliczenia numeryczne. W ramach pracy zaproponowano autorską procedurę homogenizacji muru, opierającą się na wynikach badań normowych. Podejście to zapewnia powtarzalność i dzięki temu może być weryfikowane przez innych badaczy. Ponadto wykonano analizy numeryczne z wykorzystaniem sprężysto-plastycznego modelu materiałowego z degradacją do odzwierciedlenia zachowania się ścian usztywniających. Rozdział 8 zawiera dyskusję wyników badań w zakresie wyznaczania sztywności ścian w fazie sprężystej i post-sprężystej z uwzględnieniem zarysowania ściany, położenie środka skręcania budynku oraz propozycję inżynierskiej metody analizy numerycznej ścian. W rozdziale 9 zebrano najważniejsze wnioski wynikające z przeprowadozynch analiz. W załączniku zawarto zdetalizowane rysunki konstrukcyjne ścian, umożliwiające powtórzenie (dokładne odwzorowanie) badań.

Na podstawie przeglądu literatury stwierdzono, że:
- badania ścian usztywniających obciążonych monotonicznie należą do rzadkości,
- większość analiz niezbrojonych konstrukcji murowych dotyczy obciążeń cyklicznych,
- przemieszczenia poziome ścian usztywniających obejmują deformacje spowodowane ścinaniem (deformacje postaciowe) oraz spowodowane zginaniem (deformacje giętne),
- udział poszczególnych deformacji w całkowitym odkształceniu ścian nie zależy od wstępnego obciążenia ściskającego – zależy wyłącznie od geometrii konstrukcji,
- nośność ścian usztywniających uwarunkowana jest poziomem wstępnych naprężeń ściskających – zwiększenie naprężeń ściskających powoduje wzrost nośności ściany na ścinanie w swojej płaszczyźnie,
- wstępne naprężenia ściskające mają wpływ na morfologię zarysowania ściany – przy niewielkim obciążeniu pionowym rysy mają charakter schodkowy, przy znaczących wartościach naprężeń ściskających, rysy przebiegają ukośnie

również przez elementy murowe,

- fragmenty ścian poprzecznych do ścian usztywniających biorą udział w przenoszeniu obciążeń poziomych (są to tzw. szerokości współpracujące),
- sztywność niezbrojonej konstrukcji murowej spada znacząco w przypadku wykonania otworów w ścianie,
- obecność otworów zmienia rzeczywistą geometrię filarków międzyotworowych i obraz zarysowania konstrukcji,
- niesymetryczny rozkład perforacji w budynku determinuje skręcanie konstrukcji obciążonej poziomo.

Własny program badań doświadczalnych zaprojektowano według następujących kryteriów:
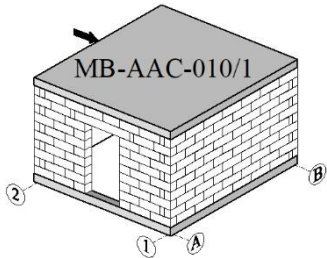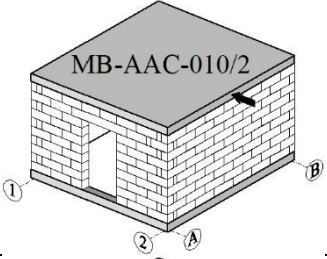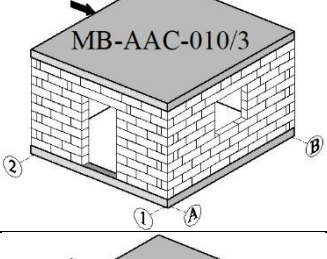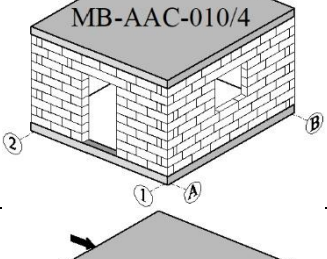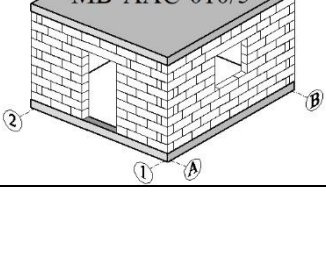
- modele wykonane są z elementów murowych z autoklawizowanego betonu komórkowego,
- ściany są wzniesione w technologii na cienkie spoiny wsporne i niewypełnione spoiny pionowe (czołowe) – połączenia typu pióro-wpust,
- wszystkie modele są niezbrojonymi konstrukcjami murowymi,
- modele badawcze składają się ze ścian murowanych i stropu żelbetowego, który stanowi sztywną tarczę przez którą przekazywane są obciążenia poziome na ściany,
- wielkość wstępnych naprężeń ściskających odpowiada obciążeniu jednokondygnacyjnego budynku w zabudowie mieszkalnej i obejmuje ciężar własny, ciężar warstw wykończeniowych oraz obciążenie zmienne (użytkowe),
- badania mogą zostać w przyszłości rozszerzone do analizy budynków wielokondygnacyjnych poprzez zwiększenie wstępnych naprężeń ściskających,
- geometria ścian sprawia, że dominującymi odkształceniami są deformacje postaciowe – nie giętne, współczynnik wysokości do długości ściany usztywniającej jest mniejszy od jedności $h/l <1$,
- w wybranych modelach budynków wykonano otwory drzwiowe i okienne, o geometrii odpowiadającej rzeczywistym gabarytom takich otworów,
- zaprojektowane stanowisko badawcze umożliwia badania pełnoskalowych modeli budynków w schemacie statycznym utwierdzenia ścian u podstawy, przy zadaniu wstępnych naprężeń ściskających ściany.

Modele zaprojektowano w taki sposób aby umożliwić zrealizowanie postawionych celów pracy. Program badawczy obejmuje osiem pełnoskalowych modeli budynków, wzniesionych na planie kwadratu 4,0x4,0 m, przy wysokości całkowitej budynku równej 2,85 m i grubości ścian 0,18 m. Każdy model składa się z dwóch ścian usztywniających, oznaczonych literami A i B oraz dwóch ścian prostopadłych oznaczonych cyframi 1 i 2. Modele oznaczono symbolami literowo- cyfrowymi MB-
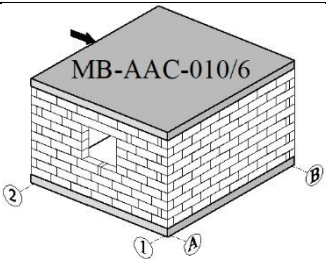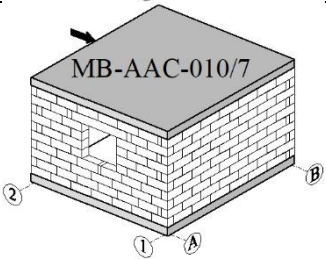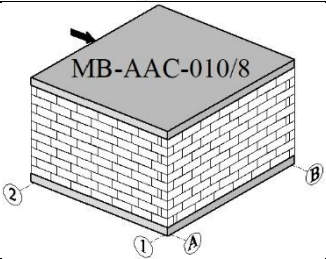
AAC-010/N, gdzie N oznacza kolejne modele budynków. Program badawczy składa się z czterech typów modeli – typ I to modele z jednym otworem drzwiowym, typ II to otwór drzwiowy w ścianie usztywniającej i otwór okienny w ścianie prostopadłej. Typ III to modele z dwoma otworami w ścianach usztywniających, a typ IV to jeden model referencyjny pozbawiony otworów. Zestawienie badanych modeli budynków pokazano w tabeli 1.

Tabela 1

Lista modeli badawczych budynków murowanych

Oznaczenie modelu / widok 3D		Oznaczenie ściany	Otworowanie	Opis ściany
MB-AAC-010/1	MB-AAC-010/1	Ściana A	otwór drzwiowy	usztywniająca
		Ściana B	pełna	
		Ściana 1	pełna	prostopadła
		Ściana 2	pełna	
MB-AAC-010/2	MB-AAC-010/2	Ściana A	otwór drzwiowy	usztywniająca
		Ściana B	pełna	
		Ściana 1	pełna	prostopadła
		Ściana 2	pełna	
MB-AAC-010/3	MB-AAC-010/3	Ściana A	otwór drzwiowy	usztywniająca
		Ściana B	pełna	
		Ściana 1	otwór okienny	prostopadła
		Ściana 2	pełna	
MB-AAC-010/4	MB-AAC-010/4	Ściana A	otwór drzwiowy	usztywniająca
		Ściana B	pełna	
		Ściana 1	otwór okienny	prostopadła
		Ściana 2	pełna	
MB-AAC-010/5	MB-AAC-010/5	Ściana A	otwór drzwiowy	usztywniająca
		Ściana B	pełna	
		Ściana 1	otwór okienny	prostopadła
		Ściana 2	pełna	

MB-AAC-010/6	MB-AAC-010/6	Ściana A	otwór okienny	usztywniająca
		Ściana B	otwór drzwiowy	
		Ściana 1	pełna	prostopadła
		Ściana 2	pełna	
MB-AAC-010/7	MB-AAC-010/7	Ściana A	otwór okienny	usztywniająca
		Ściana B	otwór drzwiowy	
		Ściana 1	pełna	prostopadła
		Ściana 2	pełna	
MB-AAC-010/8	MB-AAC-010/8	Ściana A	pełna	usztywniająca
		Ściana B	pełna	
		Ściana 1	pełna	prostopadła
		Ściana 2	pełna	

Aby skrócić czas wznoszenia poszczególnych modeli zdecydowano się na zaprojektowaniu stropu, który mógłby być podnoszony po badaniu modelu budynku i wykorzystany ponownie w kolejnym teście. W tym celu wykorzystano prefabrykowane panele stropowe (zwane elementami panelowymi). Są to segmenty sprężone składające się z żeber i płyty dolnej. Pomiędzy żebra włożono styropian pozwalający na zredukowanie ciężaru własnego stropu – ograniczenie to wynikało z tonażu suwnicy. Elementy panelowe układano na kształtkach wieńcowych, a całość konstrukcji stropu monolityzowano nadbetonem – rys. 1.

a)   b)
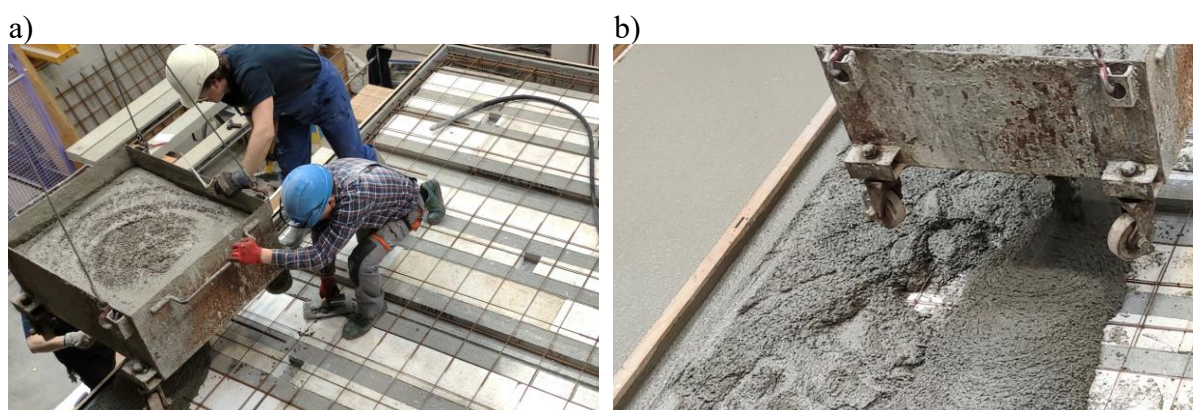
Rys. 1 Betonowanie stropu: a) zasobnik z mieszanką betonową, b) układanie mieszanki betonowej.

Modele badawcze wznoszono w kilku etapach – rys. 2:

- wzniesienie pierwszego modelu,
- badanie pierwszego modelu,
- odcięcie stropu od ścian i podniesienie stropu suwnicą,
- ułożenie stropu na stalowej konstrukcji wsporczej,
- rozbiórka ścian,
- wzniesienie nowych ścian kolejnego modelu i ułożenie stropu.
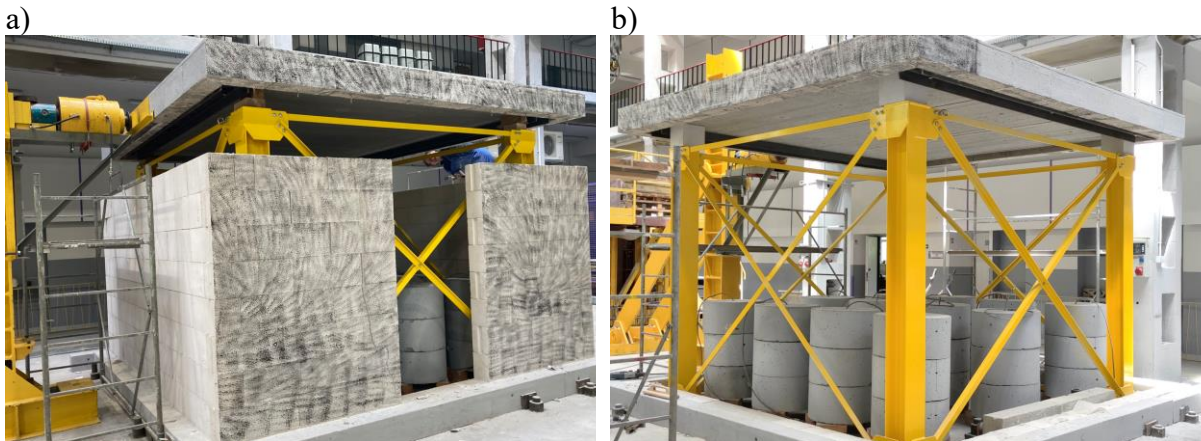
Rys. 2 Procedura ponownego wykorzystania stropu: a) wyburzenie ścian modelu po badaniu, b) strop ułożony na stalowej konstrukcji wsporczej

Stanowisko zaprojektowano w sposób umożliwiający zadanie obciążenia pionowego jak również poziomego. Model badawczy utwierdzono w płycie wielkich sił. Zamocowanie zrealizowano za pomocą zewnętrznych belek okalających dolny wieniec modelu, zaklinowanych o śruby średnicy 65 mm, które były przykręcone do hali laboratorium. Obok modelu umiejscowiono stalowy słup z zastrzałem – do niego przymocowano stalową konstrukcję podpierającą siłownik hydrauliczny. Pomiar siły odbywał się za pomocą siłomierza o zakresie pracy 250 kN ± 0.1 kN. Obciążenie poziome przyłożone w środku ciężkości stropu i w połowie długości ściany prostopadłej do ścian usztywniających. Obciążenia pionowe wywołano obciążnikami podwieszonymi do stropu. Pojedynczy odważnik miał średnicę 60 cm i wysokość 30 cm. Sumarycznie podwieszono po trzy odważniki o ciężarze 204 kg w dwunastu punktach (73.44 kN). W tym celu w wykonanym stropie uprzednio wywiercono otwory o średnicy 25 mm do przepuszczenia stalowych cięgien podwieszających obciążniki. Otwory były zlokalizowane pomiędzy sprężonymi żebrami stropu panelowego – by nie uszkodzić cięgien sprężających. W miejscu przykładania obciążenia kształtki wieńcowe zamieniono na ceownik stalowy, umożliwiający bezpieczne przekazanie obciążenia na konstrukcję stropu. Widok modelu badawczego na stanowisku pokazano na rys. 3. Pomiary przemieszczeń prowadzono z wykorzystaniem transformatorowych przetworników przemieszczeń liniowych (LVDT). Analizę propagacji zarysowań oraz odkształceń modeli wykonano za pomocą systemu Aramis 6M.
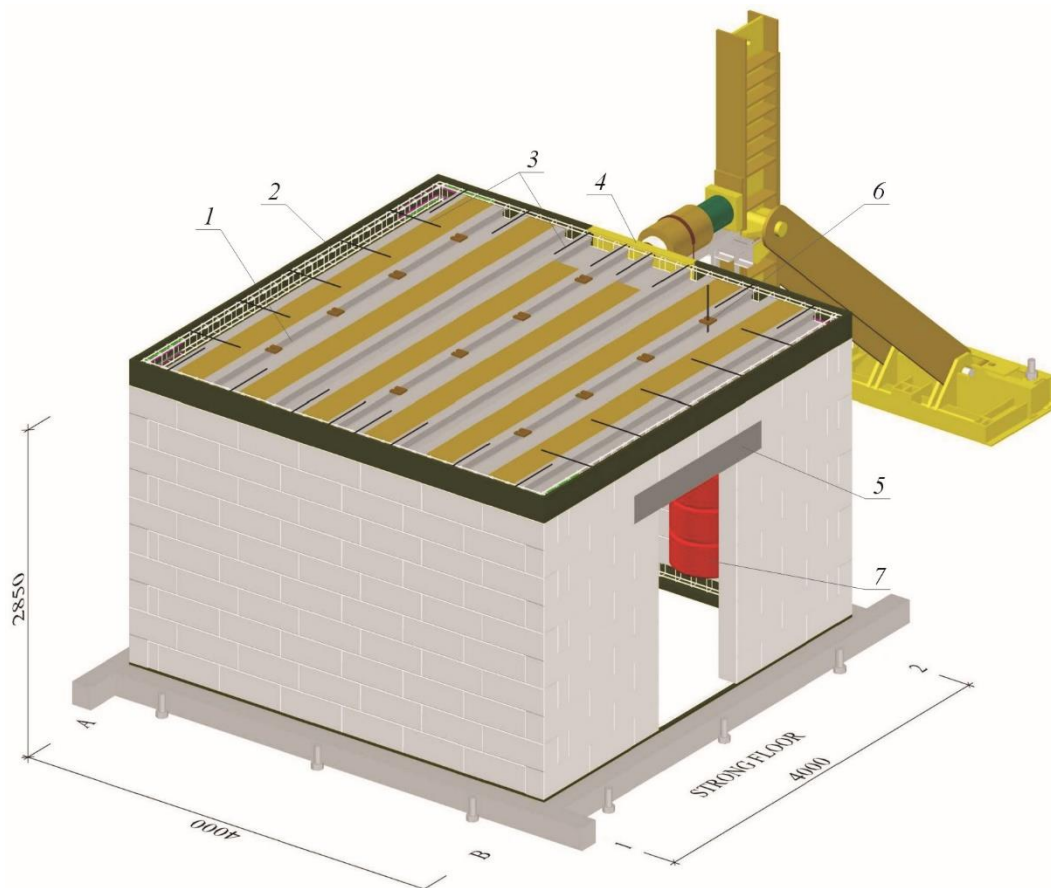
Rys. 3 Model badawczy na stanowisku: 1 – prefabrykowane, sprężone element panelowe stropu, 2 – zbrojenie górnego wieńca, 3 – zbrojenie górne stropu, 4 – ceownik stalowy, 5 – prefabrykowane nadproże, 6 – punkty podwieszenia obciążenia pionowego, 7 – widoczne obciążniki

Zachowanie się ścian usztywniających i ścian prostopadłych przedstawiono w formie wykresów zależności znormalizowanej siły poziomej (H_i/H_u) do kąta odkształcenia postaciowego. Przykładowe rezultaty pokazano na rys. 4. Znając kąty odkształcenia deformacji postaciowej obliczono również wielkości poziomych przemieszczeń ścian.
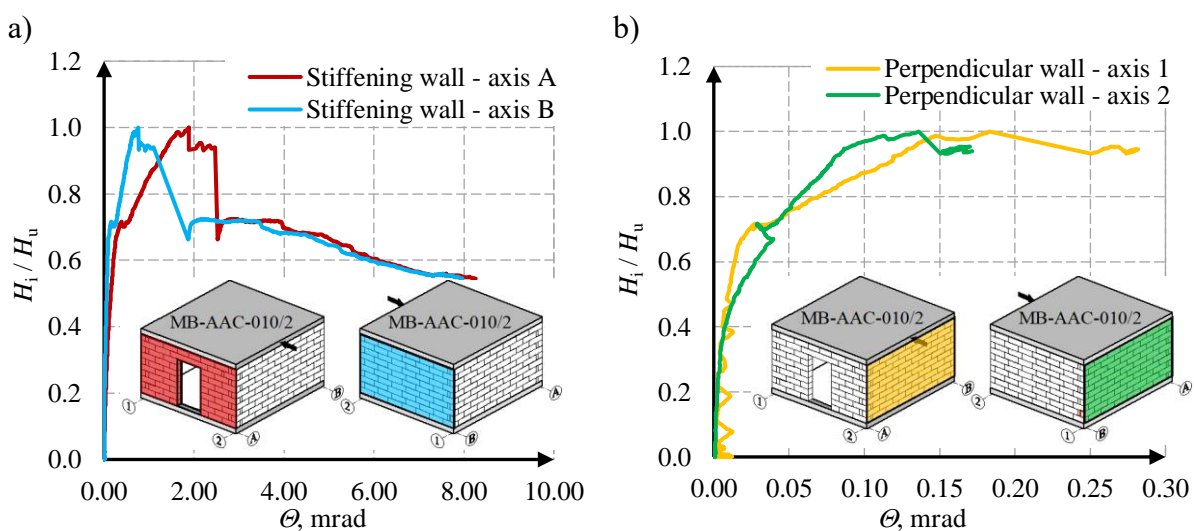
Rys. 4 Zależność pomiędzy obciążeniem poziomym, a kątem odkształcenia postaciowego dla modelu MB-AAC-010/2: a) wyniki dla ścian usztywniających A i B, b) wyniki dla ścian prostopadłych 1 i 2

245

Analiza wyników badań pozwoliła na określenie faz pracy zachowania się ścian usztywniających z otworami i bez otworów. Wyróżniono fazę początkową (faza I), w której jako pierwszy uszkodzeniu ulega rozciągany narożnik otworu. Następnie ma miejsce zarysowanie samej ściany murowanej, co jest tożsame z granicą sprężystej pracy konstrukcji (faza II). W dalszej kolejności dochodzi do postępujących zarysowań schodkowych ściany w zakresie post-sprężystym (faza III). Po przekroczeniu siły niszczącej (maksymalnej) – ściana ulega poziomej translacji (faza rezydualna IV) – rys. 5.

Bazując na wynikach badań opracowano empiryczną metodę wyznaczania sztywności ścian. Jako podejście referencyjne zaproponowano również metodę całkowitej sztywności. Porównanie obu metod pozwoliło na określenie redystrybucji sił wewnętrznych w ścianach – której wielkość określono na ok. 10%.
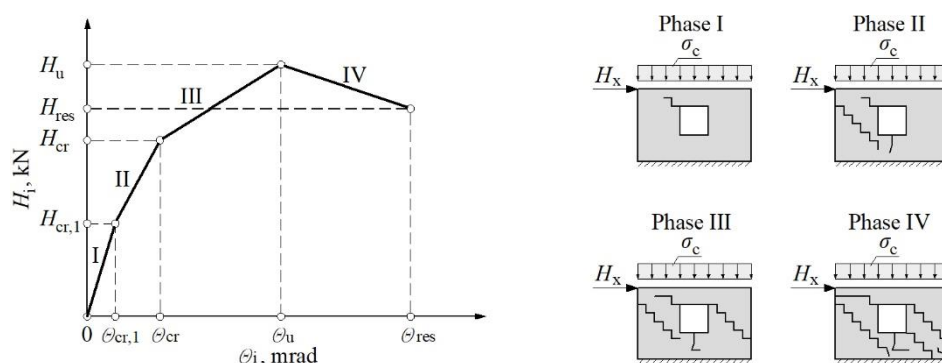
Rys. 5 Fazy pracy ścian usztywniających z otworem okiennym

Analiza propagacji i morfologii zarysowań ścian (rys. 6) pozwoliły na określenie rzeczywistej geometrii filarków międzyotworowych. W pracy zaproponowano korektę geometrii filarków, pozwalającą na wyznaczenie sztywności postsprężystej ściany w fazie zarysowanej. Ponadto przeanalizowano zjawisko obrotu budynku na skutek działania obciążenia poziomego - rys. 7.
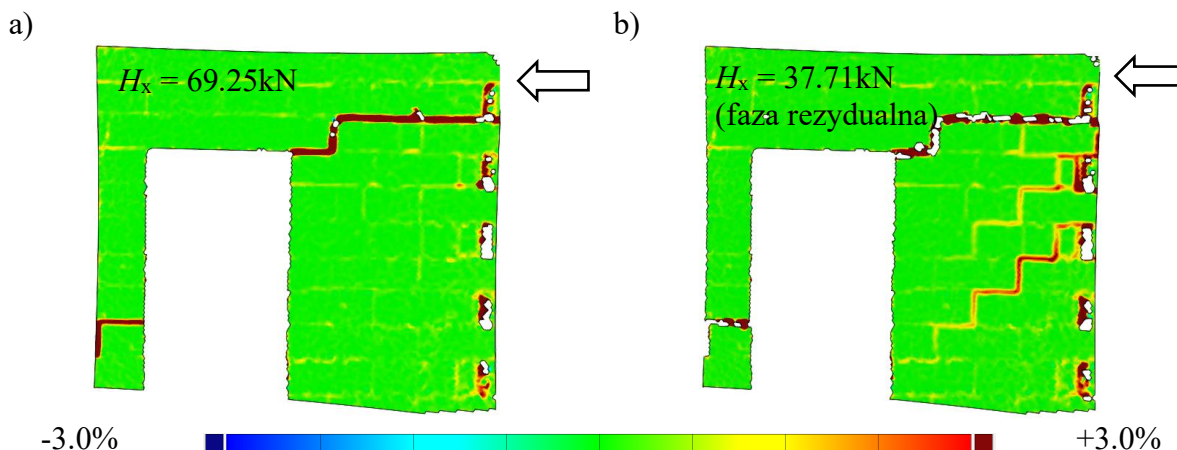
Rys. 6 Propagacja zarysowań ściany usztywniającej A - model MB-AAC-010/2: a) obraz zarysowań przy sile poziomej H_x = 69,25 kN, b)) obraz zarysowań przy sile poziomej H_x = 37,71 kN

a)
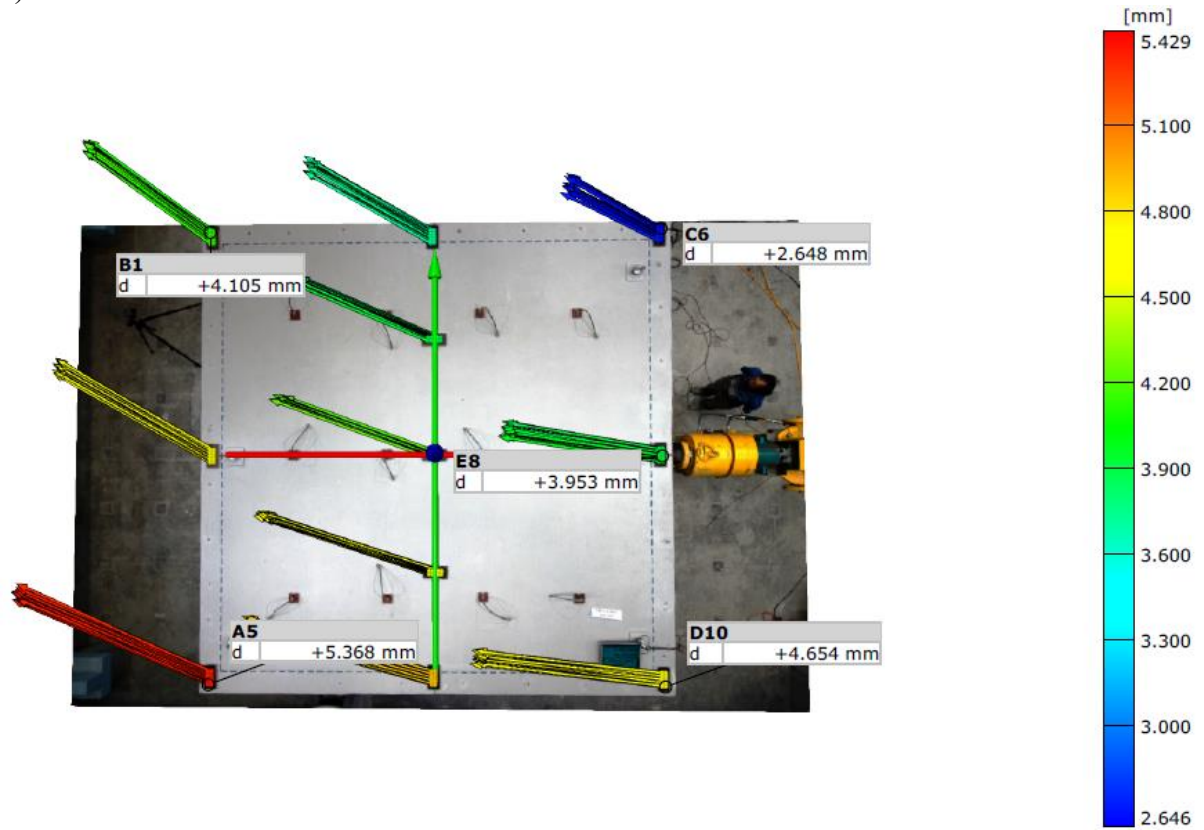
b)
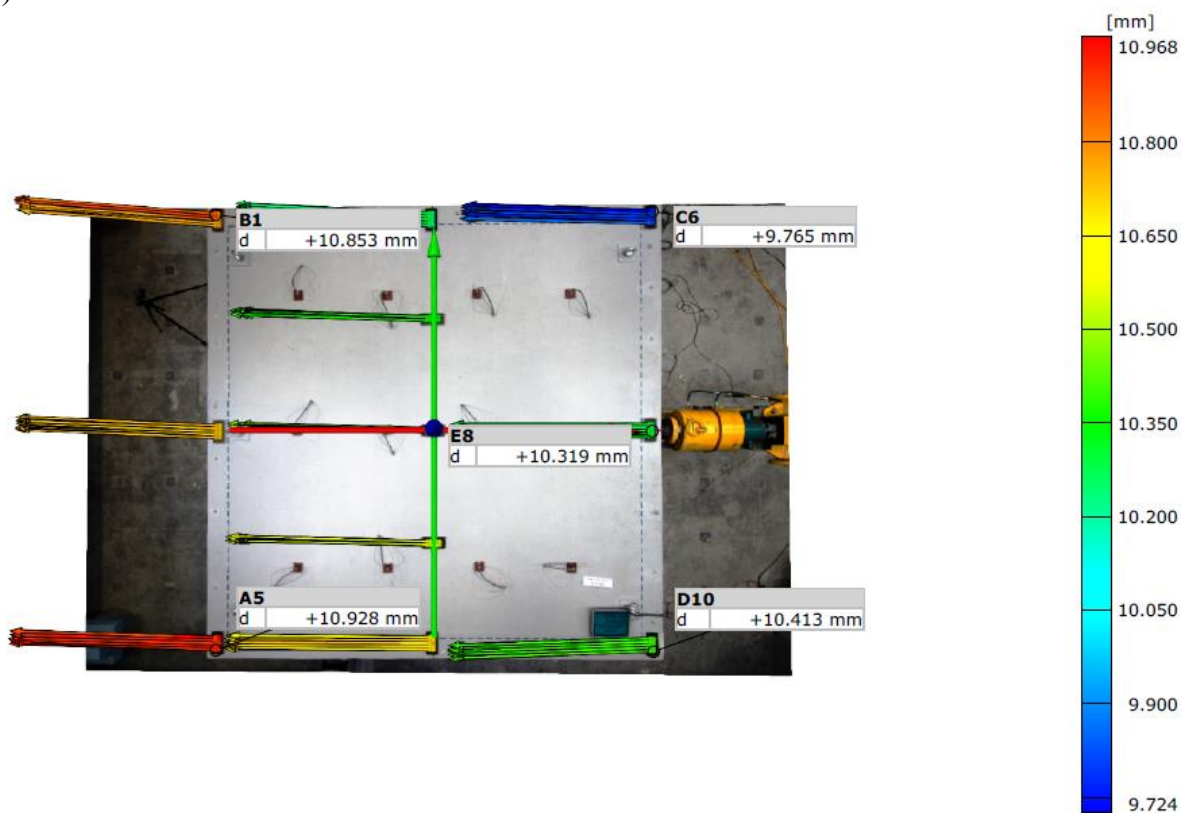
Rys. 7 Wektory przemieszczeń poziomych narożników stropu – model MB-AAC-010/2: a) przy sile poziomej $H_x = 64,49$ kN, b) przy sile poziomej $H_x = 46,85$ kN

Pomiary poziomych przemieszczeń narożników stropu i analiza wektorów przemieszczenia wypadkowego wskazała, że budynek w fazie początkowej i sprężystej podlega niewielkiemu przemieszczeniu poziomemu i obrotowi. Na skutek postępujących zarysowań ścian dochodzi do redystrybucji sił wewnętrznych i wyrównania sztywności ścian. W fazach postsprężystych budynek ma tendencje do stosunkowo dużej translacji, a zjawisko obrotu konstrukcji jest marginalne. Zaproponowana w pracy procedura wyznaczania położenia środka skręcania budynku umożliwiła na analityczne określenie współrzędnych środka obrotu. Wykorzystując wyniki badań stwierdzono, że położenie to zmienia się w trakcie zwiększania obciążenia, na skutek postępujących zmian sztywności (spowodowanych zarysowaniem).

W ramach rozprawy doktorskiej wykonano zaawansowane (nieliniowe) obliczenia numeryczne. W tym celu wykorzystano autorską procedurę homogenizacji konstrukcji murowej. Walidacje obliczeń numerycznych prowadzono w oparciu o wyniki badań i dwa kryteria walidacyjne. Kryterium A polegające na porównaniu globalnego zachowania się modelu, w którym porównywano zależności siła pozioma – przemieszczenie poziome ścian. Kryterium B dotyczyło porównania obrazów uszkodzeń i zarysowań ścian. Kalibrowano wybrane parametry mechaniczne modelu materiałowego. Redukcja wytrzymałości na rozciąganie pozwoliła na lepsze dopasowanie sił niszczących, jednak prowadziła do znacznego rozmiękczenia modelu – kalibracja energii pękania umożliwiła na dopasowanie obrazów uszkodzeń ścian (obszary osłabienia materiału w modelu numerycznym), przy jednoczesnym braku satysfakcjonującej zbieżności zachowania się modelu numerycznego w odniesieniu do wyników badań.

Jako, że w praktyce inżynierskiej stosowanie nieliniowych modeli materiałowych w obliczeniach numerycznych jest niepraktyczne ze względu na stopień złożoności modelu i czasochłonność obliczeń – zaproponowano podejście uproszczone. W tym celu posłużono się modelem sprężystym budynku, w którym nie modelowano otworów. Ściany z otworami zastąpiono ścianami bez otworów o zredukowanej sztywności. Podejście to pozwoliło na dopasowanie sztywności budynku poprzez kalibrację modułu sprężystości. Podobny efekt można również uzyskać redukując grubość ścian w modelu numerycznym.

Autor jest świadomy, że niniejsze opracowanie ma charakter badań rozpoznawczych, pozwalających na wyznaczenie dalszych kierunków prac, które powinny obejmować:

- analizy numeryczne na mikromodelach, pozwalających na dokładne odwzorowanie zachowania się modeli budynków i umożliwiających porównanie sił wewnętrznych,
- powtórzenie badań na modelach w skali, przy jednoczesnym zapewnieniu powtarzalności eksperymentu,
- rozszerzenie programu badań o analizy modeli budynków ze zwiększonym obciążeniem pionowym (o zwiększonych naprężeń ściskających ściany).
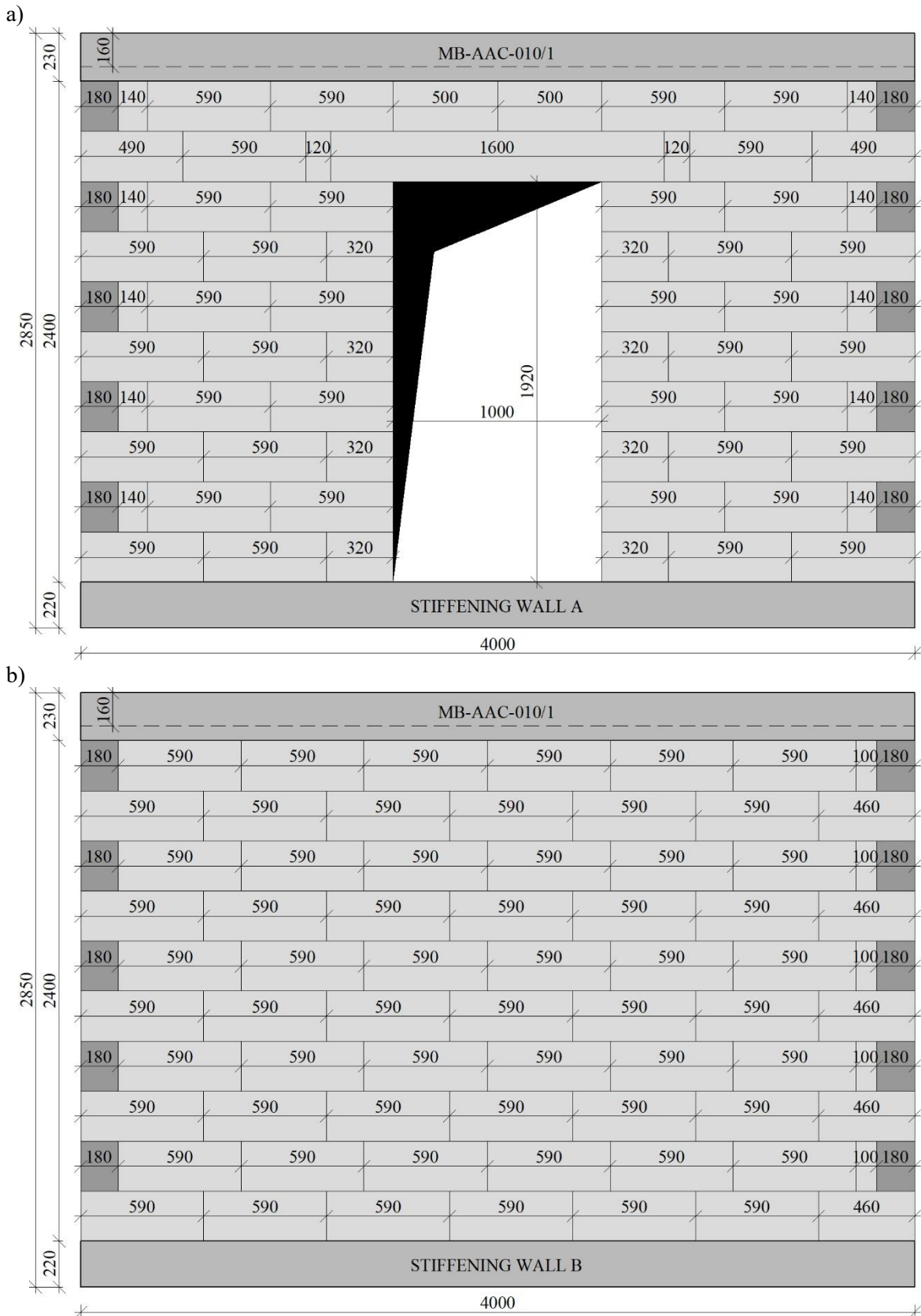
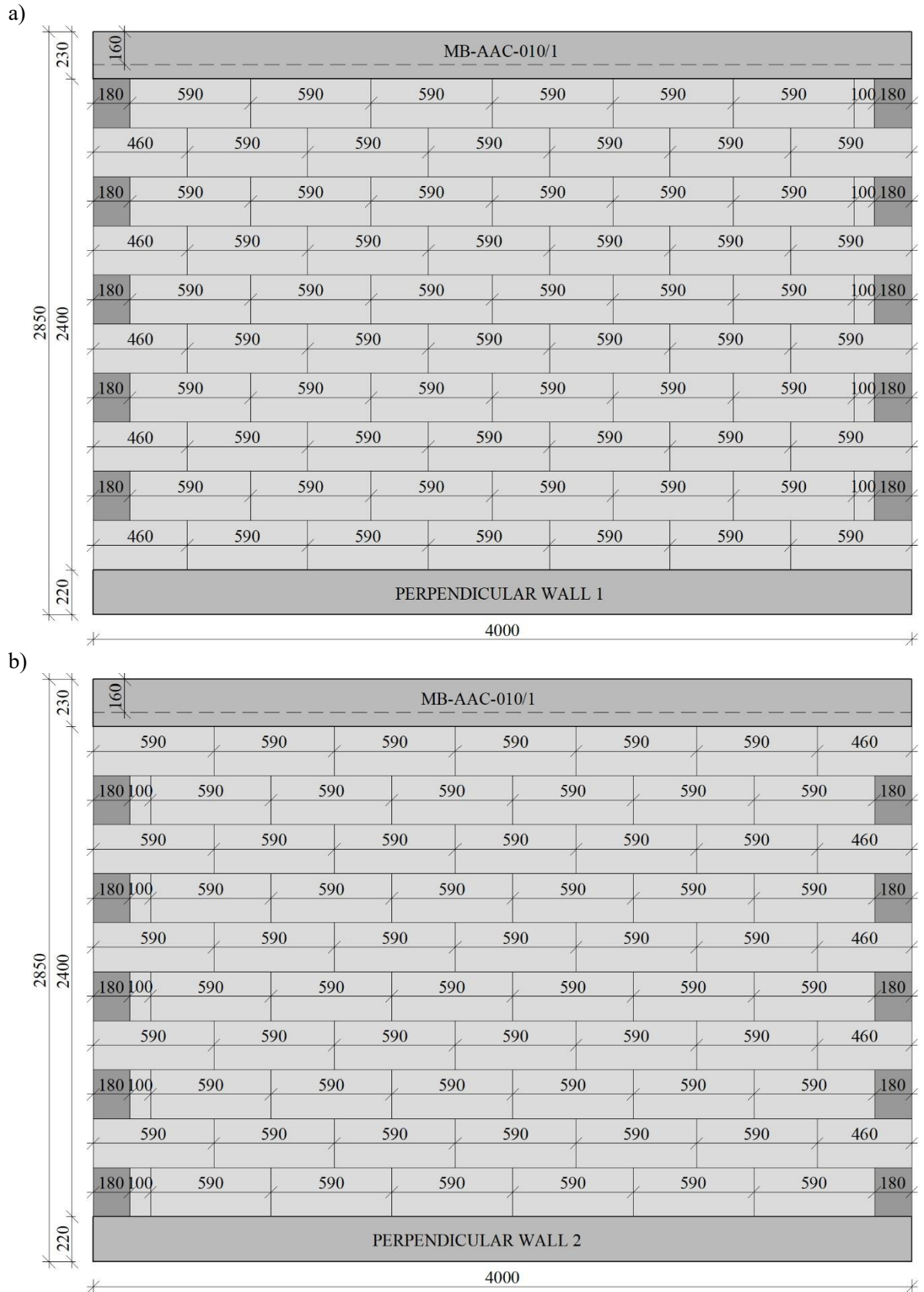Fig. A.1 Design of the MB-AAC-010/1 model: a) stiffening wall A, b) stiffening wall B

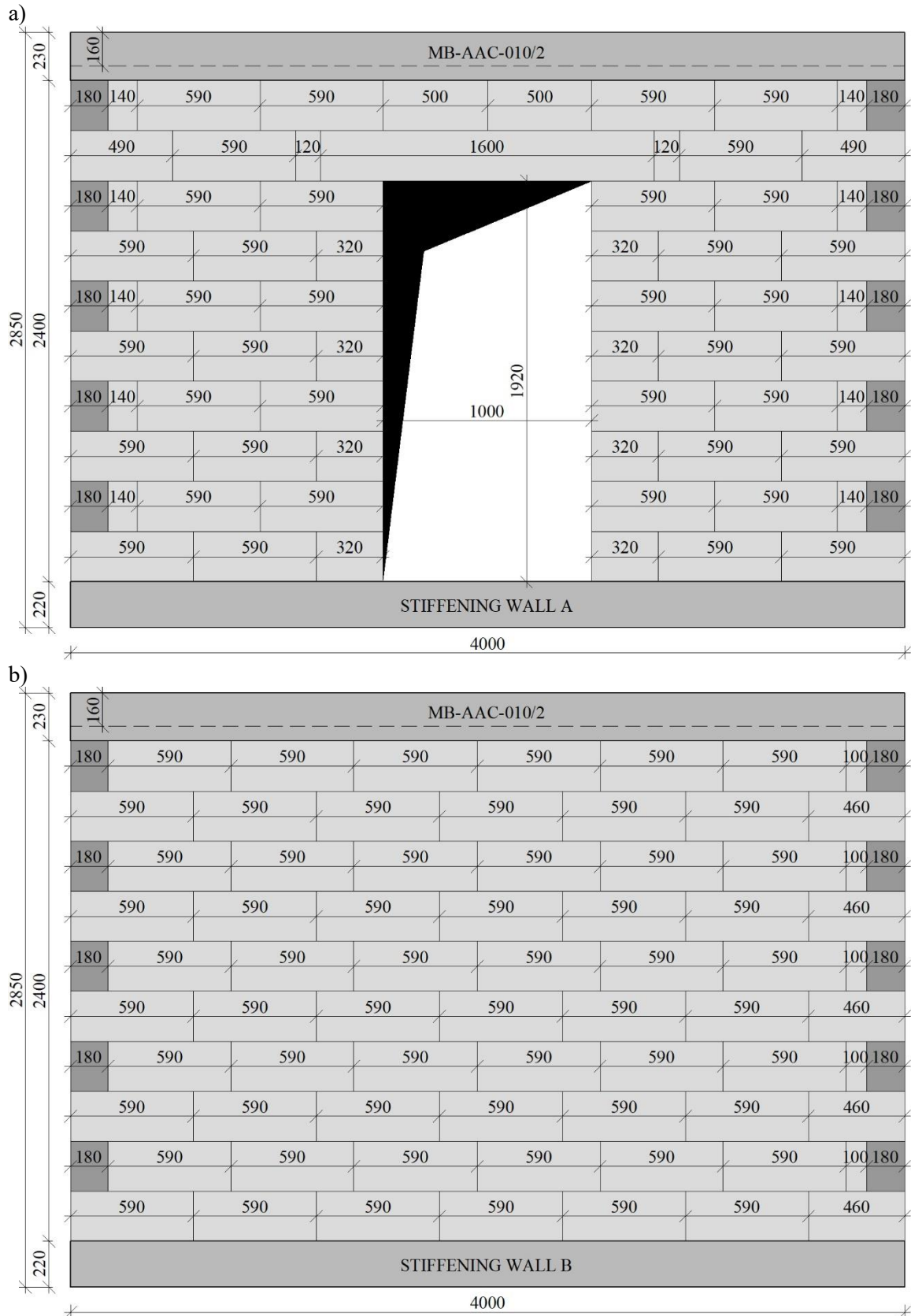Fig. A.2 Design of the MB-AAC-010/1 model: a) perpendicular wall 1, b) perpendicular wall 2

250

Fig. A.3 Design of the MB-AAC-010/2 model: a) stiffening wall A, b) stiffening wall B
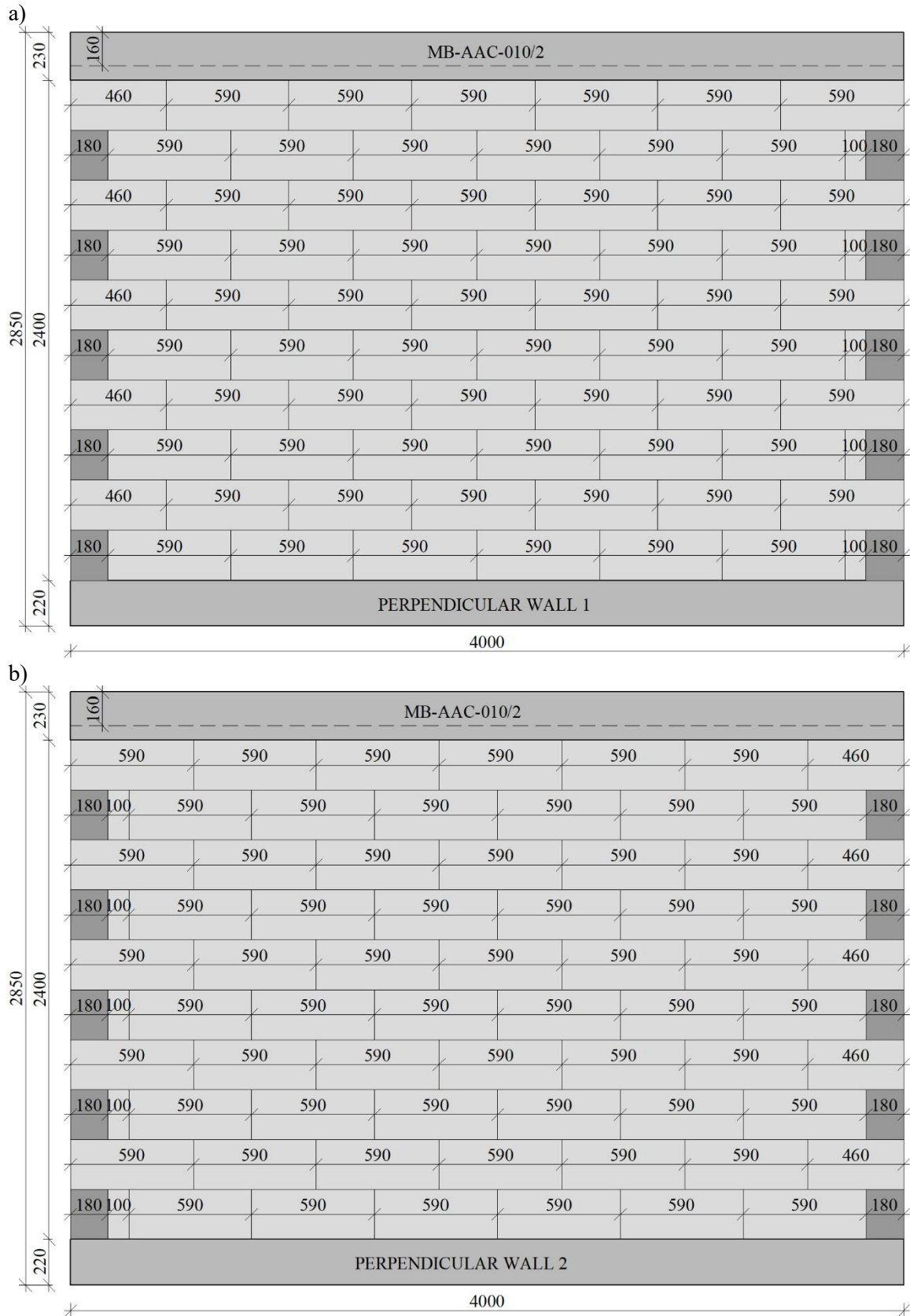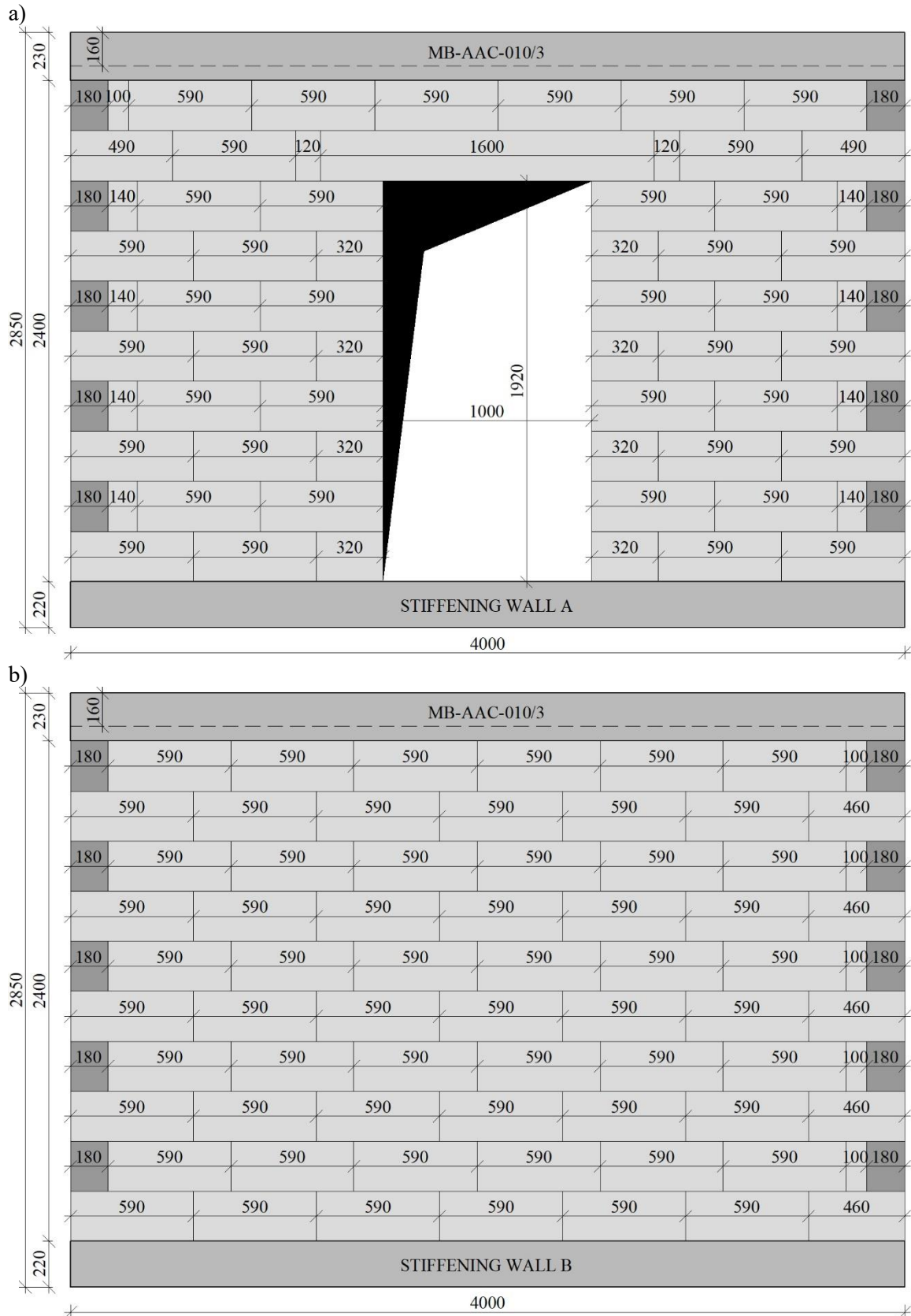
251

Fig. A.4 Design of the MB-AAC-010/2 model: a) perpendicular wall 1, b) perpendicular wall 2

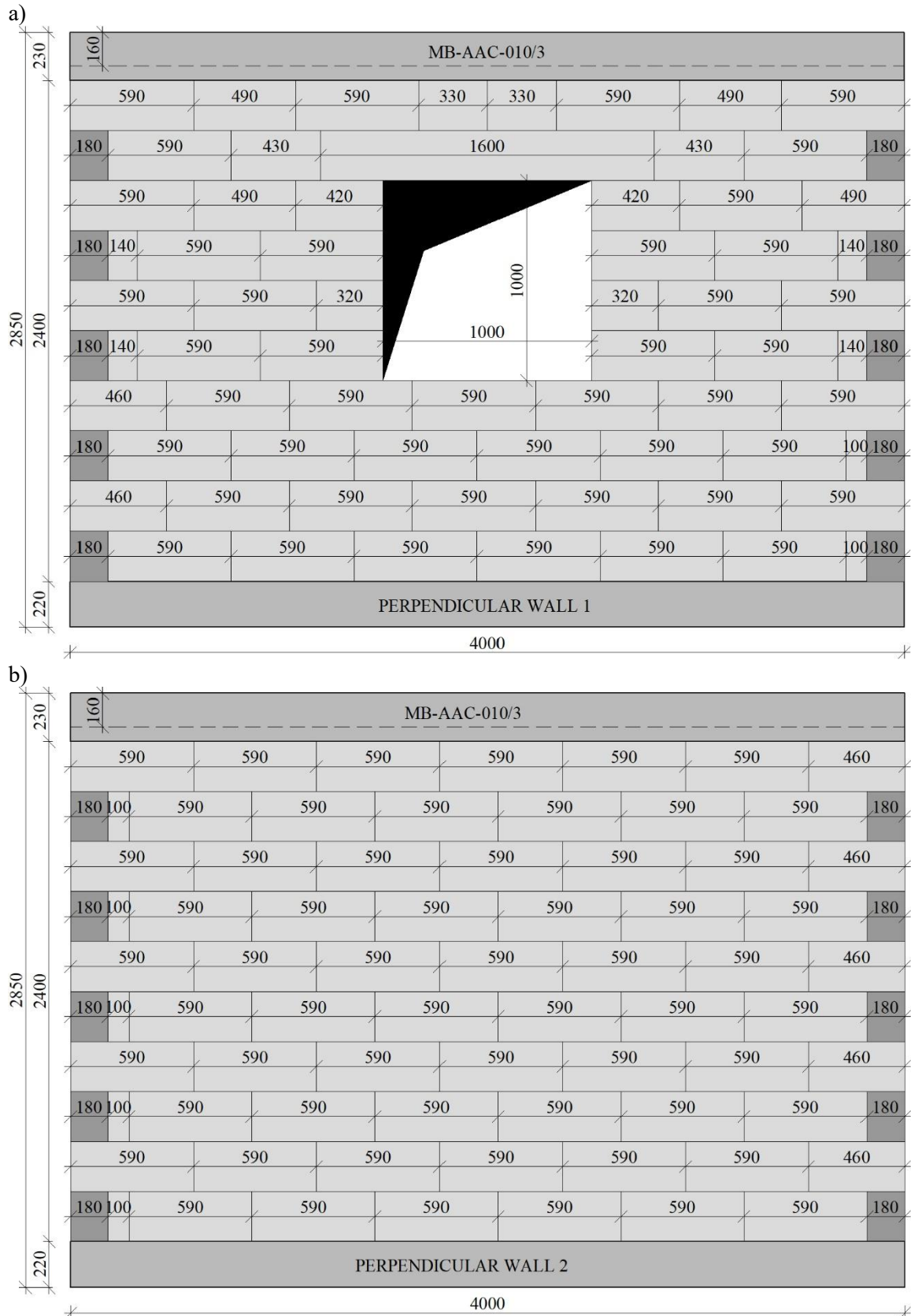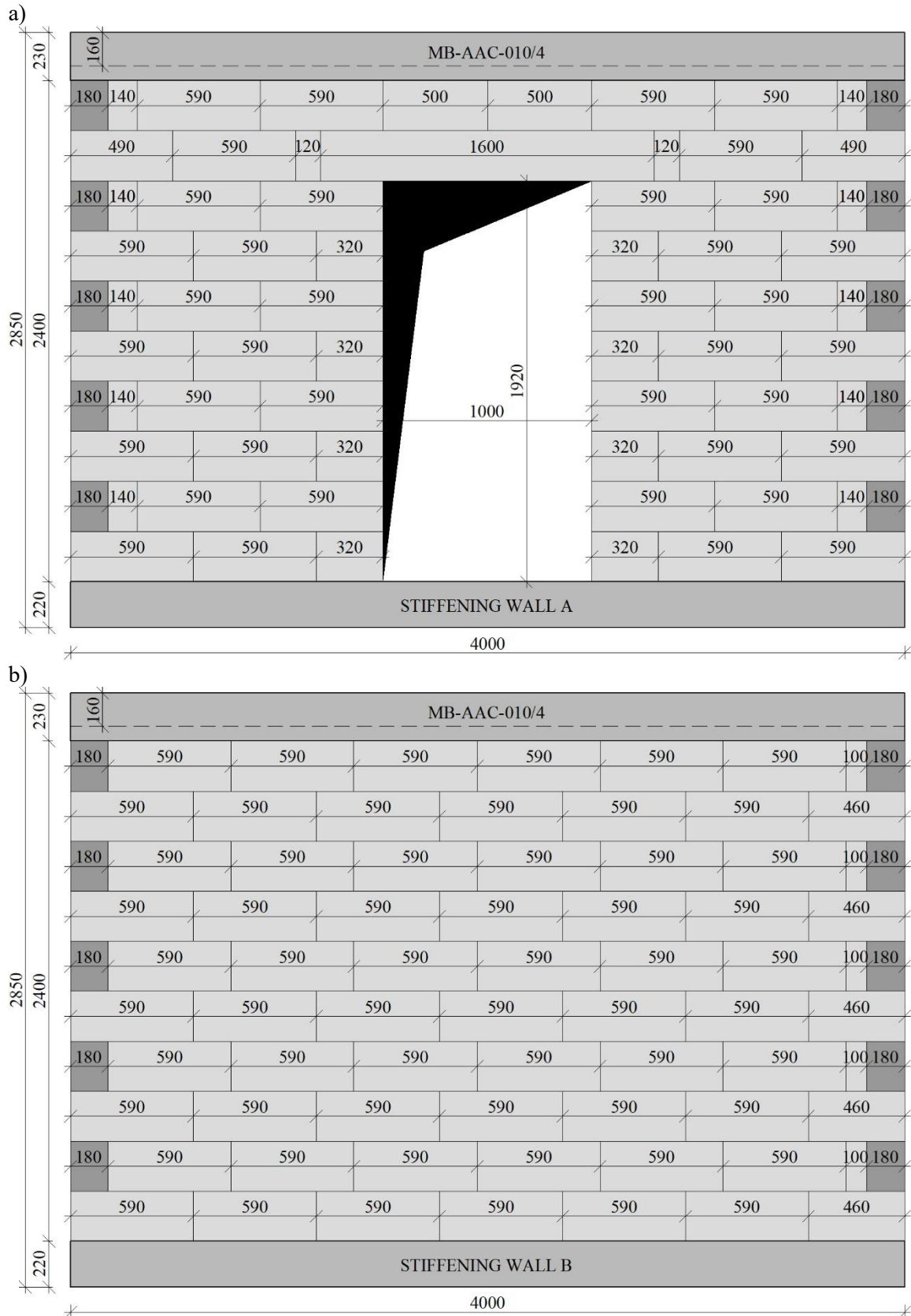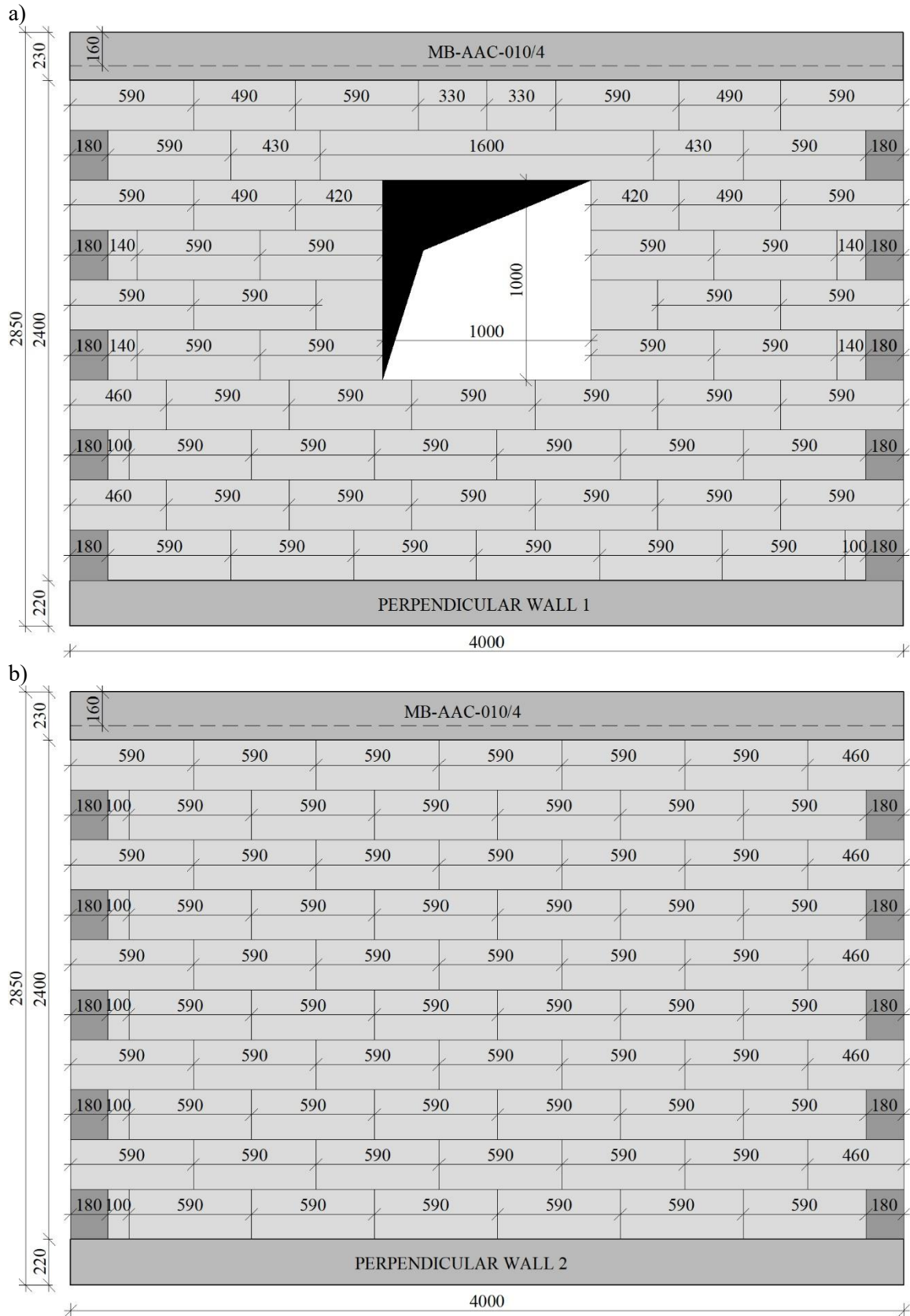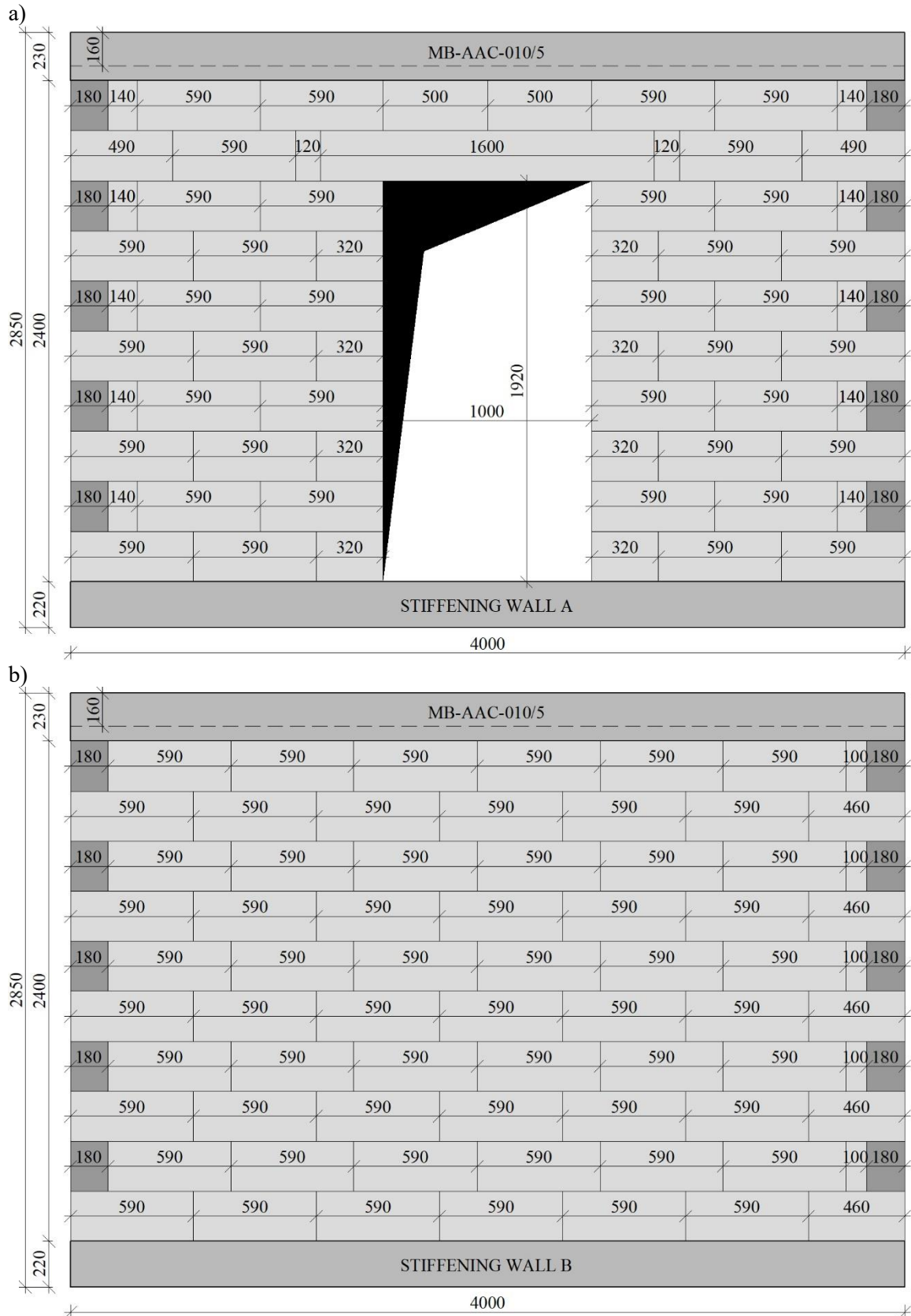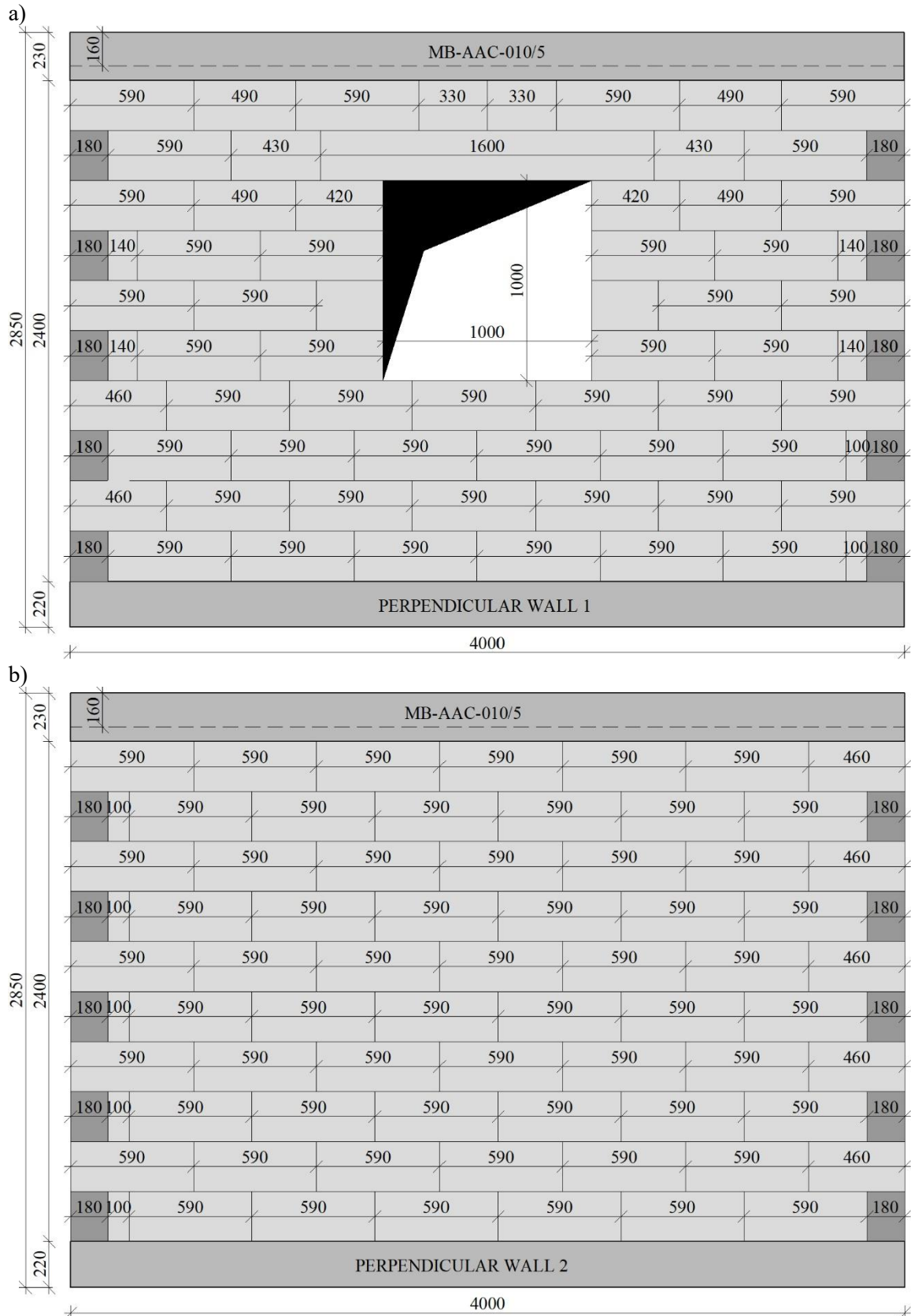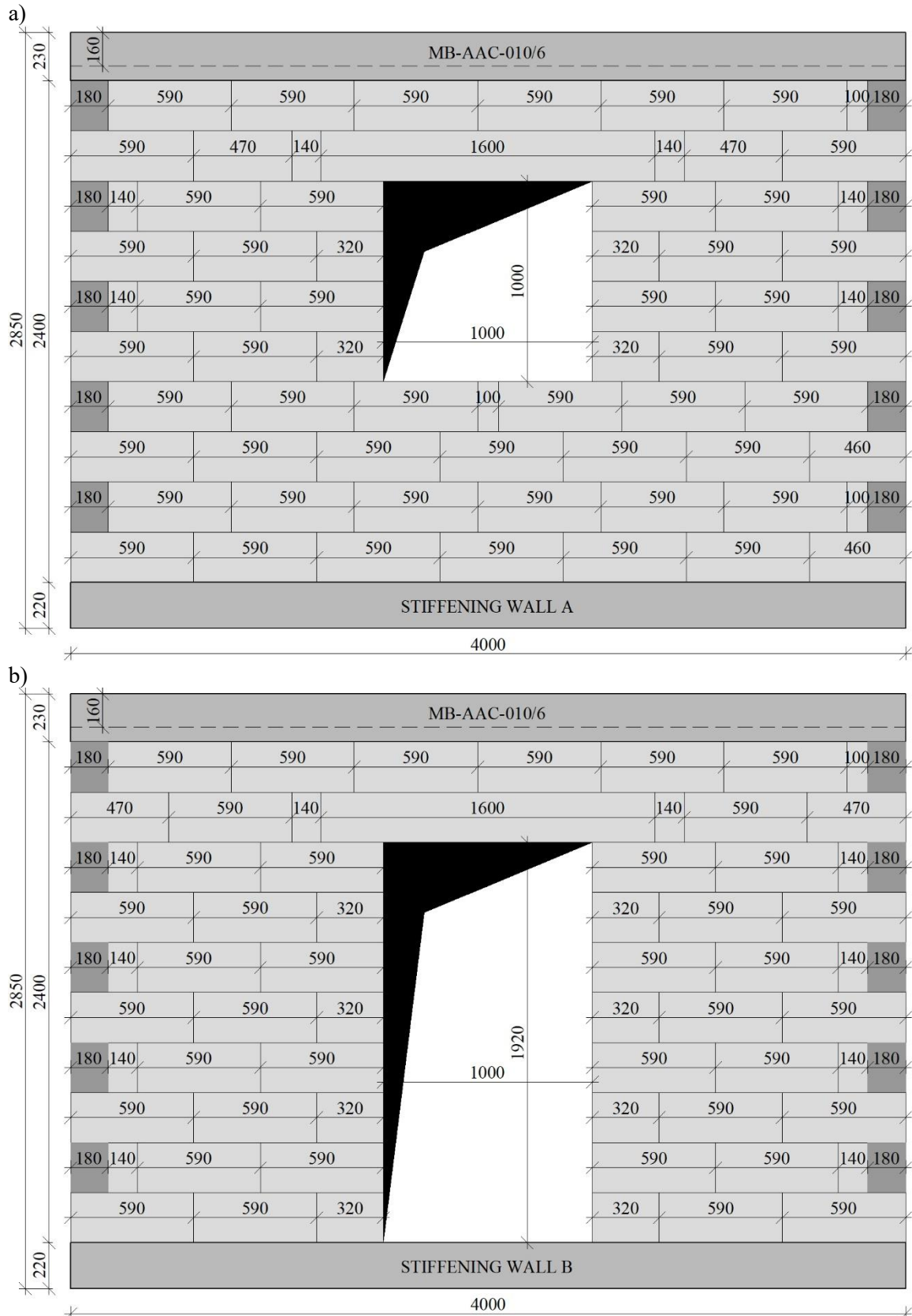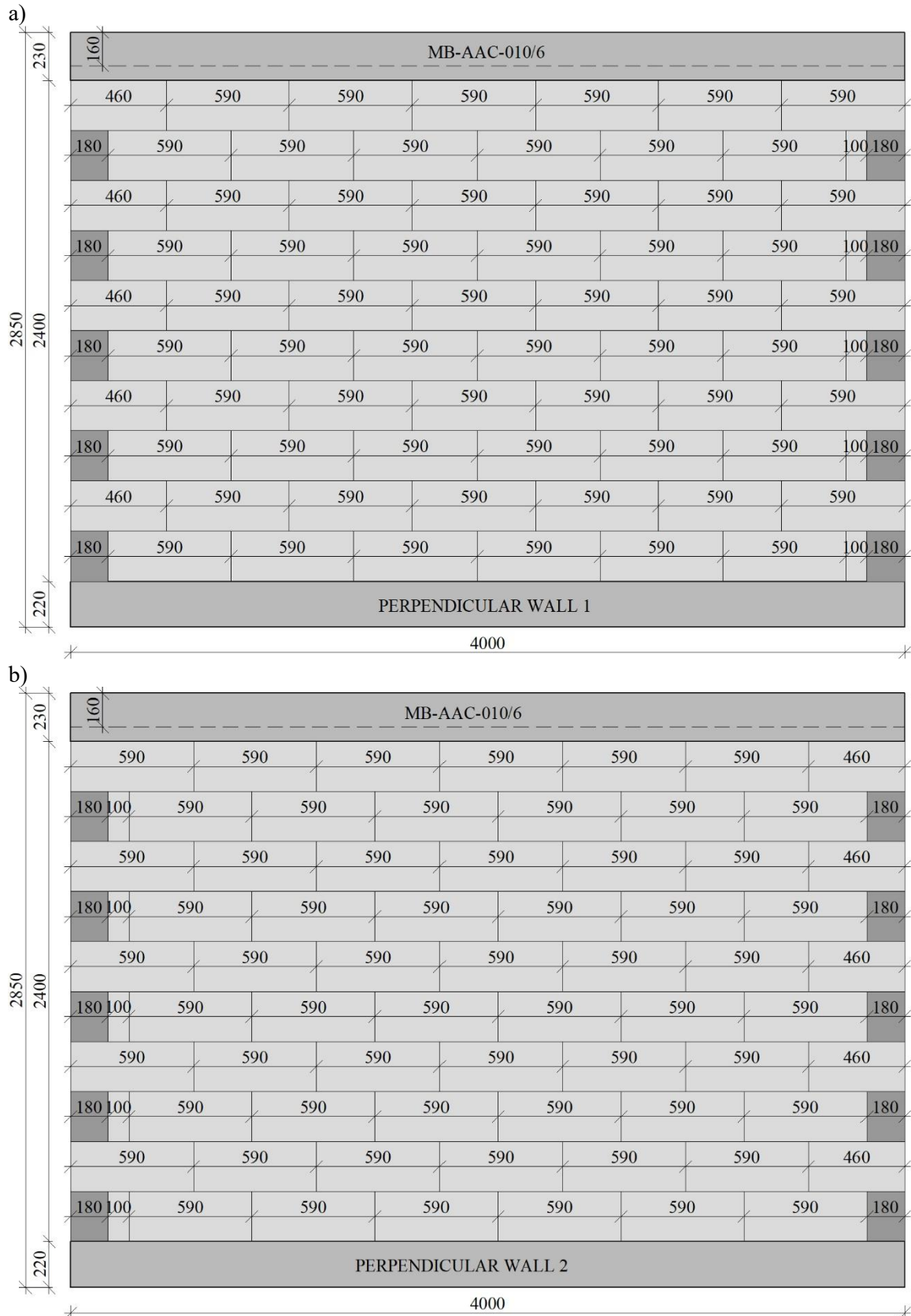Fig. A.5 Design of the MB-AAC-010/3 model: a) stiffening wall A, b) stiffening wall B

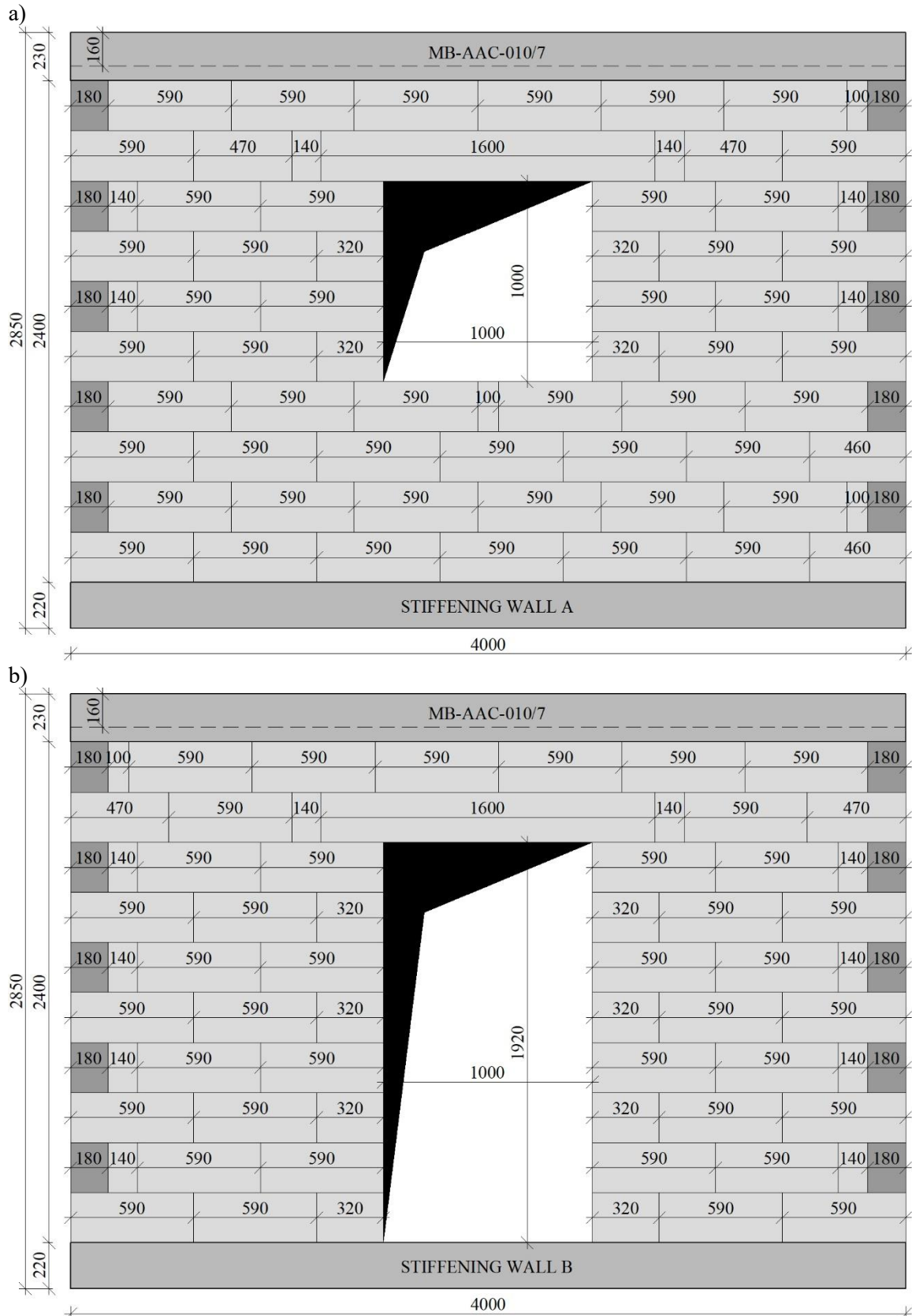Fig. A.6 Design of the MB-AAC-010/3 model: a) perpendicular wall 1, b) perpendicular wall 2

254

Fig. A.7 Design of the MB-AAC-010/4 model: a) stiffening wall A, b) stiffening wall B

Fig. A.8 Design of the MB-AAC-010/4 model: a) perpendicular wall 1, b) perpendicular wall 2

Fig. A.9 Design of the MB-AAC-010/5 model: a) stiffening wall A, b) stiffening wall B

257

Fig. A.10 Design of the MB-AAC-010/5 model: a) perpendicular wall 1, b) perpendicular wall 2

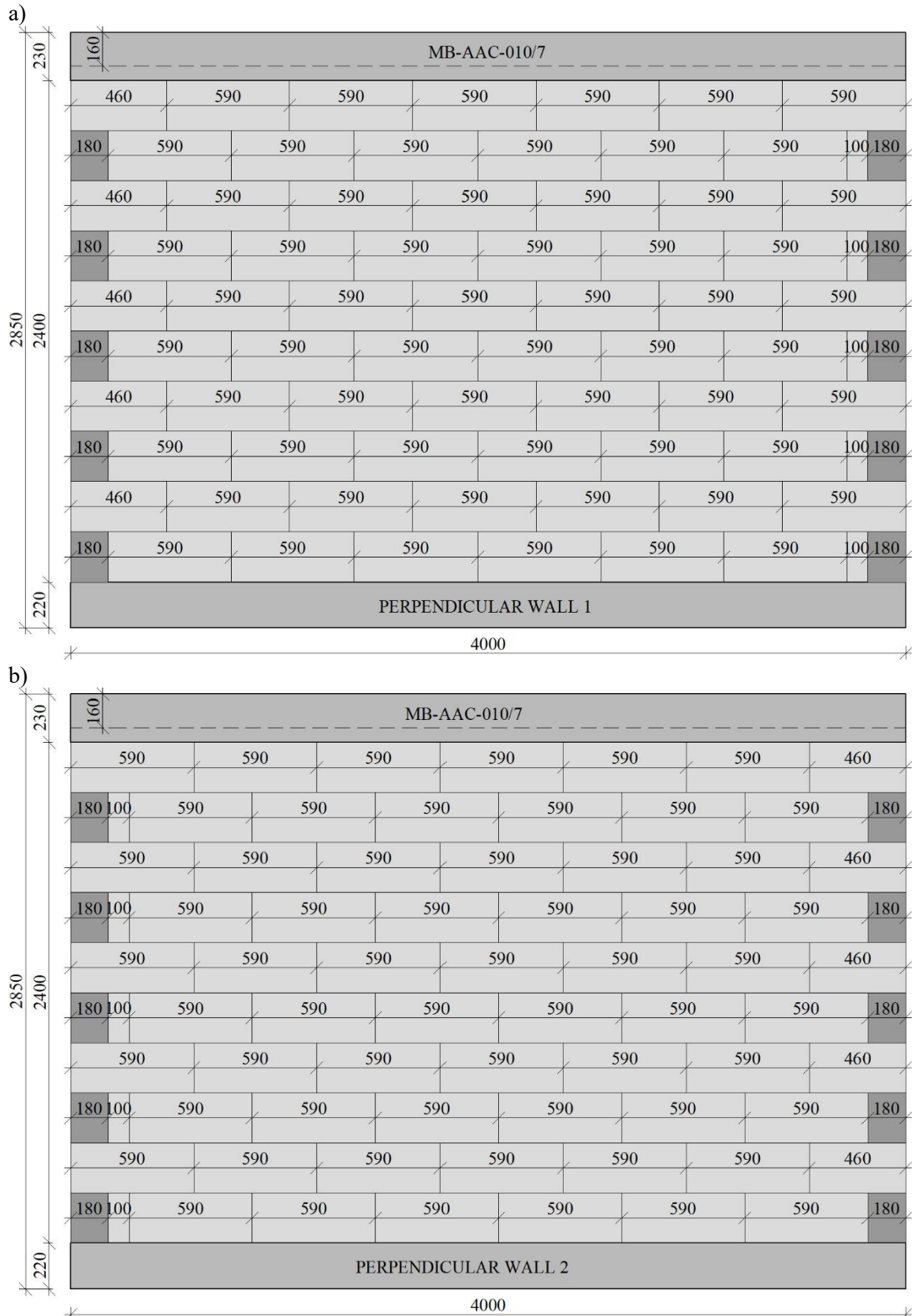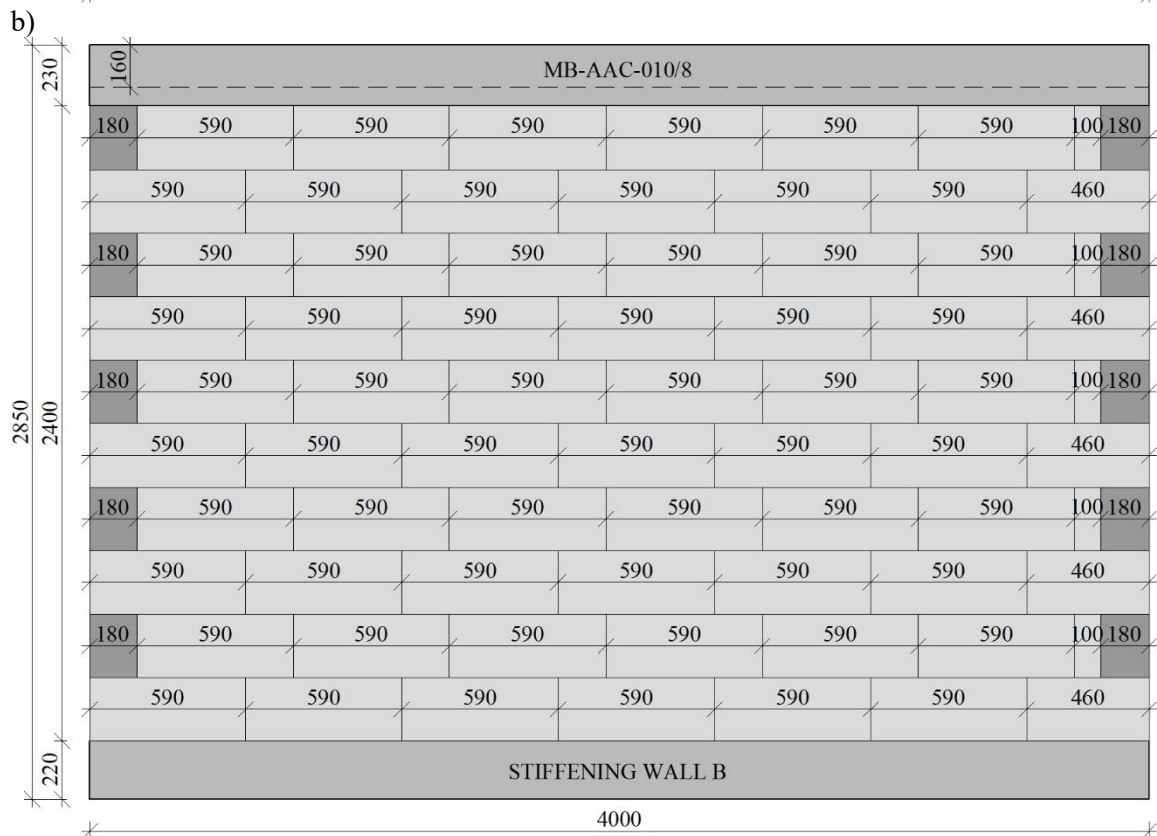Fig. A.11 Design of the MB-AAC-010/6 model: a) stiffening wall A, b) stiffening wall B

259

Fig. A.12 Design of the MB-AAC-010/6 model: a) perpendicular wall 1, b) perpendicular wall 2

a)

MB-AAC-010/7

STIFFENING WALL A

b)

MB-AAC-010/7

STIFFENING WALL B

Fig. A.13 Design of the MB-AAC-010/7 model: a) stiffening wall A, b) stiffening wall B

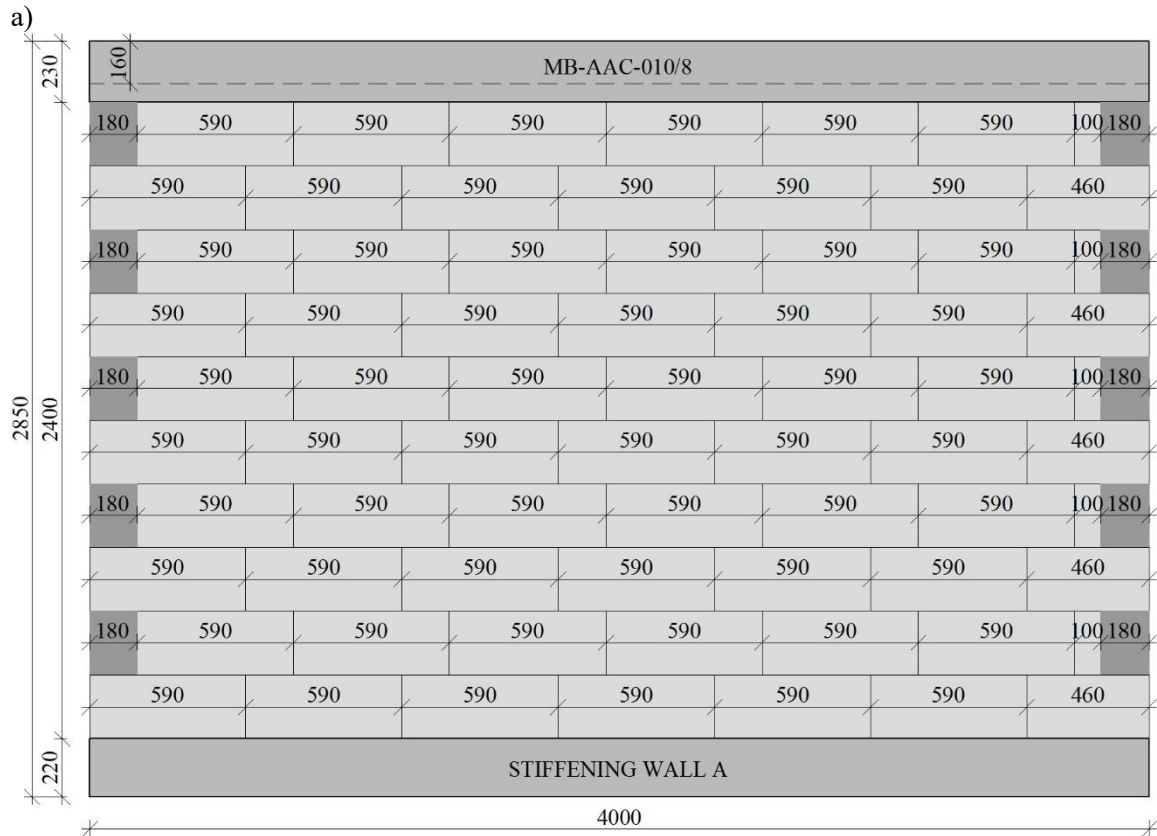Fig. A.14 Design of the MB-AAC-010/7 model: a) perpendicular wall 1, b) perpendicular wall 2

Fig. A.15 Design of the MB-AAC-010/8 model: a) stiffening wall A, b) stiffening wall B
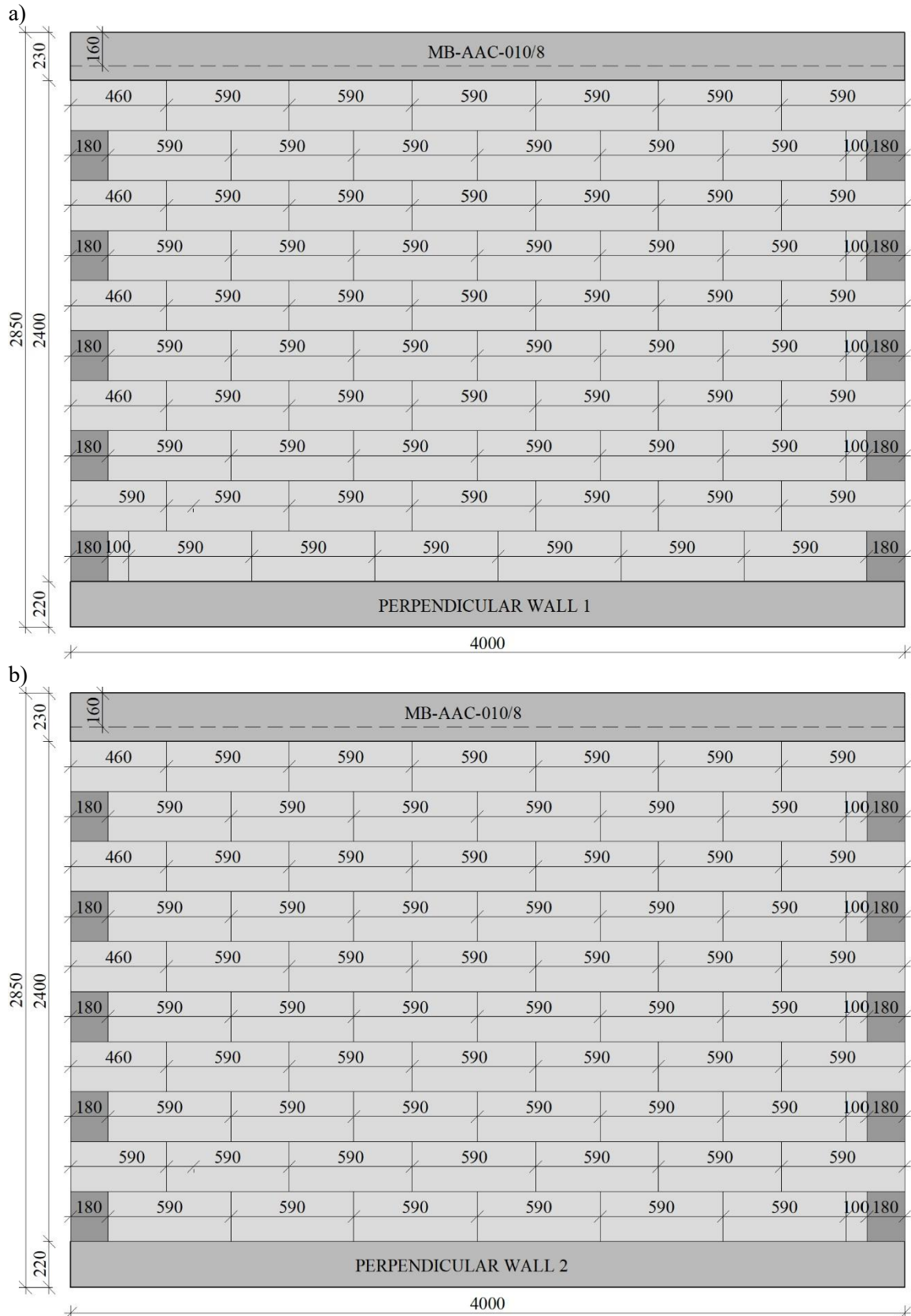
263

Fig. A.16 Design of the MB-AAC-010/8 model: a) perpendicular wall 1, b) perpendicular wall 2